



HAL
open science

The contributions of short waves to storm surges in coastal zones

Laura Lavaud

► **To cite this version:**

Laura Lavaud. The contributions of short waves to storm surges in coastal zones. Earth Sciences. Université de La Rochelle, 2022. English. NNT : 2022LAROS007 . tel-03814674

HAL Id: tel-03814674

<https://theses.hal.science/tel-03814674>

Submitted on 14 Oct 2022

HAL is a multi-disciplinary open access archive for the deposit and dissemination of scientific research documents, whether they are published or not. The documents may come from teaching and research institutions in France or abroad, or from public or private research centers.

L'archive ouverte pluridisciplinaire **HAL**, est destinée au dépôt et à la diffusion de documents scientifiques de niveau recherche, publiés ou non, émanant des établissements d'enseignement et de recherche français ou étrangers, des laboratoires publics ou privés.



La Rochelle Université

ÉCOLE DOCTORALE EUCLIDE

THÈSE

présentée par

Laura LAVAUD

Pour obtenir le grade de

DOCTEUR

Spécialité: Terre, Enveloppes fluides

**The contributions of short waves
to storm surges in coastal zones**

Soutenue le 27 janvier 2022 :

Devant la commission d'examen formée de :

Philippe Bonneton	Directeur de Recherche au CNRS, UMR 5805 EPOC	Rapporteur
Marta Marcos	Professeur IMEDEA	Rapportrice
Lucia Pineau-Guillou	Chercheur IFREMER	Examinatrice
Déborah Idier	Ingénieur-Docteur HDR, BRGM	Examinatrice
Laurent Testut	Physicien CNAP, UMR 7266 LIENSs	Examineur
Jean-François Breilh	Ingénieur-Docteur UNIMA	Invité
Kévin Martins	Post-doctorant, UMR 5805 EPOC	Co-Directeur
Xavier Bertin	Directeur de Recherche au CNRS, UMR 7266 LIENSs	Directeur

This PhD thesis was funded by Region Nouvelle-Aquitaine
and the UNIMA engineering company.

Remerciements, Acknowledgements

Il me tient à cœur que ces quelques lignes que je m'apprête à écrire, reflètent l'immense sympathie et gratitude que j'ai envers toutes les personnes dont j'ai croisé le chemin jusqu'à maintenant, et qui ont participé, de près ou de loin, à cette aventure haute en couleurs que j'ai vécue pendant 3 ans, la thèse.

Bien qu'étant originaire de l'île de Ré, je m'expatrie dans l'Est de la France après ma prépa, à l'INSA Lyon, pour y suivre des études de génie civil. J'y développe un goût prononcé pour la mécanique des fluides et en particulier l'hydrodynamique et l'hydraulique, ce qui m'amène à partir une année en échange à Polytechnique Montréal au Québec, où je me spécialise en génie fluvial. Je reviens alors en France pour réaliser mon stage de fin d'études chez SCE Aménagement et Environnement à Toulouse, où je travaille à modéliser le risque d'inondation fluvial en Occitanie. Merci à l'équipe du Pôle Eau, notamment Yann Comeaud et Damien Salgues, de m'avoir accueillie et permis de faire mes armes en modélisation. C'est alors qu'à la fin de mon stage, l'océan me rappelle au galop : comme une lumière qu'on allume, je sais maintenant que je veux étudier la physique de l'océan, et plus précisément, appliquer mes compétences en hydrodynamique et en modélisation pour étudier les submersions marines. Petit hic, je n'y connais pas grand-chose en océanographie... Alors que je cherche des masters spécialisés dans le monde entier, je finis par me rendre compte qu'il n'y a pas besoin de chercher si loin, puisque tout près de chez moi, à l'Université de La Rochelle, se trouve le LIENSs, un laboratoire de recherche interdisciplinaire qui abrite notamment une équipe étudiant la dynamique physique du littoral. Ni une ni deux, je contacte le responsable de l'équipe, Xavier Bertin, avec ma casquette d'ingénieure en génie civil spécialité marin d'eau douce, qui cherche à reprendre coûte que coûte le chemin de l'océan. C'est alors que l'aventure commence, Xavier me propose un contrat d'ingénieur d'études pour travailler sur la modélisation opérationnelle des surcotes, dans le cadre du projet OPENCoastS mené par le Laboratoire National de Génie Civil du Portugal (Le LNEC). Ces 8 mois vont me permettre de m'initier au monde de la recherche et d'en apprendre davantage sur les vagues, les marées, les tempêtes et les surcotes ! Au terme de ce travail, une bourse de thèse se confirme pour étudier les contributions des vagues dans les surcotes de tempête en zones littorales. Le sujet me fait rêver, et ce rêve ne tarde pas à se réaliser puisque Xavier m'accorde une nouvelle fois sa confiance en me permettant d'entreprendre cette thèse. 3 ans s'écoulent alors à étudier sans relâche les surcotes et le wave setup, au travers de campagnes de terrain, d'analyses de données, de discussions captivantes, de 1000 et 1 simulations numériques et de l'écriture d'articles scientifiques ! Merci à la Région Nouvelle Aquitaine et à l'UNIMA, en particulier Jean-François Breilh, qui ont cofinancé cette thèse de doctorat.

Ces 3 ans ont été extrêmement formateurs, tant du point de vue scientifique que personnel. Xavier, je te remercie de m'avoir fait confiance, mais surtout je te remercie d'avoir été si présent et disponible tout au long de ma thèse, d'avoir partagé ton savoir, ton enthousiasme

et ta passion débordante pour la physique du littoral, qui me donnaient toujours envie d'aller de l'avant. Tu as associé Kévin Martins à l'aventure, en lui permettant d'être co-directeur de ma thèse. Kévin, merci pour ces longs échanges à analyser finement les résultats. Le dénouement était parfois très concluant, parfois un peu moins avec ton fameux "C'est louche", alors on creusait encore ! Comme tu disais souvent, une thèse, c'est les montagnes russes. Et bien je crois que j'ai appris à franchir chaque sommet, les uns après les autres, même quand la pente était plus raide. Xavier, Kévin, j'ai eu une chance absolument incroyable de vous avoir eus comme directeurs de thèse. Merci pour tout.

In the scope of my thesis, I had the chance to participate to an international conference, *Coastal Sediments*, which took place in Florida in 2019, before the coronavirus pandemic forced us to stay behind our screen ... Besides the people I met during these congresses, I want to warmly thank the researchers with whom I had the opportunity to collaborate in France but also abroad: André Fortunato, Anabela Oliveira, Alberto Azevedo, Diogo Mendes, Maitane Olabarrieta, Joanna Staneva, Gael Arnaud, Marie-Noëlle Bouin, Bruno Castelle, Damien Sous, Héloïse Michaud, as well as the members of my thesis jury : Philippe Bonneton, Marta Marcos, Lucia Pineau-Guillou, Déborah Idier, Laurent Testut et Jean-François Breilh. I also want to thank Joseph Zhang, who is the main developer of the modelling system SCHISM I used during my thesis. I hope to have contributed to its development, in spite of a couple of unsuccessful simulations that made me want to tear my hair out !

Je tiens également à remercier l'ensemble des collègues et amis du LIENSs, pour cette ambiance chaleureuse et sympathique dans laquelle j'ai pu évoluer et pour leurs encouragements dans la dernière ligne droite. J'ai longtemps investi le bureau 114 avec Jérôme, fidèle au poste, JB, et Béné par la suite. Jérôme, merci pour ces innombrables cafés à l'Italienne qui me réveillaient tous les matins et pour tes remontrances quand je restais trop tard le soir ! JB, après avoir vogué entre Lyon, Montréal et Toulouse, j'ai redécouvert les bars de La Rochelle avec Céline et toi ! Béné, ce fut court mais intense, j'ai adoré nos bavardages et délires quotidiens ! Merci à tous les 3 pour ces bons moments ! Vous ne m'en avez pas voulu mais j'ai fini par changer de bureau car les travaux d'ILE 2 se faisaient bruyants. Me voilà chez "150 représente !" pour les 6 derniers mois de ma thèse, en compagnie de Mireia, Laurianne et Vincent. Je ne suis pas arrivée au meilleur moment car j'étais déjà lancée à plein régime dans l'écriture de mon dernier papier de thèse et la rédaction de mon manuscrit, mais on a bien rigolé et on va continuer car nous sommes encore là Vincent et moi pendant nos quelques mois de post-doc. On va finir par le faire ce repas de Noël ! Merci pour votre bonne humeur et vos encouragements dans ce moment très très intense qu'est la rédaction du manuscrit. Aucune campagne de terrain n'aurait été possible sans les compétences en instrumentation/logistique de terrain/levés bathymétriques, de Thibault et Denis, ainsi que les super structures en inox de Nicolas, qui ont servi à protéger les instruments lors des déploiements sur l'estran rocheux de La Cotinière. Merci à vous 3 pour votre aide indispensable ! Merci aussi à Laetitia pour avoir préparé mes ordres de mission de dernière minute (car tempête oblige !) en un temps record. Un clin d'œil particulier à Marc, avec qui nous nous sommes plongés corps et âme dans les méandres de SCHISM et WWM, pour en percer les plus profonds mystères et finalement finir nos thèses en même temps, avec quelques belles publications scientifiques à la clé. Merci pour nos longs échanges et discussions, qui ont été très complémentaires je crois (le streaming restera le top 1) et ton aide pendant les campagnes de terrain ! On se croisera sûrement dans un avenir proche, bonne route à Brest !

Un énorme merci aux copains du LIENSs et de La Rochelle en général, pour m'avoir

soutenue, encouragée et conseillée pour ceux/celles qui ont été docteur avant moi: Antoine, Diane, Céline, Fanny, Renaud, Clément, Dimitri, Carole, Treden, Baptiste, Marc ainsi que mes collègues de bureau cités un peu plus haut. Une pensée toute particulière à Anabelle, tu as pris le temps de corriger mon diaporama de soutenance et de me faire répéter, merci pour ton aide précieuse. Je tiens à remercier également tous mes amis qui vivent un peu plus loin. Nous nous sommes plus souvent eus au téléphone que vus ces derniers mois mais je vais maintenant pouvoir y remédier : Barbara, Léa, Bastien, Elodie, François, Alice, Matthieu, Romane et Lucie. Merci à tous pour votre soutien inconditionnel, que ce soit pour mon travail ou les moments personnels un plus durs auxquels j'ai dû faire face pendant ma thèse. Je n'en sors que plus forte.

Pour terminer, mon plus précieux pilier, ma famille. Merci à mes parents, Frédéric et Bénédicte, mon frère et ma sœur, Enguerrand et Sarah, ma grand-mère Mamé, mes oncles, mes tantes, cousins, cousines de Touraine et de Châtellerauld. Vous m'avez tous, à votre manière, énormément soutenue pendant ces 3 ans. Tatie Isa, les larmes me viennent en écrivant ces lignes car malheureusement tu n'auras pas vu la fin de cette odyssée. Mais je sais que tu as été là pendant ces derniers mois et que tu seras toujours là, tout près de chacun d'entre nous. Du haut de ta nouvelle maison, le phare de Cordouan, tu dois certainement observer les vagues chaque jour et essayer de belles tempêtes ! Tu finiras par mieux comprendre les vagues que moi ! Je t'embrasse. Mamé, merci pour tous ces petits plats que tu m'as préparés à chacun de tes passages à La Rochelle. Mes autres grands-parents qui sont là-haut, Gérard, Nicole et Papé, je sais que vous étiez là aussi. Papé, je sais à quel point tu aurais aimé me voir cheminer à travers la thèse de doctorat, toi qui me faisais faire mes exercices de maths plus jeune. Je sais que tu serais fier. A toi Papé, je te dédis ce manuscrit de thèse. Je ne pourrai jamais assez remercier mes parents, pour leur soutien indéfectible, la force qu'ils m'ont transmise, leur attention et leurs encouragements dans les très bons comme dans les moments plus difficiles de la thèse. Merci également pour cette incroyable soirée post-soutenance que vous m'avez organisée, je ne suis pas prête de l'oublier. Ma petite sœur, nous sommes là l'une pour l'autre et ce n'est que le début. Un grand merci également à Isabelle et Corinne pour leur bonne humeur et leurs encouragements continus, j'ai été heureuse de vous avoir comme voisines aux Minimes ! Pat' merci à toi pour ces fous rires et ces discussions sur le sens profond de la vie ! Enfin, une petite pensée pour mon chat Reef (non non pas de déformation professionnelle), et mon cheval, qui ont ponctué cette thèse de bouffées d'oxygène pleines de douceur et d'évasion, indispensables pour recharger les batteries et aller jusqu'au bout de cette aventure !



Scientific valorisation

Published Journal Articles

- Bertin, X., Mendes, D., Martins, K., Fortunato, A. B., and **Lavaud, L.** (2019), The closure of a shallow tidal inlet promoted by infragravity waves, *Geophysical Research Letters*, 46(12), 6804-6810, doi:10.1029/2019GL083527.
- Lavaud, L.**, Bertin, X., Martins, K., Arnaud, G., and Bouin, M.-N. (2020), The contribution of short-wave breaking to storm surges : the case Klaus in the Southern Bay of Biscay, *Ocean Modelling*, 156, 101710, doi:10.1016/j.ocemod.2020.101710.
- Lavaud, L.**, Pezerat, M., Coulombier, T., Bertin, X., and Martins, K. (2020), Hydrodynamics on a Rocky Shore under Moderate-energy Wave Conditions, *Journal of Coastal Research*, 95(SI), 1473-1479, doi:10.2112/SI95-284.1.
- Bertin, X., Mengual, B., de Bakker, A., Guérin, T., Martins, K., Pezerat, M., and **Lavaud, L.** (2020), Recent Advances in Tidal Inlet Morphodynamic Modelling, *Journal of Coastal Research*, 95(SI), 1016-1020, doi: 10.2112/SI95-198.1.
- Oliveira, A., Fortunato, A. B., Rogeiro, J., Teixeira, J., Azevedo, A., **Lavaud, L.**, Bertin, X., Gomes, J., David, M., Pina, J., Rodrigues, M., and Lopes, P. (2020), OPENCoastS: An open-access service for the automatic generation of coastal forecast systems, *Environmental Modelling & Software*, 124, 104585, doi:10.1016/j.envsoft.2019.104585.
- Mendes, D., Fortunato, A. B., Bertin, X., Martins, K., **Lavaud, L.**, Silva, A. N., Pires-Silva, A. A., Coulombier, T., and Pinto, J. P. (2020), Importance of infragravity waves in a wave-dominated inlet under storm conditions, *Continental Shelf Research*, 192, 104026, doi:10.1016/j.csr.2019.104026.
- Oliveira, A., Fortunato, A. B., Rodrigues, M., Azevedo, A., Rogeiro, J., Bernardo, S., **Lavaud, L.**, Bertin, X., Nahon, A., de Jesus, G., Rocha, M., and Lopes, P. (2021), Forecasting contrasting coastal and estuarine hydrodynamics with OPENCoastS, *Environmental Modelling & Software*, 143, 105132, doi:10.1016/j.envsoft.2021.105132.
- Lavaud, L.**, Bertin, X., Martins, K., Dausse, D., Coulombier, T., and Pezerat, M. (2022), Wave dissipation and mean circulation on a shore platform under storm wave conditions, *Journal of Geophysical Research: Earth Surface*, 127, e2021JF006466, doi:10.1029/2021JF006466.
- Pezerat, M., Bertin, X., Martins, K., **Lavaud, L.** (2022), Cross-shore distribution of the wave-induced circulation over a dissipative beach under storm wave conditions, *Journal of Geophysical Research: Oceans*, 127, e2021JC018108, doi:10.1029/2021JC018108.

Published conference proceedings

- Lavaud, L.**, Bertin, X., Martins, K., and Arnaud, G. (2019), The contribution of short wave breaking in the storm surge associated with Klaus (January 24, 2009) in the Southern Bay of Biscay, *In: Coastal Sediments 2019: Proceedings of the 9th International Conference*, 1411-1423, doi:10.1142/9789811204487_0123.
- Lavaud, L.**, Lechevalier, A., Coulombier, T., Bertin, X., and Martins, K. (2020), Effet de la végétation sur la dissipation des vagues au niveau d'un pré salé, *In: XVIèmes Journées Nationales Génie Côtier - Génie Civil, Paralia Editions*, 85-94, doi:10.5150/jngcgc.2020.010.

Conferences and seminars

- Lavaud, L.**, Bertin, X., Martins, K., and Arnaud, G., The contribution of short wave breaking in the storm surge associated with Klaus (January 24, 2009) in the Southern Bay of Biscay, *Coastal Sediments 2019, Tampa/St Petersburg, Florida, USA, 27-31 May 2019*, oral presentation.
- Lavaud, L.**, Oliveira, A., Bertin, X., Fortunato, A. B., Rogeiro, J., Azevedo, A., and Teixeira, J., Coastal circulation on-demand forecasts: the OPENCoastS service, *ICE Coastal Management 2019, La Rochelle, France, 24-26 September 2019*, oral and poster presentations.
- Lavaud, L.**, Lechevalier, A., Coulombier, T., Bertin, X., Martins, K., Wave current vegetation interactions over a schorre along the Western Coast of France, *Smart Urban Coastal Sustainability Days, online from La Rochelle, France, 8-9 April 2021*, oral presentation.
- Lavaud, L.**, Pezerat, M., Coulombier, T., Bertin, X., Martins, K., Hydrodynamics on a Rocky Shore under Moderate-energy Wave Conditions, *International Coastal Symposium 2021, online from Seville, Spain, 3-5 May 2021*, oral presentation.
- Lavaud, L.**, Bertin, X., Martins, K., Pezerat, M., Guérin, T., The contribution of wave setup to sea-level variations: from the surf zone to lagoons and estuaries, *NOAA Coastal Ocean Modeling Science Seminar, online, 18 May 2021*, oral presentation.
- Lavaud, L.**, Bertin, X., Martins, K., Pezerat, M., Coulombier, T., Dausse, D., Wave dissipation and mean circulation on a rocky shore platform under storm conditions, *Coastal Dynamics 2021, online from Delft, Netherlands, 28 June - 2 July 2021*, oral presentation.

Title: The contributions of short waves to storm surges in coastal zones

Abstract: Storm surges and associated coastal flooding can result in major catastrophes. Storm surges correspond to a temporary rise in sea level driven by atmospheric pressure gradients, wind and short waves. In particular, the dissipation of short waves in the nearshore drives a mean water level increase, the wave setup, which contributes to storm surges. This PhD thesis examines the contributions of short waves to storm surges, notably the wave setup, in contrasting coastal environments. To that end, the analysis of field data is combined with high-resolution numerical modelling. First, this work investigates the contribution to storm surges of very large storm waves breaking at the inlet of two wave-sheltered environments. The results indicate that the resulting wave setup contributes up to 40 % and 23 % to the storm surge peak in the Adour Estuary and the Arcachon Lagoon respectively. Second, the dissipation of storm waves and the resulting depth-varying circulation are analysed at a rock shore platform. Two counteracting effects of the high bottom roughness on the wave setup are identified: (1) waves suffer a strong dissipation by bottom friction, which reduces the wave setup compared to a smooth bottom; (2) the wave-induced circulation over a rough bottom enhances the wave setup. Lastly, waves and wave setup dynamics are investigated on a salt marsh. During the studied wind sea event, the halophytic vegetation of the salt marsh accounts for 65 % of the wave dissipation, which reduces the wave setup compared to a case without vegetation. New field measurements on salt marshes are needed to explore the effect of wave non-linearities on the wave setup in vegetation fields.

Keywords: storm surges, short waves, wave setup, coastal zone, 3D numerical modelling, in-situ measurements

Titre : Contributions des vagues dans les surcotes de tempête en zones littorales

Résumé : Les surcotes et submersions marines associées aux tempêtes peuvent entraîner des catastrophes majeures. Les surcotes correspondent à une élévation temporaire du niveau moyen de la mer, induite par les gradients de pression atmosphérique, le vent et les vagues. La dissipation des vagues en zone littorale génère une augmentation du niveau moyen à la côte, le wave setup, qui contribue aux surcotes. Cette thèse de doctorat examine les contributions des vagues aux surcotes, notamment le wave setup, dans différents milieux littoraux en combinant l'analyse de données in-situ et la modélisation numérique à haute résolution. En premier lieu, la contribution du déferlement de vagues de tempête à l'embouchure de deux environnements abrités des vagues est étudiée. Les résultats montrent que le wave setup généré représente 40 % du pic de la surcote dans l'Estuaire de l'Adour et 23 % dans le Bassin d'Arcachon. La dissipation des vagues et la circulation moyenne induite sont ensuite analysées sur un estran rocheux. La forte rugosité de l'estran a deux effets antagonistes sur le wave setup : (1) les vagues sont fortement dissipées par frottement au fond, ce qui réduit le wave setup par rapport à un fond sableux ; (2) la circulation induite par les vagues sur un fond rugueux augmente le wave setup. Enfin, la dissipation des vagues et le wave setup sont examinés sur un pré salé. Lors de l'épisode de mer de vent étudié, la végétation halophyte du pré salé explique 65 % de la dissipation des vagues, ce qui réduit le wave setup par rapport à un cas sans végétation. De nouvelles mesures sont nécessaires pour analyser l'effet sur le wave setup des non-linéarités des vagues sur un fond végétalisé.

Mots clés : surcotes, vagues, wave setup, zone littorale, modélisation numérique 3D, mesures in-situ

Contents

1	Introduction	23
2	State of the art	31
2.1	Storm surge generation mechanisms	31
2.1.1	Atmospheric forcing	32
2.1.2	The effects of short waves	33
2.1.3	Additional processes and parameters controlling storm surges	37
2.2	Progress in storm surge numerical modelling	38
2.2.1	Overview of the historical development of storm surge modelling	38
2.2.2	Importance of accounting for waves in storm surge modelling	41
2.3	Modelling the effects of short waves on the mean circulation	43
3	The modelling system	47
3.1	The spectral wave model WWM-II	49
3.1.1	Governing equations	49
3.1.2	Source terms S_{nl3} and S_{nl4}	50
3.1.3	Source terms S_{in} and S_{ds}	50
3.1.4	Source terms S_{br} and S_{bot}	51
3.1.5	Source term S_{veg}	54
3.1.6	Surface roller model	54
3.1.7	Numerical approaches	55
3.2	Hydrodynamic model	56
3.2.1	3D configuration - Vortex force formalism	56
3.2.2	2DH configuration - Radiation stress formalism	61
3.2.3	Numerical approaches	63
4	Data acquisition and processing	65
4.1	Data acquisition techniques	65
4.1.1	In-situ observations of random waves	65

4.1.2	In-situ observations of water levels	67
4.1.3	In-situ observations of currents	68
4.2	Data processing	69
4.2.1	Estimation of storm surges	69
4.2.2	Relative estimation of wave setup	70
4.2.3	Reconstruction of the free surface from pressure measurements	71
5	Spatial extension of the wave setup in estuaries and lagoons	81
5.1	Introduction	81
5.2	The studied area and storm	82
5.2.1	Study area	82
5.2.2	The storm Klaus	83
5.3	Model implementation	84
5.4	Wave and water level observations	85
5.5	Modelling results	85
5.5.1	Atmospheric forcing	86
5.5.2	Wave predictions	86
5.5.3	Storm surge and water level predictions	87
5.6	Contribution of wave breaking to storm surges	90
5.6.1	Model predictive skills	90
5.6.2	Momentum balance	91
5.6.3	Tidal modulation of the wave setup	94
5.6.4	Sensitivity of storm surge and wave setup calculation to spatial resolution	96
5.7	Conclusion	97
6	Wave dissipation and mean circulation on a shore platform	101
6.1	Introduction	101
6.2	Study area and field experiments	103
6.2.1	Study area	103
6.2.2	Field experiments	105
6.3	Model implementation	106
6.4	Results	108
6.4.1	Wave predictions	108
6.4.2	Cross-shore and long-shore current predictions	111
6.4.3	Storm surge and wave setup predictions	112
6.5	Discussion	113

6.5.1	Model sensitivity to parameterizations	113
6.5.2	Relative importance of wave breaking to frictional dissipation on the platform	115
6.5.3	Effect of the wave-induced circulation on wave setup	116
6.6	Conclusion	120
7	Wave dissipation and mean circulation on a salt marsh	121
7.1	Introduction	121
7.2	Study area	124
7.3	Field campaign	125
7.4	Model implementation	128
7.5	Results	129
7.5.1	Incident wave conditions	129
7.5.2	Wave transformation along the cross-shore transect	129
7.5.3	Energy density spectra evolution along the cross-shore transect . . .	131
7.5.4	Water level predictions along the cross-shore transect	133
7.6	Discussion and perspectives	135
7.6.1	Discussion	135
7.6.2	Future field campaign	136
8	Conclusions and perspectives	139

List of Figures

1.1	(a) Coastal flooding during hurricane Katrina in the Gulf of Mexico and (b) in March 2010 at Wissant (France) (credits: (a) NOAA ; (b) www.geodunes.fr).	24
1.2	(a) Damages caused by (a) the storm Xynthia in the village of La Faute-sur-Mer (France), (b) cyclone Nargis in the Gulf of Bengal and (c) hurricane Katrina in New Orleans (USA) (credits: (a) actu.fr ; (b) www.burmapartnership.org ; (c) www.rts.ch).	24
1.3	Schematic processes that contribute to the total water level at the coast.	26
1.4	Photos of (a) the shore platform near La Cotinière on Oléron Island and (b) the salt marsh of Brouage (France), on which wave and wave-induced hydrodynamics have been studied in this work (credits: (a) Laura Lavaud ; (b) Antoine Lechevalier).	28
2.1	(a) Data assimilated wind field during hurricane Ike (2008) in the Gulf of Mexico, (b) simulated storm surge with Coriolis forcing and (c) simulated storm without Coriolis forcing. Adapted from <i>Kennedy et al.</i> (2011).	33
2.2	Profile of the mean water level and the envelope of the wave height for two experiments conducted by <i>Bowen et al.</i> (1968). Adapted from <i>Dodet et al.</i> (2019b).	36
2.3	Scheme for operational surge forecasting. From <i>Flather</i> (1979).	39
3.1	Schematic description of the modelling system with forcing conditions and exchanged variables described in the following sections. *WW3 referred to the WaveWach III spectral wave model of <i>Tolman</i> (1992).	48
3.2	(a) Hybrid SZ vertical coordinate system and (b) 3D computational unit in SCHISM where variables are solved. Figure adapted from <i>Zhang and Baptista</i> (2008).	63
4.1	Non-directional Biscay buoy (station 62001) located at 45.230 N 5.000 W in the Bay of Biscay (at 4500 m depth) operated by UK Met Office and Meteo France (credits : www.ndbc.noaa.gov).	66
4.2	Instruments deployed in the subtidal zone during the field campaign on the shore platform : (a) 600 kHz ADCP on a weighted tripod structure and (b) pressure sensor housed in a steel tube fixed to an anchor.	68

4.3	Instruments deployed in the intertidal zone during the field campaign on the shore platform : (a) ADCP, (b) ADV and (c) pressure sensors. They are housed in stainless steel tubes screwed to the bedrock to protect them from stone motions (credits : Laura Lavaud).	69
4.4	(a) Water surface elevation and tidal prediction and (b) storm surge, during the storm Xynthia (2010) at La Pallice tide gauge (La Rochelle, France). . .	70
4.5	Sketch detailing the variables used in the procedure for computing the wave setup between different pressure sensors. d_i is the bathymetry relative to mean sea level (MSL), h_i is the mean water depth and $\bar{\eta}_i$ is the mean free surface elevation with $i = 1, 2$. $\bar{\eta}_s$ corresponds to the wave setup at PT 2. . .	71
4.6	Physical variables considered in the problem. d is the bathymetry relative to mean sea level at $z = 0$, $\bar{\eta}$ is the mean free surface elevation corresponding to the low-frequency contributions to the free surface variations (tides, storm surges including wave setup) and the blue star indicates the position of the pressure sensor in the water column.	72
4.7	Comparison of the noise floor between a RBR Solo and NKE Sp2T pressure sensors. For the NKE sensor, the noise floor appears from 0.5 Hz and reaches $\sim 10^{-5} \text{ m}^2 \cdot \text{Hz}^{-1}$, while for the RBR sensor, the noise floor appears from 0.6 Hz and is one order of magnitude lower.	74
4.8	Comparison of (a) the mean water depth, (b) significant wave height H_{m0} , (c) mean wave period T_{m02} and (d) continuous peak period T_{pc} computed from the free surface recorded by the AST ($f_{max} = 0.2 \text{ Hz}$) and from the free surface reconstructed with the TFM ($f_{max} = 0.2 \text{ Hz}$), from bottom-mounted pressure sensor measurements. (e) Dispersion parameter μ computed at the peak frequency where the black dotted line corresponds to $\mu = 0.3$	77
4.9	(a) and (b), comparison of the energy density spectra calculated with the TFM and the SNL, with the spectra obtained from the AST data, for the bursts 585 ($H_{m0}=2.90 \text{ m}/T_{pc}=19 \text{ s}/\mu=0.17$) and 790 ($H_{m0}=2.45 \text{ m}/T_{pc}=15 \text{ s}/\mu=0.26$). The vertical light-blue dashed lines correspond to the cut-off frequency applied to the TFM ($f_{max} = 0.2 \text{ Hz}$).	78
4.10	Fraction of the time-series of the cross-shore current at the ADV. The blue line corresponds to the despiking data at 16 Hz, the red line is the low-pass filtered (despiking) data with a 0.04 Hz cut-off frequency and the orange line is the 20 min-averaged (despiking) data.	79
4.11	Levelling procedure during the field campaign on the shore platform (credits : Laura Lavaud).	80
5.1	(A) Bathymetric map and extension of the computational domain (red dash-dotted line), the storm track (blue dashed line and crosses) and the wave buoys (blue triangles) used in this study. (B) and (C) Detailed bathymetry of the studied areas with location of the tide gauges (black stars). The black box in (B) corresponds to the adjacent beach where the sensitivity of storm surge and wave setup predictions to the grid resolution is analysed.	83
5.2	Modelled (blue solid line) against observed wind speeds and sea level pressure (black dots) at Cap Ferret (A) and Bayonne (B) stations.	86

5.3	Observed (black dots) against modelled wave parameters (blue solid line) at Cap Ferret, Biscay and Bilbao buoys during Klaus.	87
5.4	Observed (black dots) against modelled storm surges with the (3D) baseline model (red solid line) and the (3D) model without wave forces (blue dashed line) at Bayonne (left) and Arcachon (right).	88
5.5	Storm surge (in m) simulated with wave forces (a,b), without wave forces (c,d) and their difference (e,f), at the Adour Estuary (left) and the Arcachon Lagoon (right). The white color corresponds to dry nodes in the tide-only simulation.	89
5.6	Observed (black dots) against modelled storm surges with the 3D baseline model (red solid line) and the 2DH model (blue dashed line) at Bayonne (left) and Arcachon (right).	91
5.7	Leading terms of the momentum balance at mid-ebb and mid-flood : wave forces (a-b), barotropic pressure gradient term (c-d), bottom stress term (e-f) and wind stress term (g-h), at mid-ebb (left) and mid-flood (right). The magnitude and direction of each term are represented by the map colors and the vectors respectively.	93
5.8	(A) Constant water elevations prescribed at the open boundary (blue circles). (B) Tidal modulation of the wave setup at Arcachon (green squares) and Bayonne (red circles) during a tidal cycle.	95
5.9	Simulated storm surge in the inner part of the lagoon and at the adjacent beach to the south, with the baseline model resolution, 200 m resolution and 1000 m resolution.	97
5.10	(A) Measured (black crosses) against CFSR wind speed with correction (red dashed line) and original data (blue line). (B) Observed (black dots) against modelled storm surges with the corrected wind speed (red dashed line) and the original wind speed (blue line).	99
6.1	Location of the study area (red square), Oléron wave buoy (blue triangle), meteorological station (green star) and extension of the computational domain (blue line) (a). Bathymetry of the study area relative to mean sea level (MSL) with location of stations 1 and 2 (b) and stations 3 to 11 (c), deployed during the field campaign in storm wave conditions.	104
6.2	Cross-shore profile of the intertidal zone with location of the stations 3 to 11 deployed during storm wave conditions.	104
6.3	Sea surface elevation on March 12 afternoon at high tide at the intertidal sensors without correction (a) and corrected from the wave setup obtained from the model (b).	106

6.4	Observed (black dots) against significant wave height H_{m0} modelled with the baseline model using Madsen's formulation with $k_n = 0.13$ m for rocky areas and 0.05 m outside (model 1), the model using the Madsen's formulation with k_n set uniform to the default value 0.05 m (model 2) and the model using the JONSWAP formulation with $C_f = 0.038$ m ² .s ⁻³ (model 3), at the second high tide along the intertidal transect instrumented during fair weather conditions. The black crosses correspond to where statistical errors are computed (RMSE, BIAS).	108
6.5	Assessment of the model at the offshore Oléron buoy with comparisons of the modelled (blue line) against observed significant wave height H_{m0} , peak direction P_{dir} (black dots), mean wave period $T_{m0,2}$ (red dots) and peak period T_p (green dots).	109
6.6	Assessment of the model at the subtidal sensors (PT 1 and PT 2) with comparisons of the modelled (blue line) against observed water depth, H_{m0} and $T_{m0,2}$ (black dots).	110
6.7	Modelled (blue line) against observed water depth at the subtidal sensor PT 1 (panel a) and assessment of the model at the intertidal sensors (from PT 4 to PT 10) with comparisons of the modelled (red line) against observed H_{m0} (black dots) (panels b to g).	111
6.8	Water depth at PT 6 (a). Measured cross-shore (b) and longshore (c) currents (black dots) against modelled quasi-Eulerian velocities (blue line) at the vertical position of the ADV (0.25 m above the bed, PT 7 location).	112
6.9	Observed (black dots) against modelled storm surges with the baseline model (blue line), with the default JONSWAP formulation (red dashed line) and with $B = 1$ in the depth-induced breaking formulation (orange dashed dotted line), at the intertidal PTs.	113
6.10	Water levels (a,b), H_{m0} (c,d), rates of wave energy dissipation by depth-induced breaking and bottom friction normalized by the water density (e,f) and their contribution to total wave energy flux dissipation (g,h) along the transect from the subtidal to the intertidal zone, in fair weather and storm wave conditions. The instrumented profiles during the two field campaigns were not exactly the same (200 m spacing), explaining the differences observed in the bathymetry (black lines in (a) and (b)).	116
6.11	Observed against modelled surges with a 3D (blue circles) and a 2DH simulation (red squares). The dashed lines correspond to the 0.8 :1 and 0.7 :1 lines.	117
6.12	Contribution of each right-hand side terms of Eq. 6.1 to the wave setup ($\bar{\eta}_{\hat{u}}$, $\bar{\eta}_{\hat{w}}$, $\bar{\eta}_{\nu}$ and $\bar{\eta}_{wf}$), total contribution of these terms ($\bar{\eta}_{\hat{u}+\hat{w}+\nu+wf}$), compared to the wave setup obtained from the model ($\bar{\eta}_{model}$), on a sandy beach and on a rock platform for 1 :200, 1 :50 and 1 :20 slopes.	119
7.1	(a) Location of the study area in the Bay of Biscay (red square), open boundary of the computational grid (blue line) and Oléron buoy (blue triangle). (b) Study area with location of the studied transect on the salt marsh of Brouage (red star).	125

7.2	Photos of (a) <i>Spartina maritima</i> and (b) <i>Halimione portulacoides</i> . (c) Location of the sensors and plant species along the cross-shore transect.	125
7.3	(a) Wind speed, (b) wind direction, (c) tides at the nearby tide gauge of Aix Island and (d) significant wave height at the ADV.	126
7.4	Deployment of (a) the ADCP and (b) a pressure sensor on the cross-shore transect (credits : Antoine Lechevalier).	127
7.5	Comparison between modelled and observed (a) water depth, (b) significant wave height H_{m0} and (c) mean wave period T_{m02} at the first sensor (ADV) on the studied transect. The black dashed line corresponds to the time of the time-series presented in Figure 7.6.	129
7.6	(a) Comparison between observed and modelled significant wave height H_{m0} obtained from VEG (blue line) and NOVEG (red dashed line) simulations, along the studied transect during the high tide of March 09 afternoon. (b) Bathymetry (black line) and surface elevation (blue line) along the transect (both given relative to the topographic elevation of the first sensor). The water depth is computed as the difference between the blue and black lines along the transect.	130
7.7	(a) Measured against modelled wave height obtained from (a) VEG and (b) NOVEG simulations at all sensors during the entire experiment period. The dashed lines correspond to the 0.8 :1 and 1.2 :1 lines. The statistical errors at calculated at the ADCP and the PTs.	130
7.8	Evolution of the measured energy density including in a period of 2 h hours centered on the high tide of March 09 afternoon. At PT 1, the spectra are truncated since the sensor stopped measuring at that time. The black lines correspond to a change in order of magnitude.	131
7.9	Comparison between measured and modelled energy density spectra with VEG and NOVEG simulations (from the ADV to PT 4) at high tide on March 09 afternoon. The vertical orange dashed lines correspond to the cut-off frequencies. The grey curves in panels (e) and (f) indicate energy associated with instrument noise.	133
7.10	(a) Topography (black line) and surface elevation (blue and red lines) along the transect (both given relative to the topographic elevation of the first sensor). The water depth is computed as the difference between the blue/red and black lines along the transect. (b) Observed and modelled significant wave height with VEG and NOVEG simulations. (c) Modelled wave setup that develops from the ADV, computed as the change in mean free surface elevations between the ADV and shoreward computational grid nodes. . . .	134
7.11	Photo of waves propagating on the salt marsh of Brouage during the field campaign conducted in 2016. We can note a net decrease in the wave height when waves entering the vegetation field (credits : Antoine Lechevalier). . .	137

Chapitre 1

Introduction

Coastal areas have always been attractive due to the invaluable environment that they offer for the development of societal, economic and cultural activities. The near-coast zone, defined as the region closer than 100 km from the coastline and elevation less than 100 m above mean sea level (*Kummu et al.*, 2016), has been densely urbanized over the 20th and early 21st centuries, with urbanisation rates rising from 25% in year 1900 to 63% in year 2010. Subsequently, the population living in these areas increased from 0.4 billion in year 1900 to 1.9 billion in 2010, with 17 megacities hosting more than 5 million inhabitants (*Kummu et al.*, 2016). Current trends as well as scenarios indicate that demographic growth in coastal zones will continue (*Neumann et al.*, 2015; *Kummu et al.*, 2016). For instance, *Neumann et al.* (2015) suggested that the population living in low-lying coastal zones (elevation less than 10 m above mean sea level) in 2000 will increase by 50% by 2030 and will double by 2060. While hosting a growing part of the population worldwide, coastal zones are particularly threatened by the ongoing climate change through the combination of sea level rise and possible changes in storminess (e.g., *Pachauri et al.*, 2014; *Tasnim et al.*, 2015; *Oppenheimer et al.*, 2019). With current rates of about 3-4 mm/yr, sea level rise promotes shoreline erosion (*Anderson et al.*, 2015) and groundwater salinization (*Ketabchi et al.*, 2016), modifies wave dynamics (*Mentaschi et al.*, 2017), and exacerbates the severity and frequency of coastal flooding (*Vitousek et al.*, 2017), among other adverse effects.

Coastal flooding hazard is one of the most destructive natural catastrophes (*Smith*, 2013). It results from extreme sea levels, which mostly occur when a high spring tide coincides with a large storm surge, although the importance of this combination depends on the ratio between the storm surge and the local tidal range (*Pugh*, 1987; *Flather*, 2001; *Resio and Westerink*, 2008). Storm surges correspond to variations of the ocean free surface induced by tropical cyclones or extra-tropical storms (*Flather*, 2001). As attested by historical dramatic events, storm surges can drive devastating coastal flooding which inflicts major social, economic and environmental impacts (*Resio and Westerink*, 2008; *Hinkel et al.*, 2014; *Needham et al.*, 2015). For instance, hurricane Katrina (2005) induced storm surges of up to 9 m in the Gulf of Mexico, which caused insured damages valued at \$80 billion and more than 1800 casualties (*Fritz et al.*, 2007). The 1953 North Sea flooding (*Rossiter and Doodson*, 1954; *Flather*, 1984), cyclone Nargis (2008) in the Gulf of Bengal (*Fritz et al.*, 2009) and storm Xynthia (2010) in the Bay of Biscay (*Bertin et al.*, 2014), are other examples of major catastrophes associated with storm-induced flooding (Fig. 1.1 and Fig. 1.2). As coastal flooding risk increases under the combined effects of demographic growth and sea level rise, there is an urgent need to identify adaptation strategies in order to reduce risk exposure and improve coastal communities resilience in the near future

(Nicholls, 2018). Toward that end, an ever deeper understanding of the physical processes driving storm surges is fundamental to accurately predict these phenomena and mitigate their impacts.

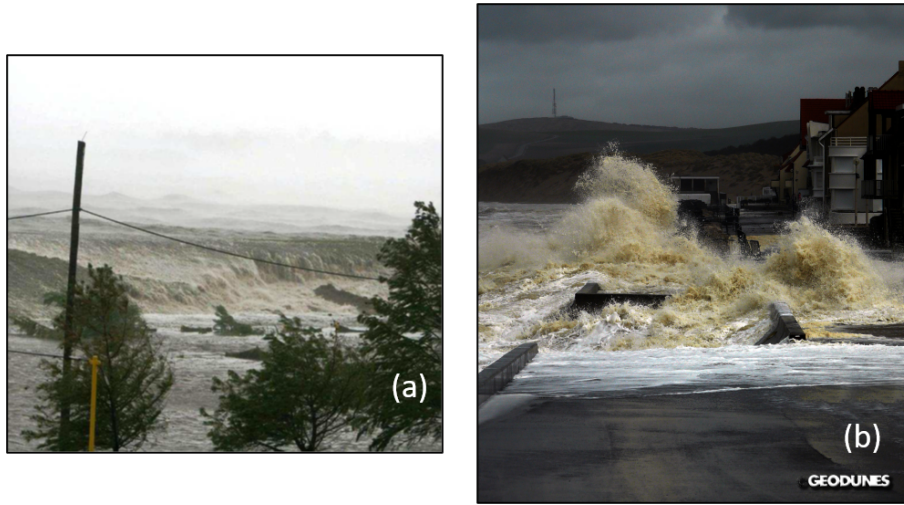


FIGURE 1.1 – (a) Coastal flooding during hurricane Katrina in the Gulf of Mexico and (b) in March 2010 at Wissant (France) (credits : (a) NOAA ; (b) www.geodunes.fr).

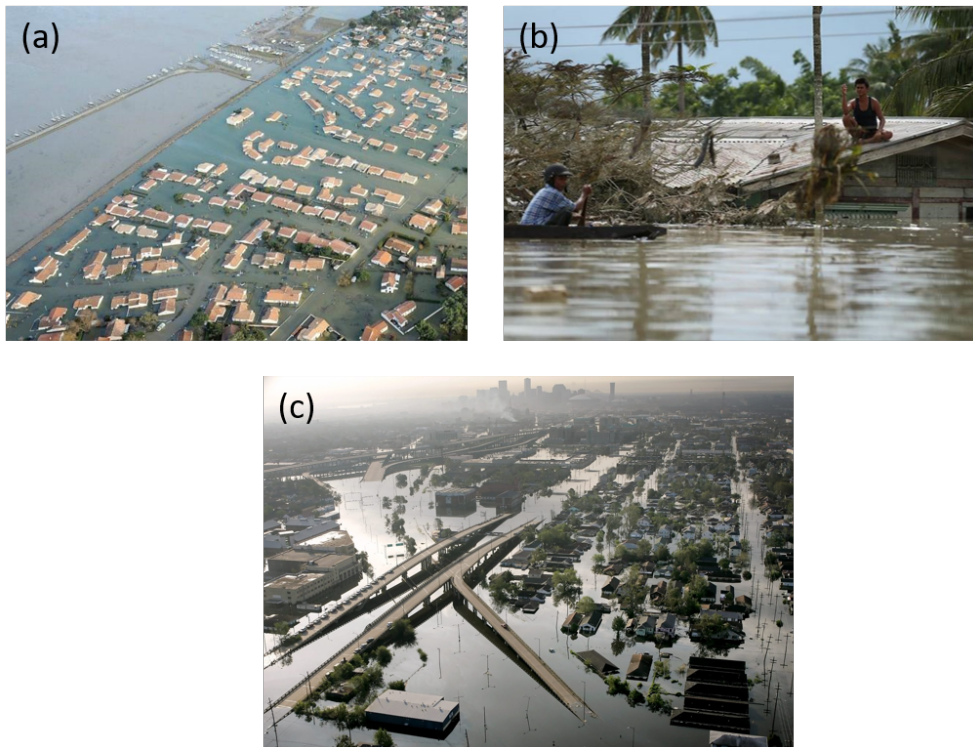


FIGURE 1.2 – (a) Damages caused by (a) the storm Xynthia in the village of La Faute-sur-Mer (France), (b) cyclone Nargis in the Gulf of Bengal and (c) hurricane Katrina in New Orleans (USA) (credits : (a) actu.fr ; (b) www.burmapartnership.org ; (c) www.rts.ch).

Since the early 20th century, wind-induced surface stress and atmospheric pressure gradients associated with these extreme storm events have been identified as the primary

drivers to storm surges (*Doodson, 1924*) and were accounted for in pioneering modelling approaches to predict these phenomena (*Jelesnianski, 1965; Heaps and Proudman, 1969*). Tide-surge interactions were also shown early to significantly influence the development of storm surges locally (e.g., *Proudman, 1957; Prandle and Deacon, 1975; Flather, 1981*). In the 1950s, a few studies highlighted for the first time that wind-generated waves (frequency range ~ 0.04 Hz-0.4 Hz, hereafter referred to as short waves) can contribute to storm surges through several mechanisms (e.g., *Harris, 1963*). For a long time, the wind surface stress has been commonly parameterized as a function of the wind speed and a drag coefficient representing the sea surface roughness, which increases linearly with the wind speed under low to moderate winds (e.g., *Smith and Banke, 1975*). However, based on the earlier work of *Charnock (1955)*, *Stewart (1974)* suggested that the parameterization of the sea surface roughness should also vary with the wave age (representing the degree of development of the sea), such that a younger sea state induces a rougher sea surface roughness, and in turn a higher surface stress and storm surge. These pioneer results have been corroborated later by *Donelan et al. (1993)*, *Drennan et al. (2003)*, *Mastenbroek et al. (1993)*, *Bertin et al. (2015a)* and *Pineau-Guillou et al. (2020)*, among others. In shallow water, waves can also enhance the bottom stress. Indeed, the orbital velocities associated with short-wave propagation increase the level of turbulence in the wave bottom boundary layer, which causes currents to experience higher bottom resistance (*Rosales et al., 2008*). Besides these processes, the dissipation of short-wave energy in the nearshore drives an increase in mean water levels in the surf zone, referred to as wave setup. The wave setup has been investigated through a number of laboratory experiments (e.g., *Saville, 1961; Bowen et al., 1968; Battjes, 1972; Stive and Wind, 1982*) and field measurements (e.g., *Munk, 1949; Goda, 1975; Guza and Thornton, 1981; Lentz and Raubenheimer, 1999*). The original theoretical model that first explained this process is the radiation stress formalism of *Longuet-Higgins and Stewart (1962, 1964)*, where radiation stresses correspond to the momentum flux associated with the propagation of short waves. The dissipation of short-wave energy in the nearshore induces spatial gradients of radiation stresses, which act as a horizontal pressure force driving currents and a wave setup along the shoreline.

Another wave-induced process that contributes to the total water level at the coast is the wave runup, which corresponds to the instantaneous water-level maxima across the swash zone. The swash zone, located at the landward edge of the surf zone, is alternatively covered and exposed by waves travelling up (uprush) and down (backwash). This water displacement is called the swash and is driven by the contributions of both short waves and infragravity waves (frequency range ~ 0.004 Hz-0.04 Hz). The wave runup is defined as including the wave setup (slowly varying component) and the swash (fluctuating component) (Fig. 1.3). When the wave runup exceeds the top of a dike (or a dune), overtopping (or overwash) occurs and can cause flooding.

Overall, total water levels at the coast can be decomposed into a (slowly-varying) mean water level associated with tides and storm surges, including the wave setup, and a fluctuating component, the swash (Fig. 1.3).

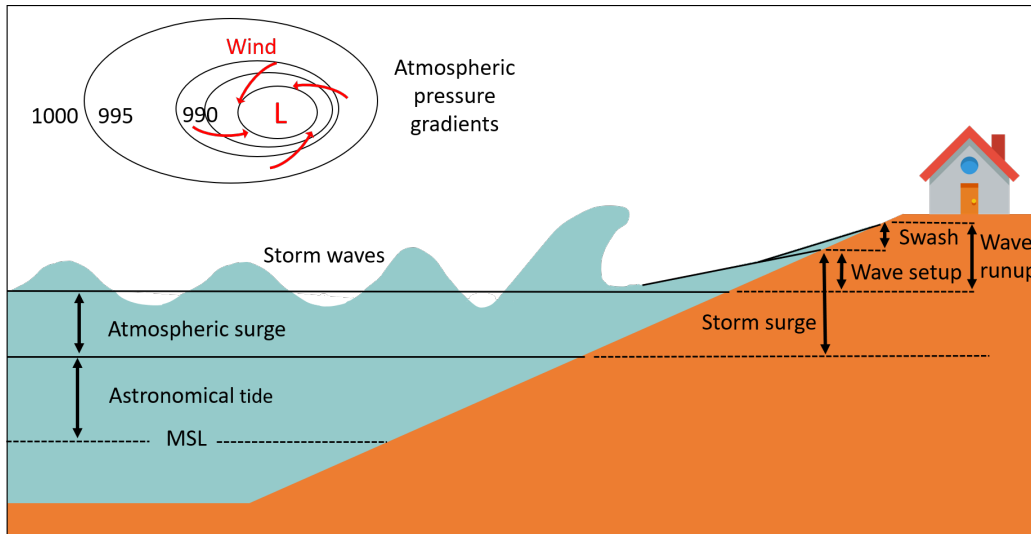


FIGURE 1.3 – Schematic processes that contribute to the total water level at the coast.

The need for predicting storm surge gave rise to a number of hydrodynamic models, which are predominantly based on the resolution of the depth-integrated shallow water equations. A common approach to represent the effects of short waves on the mean circulation is to couple a 2DH hydrodynamic model with a spectral phase-averaged wave model. Phase-averaged wave models do not solve the full wave motion but describe instead the evolution of the wave energy spectrum which is a phase-averaged quantity. Hence, such wave model can provide phase-averaged forces to represent the effect of waves on the mean circulation and particularly the wave setup, but cannot reproduce the wave runup, since the latter requires the resolution of the wave motion (individual waves). Phase-averaged wave forces are generally represented by the (depth-uniform) radiation stress formalism (2D RS) of *Longuet-Higgins and Stewart* (1964). While 2D RS has shown to improve storm surge predictions through the representation of the wave setup in regional storm surge modelling (e.g., *Roland et al.*, 2009b), this approach cannot reproduce the vertical structure of the wave-induced circulation. Over the last 15 years, new 3D theories have been developed such as the depth-varying 3D RS approaches (*Mellor*, 2003, 2008; *Xia et al.*, 2004) or the vortex force (VF) formalism (*McWilliams et al.*, 2004; *Ardhuin et al.*, 2008b; *Bennis et al.*, 2011). While there is still a lack of consensus on the correctness and applicability between 3D RS and VF methods, both approaches are now commonly applied in 3D circulation models by the ocean and coastal scientific communities to simulate the depth-varying wave-induced circulation (*Xia et al.*, 2020). Using a fully coupled wave-current modelling system with a VF formalism, *Guérin et al.* (2018) reported that the wave-induced depth-varying circulation in surf zones can increase the maximum wave setup along the shoreline of sandy beaches. However, this study was based on idealized numerical modelling and should be verified on the field. This would help to evaluate the potential benefit to model the wave setup and hence the storm surge with a 3D fully-coupled modelling system.

The wave setup has been shown to substantially contribute to storm surges under energetic wave conditions, ranging from tens of centimetres to values of about 1 m near the shoreline (*Pedreiros et al.*, 2018; *Guérin et al.*, 2018). In specific areas such as coasts bordered by narrow to moderately-wide shelves (*Dean and Bender*, 2006; *Lerma et al.*, 2017) or volcanic islands (*Kim et al.*, 2010; *Kennedy et al.*, 2012; *Pedreiros et al.*, 2018), the wave setup can even dominate upon the other storm surge components. Also, several studies reported that

the breaking of short waves occurring close to and over the ebb deltas of shallow inlets (*Malhadas et al.*, 2009; *Olabarrieta et al.*, 2011; *Dodet et al.*, 2013; *Wargula et al.*, 2018) or large estuaries (*Bertin et al.*, 2015a; *Fortunato et al.*, 2017) can induce a wave setup that extends at the scale of the whole lagoon or estuary. The wave setup can thus raise the water level in coastal environments sheltered from the direct action of waves, such as lagoons, harbours or estuaries. In spite of these findings, the potential contribution of the wave setup to the water level in wave-sheltered environments is not clearly recognized in the scientific community and often considered as negligible by a number of global-scale studies conducting coastal risk assessments (e.g., *Melet et al.*, 2018; *Lambert et al.*, 2020; *Almar et al.*, 2021). In this context, further research is needed to clarify the mechanisms through which the wave setup can raise the water level in wave-sheltered environments.

At a finer scale, the dynamics of the wave setup have been mainly investigated through field measurements in sandy environments, which have been the main focus of nearshore hydrodynamics until recently (*Komar*, 1998). In contrast, little attention has been paid to the dynamics of the wave setup in other widespread coastal environments such as rock shore platforms, steep rock shores (*Dodet et al.*, 2018) or vegetated coastal systems (*van Rooijen et al.*, 2016), although they can be substantially different from that on sandy beaches. This can be attested by the relatively limited number of wave measurements and near-absence of wave setup observations from field experiments on shore platforms and vegetated coastal systems.

Shore platforms are distinctive landforms of rocky coasts, which are one of the most common environments of the world's coastal zones (*Trenhaile*, 2002; *Griggs et al.*, 2019). They correspond to erosional rock surfaces which are found within or close to the intertidal zone and are usually backed by coastal cliffs, but can also be topped by beaches, dunes or coastal structures. They can act as the buffer against coastal hazards, by protecting coastal cliffs from the erosion of waves (*Trenhaile and Kanyaya*, 2007) or potentially limiting flooding risks when they are backed by low-lying coastal zones, although the latter has yet to be more investigated. Also, shore platforms constitute the most common habitat worldwide for a diversity of aquatic plants and animals (*Thompson et al.*, 2002). They have been widely used as a model system for studying the fundamental mechanisms of the intertidal biodiversity over the past 50 years (*Connell*, 1961; *Dayton*, 1971). Although wave-induced transport and forces have a key control on the dynamics of this ecosystem and on the morphological evolution of the shore platform, wave transformation and induced-circulation in this environment have been little studied (*Naylor et al.*, 2010; *Stephenson*, 2000a). There are few field-based studies of wave processes conducted on shore platforms compared to beaches or estuaries, which have concentrated more scientific interests, and have been considered as more vulnerable to sea level rise due to faster morphological dynamics (*Trenhaile*, 2002). Very recently, wave transformation on shore platforms has been advanced thanks to a number of field experiments (e.g., *Beetham and Kench*, 2011; *Ogawa et al.*, 2015; *Poate et al.*, 2018). Yet, few studies investigated wave processes using numerical models (*McCall et al.*, 2017; *Poate et al.*, 2018) and there still are a number of gaps in knowledge, such as the understanding of wave processes under storm wave conditions in which a very limited number of datasets has been collected (*Ogawa et al.*, 2015). Also, only one study reported wave setup observations but did not examine the underlying mechanisms (*Ogawa et al.*, 2015). In particular, the role of bottom roughness on both waves (*McCall et al.*, 2017; *Poate et al.*, 2018) and wave setup dynamics has been very little addressed, although bottom roughness can significantly affect these processes (*Dean and Bender*, 2006; *Buckley et al.*, 2016). For instance, the contribution of the wave-induced circulation to the wave setup highlighted by *Guérin et al.* (2018) on sandy beaches, has yet to be evaluated on

such rough bottoms.

In recent years, vegetated coastal habitats have received a growing interest in the scientific community owing to their natural capacity in mitigating coastal hazards that worsen under the ongoing sea level rise. Aquatic vegetation, such as salt marshes, seagrasses, mangroves or kelps, is known to dissipate wave energy (e.g., Möller *et al.*, 1999), reduce wind-induced storm surges (e.g., Wamsley *et al.*, 2010) and mean flow velocities (e.g., Nepf, 1999). Number of studies have contributed to better understand these wave-vegetation interactions through both numerical models (e.g., Dalrymple *et al.*, 1984) and experiments. Although some of these experiments were conducted in the field (e.g., Yang *et al.*, 2012), the majority is based on laboratory measurements with vegetation mimics (e.g., Augustin *et al.*, 2009), which can question the validity of their findings in real physical conditions. Recently, van Rooijen *et al.* (2016) reported from laboratory observations that the wave setup can be reduced due to wave-vegetation interactions at the intrawave scale. Their findings have to be confirmed in in-situ conditions, in which the effect of the vegetation on the wave setup has not yet been measured. A better understanding and quantification of the influence of the vegetation on both wave and wave setup dynamics can contribute to their appropriate use as nature-based flood defences (Duarte *et al.*, 2013).

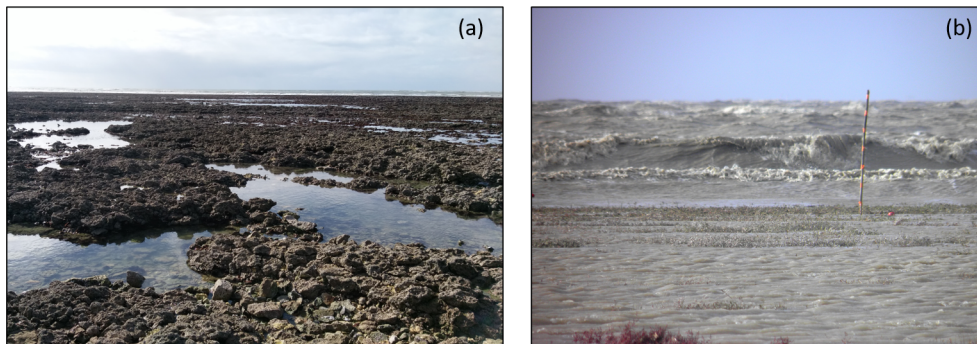


FIGURE 1.4 – Photos of (a) the shore platform near La Cotinière on Oléron Island and (b) the salt marsh of Brouage (France), on which wave and wave-induced hydrodynamics have been studied in this work (credits : (a) Laura Lavaud ; (b) Antoine Lechevalier).

In this context, the present research work examines the contributions of short waves to storm surges in contrasting coastal environments. First, the contribution of wave dissipation to storm surges is investigated in wave-sheltered environments, namely lagoons and estuaries. Second, wave dissipation and wave setup dynamics are analysed on a shore platform and on a salt marsh, which are common coastal environments while little studied through field-based studies. More specifically, this PhD thesis addresses the three main following objectives :

Objective 1 : Investigate the contribution of short-wave dissipation to storm surges in estuaries and lagoons sheltered from the direct action of waves. To that end, a high-resolution 3D hindcast of the sea state and storm surge associated with the storm Klaus that made landfall in January 2009 in the Southern Bay of Biscay is performed. Since this storm produced very energetic waves and significant storm surges in certain coastal embayments of this region, it provides a unique opportunity to investigate the contribution of wave breaking to storm surges in wave-sheltered environments. The following questions raised :

- What are the underlying physical processes at the inlets during the storm ?

- Are the wave setup and the storm surge better predicted with a 3D than a 2DH simulation ?
- What is the mesh resolution needed in the surf zones to properly compute the wave setup ?

Objective 2 : Investigate short-wave dissipation and wave setup dynamics on a shore platform by combining new field observations and high-resolution 3D numerical modelling. The following questions raised :

- Can wave transformation on the shore platform be reproduced with the default parameterizations generally used in the spectral model, and what is the impact on the prediction of the wave setup ?
- Through which mechanisms the bottom roughness affects wave setup dynamics ? In particular, what is the contribution of the wave-induced depth-varying circulation to the wave setup on a rough bottom ?

Objective 3 : Investigate short-wave dissipation and wave-setup dynamics on a salt marsh by combining field data analysis and high-resolution 2DH numerical modelling. The following questions raised :

- Can we accurately reproduce wave dissipation by the vegetation present on the salt marsh with the model ?
- To which extent the vegetation contributes to wave dissipation ?
- Through which mechanisms the presence of vegetation affects wave setup dynamics ?

OUTLINE OF THE THESIS

This thesis is organized in 8 chapters :

Following the introduction given in this first chapter, Chapter 2 provides a literature review of storm surge generation mechanisms, exposes the key milestones of storm surge modelling development and presents the different theoretical approaches to represent the effects of short waves on the mean circulation.

Chapter 3 presents the different methods of data acquisition used in this thesis, from permanent sea surface monitoring techniques to complementary field measurements. Procedures of data processing are then detailed and in particular, the methods that have been considered in this work to reconstruct the free surface elevation of surface waves and compute wave setup from bottom pressure measurements.

Chapter 4 describes the modelling system used in this thesis. The governing equations and numerical approaches of both the circulation and spectral phase-averaged models are described.

Chapter 5 investigates the contribution of wave breaking to storm surges in the Arcachon Lagoon and the Adour Estuary (France), through the hindcast of the storm surge and sea state associated with the storm Klaus. The underlying physical processes are analysed. In addition, the potential benefit of 3D fully-coupled (wave-current) simulations to compute

storm surges at regional scale and the importance of the mesh resolution in surf zones to accurately reproduce the wave setup are evaluated.

Chapter 6 is dedicated to the study of the wave dissipation and mean circulation on a shore platform located along the western coast of Oléron Island (France). The 3D fully-coupled modelling system is applied to a new field experiment conducted in February 2020 under storm wave conditions. The predictive skills of the model in reproducing wave levels, wave transformation and the associated circulation are assessed. Wave setup dynamics are examined through the analysis of the role of bottom roughness on both wave energy dissipation and wave-induced circulation.

Chapter 7 examined wave dissipation and wave setup dynamics on the salt marsh of Brouage (France). Field data analysis is combined with 2DH fully-coupled simulations in which the effect of the vegetation is analysed. Perspectives for a future field campaign are presented.

Finally, Chapter 8 summarizes the main findings of this thesis and discusses several questions and perspectives raised during this work that deserve further investigations.

Chapitre 2

State of the art

2.1 Storm surge generation mechanisms

Storm surges result from a number of physical processes. While the wind effect and atmospheric pressure variations associated with tropical cyclones and extra-tropical storms are usually the primary drivers of a storm surge, other forcings and particularly waves, can also be important contributors. In addition, the generation of a storm surge can be affected by non-linear interactions between these different forcings and by several factors such as local topographic features. This section details the processes through which these different forcings and factors build and impact storm surges.

Storm surges propagate to the coast as shallow water waves, with heights up to ~ 10 m and wavelengths of the order of hundreds of kilometres. Since horizontal scale length of the surge is much larger than the water depth, the generation and dynamics of storm surges are generally well described by the depth-integrated shallow-water equations (*Gill, 1982*). These are the Saint-Venant equations with additional source terms representing the atmospheric and wave forcings :

$$\frac{\partial \bar{\eta}}{\partial t} + \frac{\partial(hU)}{\partial x} + \frac{\partial(hV)}{\partial y} = 0 \quad (2.1)$$

$$\frac{\partial U}{\partial t} + U \frac{\partial U}{\partial x} + V \frac{\partial U}{\partial y} = fV - g \frac{\partial \bar{\eta}}{\partial x} + \frac{\tau_{s,x} - \tau_{b,x}}{\rho h} - \frac{1}{\rho} \frac{\partial P_A}{\partial x} - \frac{1}{\rho h} \left(\frac{\partial S_{xx}}{\partial x} + \frac{\partial S_{xy}}{\partial y} \right) \quad (2.2)$$

$$\frac{\partial V}{\partial t} + U \frac{\partial V}{\partial x} + V \frac{\partial V}{\partial y} = -fU - g \frac{\partial \bar{\eta}}{\partial y} + \frac{\tau_{s,y} - \tau_{b,y}}{\rho h} - \frac{1}{\rho} \frac{\partial P_A}{\partial y} - \frac{1}{\rho h} \left(\frac{\partial S_{yy}}{\partial y} + \frac{\partial S_{xy}}{\partial x} \right) \quad (2.3)$$

with (x,y) are the Cartesian coordinates, $\bar{\eta}$ is the mean free surface elevation, h is the total water depth ($h = d + \bar{\eta}$ with d the bathymetry), U and V are the horizontal components of the depth-integrated velocity, f is the Coriolis parameter, P_A is the sea-level atmospheric pressure, τ_s and τ_b are the surface and bottom stress respectively, ρ is the water density and g is the gravitational acceleration. The last right-hand side terms in Eqs 2.2 and 2.3 correspond to the wave force terms with S_{xx} , S_{yy} and S_{xy} being the components of the radiation stress tensor (*Longuet-Higgins and Stewart, 1962, 1964*).

Considering a profile perpendicular to an alongshore-uniform shoreline (x-axis) under steady state, the momentum equation given by Eq. 2.2 can be simplified as follows :

$$g \frac{\partial \bar{\eta}}{\partial x} = fV + \frac{\tau_{s,x}}{\rho h} - \frac{1}{\rho} \frac{\partial P_A}{\partial x} - \frac{1}{\rho h} \frac{\partial S_{xx}}{\partial x} \quad (2.4)$$

The right-hand side terms correspond to the Coriolis acceleration, the wind-induced stress, the atmospheric pressure gradients and the wave force terms. They are the main forcing processes for storm surges, which is detailed in the following subsections.

2.1.1 Atmospheric forcing

Storm surges are generated under extreme events and can last several hours to days (up to ~ 3 days) (*Kim*, 2019). The primary drivers of storm surges are the wind-induced surface stress and atmospheric pressure gradients associated with these extreme events. In deep water, the storm surge is mainly generated by the latter process through the so-called "inverse barometer" effect. The mean atmospheric pressure at sea level is 1013 hPa. 1 hPa drop in pressure with respect to this value induces a rise of approximately 1 cm in water level (e.g., *Doodson*, 1924; *Pugh*, 2004). For instance, the atmospheric pressure recorded during storm Xynthia decreased to 970 hPa, which corresponds to a barometric surge of 0.43 m. In shallower depths, the storm surge amplitude becomes more sensitive to the wind effect since the latter is inversely proportional to the water depth (Eq. 2.4). Hence, over large and shallow continental shelves, the wind-induced surface stress dominates and enhances storm surge generation (*Flather*, 2001; *Rego and Li*, 2010; *Resio and Westerink*, 2008; *Kennedy et al.*, 2012), which makes adjacent low-lying coastal zones particularly vulnerable to storm-induced flooding.

Storm surge generation can also be highly influenced by the Coriolis effect. The wind-induced surface stress drives currents in the upper ocean boundary layer, which are deviated to the right (respectively to the left) from the wind direction in the Northern (resp. Southern) Hemisphere due to Earth rotation (*Ekman*, 1905). In more details, surface currents drift is theoretically directed 45° but several studies reported smaller values of the order of 20° (e.g., *Holmedal and Wang*, 2015). This surface drift forces a circulation in the underlying layers with a decreasing current magnitude and a progressive stronger shift to the right (resp. to the left) in direction across each subsequent layer. This process, known as the Ekman spiral, occurs on the Ekman layer, defined from the ocean surface to the water depth at which the energy transferred between each layer is fully dissipated. In deep water, the wind-driven net transport (i.e. the Ekman transport) is oriented 90° to the right (resp. to the left) of the wind direction. However, this value decreases in shallower water owing to the increase in bottom stress (*Rego and Li*, 2010). This process can drive an "Ekman setup" when a storm approaches the coast, with a larger storm surge impacting the coastal region to the right-side (resp. left-side) of the storm track in the Northern (resp. Southern) Hemisphere. This phenomenon explains the higher storm surge observed along the coasts of Louisiana and Texas (USA) which occurred 12-24 h prior to the landfall of hurricane Ike (2008) in the Gulf of Mexico (*Kennedy et al.*, 2011) (Fig. 2.1). Similar to the "forerunner surge" during Ike, the Ekman setup can drive an "after-runner surge" which occurs after the main surge, such as the one that developed 15-18 h after the passage of a typhoon along the Sanin coast of Japan (*Kim et al.*, 2014).

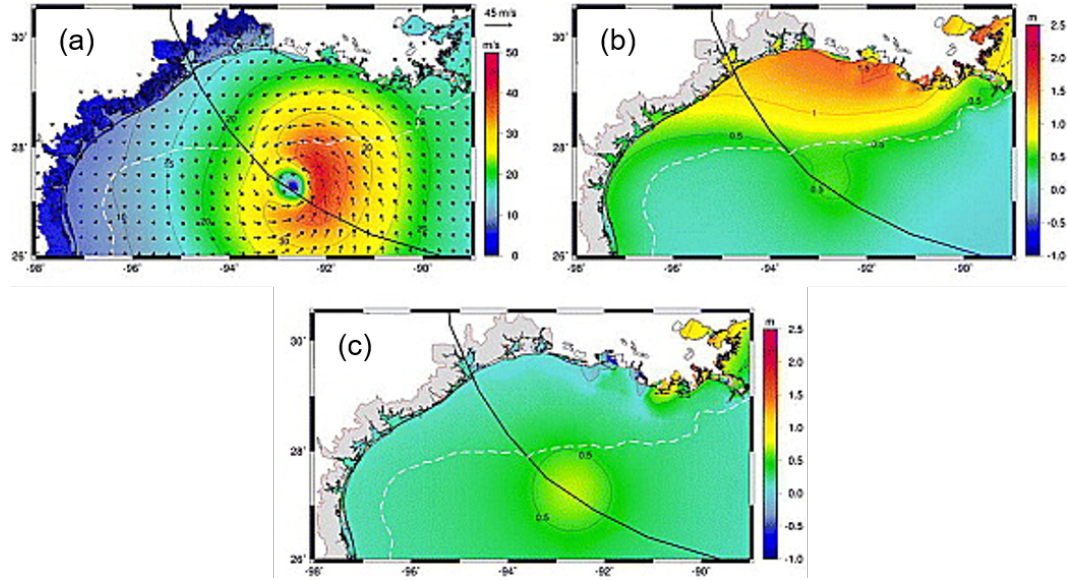


FIGURE 2.1 – (a) Data assimilated wind field during hurricane Ike (2008) in the Gulf of Mexico, (b) simulated storm surge with Coriolis forcing and (c) simulated storm without Coriolis forcing. Adapted from Kennedy et al. (2011).

2.1.2 The effects of short waves

2.1.2.1 Wave effect on the surface stress

In circulation models, the wind surface stress τ_s is commonly parameterized with a bulk formula of the form :

$$\tau_s = \rho_a C_d U_{10}^2 \quad (2.5)$$

where ρ_a is the air density, U_{10} is the wind speed at 10 m height above the sea surface and C_d is a drag coefficient related to the sea surface roughness z_0 through the following relationship in neutral conditions (with wind at 10 m height above mean sea level) :

$$C_d = \frac{\kappa^2}{[\log(\frac{10}{z_0})]^2} \quad (2.6)$$

where κ is the von Kármán's constant ($\kappa = 0.4$). C_d has been usually computed as a function of U_{10} for low to moderate winds (i.e., *Smith and Banke, 1975; Pond and Pickard, 1983; Geernaert et al., 1987*). However, in the 50s, *Van Dorn (1953)* has shown experimentally that the presence of waves can substantially increase the surface stress. This effect depends on the sea state, which can be characterized by the wave age, expressed as :

$$\xi = \frac{c_p}{u_*} \quad (2.7)$$

where c_p is the phase velocity at the peak wave frequency and u_* is the friction velocity. Alternatively, the wave age can be formulated as :

$$\xi = \frac{c_p}{U_{10}} \quad (2.8)$$

A low wave age is characterized by steep waves propagating more slowly than the wind while a larger wave age describes a mature sea with smoother fully-developed waves moving faster than the wind. A younger sea state (low wave age) can hence increase the roughness of the sea surface and subsequently the surface stress compared to an old sea state. In particular, the wind surface stress is expected to increase in coastal areas (*Lange et al., 2004; Zheng et al., 2018*) since the wave phase speed decreases with the water depth. The wave effect on the wind surface stress has been accounted for through a number of parameterizations that depend for instance on the wave age (*Donelan et al., 1993; Drennan et al., 2003; Oost et al., 2002*) or the wave-supported stress (*Janssen, 1991*). Several studies have shown that wave-dependent formulations can improve storm surge predictions compared to bulk (wind speed-dependent) formulas (e.g., *Mastenbroek et al., 1993; Zhang and Li, 1996; Kim et al., 2010; Bertin et al., 2015a; Staneva et al., 2016; Pineau-Guillou et al., 2020*). While the wave effect on the wind surface stress is known and investigated for 70 years now, there is still a lack of consensus in the scientific community on how to represent this process. More recently, field experiments have reported that under strong winds, the sea roughness could be capped or even decrease due to the generation of sprays and foams at such wind speed (*Powell et al., 2003; Takagaki et al., 2012*). Hence, a threshold or a decrease in the drag coefficient is usually used in numerical models for strong wind speeds ($> 20\text{-}25 \text{ m.s}^{-1}$) (*Dietrich et al., 2011; Zijlema et al., 2012*). *Kim et al. (2015)* showed that using either wind speed or wave-dependent formulations without any treatment for the drag coefficient at high wind speeds led overestimated storm surges compared to observations.

2.1.2.2 The wave setup

In coastal zones, waves can further contribute to the storm surge through the mechanism of wave setup. This process has been investigated for more than 50 years through a number of laboratory experiments (e.g., *Fairchild, 1958; Saville, 1961; Bowen et al., 1968; Battjes, 1972; Stive and Wind, 1982*) and field measurements (e.g., *Munk, 1949; Goda, 1975; Guza and Thornton, 1981; Lentz and Raubenheimer, 1999; Raubenheimer et al., 2001*).

Theoretically, the wave setup was first explained by the radiation stress concept of *Longuet-Higgins and Stewart (1962, 1964)*, introduced in their analysis of the depth-integrated momentum flux of linear waves propagating over a horizontal bottom. Wave-induced momentum flux is equivalent to a stress. *Longuet-Higgins and Stewart (1964)* referred this stress as "radiation stress", defined as the excess flow of momentum due the presence of waves. Horizontal gradients in radiation stress are equivalent to horizontal pressure forces acting on the water. In coastal zones, and especially in surf zones, the dissipation of short waves can induce substantial gradients of radiation stress, which can drive currents and a mean sea level increase along the shoreline, i.e. the wave setup. The free surface elevation is tilted until a balance is reached between the wave forces (i.e. radiation stress gradients) and the subsequent barotropic pressure gradient.

This balance can be shown in Eq. 2.4 when neglecting atmospheric pressure gradients, Coriolis and surface stress terms :

$$\underbrace{\rho gh \frac{\partial \bar{\eta}}{\partial x}}_{\text{barotropic pressure gradient}} + \underbrace{\frac{\partial S_{xx}}{\partial x}}_{\text{radiation stress gradient}} = 0 \quad (2.9)$$

The cross-shore component of the radiation stress tensor S_{xx} in Eq. 2.9 is expressed as

(Eq. 7 of *Longuet-Higgins and Stewart (1964)*) :

$$S_{xx} = \overline{\int_{-h}^{\eta} (p + \rho u^2) dz} - \int_{-h}^{\bar{\eta}} p_0 dz \quad (2.10)$$

where z is the vertical coordinate (positive upward from the still water depth). The first term of the right-hand side is the total horizontal momentum flux while the second term corresponds to the horizontal momentum flux in the absence of waves. p is the pressure at any point in the water column, p_0 is the hydrostatic pressure and u is the horizontal component of the wave orbital velocity in the cross-shore direction.

S_{xx} can be rewritten as :

$$S_{xx} = \underbrace{\overline{\int_{-h}^{\eta} \rho u^2 dz}}_{S_{xx}^{(1)}} + \underbrace{\overline{\int_{-h}^{\bar{\eta}} (p - p_0) dz}}_{S_{xx}^{(2)}} + \underbrace{\overline{\int_{\bar{\eta}}^{\eta} p dz}}_{S_{xx}^{(3)}} \quad (2.11)$$

Following the approach of *Longuet-Higgins and Stewart (1964)* to evaluate Eq. 2.11, the mean dynamic pressure below $\bar{\eta}$ (integrand of $S_{xx}^{(2)}$) is approximated as $-\rho w^2$ with w the vertical component of the wave orbital velocity, and the mean dynamic pressure above $\bar{\eta}$ (integrand of $S_{xx}^{(3)}$) is considered as hydrostatic. Since the integrand of $S_{xx}^{(1)}$ is of second order in amplitude (the orbital velocity being proportional to the amplitude), the range $\bar{\eta} < z < \eta$ contributes to a third-order term and can thus be neglected in a second-order approximation. Under these assumptions, Eq. 2.11 reads :

$$S_{xx} = \int_{-h}^{\bar{\eta}} \rho (\overline{u^2 - w^2}) dz + \frac{1}{2} \rho g \bar{\eta}^2 \quad (2.12)$$

Using the approximations from the linear wave theory for u , w and η , S_{xx} finally reads :

$$S_{xx} = (2n - \frac{1}{2})E \quad (2.13)$$

where n is the ratio of the group velocity over the phase velocity c_g/c and E is the total wave energy.

From Eq. 2.9, positive gradients in radiation stress, typically observed in the shoaling zone, implies that the mean surface slope is negative, causing a wave set-down in this region. In the surf zone, short-wave dissipation drives negative gradients in radiation stress, which implies that the mean surface slope is positive, resulting in a wave setup maximum along the shoreline. These variations in mean free surface elevation induced by the transformation of short waves in coastal zones are well illustrated by the laboratory experiments of *Bowen et al. (1968)* in a wave channel (Fig. 2.2).

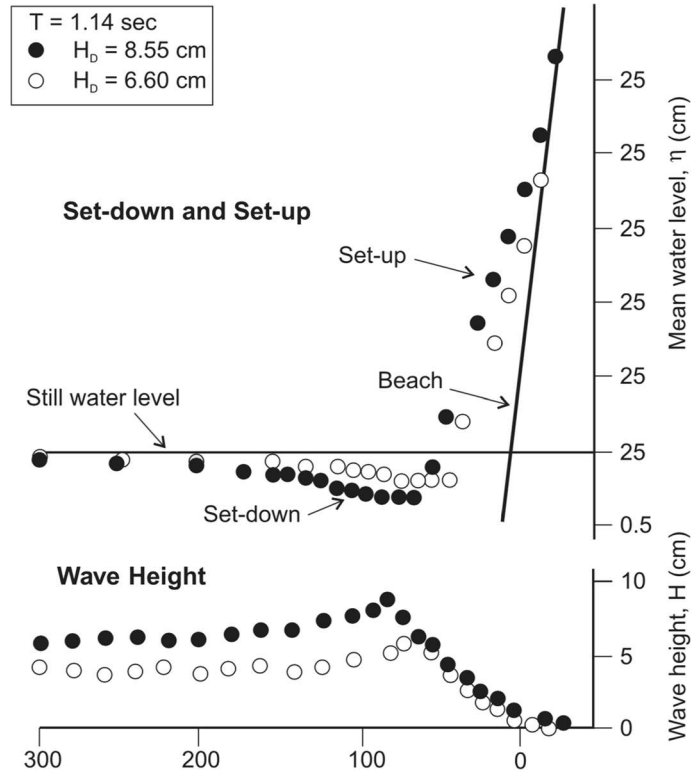


FIGURE 2.2 – Profile of the mean water level and the envelope of the wave height for two experiments conducted by Bowen *et al.* (1968). Adapted from Dodet *et al.* (2019b).

2.1.2.3 Wave effect on the bottom stress

In shallow water, the presence of waves also affects the bottom stress. The orbital motion of waves induces an alternating current within the wave bottom boundary layer (WBBL). This mechanism increases the level of turbulence in the WBBL, which in turn enhances the bottom stress felt by the current. In phase-averaged models, the bottom stress under the combined action of waves and currents has been computed with different parameterizations such as the ones of *Soulsby* (1997) and *Grant and Madsen* (1979), based on the near-bottom wave orbital velocity, or the mixing parameterization of *Mellor* (2002), that represents the near-bottom wave-induced turbulence on the mean current. The latter parameterization has been further extended to nearshore applications by *Bennis et al.* (2014) who additionally accounted for turbulence induced by breaking waves.

2.1.3 Additional processes and parameters controlling storm surges

2.1.3.1 Storm characteristics

The amplitude of the storm surge varies in time and space depending on the meteorological aspects of the storm including its intensity, its track, its temporal and spatial scales (Flather, 2001; Rego and Li, 2009). In particular, the storm track and associated wind direction dictate the Ekman transport and control the fetch width, and subsequently the sea state, which can affect the wind surface stress as shown earlier in this chapter.

2.1.3.2 Topographic features

Topographic features such as the nearshore bathymetry, controlling the development of the wave setup, along with the width and the slope of the continental shelf, are important factors that control the impact of the storm surge at the coast. In addition, coastal morphology can also play a key role in the distribution of the storm surge (Flather, 2001). For instance, concave coasts and funneled-shape estuaries contain the storm surge, resulting in elevated water levels while convex coasts tend to spread the storm surge.

2.1.3.3 Tide-surge interactions

Non-linear interactions exist between tides and storm surges (Wolf, 1981; Flather, 2001; Horsburgh and Wilson, 2007; Zhang et al., 2010; Idier et al., 2012, among others) and can locally increase or decrease the storm surge (Idier et al., 2012; Krien et al., 2017). For instance, Idier et al. (2012) reported that tide-surge interactions contributed up to 0.75 m to the storm surge in the English Channel during the November 2007 North Sea and March 2008 Atlantic storms. A detailed analysis of the shallow water equations can show that the non-linear effects arise from : (1) non-linear terms related to the water depth (advection term in the continuity equation Eq. 2.1, surface and bottom stress terms in the momentum equations Eqs. 2.2 and 2.3, which are divided by the water depth); (2) the advection terms in the momentum equations; and (3) the quadratic formulation of the bottom stress (Flather, 2001; Zhang et al., 2010). Through these non-linear effects, tidal water level and current directly interact with surge-induced hydrodynamics. Several empirical and theoretical studies showed that these interactions increase with larger storm surge and tidal range (e.g., Cartwright et al., 1968; Prandle and Wolf, 1978). As a notable effect of tide-surge interactions, several authors have reported in certain areas that the peak storm surge preferentially occurs during the (early) flood (Prandle and Wolf, 1978; Horsburgh and Wilson, 2007; Idier et al., 2012). While the development of the surge is modulated by the tidal stage, the surge induces a phase shift on tides (Horsburgh and Wilson, 2007). For instance, Plüß (2003) reported that mean water level changes significantly modulate tidal dynamics in shallow coastal areas, owing to the change in basin geometry and flooding of the flat zones. Overall, it has been demonstrated for a long time that tide-surge interactions are far from being negligible at specific locations and should be accounted for to improve predictions of storm surges, by simulating these phenomena simultaneously with tides (e.g., Flather, 1976).

2.1.3.4 Resonant mechanisms

Storm surges can be amplified by resonant mechanisms such as Proudman, Greenspan, Helmholtz (i.e. seiches) or shelf resonance (*Moon et al.*, 2009; *Bertin et al.*, 2012). For instance, *Bertin et al.* (2012) explained that the development of ~ 6 h oscillations in the storm surge associated with storm Xynthia in the Bay of Biscay was due to a resonant process, caused by interactions of the storm surge with the continental shelf. Resonant effects can also cause the amplification of meteotsunamis. Meteotsunamis are sea-level perturbations generated by fast-moving atmospheric disturbance such as pressure jumps, squall lines or frontal passages, which can be amplified near the coast by resonant effects. Destructive meteotsunamis often result from a combination of resonant mechanisms, e.g., an atmospherically-induced ocean wave, enhanced through Proudman resonance (*Proudman*, 1929) over the shelf, can reach the entrance of a semi-closed coastal basin (harbour, bay or inlet), where it can be further amplified by Helmholtz resonance resulting in intensive and hazardous harbour sea level oscillations (i.e. seiches). For more details about meteotsunamis, the reader is referred to *Montserrat et al.* (2006), *Pattiaratchi and Wijeratne* (2015), *Thompson et al.* (2020) and *Shi et al.* (2020).

2.1.3.5 Compound flooding and mean sea level variations

In deltas and estuaries, rainfall and river discharges can occur concomitantly with storm surges which leads to compound events that strongly increase the potential risk of flooding (e.g., *Wahl et al.*, 2015; *Zheng et al.*, 2014; *Ward et al.*, 2018). Traditionally, these processes have been analysed and simulated separately, however, research efforts are actively ongoing to investigate their interactions and compound effects, notably through the development of coupled ocean-hydrological modelling systems (e.g., *Ye et al.*, 2020).

The total water level is also influenced by seasonal and annual variations of the mean sea level due for instance, to the combination of seasonal atmospheric settings and thermosteric dilatation (*Payo-Payo and Bertin*, 2020).

The following section reviews the evolution of storm surge modelling, from the pioneer stand-alone circulation models to fully-coupled modelling systems.

2.2 Progress in storm surge numerical modelling

2.2.1 Overview of the historical development of storm surge modelling

Storm surge events and their potential destructive impacts on coastal communities have long fostered the need for developing efficient storm surge predictive tools to mitigate coastal risks. In response to this necessity, coastal and shelf-sea numerical modelling have been developed in the 1960s, which progressively led to the establishment of the first operational storm surge forecasting systems (hereafter OSSF systems) in the mid-1970s. Storm surges associated with tropical cyclones or extra-tropical storms are often considered to be distinct events, which has long conducted to a "geographic divide" in modelling groups (*Bode and Hardy*, 1997). In Europe, the major North Sea 1953 Storm caused devastating flooding in the Netherlands and in southeastern England, which marked the launch of storm surge warning systems and water managements plans. In particular, the UK created the STWS (Storm Tide Warning Service) which was first based on empirical approaches that relate

storm characteristics to the observed storm surges. However, the understanding of the mechanisms driving storm surges was limited with this method and the lack of historical observations hampered statistical analysis, which fostered in the late 1960s the development of two-dimensional (2D) storm surge numerical models. *Heaps* (1983) provides a comprehensive review of advances in research and modelling related to storm surges on the period of 1967-1982 while focusing mainly on the work carried out on the North Sea and the west coast of Great Britain. Over these years, the Institute of Oceanographic Sciences, Bidston, developed a number of 2D storm surge models (*Heaps*, 1977). The earliest one used the linearized depth-integrated hydrodynamic equations in spherical polar coordinates solved on a finite difference grid covering the North Sea and shelf region of the British Isles (*Heaps and Proudman*, 1969). Other 2D models have been implemented on the North Sea and River Thames (e.g., *Prandle and Deacon*, 1975) in which investigations on tide-surge interactions have been initiated and pursued by *Prandle and Wolf* (1978) and *Flather* (1981) among others. This research led to the establishment of an OSSF system in the UK in 1978 covering mostly the North Sea (e.g., *Flather*, 1979) and forced by forecasts of atmospheric pressure and winds originated from an atmospheric model (Fig. 2.3). Storm surges were computed as the difference between a tide-only simulation and a simulation including both tides and atmospheric forcing, tide-surge interactions were therefore considered. At this stage, *Donelan* (1982) already suggested that the parameterization of the wind stress in storm surge models should depend on the sea state. During the same period, 2D storm surge modelling and OSSF systems have been developed in the Netherlands, Denmark, Belgium, Germany and Norway but also further south in Europe, in the Adriatic Sea, where Venice experienced severe flooding (*Heaps*, 1983). Some attention has been paid to the use of real-time assimilation data (*Flather and Proctor*, 1983) and wave-current interactions (*Hasselmann*, 1982) but further investigations were still needed. While 2D models were used for storm surge predictions, the offshore oil industry has raised the need for understanding the vertical structure of currents, which promoted the development of 3D numerical models in the early 1980s (e.g., *Davies*, 1981; *Proctor*, 1981), while additional current measurements, particularly during storms, were required to support modelling.

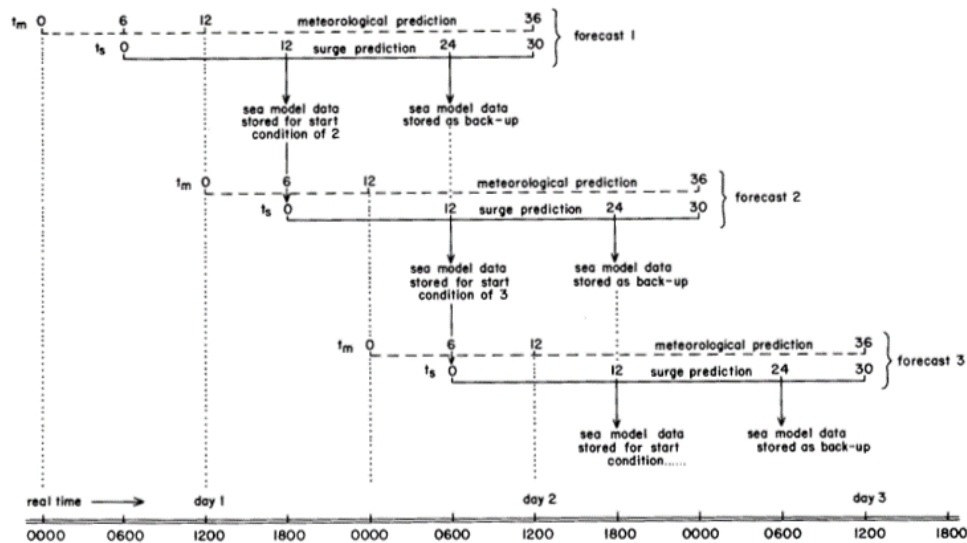


FIGURE 2.3 – Scheme for operational surge forecasting. From *Flather* (1979).

In other regions of the world exposed to storm surges generated by tropical cyclones, OSSF systems have been developed to minimize the impacts of these extreme phenomena. In the USA, OSSF systems became also a progressive alternative to statistical models although major advances in hurricane surge modelling have occurred later, in the late 1980s and the early 1990s (*Westerink and Gray, 1991*). A linear two-dimensional depth-integrated finite difference model, known as SPLASH, has been developed at the US National Weather Services's (NWS) National Hurricane Center (NHC), based on the pioneer works of *Jelesnianski (1967)* and his research in the following years. It did not include non-linear terms and has a fixed boundary at the water-land interface. It was created to forecast hurricane surges along the Atlantic and Gulf coasts of the USA. Also, the US Army Coastal Engineering Center established another 2D storm surge model using orthogonal curvilinear coordinates, known as SSURGE (*Wanstrath et al., 1976*), for the design of coastal defence structures and coastal zone management. 3D numerical models have also been developed to simulate the vertical structure of hurricane-generated currents (e.g., *Forristall, 1974; Cooper and Pearce, 1982*). In addition, other 2D numerical studies and forecasts have been conducted, notably on storm surges associated with typhoons in Japan (*Isozaki, 1968*) and tropical storms in the Bay of Bengal (e.g., *Das, 1972; Johns et al., 1981*).

In the mid-1980s and early 1990s, several more sophisticated storm surge models have emerged, either based on the pre-existing circulation models described below (among others) or newly developed. While the models already relied on a matured physical understanding of the main storm surge physics (*Gill, 1982*), improvements since the mid-1990s have mainly focused on computational efficiency, taking advantage of the development of parallel computing techniques, and also unstructured grids, horizontal and vertical coordinates systems, wetting and drying algorithms, coupling strategy between several models (e.g., wave-current or riverine-current models), among others features (*Dube et al., 2010; Kohno et al., 2018*). In particular, an active research has been conducted on numerical methods since the earliest use of finite difference schemes. While this method has proved to be robust, it is mostly used on structured grids, which prevents from refining the grid at the coasts to represent complex shorelines and coastal features. This has been partly improved by the use of curvilinear grids, in which the grid resolution increases towards the shoreline but does not allow local refinements in coastal areas (e.g., *Jarvinen and Lawrence, 1985*). Another technique is the grid nesting (e.g., *McInnes et al., 2002*), in which grids of increasingly fine resolution are nested inside another. Later, the finite element method has also been progressively applied to the shallow water equations, which has enabled the use of unstructured grids in which the spatial grid resolution can vary in the modelled domain, being coarse in the deep ocean (several kilometres to tens of kilometres) and refined to a few hundreds of meters or less in the nearshore. The coarse resolution in the deep ocean, where storm surges are mainly driven by the inverse barometer (section 2.1.1), saves computational time while the use of a finer mesh in coastal zone allows to better represent the growth of the wind-driven surge in shallow waters, as well as complex shorelines, nearshore bathymetry and coastal features (barrier islands, inlets and bays). In addition, modelling efforts have been made to improve storm surge predictions through a better understanding of complex physical processes such as air/sea and wave/current interactions and through several features that impact the predictive skills of the model, such as bathymetry up-to-date data and improved accuracy of the meteorological forcings (*Janssen, 2008*). Storm surge modelling was progressively supported by a growing observational networks of tide gauges and wave buoys, used in the development stage of models and also for forecasting systems, through data assimilation.

Some of the numerical models that are currently used worldwide for storm surge model-

ling are presented below. In the USA, the NWS developed a new OSSF system, known as SLOSH (*Jarvinen and Lawrence, 1985; Jelesnianski, 1992*), for Sea, Lake, and Overland Surges from Hurricane, which is a 2D finite difference model as SPLASH but includes additional features (polar grid system, representation of sub-grid scale features and inland water bodies). SLOSH solves a set of equations derived from the shallow water equations in which the advective terms are neglected, but in contrast with SPLASH, this omission is compensated by the inclusion of small amplitude effects (*Jelesnianski, 1992*). SLOSH model does not include neither the tides due to the inherent difficulty to predict accurately the peak of a hurricane surge in time, nor short waves and river inflows. Tides are separately added to the predicted storm surges. Besides forecasting storm surges, SLOSH is used to establish evacuation plans and map storm surge flood plains in the U.S. Gulf and East coasts (*Glahn, 2009*). In parallel, the United States Army Corps of Engineers (USACE) developed the ADCIRC model (*Luetlich et al., 1992*), which solves the shallow-water equations using a finite element scheme. Over the years, several improvements have been made to the model such as the implementation of a wetting and drying algorithm for accurately modelling inundated areas and the model has been parallelized for higher computational efficiency. In the mid-1980s, Delft Hydraulics (Deltares now) started to develop a 3D hydrodynamic model, known as Delft3D-FLOW, which uses finite difference methods to solve the shallow-water equations on structured grids. Delft3D-FLOW has been parallelized in the late 1990s. For 10 years now, an unstructured-grid model has been under development, known as Delft3D Flexible Mesh Suite (*Kernkamp et al., 2011*), with a first official version released in 2015 (see *Verlaan et al., 2005; De Goede, 2020*, for more details about storm surge modelling in the Netherlands). Other storm surge models have been developed worldwide (e.g., see *Flather, 2000; Dube et al., 2010; Umgiesser et al., 2021*, for a review), including the 3D unstructured-grid finite volume hydrodynamic model FVCOM (*Chen et al., 2003; Rego and Li, 2009*) and the 3D finite difference models POM (*Blumberg and Mellor, 1987; Peng et al., 2004*) and CH3D (*Sheng, 1986; Sheng et al., 2010a,b*) using orthogonal and non-orthogonal curvilinear grids, respectively. In the present work, the 3D unstructured-grid finite element hydrodynamic model SCHISM is used (*Zhang et al., 2016*), which is derived from the model SELFE (*Zhang and Baptista, 2008*).

2.2.2 Importance of accounting for waves in storm surge modelling

As shown in section 2.1, the mechanisms by which waves affect surge elevations, in particular wave effect on the surface stress, and the wave setup, have been identified since the 1950s. Hence, the need for a wave model to predict storm surges progressively arose and early attempts of wave-current coupling emerged in the 1990s-2000s. The study of *Mastenbroek et al. (1993)* presents one of the first proper implementation of a coupling between a phase-averaged and circulation models, through which the authors reported that a wave-dependant stress results in significant improvements in the surge calculations compared to a bulk formula. In the MAST III PROMISE (Pre-Operational Modelling In the Seas of Europe) project, two existing pre-operational wave (WAM-PRO, *Monbalieu et al., 2000*) and circulation models were integrated into a coupling framework (*Ozer et al., 2000*). Its application to the North Sea suggested that a wave-dependant surface stress should be preferentially used for storm surge modelling. In the following years, the development of parallel computing and the access to more computational resources enabled the emergence of several coupled wave-current models (e.g., *Zhang and Li, 1996; Osuna and Monbalieu, 2004; Wolf, 2004*). The widely-used unstructured-grid model ADCIRC has been coupled to several structured-grid wave models, the nearshore STEADY-state WAVE model

STWAVE being nested inside the deep ocean, coarser, WAM model (e.g., *Bunya et al.*, 2010; *Dietrich et al.*, 2010). However, in such coupling, the circulation and wave models run on different grids, which requires interpolation of the boundary conditions between the nested wave structured grids and interpolation of water levels, currents and wave characteristics between the structured wave and unstructured circulation grids. This coupling is called "loose" coupling, since this intra-model interpolation introduces inaccuracies and reduces the efficiency of the simulation. The development of unstructured wave models (e.g., SWAN unstructured version; *Zijlema*, 2010) allowed to vary the mesh resolution from deep to coastal waters without any nesting. In addition, both circulation and wave models can be run on a same unstructured grid, avoiding interpolation of variables between these models, which is referred as "tight coupling". *Dietrich et al.* (2011) implemented a "tight coupling" between ADCIRC and SWAN. Delft3D-FLOW has also been coupled to SWAN in 1995 while SCHISM has been coupled to WWM-II by *Roland et al.* (2012).

The increasing computational power also allowed to refine the mesh resolution in coastal areas. This is of primary importance to compute the wave setup since this process requires very fine meshes in surf zones to be accurately computed. Hence, since this time, several numerical studies accounting for radiation stress gradients were able to represent the wave setup in coastal areas, showing that it can substantially contribute to the storm surge (*Brown*, 2010; *Kim et al.*, 2010; *Sheng et al.*, 2010a,b; *Brown et al.*, 2011; *Guérin et al.*, 2018) and can modify the spatial extent of coastal inundations (e.g., *Xie et al.*, 2008, 2016; *Murty et al.*, 2019). Nevertheless, the exact mesh resolution needed in surf zones to compute the wave setup remains unclear in the scientific community and should be better quantified. While the effect of waves on the surface stress and the wave setup appear to be the dominant contributions to storm surges, the effect of waves on tides and surges through an enhanced bottom friction (*Rosales et al.*, 2008) has also been highlighted through numerical modelling (e.g., *Roland et al.*, 2012).

Overall, it is now well recognized that accounting for waves in storm surge modelling improves the accuracy of the predictions. Hence, while in the 2000s, OSSF were usually based on a circulation model only (*Flather*, 2000), the use of coupled wave-current models is progressively extended nowadays to OSSF systems implemented at a regional or country scale (e.g., *Gillibrand et al.*, 2011; *Ferrarin et al.*, 2013; *Sembiring et al.*, 2015). However, this is not yet the norm at larger scales, such as global OSSF systems (GLOSSIS, *Verlaan et al.*, 2015), which can be partly explained by the additional computational cost required at such scale to run a wave model and define a fine-enough resolution in coastal zones to compute the wave setup.

Apart from notable exceptions (e.g., *Kennedy et al.*, 2010, 2011), one can note through the analysis of the existing literature on storm surge modelling, that numerical results of wave-current models are generally validated against wave parameters measured by deep water wave buoys and water levels monitored by tide gauges located in bays or harbours. However, these observations are limited and do not allow to verify the model parameterizations of shallow-water wave dissipation processes such as depth-induced breaking and bottom friction and the predicted wave setup along open-ocean coasts. This stresses the need to collect hydrodynamic data in various coastal environments in order to better understand the associated processes and verify the predictive skills of the model in these environments.

On a more theoretical perspective, most of storm surge modelling studies that account for the wave effects on the mean circulation are based on the 2D radiation stress formalism of *Longuet-Higgins and Stewart* (1964). Over the last 20 years, new theories which represent the wave effects on the mean circulation in 3D have emerged. They are presented in the

following section.

2.3 Modelling the effects of short waves on the mean circulation

The hydrodynamics of the coastal zone is usually characterized by the simultaneous presence of currents, wave and turbulent motions that interact each other through several mechanisms and energy transfers. One of the difficulty in representing the circulation in the presence of waves is the difference in time scales between the (orbital) wave motion and the slow-varying motion, induced for instance by tidal and wind-driven currents. Phase-resolving models explicitly describe the evolution of the free surface and hence resolve the wave motion. They are based for instance on the Boussinesq equations (e.g., FUN-WAVE; Kirby *et al.*, 1998), the Reynolds-averaged Navier-Stokes equations (RANS models, e.g., NHWAVE; Ma *et al.*, 2012) or the non-linear shallow water equations including non-hydrostatic pressure (e.g., SWASH; Zijlema *et al.*, 2011). While phase-resolving models have demonstrated very good predictive skills in simulating wave-current interactions (e.g., Yoon, 2014), they are computationally expensive, which limits their use to small scale applications (typically $O(1 \text{ km}^2)$). For larger scale applications conducted over relatively long periods compared to the wave motion (e.g., from few days to several months), the flow velocity can be averaged over the wave phase, such that the effects of waves on the mean flow are represented without explicitly resolving the wave motion. In this framework, the total flow velocity \mathbf{u} can be split into two components, namely the mean (phase-averaged) flow velocity $\langle \mathbf{u} \rangle$ and the wave motion $\tilde{\mathbf{u}}$ (the turbulent fluctuations being neglected here) :

$$\mathbf{u} = \langle \mathbf{u} \rangle + \tilde{\mathbf{u}} \quad (2.14)$$

While their leading-order motion is periodic, short waves induce a net drift along the direction of wave propagation, the so-called "Stokes drift" (e.g., Stokes, 1847; Longuet-Higgins, 1953), which is proportional to the square of the wave steepness. The Stokes drift can also be seen as the difference between mean velocities following a fluid particle (Lagrangian velocity) and in a fixed reference frame (Eulerian velocity). The (Lagrangian) mean flow can thus be decomposed into two components, the (Eulerian) mean circulation (also expressed as mean current) and the Stokes drift. The total mean momentum \mathbf{m}^T can be expressed as the sum of the momentum of the mean circulation \mathbf{m} and the mean wave momentum \mathbf{m}^W :

$$\mathbf{m}^T = \mathbf{m} + \mathbf{m}^W \quad (2.15)$$

In addition to the contribution of the Stokes Drift, momentum transfers occur from the wave motion to the mean flow, which can be particularly intense at the coast and generate sea level variations (i.e wave set-down/wave setup) and longshore currents (Longuet-Higgins, 1970a,b) as described in section 2.1.2.2. The concept of radiation stress introduced by Longuet-Higgins and Stewart (1962, 1964) was used by these authors, and later by Phillips (1977), to propose the first depth-integrated (2DH) formulations of the conservation of the total mean momentum \mathbf{m}^T in the presence of waves. While these pioneer approaches have been widely used, other methods have been developed in which the conservation of the momentum of the mean circulation \mathbf{m} and waves \mathbf{m}^T are formulated with two distinct equations (Garrett *et al.*, 1976; Smith, 2006). The equation for \mathbf{m} , which includes

wave-induced forcings terms for the mean circulation only, allows a new interpretation of the physics. 2DH approaches can be particularly suitable for the study of wave-current interactions in the coastal zone, where the horizontal dimensions are large compared to the vertical dimension, allowing to study a wide range of wave-induced hydrodynamics in the nearshore. Yet, these 2DH approaches do not allow to represent the vertical structure of the mean horizontal circulation such as the vertical shear in the cross-shore mean current near the coast. Indeed, the onshore-directed mass flux associated with the Stokes Drift near the surface results in a counterbalanced Eulerian offshore current referred to as undertow which is localized near the seabed in the surf zone. Also, the wave momentum source is not uniformly distributed over the depth, which contributes to the vertical shear of the cross-shore mean current in the surf zone. These vertical dynamics cannot be reproduced with 2D approaches. To address these shortcomings, fully 3D wave-current approaches have been developed over the last 20 years.

As in 2DH, the conservation of momentum of the mean circulation \mathbf{m} and waves \mathbf{m}^W can be either treated separately or not. For instance, *Mellor* (2003) developed a depth-varying radiation stress formulation (3D RS) based on the conservation of the total mean momentum \mathbf{m}^T . While 3D RS was found to perform comparably or better than 2D RS in reproducing nearshore hydrodynamics (*Bolaños et al.*, 2014), 3D RS was questioned by *Ardhuin et al.* (2008a,b), mainly because the evolution of \mathbf{m} and \mathbf{m}^W was not dissociated. Indeed, with this approach, the momentum flux induced by the wave motion is distributed into \mathbf{m} and \mathbf{m}^W (in order to conserve \mathbf{m}^T), irrespective to their specific response. In addition, the evolution of \mathbf{m} and \mathbf{m}^W is treated identically while they have different advection velocity and behaviour, notably with regard to the vertical mixing. The most criticized issue was the correctness of the vertical fluxes of wave momentum, particularly on a sloping bottom (*Bennis et al.*, 2011). This inaccuracy led *Mellor* (2013, 2015) to propose a correction to their 3D RS approach. Alternatively, a formulation for \mathbf{m} was proposed by *McWilliams et al.* (2004) based on an asymptotic theory (*Craik and Leibovich*, 1976), and by *Ardhuin et al.* (2008b) based on the GLM (General Mean Lagrangian) theory introduced by *Andrews and McIntyre* (1978). From the GLM equations, *Ardhuin et al.* (2008b) proposed an approximation to second order in wave steepness called the glm2z-RANS equations. It should be noted that the vertical integration of the glm2z-RANS equations leads to a formulation similar to the one of *Smith* (2006). *Bennis et al.* (2011) derived a set of equations based on the glm2z-RANS theory with the hypothesis that the vertical shear of the mean current is neglected in the wave forcing terms. The approaches of *McWilliams et al.* (2004), *Ardhuin et al.* (2008b) and *Bennis et al.* (2011), also denominated as vortex force (VF) formalism, constitute three dimensional sets of equations for the quasi-Eulerian velocity, in which the vertical structure of the wave-induced forcing terms on the mean circulation can be represented. The formulation of *McWilliams et al.* (2004) has been integrated to the ROMS model (*Shechepetkin and McWilliams*, 2005) and FVCOM (*Chen et al.*, 2012; *Xia et al.*, 2020), while the glm2z-RANS approach has been implemented in the MARS3D code (*Lazure and Dumas*, 2008) by *Bennis et al.* (2011), as well as in SYMPHONIE (*Marsaleix et al.*, 2008) and MOHID (*Martins*, 1999) models by *Michaud* (2011) and *Delpey* (2012) respectively. Also, the simplified glm2z-RANS approach of *Bennis et al.* (2011) has been implemented in SCHISM by *Guérin et al.* (2018).

These approaches that represent 3D effects of waves on currents are now commonly applied by the ocean and coastal scientific communities to simulate the depth-varying, wave-induced circulation (e.g., *Uchiyama et al.*, 2010; *Kumar et al.*, 2012). In particular, *Guérin et al.* (2018) used the 3D modelling system SCHISM with a VF formalism (as mentioned above) and reported that the depth-varying, wave-induced circulation in surf zones can

increase the maximum wave setup along the shoreline of sandy beaches, in comparison with a 2DH simulation that does not allow to represent 3D wave effects and the associated depth-varying circulation. Further analysis is needed to better understand the underlying processes and examine in which conditions the contribution of the wave-induced circulation can significantly increase the wave setup.

Chapitre 3

The modelling system

In the scope of this work, the contribution of short waves to storm surges is investigated by combining field observations and numerical modelling. As we focus on the development of storm surges in contrasting coastal environments, including lagoons and estuaries, the modelling system used should be capable of accurately represent complex nearshore bathymetry and shorelines, as well as coastal morphological features such as inlets and lagoons. The most appropriate model for addressing this need seems to be an unstructured grid model, in which the use of only one grid whose resolution can be refined at the coast, allows to well represent these irregular coastal features without any grid nesting.

In this context, the unstructured-grid finite-element modelling system SCHISM (Semi-implicit Cross-scale Hydroscience Integrated System Model; *Zhang et al.*, 2016), derived from the model SELFE (*Zhang and Baptista*, 2008), appears to be suitable for our purposes. SCHISM is an open-source modelling system developed by Pr. Joseph Zhang at VIMS (USA), and other research groups worldwide. The core model of the system is a 3D hydrodynamic model which solves the Reynolds-averaged Navier-Stokes equations under hydrostatic and Boussinesq approximations. As one of the main characteristics of SCHISM, the use of a semi-implicit scheme, in conjunction with an Eulerian-Lagrangian Method to treat the advection in the momentum equations, allows to relax the numerical stability constraints of the model. SCHISM is coupled to the Wind Wave Model WWM-II (*Roland*, 2009a; *Roland et al.*, 2012) which simulates the generation and propagation of short waves. The whole system is parallelized via domain decomposition and Message Passing Interface (MPI). The hydrodynamic and spectral wave models share the same unstructured grid (and domain decomposition), which eliminates errors associated with interpolation.

The use of unstructured grids, combined with robust numerical methods in both the circulation and wave models, allows to cover large spatial domains with one grid whose resolution can vary from very coarse in deep oceans (e.g., tens of kilometers) to very fine in coastal areas (e.g., < 10 m), while maintaining computational efficiency (e.g., see *Bertin et al.*, 2014; *Ye et al.*, 2020, for multiscale applications conducted with SCHISM). Another modelling system of similar characteristics and which could have been used here is TELEMAC-3D (*Hervouet*, 2007) which can be coupled to the spectral wave model TOMAWAC (*Benoit et al.*, 1997) through the radiation stress or the vortex force formalisms (see *Teles*, 2013, for the latter). However, to our knowledge, multiscale applications have not yet been conducted with TELEMAC-3D in contrast to SCHISM. In addition, developments on wave-current interactions, sediment transport and bed evolution in the modelling system SCHISM are mainly conducted at the Joint Research Unit LIENSs, which allows

to benefit from a network of collaborators (e.g., LNEC in Portugal or SCHISM research team at VIMS in the USA). For these different reasons, SCHISM has been the modelling system selected for the present work.

Besides WWM-II, the hydrodynamic model of SCHISM can be coupled with other modules incorporated in the modelling system such as turbulence, sediment transport, water quality, oil spills and biology. In our case, SCHISM/WWM-II is coupled to the General Ocean Turbulence Model (GOTM; *Burchard et al.*, 1999; *Umlauf et al.*, 2005), which is used to simulate the hydrodynamic and thermodynamic processes related to vertical mixing in the water column.

The coupling between SCHISM, WWM-II and GOTM allows to represent the different effects of short waves on the mean circulation, i.e. the wave-induced forcings on the mean circulation and the Stokes drift, the wave-induced surface and bottom stress, and the wave-induced surface and bottom mixing. Also, water levels and currents provided to WWM-II by SCHISM allow to represent their effects on waves. Current effects are the Doppler frequency shift, current-induced refraction and their influence on dissipation by whitecapping through the modification of the wave steepness (e.g., *Ardhuin et al.*, 2010; *van der Westhuysen*, 2012).

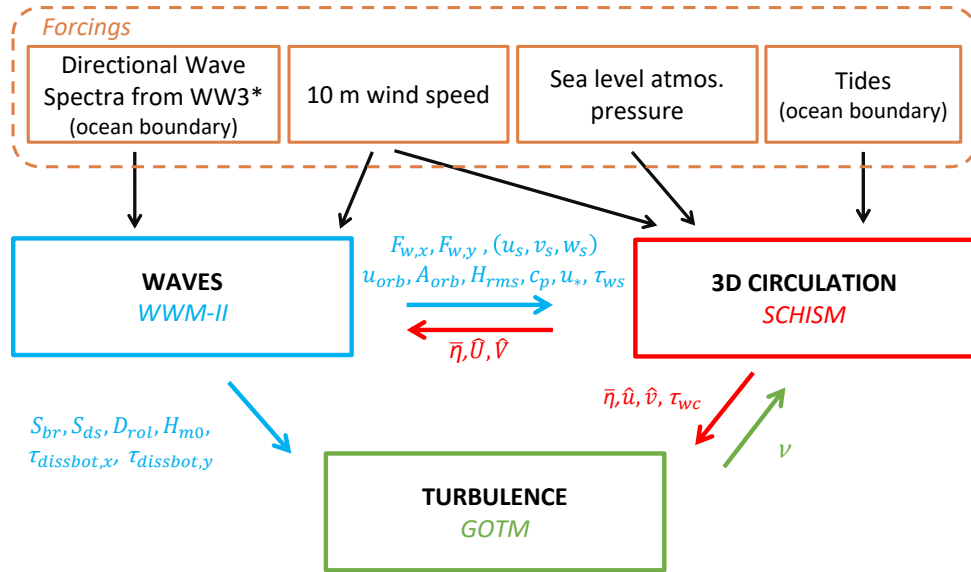


FIGURE 3.1 – Schematic description of the modelling system with forcing conditions and exchanged variables described in the following sections. *WW3 referred to the WaveWacth III spectral wave model of Tolman (1992).

3.1 The spectral wave model WWM-II

3.1.1 Governing equations

WWM-II simulates the generation and propagation of wind-generated waves by solving the wave action equation (e.g., *Komen et al.*, 1994) :

$$\frac{\partial N}{\partial t} + \nabla_{\mathbf{x}} \cdot (\dot{\mathbf{x}} N) + \frac{\partial(\dot{\sigma} N)}{\partial \sigma} + \frac{\partial(\dot{\theta} N)}{\partial \theta} = S_{tot} \quad (3.1)$$

where σ is the wave relative angular frequency, θ is the wave direction and $\nabla_{\mathbf{x}} = (\frac{\partial}{\partial x}, \frac{\partial}{\partial y})$. The wave action density $N(\sigma, \theta, \mathbf{x}, t)$, invariant in a slowly varying media (*Bretherton et al.*, 1968), is related to the wave energy density $E(\sigma, \theta, \mathbf{x}, t)$ by :

$$N(\sigma, \theta, \mathbf{x}, t) = \frac{E(\sigma, \theta, \mathbf{x}, t)}{\sigma} \quad (3.2)$$

In Eq. 3.1, $\dot{\mathbf{x}}$ corresponds to the propagation velocity in space while $\dot{\sigma}$ and $\dot{\theta}$ are the propagation velocities in frequency and direction respectively. The advection velocities in the different phase spaces are computed according to the Geometrics Optics Approximation (e.g., *Keller*, 1958) :

$$\dot{\mathbf{x}} = \mathbf{c}_{\mathbf{x}} = \frac{d\mathbf{x}}{dt} = \frac{dw}{dk} = \mathbf{c}_g + \mathbf{U}_{A(\mathbf{k})} \quad (3.3)$$

$$\dot{\theta} = c_{\theta} = -\frac{1}{k} \left[\frac{\partial \sigma}{\partial h} \frac{\partial h}{\partial m} + \mathbf{k} \cdot \frac{\partial \mathbf{U}_{A(\mathbf{k})}}{\partial m} \right] \quad (3.4)$$

$$\dot{\sigma} = c_{\sigma} = \frac{\partial \sigma}{\partial h} \left(\frac{\partial h}{\partial t} + \mathbf{U}_{A(\mathbf{k})} \cdot \nabla_{\mathbf{x}} h \right) - c_g \mathbf{k} \cdot \frac{\partial \mathbf{U}_{A(\mathbf{k})}}{\partial s} \quad (3.5)$$

where m and s are the coordinates along and perpendicular to the direction of wave propagation θ , and $h = d + \bar{\eta}$ is the mean water depth with d the bathymetry and $\bar{\eta}$ the mean (phase-averaged) free surface elevation provided by the hydrodynamic model. k is the wavenumber with $k = |\mathbf{k}|$, c_g is the group velocity, w is the wave absolute angular frequency and \mathbf{U}_A is the effective advection velocity which can be approximated as the depth-integrated current velocity, the surface current velocity or the depth-weighted average current value of *Kirby and Chen* (1989), that accounts for the effect of weak vertical current shear. In this work, the depth-integrated current velocity is considered to evaluate the propagation velocities. Since scales of variation of depths and currents are assumed to be much larger than those of an individual wave, the phase parameters can be interrelated by the dispersion relation derived from the linear wave theory and the Doppler-type equation :

$$\sigma^2 = gk \tanh kh \quad (3.6)$$

$$\omega = \sigma + \mathbf{k} \cdot \mathbf{U}_A \quad (3.7)$$

Finally, S_{tot} represents sources and sinks of wave energy and includes wind input S_{in} , dissipation due to whitecapping S_{ds} , bottom friction S_{db} and depth-induced breaking S_{br} ,

nonlinear quadruplet interactions S_{nl4} and triad interactions S_{nl3} . In addition, wave dissipation by vegetation S_{veg} is accounted for in the study conducted over the salt marsh.

3.1.2 Source terms S_{nl3} and S_{nl4}

In deep water, a pair of wave components (f_1, f_2) can interact with another pair of wave components (f_3, f_4) if the following resonance conditions are complied :

$$\begin{cases} k_1 + k_2 = k_3 + k_4 \\ w_1 + w_2 = w_3 + w_4 \end{cases} \quad (3.8)$$

These interactions, called quadruplet interactions, result in wave energy transfers amongst the four wave components. *Hasselmann* (1962) provides the full expressions for these interactions, known as the Boltzmann integral, which can be solved with exact methods such as the Webb-Resio-Tracy method (WRT, *Webb*, 1978; *Tracy and Resio*, 1982) or following *Hasselmann and Hasselmann* (1985). However, these methods can be computationally expensive and thus not a viable solution for operation models, which led to the development of approximations such that the Discrete Interaction Approximation of *Hasselmann et al.* (1985). The latter, yet less accurate, can be faster by two order of magnitude compared to exact methods and is thus adopted in WWM-II among other phase-averaged models.

As waves approach the coast, the transition to a shallow water regime allows near-resonance interactions of three wave components. These triad interactions transfer energy from the peak frequency to lower (subharmonics) and higher (superharmonics) frequencies. In the nearshore, this process plays a key role in redistributing wave energy within the spectrum, which can induce significant changes in the wave field (e.g., *Elgar and Guza*, 1985; *Herbers et al.*, 2000; *Martins et al.*, 2021a). In WWM-II, triads interactions are originally formulated with the Lumped Triad Approximation (LTA) of *Eldeberky* (1996), based on a discrete triad approximation for co-linear waves that only considers the dominant self-self interactions. The latter means that this approach only accounts for the energy transfers from the primary peak to its second harmonic at $f = 2f_p$ (with f_p the peak frequency), which in turn, contributes to the development at most of its second harmonic at $f = 4f_p$. More recently, the approach of *Salmon et al.* (2016) has been implemented, which proposed a Consistent Collinear Approximation (CCA), that addresses certain inconsistencies resulting from the collinear approximation used in the LTA.

3.1.3 Source terms S_{in} and S_{ds}

WWM-II proposes two main parameterizations to compute wave generation by wind. The first one is the WAM-Cycle 4 formulation (*Günther et al.*, 1992), based on the wave growth theory of *Miles* (1957), modified by *Janssen* (1982), and improved notably by *Janssen* (1991), *Abdalla and Bidlot* (2002) and *Bidlot et al.* (2007). The second and more recent parametrization is the one proposed by *Ardhuin et al.* (2010), which is derived from the WAM-Cycle 4. Compared to WAM-Cycle 4, *Ardhuin et al.* (2010) included a sink term to S_{in} , to reproduce observations of swell energy dissipation owing to modulations of the air-sea stresses by swell orbital velocities (*Ardhuin et al.*, 2009).

In addition, both parameterizations provide a formulation for wave energy dissipation due to whitecapping S_{ds} . The WAM-Cycle 4 formulation for whitecapping has been shown to yield inaccuracies in the presence of swell (*van Vledder and Hurdle*, 2002; *Ardhuin et al.*,

2010). For instance, because of its dependence on the mean wavenumber and steepness, this formulation underestimates the dissipation of the spectral tail in the case of a swell is present (*van Vledder and Hurdle*, 2002). Alternatively, the expression given by *Ardhuin et al.* (2010) comprises three terms : a saturation-based term relying on the approach of *Phillips* (1985), a cumulative breaking term, representing the smoothing effect of large breaking waves over smaller waves, and a wave-turbulence interaction term (*Teixeira and Belcher*, 2002; *Ardhuin and Jenkins*, 2006) related to the production of the turbulent kinetic energy induced by wave breaking processes at the surface.

3.1.4 Source terms S_{br} and S_{bot}

In shallow water, wave energy dissipation by bottom friction and depth-induced breaking become important. In WWM-II, wave energy dissipation by depth-induced breaking can be computed according to different formulations, such as the ones of *Battjes and Janssen* (1978), *Thornton and Guza* (1983) or *van der Westhuysen* (2010). In the different studies presented in this manuscript, the formulations of *Battjes and Janssen* (1978) and *van der Westhuysen* (2010) have been used.

Battjes and Janssen (1978) proposed a bore-based model in which the local mean rate of energy dissipation per unit area is given by :

$$D_{br,BJ78} = \frac{\alpha}{4} \rho g f_{mean} Q_b H_m^2 \quad (3.9)$$

where α corresponds to the breaking coefficient and is often seen as a tunable coefficient of the order of 1. ρ is the water density, g is the gravitational acceleration, f_{mean} is the mean frequency computed from $T_{m0,1}$ wave period, Q_b is the fraction of breaking waves and H_m is a maximum possible wave height, defined by *Battjes and Janssen* (1978) as a threshold height over which all waves of a random wave field will break. H_m is estimated by means of a parameterized Miche-type criterion :

$$H_m = \frac{0.88}{k} \tanh\left(\frac{\gamma kh}{0.88}\right) \quad (3.10)$$

where γ is the breaking index, that accounts for the effects of bottom slope compared to the theoretical value of 0.88 given by the Miche criterion derived for a flat bottom (*Miche*, 1944). In shallow water ($kh \ll 1$), Eq. 3.10 reduces to :

$$H_m = \gamma h \quad (3.11)$$

The fraction of breaking waves Q_b is determined considering a clipped Rayleigh probability density function for all wave heights truncated at H_m , which leads to the following expression for Q_b :

$$\frac{1 - Q_b}{-\ln(Q_b)} = \left(\frac{H_{rms}}{H_m}\right)^2 \quad (3.12)$$

where H_{rms} is the root mean square wave height ($H_{rms} = H_{m0}/\sqrt{2}$ with H_{m0} the significant wave height). *Battjes and Stive* (1985) carried out an extensive calibration and verification of this model, based on several experimental and field observations. Keeping the tunable coefficient α equal to unity, the breaking index γ varied from 0.60 to 0.83, with an average value of 0.73. The latter is considered as the default value in WWM-II.

Alternatively, the approach of *van der Westhuysen* (2010) investigated the parameterization of the breaking index based on wavefield nonlinearity. As the approach of *Thornton and Guza* (1983), *van der Westhuysen* (2010) proposed that the distribution of breaking wave heights $p_b(H)$ is a weighting of the Rayleigh probability density function for all wave heights $P(H)$:

$$Q_b = \int_0^\infty p_b(H)dH = \int_0^\infty W(H)P(H)dH \quad (3.13)$$

However, as compared to *Thornton and Guza* (1983), *van der Westhuysen* (2010) introduced an alternative weighted function $W(H)$ that incorporates wave nonlinearity effects :

$$W(H) = \left(\frac{\beta_i}{\beta_{i,ref}} \right)^n \quad (3.14)$$

where β_i is the biphas, a third-order quantity related to the wave skewness and asymmetry of the wave profile (e.g., *Hasselmann et al.*, 1963; *Elgar and Guza*, 1985). In WWM-II, the parametrization of *Eldeberky* (1996) is used to approximate the biphas as phase-averaged wave models do not compute quantities at this order. It reads :

$$\beta_i = \frac{-\pi}{2} + \frac{\pi}{2} \tanh \left(\frac{\delta}{U_r} \right) \quad (3.15)$$

where δ is a parameter set to 0.2 according to *Eldeberky* (1996). U_r is the Ursell number (*Eldeberky*, 1996; *Doering and Bowen*, 1995), computed following the spectral mean expression given by *Eldeberky* (1996) :

$$U_r = \frac{g}{8\sqrt{2}\pi^2} \frac{H_{m0}T_{m0,1}^2}{h^2} \quad (3.16)$$

where $T_{m0,1}$ is the mean wave period. Following this approach, when waves are symmetric along the vertical axis, i.e $\beta_i = 0$, the percent of broken waves is zero. As waves become more asymmetric, i.e. β_i tends to $-\frac{\pi}{2}$, the percent of broken waves increases. Yet, a scaled limit $\beta_{i,ref}$ was incorporated in the formulation of the weighting function (Eq. 3.14), since all waves are likely to break before the limit is reached. In Eq. 3.14, $\beta_{i,ref}$ and n are set to $-4\pi/9$ and 2.5 respectively, which are the values used by *van der Westhuysen* (2010) to obtain the best-fit predictions of the observed fraction of breakers in the lab experiment of *Boers* (1997). Finally, the local mean rate of energy dissipation per unit area is obtained by integrating the energy dissipation for a single broken wave multiplied by $p_b(H)$ (e.g., *Pezerat et al.*, 2021), which results in the following expression :

$$D_{br,W10} = \frac{3\sqrt{\pi}}{16} B^3 \rho g \frac{f_{mean}}{h} \left(\frac{\beta_i}{\beta_{i,ref}} \right)^n H_{rms}^3 \quad (3.17)$$

where B is the breaking coefficient that ranges between 0.5 and 1.5 (*van der Westhuysen*, 2010) and f_{mean} is the mean wave frequency computed from the $T_{m0,1}$ wave period.

In the spectral model, the local mean rate of energy dissipation D_{br} (corresponding either to $D_{br,BJ78}$ or $D_{br,W10}$) is distributed over frequencies and directions following the work of *Eldeberky and Battjes* (1996) :

$$S_{br} = -\frac{D_{br}}{E_{tot}}N \text{ where } E_{tot} = \rho g \int_0^{2\pi} \int_0^\infty E d\sigma d\theta \quad (3.18)$$

where E_{tot} is the total wave energy.

Recently, *Pezerat et al. (2021)* reported that common parameterizations for depth-induced breaking in spectral wave models yield significant over-dissipation of storm waves propagating over gently sloping shorefaces, potentially leading to an underestimation of the wave setup at the shoreline. To address this shortcoming, the authors proposed an analytical derivation of the breaking coefficient B (or α in the model of *Battjes and Janssen (1978)*) based on the local bottom slope, to account for its effect on the local energy dissipation rate. This adaptive breaking coefficient is expressed as :

$$B' = 40 \tan \beta \quad (3.19)$$

with β is the local bottom slope. Substituting B^3 (or α in the model of *Battjes and Janssen (1978)*) by B' , the authors strongly improved their storm wave predictions, which results in an increase in the modelled wave setup along the coast by a factor of up to 2 for a 1:10000 slope. This adaptive breaking coefficient proposed by *Pezerat et al. (2021)* is used in the present investigations conducted on the shore platform and on the salt marsh, where its effects on both wave dissipation and wave setup predictions is evaluated.

In intermediate to shallow water depth, corresponding to less than half of the dominant wavelength, interactions of waves with the bottom become significant and can dissipate wave energy through different mechanisms such as bottom friction (*Putnam and Johson, 1949*). In the spectral wave model, the source term due to bottom friction is expressed as (*Hasselmann and Collins, 1968; Collins, 1972; WAMDI, 1988*) :

$$S_{bf} = -C_f \frac{\sigma^2}{g^2 \sinh^2 kh} N \quad (3.20)$$

where C_f is a dissipation coefficient. The latter can be set to the empirical value of $0.038 \text{ m}^2 \cdot \text{s}^{-3}$ found by *Hasselmann et al. (1973)* during the JONSWAP experiment, or to $0.067 \text{ m}^2 \cdot \text{s}^{-3}$ as proposed by *Bouws and Komen (1983)* for wind sea conditions. Alternatively, C_f can be calculated according to the eddy-viscosity model of *Madsen et al. (1989)* :

$$C_f = f_w \frac{g}{\sqrt{2}} U_{rms} \quad (3.21)$$

where U_{rms} is the root mean square value of the maxima of the bottom orbital velocity :

$$U_{rms}^2 = \int \int \frac{N \sigma^3}{\sinh^2 kh} d\sigma d\theta \quad (3.22)$$

and f_w is a non-dimensional frictional factor which can be solved by iteration with the following equations (*Jonsson, 1967*) :

$$f_w = 0.3 \text{ for } \frac{a_b}{k_n} \leq 1.57 \quad (3.23)$$

$$\frac{1}{4\sqrt{f_w}} + \log_{10} \frac{1}{4\sqrt{f_w}} = m_f + \log_{10} \frac{a_b}{k_n} \text{ for } \frac{a_b}{k_n} > 1.57$$

in which m_f is a constant fixed to -0.08 , k_n is the Nikuradse roughness length that depends on the bottom properties and a_b is the near-bottom excursion amplitude :

$$a_b^2 = 2 \int \int \frac{N\sigma}{\sinh^2 kh} d\sigma d\theta \quad (3.24)$$

Recently, Marc Pezerat (PhD student at LIENSs 2018-2021) additionally implemented the SHOWEX moveable-bed bottom friction formulation initially proposed by *Tolman* (1994) and further adjusted by *Ardhuin et al.* (2003), that accounts for the formation of sand ripples and the transition to sheet flow regime.

3.1.5 Source term S_{veg}

In a vegetation field, wave energy is dissipated through the work done by the waves on the vegetation. The drag force model of *Mendez and Losada* (2004) is implemented in WWM-II, following a similar approach to *Suzuki et al.* (2012) for the SWAN model :

$$S_{veg} = -\frac{D_{veg}}{E_{tot}} N \quad (3.25)$$

$$D_{veg} = \frac{\rho}{2\sqrt{\pi}} \tilde{C}_{dv} b_v N_v \left(\frac{g\tilde{k}}{2\tilde{\sigma}} \right)^3 \frac{\sinh^3 \tilde{k}\alpha_v h + 3 \sinh \tilde{k}\alpha_v h}{3\tilde{k} \cosh^3 \tilde{k}h} H_{rms}^3 \quad (3.26)$$

where \tilde{C}_{dv} is the drag coefficient, b_v is the plant diameter, N_v is the vegetation density and $\alpha_v h$ is the plant height (α_v being the relative height of the plant). \tilde{k} and $\tilde{\sigma}$ correspond to the mean wavenumber and mean wave relative angular frequency computed from $T_{m0,1}$ wave period.

Following *Mendez and Losada* (2004), \tilde{C}_{dv} can be related to the Keulegan-Carpenter (K) number as follows :

$$\tilde{C}_{dv} = \frac{\exp(-0.0138Q)}{Q^{0.3}} \quad 7 \leq Q \leq 172 \quad (3.27)$$

with Q defined as :

$$Q = \frac{K}{\alpha_v^{0.76}} \quad (3.28)$$

where the Keulegan-Carpenter number K is given by :

$$K = \frac{u_c T_p}{b_v} \quad (3.29)$$

with T_p the peak wave period and u_c is a characteristic velocity acting on the plant. It is defined as the maximum horizontal velocity at the top of the plants ($z = -h + \alpha_v h$) (e.g., *Anderson and Smith*, 2014) :

$$u_c = \frac{H_{rms}\pi \cosh k\alpha_v h}{T_p \sinh kh} \quad (3.30)$$

3.1.6 Surface roller model

Surface rollers are turbulent masses of mixed air and water advected by breaking waves (*Svendson*, 1984a; *Deigaard et al.*, 1991). Surface rollers contribute to the nearshore circulation through an additional mass transport in the surf zone and by causing an onshore shift in the transfer of momentum to the water column (e.g., over bars, see *Reniers et al.*,

2004). The rate of energy dissipation by wave breaking controls the growth of surface rollers, while their energy dissipation occurs through shear stresses at the wave/roller inner interface (*Deigaard and Fredsøe, 1989*).

A surface roller model is integrated in WWM-II, which is based on the approach of *Reniers et al. (2004)* with minor adjustments. The evolution equation for the surface roller bulk energy E_{rol} can be read as follows (e.g., see *Reniers et al., 2004*) :

$$\frac{\partial E_{rol}}{\partial t} + 2\nabla \cdot (c_p + \mathbf{U}_A)E_{rol} = \alpha_r D_{br} - D_{rol} \quad (3.31)$$

where c_p is the phase velocity at the peak wave frequency, α_r is the percentage of energy transferred from breaking waves to surface rollers and D_{rol} corresponds to the rate of energy dissipated by rollers at the wave/roller interface. D_{rol} can be computed as a function of wave and roller characteristics (i.e. *Svendesen, 1984a*). However, there is some uncertainties regarding the empirical formulations of the roller area and the void ratio in rollers (*Martins et al., 2018*), it is thus preferred to calculate D_{rol} as a direct function of the roller energy E_{rol} following *Reniers et al. (2004)* :

$$D_{rol} = \frac{2g \sin \beta_{rol} E_{rol}}{c_p} \quad (3.32)$$

where β_{rol} is the angle at the wave/roller inner interface and $\sin \beta_{rol}$ is set to the common value of 0.1 (*Reniers et al., 2004*).

The contribution of surface rollers to the total mass flux is related to the surface roller energy (e.g., *Reniers et al., 2004*) :

$$(u_{S,R}, v_{S,R}) = 2 \frac{E_{rol}}{\rho c_p h} (\cos \theta_m, \sin \theta_m) \quad (3.33)$$

where θ_m corresponds to the mean wave direction. Although this transport primarily occurs near the surface, there is no consensus on its vertical distribution. We here assumed that the transport is depth-uniform.

3.1.7 Numerical approaches

In its explicit formulation, WWM-II solves the wave action equation (Eq. 3.1) using the fractional step method as described by *Yanenko (1971)*, which allows to resolve the different time-dependent dimensional problems of the equation with adapted numerical methods. The overall numerical procedure is given below :

1. First, the geographical part is solved using a Conservative Residual Distribution (CRD) N-Scheme (see *Abgrall, 2006; Roland, 2009a*).
2. Then, the Ultimate Quickest scheme (*Leonard, 1991*) which is a third order finite difference scheme, is used to treat the spectral advection in θ and σ space, following the approach implemented in WW3 (*Tolman, 1992*).
3. Finally, the source term integration is carried out in two different steps. First, the shallow water source terms S_{br} , S_{veg} , S_{bf} and S_{nl3} are integrated following the recommendations of *Hargreaves and Annan (2001)*, i.e. by using a semi-implicit scheme applied in the framework of a dynamical time stepping scheme. In the latter scheme, integration over a global time step is performed in several dynamic sub-time

steps, which depends notably on the corresponding source term and an associated maximum change in wave action density. The other source terms are integrated with a semi-implicit scheme without sub-iterations but the associated rate of change of the action density at each time step is restricted by a so-called "action density limiter" to guarantee numerical stability at relatively large time steps.

Alternatively, propagation (in geographical and spectral space) and source term integration can be treated implicitly. The non linear source terms of depth-induced breaking and vegetation dissipation are linearised by means of a Newton-Raphson iteration. The implicit scheme allows to avoid splitting errors (*Roland, 2009a*) and to use larger time steps, being thus more computationally efficient.

3.2 Hydrodynamic model

The hydrodynamic model of SCHISM solves the equation of mass conservation for an incompressible fluid, and the Reynolds-averaged Navier Stokes equations describing the momentum conservation under hydrostatic and Boussinesq approximations. The model is mainly used in its 3D barotropic configuration, with the vortex force formalism of *Bennis et al. (2011)* to account for the wave-induced forcings on the mean circulation. Since 2DH and 3D numerical simulations are compared in this work, the model is also described in its 2DH barotropic configuration (section 3.2.2), in which the vertical structure of the wave-induced circulation is not reproduced.

3.2.1 3D configuration - Vortex force formalism

The Vortex force (VF) framework considers the quasi-Eulerian velocity $(\hat{u}, \hat{v}, \hat{w})$, which equals the mean Lagrangian velocity (u_L, v_L, w_L) minus the Stokes velocity (u_S, v_S, w_S) :

$$(\hat{u}, \hat{v}, \hat{w}) = (u_L, v_L, w_L) - (u_S, v_S, w_S) \quad (3.34)$$

The mass conservation is :

$$\frac{\partial \hat{u}}{\partial x} + \frac{\partial \hat{v}}{\partial y} + \frac{\partial \hat{w}}{\partial z} = 0 \quad (3.35)$$

$$\frac{\partial \bar{\eta}}{\partial t} + \frac{\partial}{\partial x} \left(\int_{-d}^{\bar{\eta}} (\hat{u} + u_S) dz \right) + \frac{\partial}{\partial y} \left(\int_{-d}^{\bar{\eta}} (\hat{v} + v_S) dz \right) = 0 \quad (3.36)$$

and the momentum equations along the x and y-axis read :

$$\frac{\partial \hat{u}}{\partial t} + \hat{u} \frac{\partial \hat{u}}{\partial x} + \hat{v} \frac{\partial \hat{u}}{\partial y} + \hat{w} \frac{\partial \hat{u}}{\partial z} = -g \frac{\partial \bar{\eta}}{\partial x} + \frac{\partial}{\partial z} \left(\nu \frac{\partial \hat{u}}{\partial z} \right) + F_x \quad (3.37)$$

$$\frac{\partial \hat{v}}{\partial t} + \hat{u} \frac{\partial \hat{v}}{\partial x} + \hat{v} \frac{\partial \hat{v}}{\partial y} + \hat{w} \frac{\partial \hat{v}}{\partial z} = -g \frac{\partial \bar{\eta}}{\partial y} + \frac{\partial}{\partial z} \left(\nu \frac{\partial \hat{v}}{\partial z} \right) + F_y \quad (3.38)$$

in which $\bar{\eta}$ is the mean (phase-averaged) free surface elevation, ν is the vertical eddy viscosity and (F_x, F_y) corresponds to :

$$F_x = f \hat{v} - \frac{1}{\rho} \frac{\partial P_A}{\partial x} + \alpha_T g \frac{\partial \psi}{\partial x} + \frac{\partial}{\partial x} \left(\mu \frac{\partial \hat{u}}{\partial x} \right) + \frac{\partial}{\partial y} \left(\mu \frac{\partial \hat{u}}{\partial y} \right) + F_{w,x} \quad (3.39)$$

$$F_y = -f\hat{u} - \frac{1}{\rho} \frac{\partial P_A}{\partial y} + \alpha_T g \frac{\partial \psi}{\partial y} + \frac{\partial}{\partial x} \left(\mu \frac{\partial \hat{v}}{\partial x} \right) + \frac{\partial}{\partial y} \left(\mu \frac{\partial \hat{v}}{\partial y} \right) + F_{w,y} \quad (3.40)$$

where f is the Coriolis parameter, P_A is the sea-level atmospheric pressure, α_T is the effective earth-elasticity factor, ψ is the Earth tidal potential and μ is the horizontal viscosity (note that either the tidal potential nor the horizontal viscosity terms are considered in the simulations presented in this work). $(F_{w,x}, F_{w,y})$ contains the wave-induced forcing terms which are entirely computed in WWM-II :

$$F_{w,x} = \underbrace{v_s \left[f + \left(\frac{\partial \hat{v}}{\partial x} - \frac{\partial \hat{u}}{\partial y} \right) \right]}_{A1} - \underbrace{w_s \frac{\partial \hat{u}}{\partial z} - \frac{\partial J}{\partial x}}_{A2} + \underbrace{\hat{F}_{br,x} + \hat{F}_{bot,x}}_{A3} \quad (3.41)$$

$$F_{w,y} = \underbrace{-u_s \left[f + u_s \left(\frac{\partial \hat{v}}{\partial x} - \frac{\partial \hat{u}}{\partial y} \right) \right]}_{B1} - \underbrace{w_s \frac{\partial \hat{v}}{\partial z} - \frac{\partial J}{\partial y}}_{B2} + \underbrace{\hat{F}_{br,y} + \hat{F}_{bot,y}}_{B3} \quad (3.42)$$

where $(A1, B1)$ is the Vortex force introduced by *Garrett et al.* (1976) and $(A2, B2)$ is the wave-induced mean pressure term in which J reads :

$$J = \int_0^{2\pi} \int_0^\infty \frac{gkE}{\sinh(2kh)} d\sigma d\theta \quad (3.43)$$

Physically, the wave-induced mean pressure term $(A2, B2)$ represents an adjustment in the mean pressure to accommodate for the presence of waves (*Lane et al.*, 2007), while the Vortex force $(A1, B1)$ represents an interaction between the vorticity of the mean flow and the Stokes drift.

The horizontal components of the Stokes drift (u_S, v_S) read :

$$(u_S, v_S) = \int_0^{2\pi} \int_0^\infty \sigma k E \frac{\cosh(2k(z+d))}{\sinh^2(kh)} (\cos \theta, \sin \theta) d\sigma d\theta + (u_{S,R}, v_{S,R}) \quad (3.44)$$

where $(u_{S,R}, v_{S,R})$ is the contribution of the surface rollers to the horizontal Stokes drift (Eq. 3.33).

Finally, in Eqs (3.41) and (3.42), the term $(A3, B3)$ includes \hat{F}_{br} and \hat{F}_{bot} which are the non conservative wave accelerations, i.e. the source of quasi-Eulerian momentum which are equal to the sink of wave momentum owing to wave breaking processes and wave streaming respectively. One can note that the Vortex force formalism decomposes wave-induced forcing terms into conservative $(A1, B1, A2, B2)$ and non-conservative $(A3, B3)$ contributions. This representation is sound physically and allows to perform numerical experiments by turning off one or the other terms in order to better understand their respective effects on the mean circulation. In addition, this separation has a practical numerical aspect in the sense that the conservative forces have a known vertical distribution while the non-conservative ones are only known under their depth-integrated form (e.g., *Smith*, 2006), thus requiring the definition of an empirical vertical profile.

\hat{F}_{br} gathers the accelerations due to depth-induced breaking, whitecapping and surface rollers in a single term expressed as follows :

$$\begin{aligned} \left(\hat{F}_{br,x}(z), \hat{F}_{br,y}(z) \right) &= -\frac{f_{br}(z)}{\rho} \int_0^{2\pi} \int_0^\infty \rho g k [(1 - \alpha_r) S_{br} + S_{ds}] (\cos \theta, \sin \theta) d\sigma d\theta \\ &+ \frac{f_{br}(z)}{\rho} \frac{k_p}{\sigma_p} D_{rol}(\cos \theta_m, \sin \theta_m) \end{aligned} \quad (3.45)$$

where k_p and σ_p are the peak wavenumber and peak wave relative angular frequency. $f_{br}(z)$ corresponds to an empirical vertical distribution function which can be defined with different expressions (*Uchiyama et al.*, 2010). In this study, $f_{br}(z)$ is defined such that accelerations by breaking-induced processes are applied in the surface layer (*Guérin et al.*, 2018), which is similar to representing them as surface stresses (*Deigaard*, 1993; *Delpy et al.*, 2014). As highlighted by *Rasche et al.* (2006), the wave-enhanced vertical mixing associated with the production of turbulence by breaking waves (see section 3.2.1.3) mostly controls the vertical shear of the horizontal current velocity such that the near surface distribution of the breaking accelerations is not very important.

In intermediate to shallow water depths, the wave energy dissipated by bottom friction within the wave boundary layer induces a near-bottom current in the direction of wave propagation referred to as wave streaming (*Longuet-Higgins*, 1953; *Phillips*, 1977; *Xu and Bowen*, 1994). The acceleration associated with wave bottom streaming \hat{F}_{bot} is computed as follows :

$$\left(\hat{F}_{bot,x}(z), \hat{F}_{bot,y}(z) \right) = -\frac{f_{bot}(z)}{\rho} \int_0^{2\pi} \int_0^\infty \rho g k S_{bot} (\cos \theta, \sin \theta) d\sigma d\theta \quad (3.46)$$

The streaming acceleration is assumed to decrease upward across the wave boundary layer according to the vertical function $f_{bot}(z)$ (*Uchiyama et al.*, 2010) given by :

$$f_{bot}(z) = \frac{1 - \tanh(k_{wd}(z + d))^2}{\int_{-d}^{\bar{\eta}} 1 - \tanh(k_{wd}(z + d))^2 dz} \quad (3.47)$$

where $k_{wd} = 1/(a_{wd}\delta_{wd})$ is a decay length in which δ_{wd} is the wave bottom boundary layer thickness computed according to *Fredsøe and Deigaard* (1992) in the circulation model :

$$\delta_{wd} = 0.09(30z_0^{bot,w}) \left(\frac{A_{orb}}{30z_0^{bot,w}} \right)^{0.82} \quad (3.48)$$

with A_{orb} the near-bottom excursion amplitude and $z_0^{bot,w}$ the apparent bottom roughness length under the combined effects of waves and currents (see section 3.2.1.1). With $a_{wd} = 1$, we retrieve the theoretical thickness of the wave bottom boundary layer under monochromatic waves. In the study related to the shore platform, a_{wd} is fixed to 5, which is discussed in the corresponding chapter.

3.2.1.1 Vertical boundary conditions

The differential momentum equations require vertical boundary conditions to be solved. SCHISM enforces the balance between the internal Reynolds stress with the wind stress $\boldsymbol{\tau}_s = (\tau_{s,x}, \tau_{s,y})$ at the surface and with the bottom shear stress $\boldsymbol{\tau}_b = (\tau_{b,x}, \tau_{b,y})$ at the bottom :

$$\nu \frac{\partial \hat{\mathbf{u}}}{\partial z} = \frac{1}{\rho} \boldsymbol{\tau}_s, \text{ at } z = \bar{\eta} \quad (3.49)$$

$$\nu \frac{\partial \hat{\mathbf{u}}}{\partial z} = \frac{1}{\rho} \boldsymbol{\tau}_b, \text{ at } z = -d \quad (3.50)$$

with $\hat{\mathbf{u}} = (\hat{u}, \hat{v})$. The parameterization of the wind stress is discussed in section 3.2.1.2. Besides, the bottom stress is given by the following quadratic expression in a turbulent boundary layer (*Blumberg and Mellor, 1987*) :

$$\boldsymbol{\tau}_b = \rho C_d^{bot} |\hat{\mathbf{u}}_b| \hat{\mathbf{u}}_b \quad (3.51)$$

where C_d^{bot} is the bottom drag coefficient and $\hat{\mathbf{u}}_b$ is the velocity at the top of the bottom computational cell.

In the interior of the bottom boundary layer, the velocity profile obeys to a logarithmic law, by assuming that the vertical mesh is sufficiently resolved at the bottom such that the bottom cell is inside the boundary layer. From the latter consideration and with the expression of the vertical eddy viscosity ν given by the turbulence closure theory (section 3.2.1.3), the drag coefficient can be calculated as follows :

$$C_d^{bot} = \left(\frac{\kappa}{\ln \frac{\delta_{bot}}{z_0^{bot}}} \right)^2 \quad (3.52)$$

where κ is the von Kármán's constant ($\kappa = 0.4$), δ_{bot} is the thickness of the bottom computational cell and z_0^{bot} is the bottom roughness length, which is provided by the user, either constant or spatially-varying over the modelled domain. As terrain-following s-coordinates are used on the vertical (see section 3.2.3), a minimum threshold value for δ_{bot} is used to avoid that C_d^{bot} blows up in very shallow depths.

The bottom stress $\boldsymbol{\tau}_{wc}$ under the combined action of waves and currents in SCHISM can be accounted for by the model of *Grant and Madsen (1979)* or *Soulsby (1997)*. In our case, the latter model is retained, following which $\boldsymbol{\tau}_{wc}$ is expressed as :

$$\boldsymbol{\tau}_{wc} = \boldsymbol{\tau}_b \left[1.0 + 1.2 \left(\frac{|\boldsymbol{\tau}_w|}{|\boldsymbol{\tau}_w| + |\boldsymbol{\tau}_b|} \right)^{3.2} \right] \quad (3.53)$$

in which $\boldsymbol{\tau}_w$ is the wave-induced bottom stress, computed as :

$$\boldsymbol{\tau}_w = \frac{1}{2} \rho f_{ws} |\mathbf{u}_{orb}| \mathbf{u}_{orb} \quad (3.54)$$

where f_{ws} is the wave friction factor computing according to *Soulsby (1997)* and \mathbf{u}_{orb} is the bottom wave orbital velocity.

3.2.1.2 Parameterization of the wind surface stress

At the surface, the wind stress is commonly parameterized with a bulk formula of the form :

$$\boldsymbol{\tau}_s = \rho_a C_d |\mathbf{U}_{10}| \mathbf{U}_{10} \quad (3.55)$$

where ρ_a is the air density, \mathbf{U}_{10} is the wind speed at 10 m height above the sea surface and C_d is a drag coefficient which represents the sea surface roughness z_0 . The drag coefficient is usually computed as a linear function of U_{10} , which can be done in SCHISM following

the formulations of *Pond and Pickard* (1983) or *Hwang et al.* (2019). However, as shown in chapter 2, the sea surface roughness also varies with the sea state, which in turn can impact the surface stress. To account for wave effects on the surface stress, the surface roughness can be related to wave parameters such as the wave age (*Donelan et al.*, 1993) or the wave-supported stress (*Janssen*, 1991). In SCHISM, both approaches were implemented. The formulation proposed by *Donelan et al.* (1993) reads as follows :

$$\frac{z_0}{H_{rms}} = 6.7 \cdot 10^{-4} \left(\frac{|U_{10}|}{c_p} \right)^{2.6} \quad (3.56)$$

where H_{rms} and c_p (computed at the peak wave frequency) are provided by the wave model. The surface stress is obtained after computing C_d with the following relationship :

$$\sqrt{C_d} = \frac{\kappa}{\log\left(\frac{z_{obs}}{z_0}\right)} \quad (3.57)$$

where z_{obs} is the height at which the wind is taken ($z_{obs} = 10$ m).

Alternatively, the wind stress can be expressed as the air-side stress τ_a minus the momentum flux absorbed by waves (wave-supported stress) τ_{ws} :

$$\tau_s = \tau_a - \tau_{ws} \quad (3.58)$$

in which τ_a is related to the wind friction velocity u_* through the following quadratic function :

$$\tau_a = \rho_a u_*^2 \quad (3.59)$$

and τ_{ws} , the wave-supported stress, is expressed as :

$$\tau_{ws} = \int_0^{2\pi} \int_0^\infty \rho g k S_{in} d\sigma d\theta \quad (3.60)$$

3.2.1.3 Turbulence closure model

In SCHISM, the hydrodynamic model is coupled to the General Ocean Turbulence Model (GOTM; *Burchard et al.*, 1999; *Umlauf et al.*, 2005) which is a one vertical dimensional (1DV) model that simulates the hydrodynamic and thermodynamic processes related to vertical mixing in the water column. The model solves a generic length scale (GLS) two-equation turbulence closure model. The two equations describe the production and dissipation of turbulent kinetic energy (TKE) K , as well as the evolution of the GLS ψ , which are related by the following equation :

$$\psi = (c_\mu^0)^p K^m l^n \quad (3.61)$$

where l is the turbulent mixing length and c_μ^0 is a stability coefficient (~ 0.54). Classic turbulence closure schemes can be retrieved from the GLS model through the definition of the coefficients p , m and n . In this work, the k - ω turbulence scheme is considered and reproduced with $p = -1.0$, $m = 0.5$ and $n = -1.0$.

Wave breaking processes at the surface are an important source of turbulence which can greatly affect the vertical mixing across the water column (*Agrawal*, 1992). The injection of

TKE at the surface by breaking waves is modelled through the following flux-type boundary condition at the surface ($z = \bar{\eta}$) (*Craig and Banner, 1994; Feddersen and Trowbridge, 2005*) :

$$\frac{\nu}{\sigma_K} \frac{\partial K}{\partial z} = F_K \left(\frac{z_0^s - z'}{z_0^s} \right)^{\frac{3}{2}\alpha_K} \quad (3.62)$$

where σ_K is the turbulent Schmidt number for K , F_K [$\text{m}^3 \cdot \text{s}^{-3}$] is the flux of energy injected into the water column, α_K is the spatial decay rate in the wave-enhanced layer, z' is half the height of the top cell and z_0^s is the surface mixing length that dictates the distribution of the TKE in the water column. z_0^s has a strong influence on vertical profiles of currents but is difficult to measure, a number of parametrizations have thus been proposed for this quantity (*Moghimi et al., 2016*). It has been either defined as a constant ($z_0^s = 0.2 \text{ m}$; *Feddersen and Trowbridge, 2005*) or proportional to the significant wave height H_{m0} : $z_0^s = \alpha_w H_{m0}$ (*Terray et al., 1996*) with α_w an $O(1)$ parameter. The latter parameterization is used in this work with α_w fixed to 0.8. Following the approach of *Feddersen and Trowbridge (2005)*, F_K is assumed to be function of the energy dissipated by wave breaking and whitecapping at the surface :

$$F_K = \frac{c_{br}}{\rho} \left[-(1 - \alpha_r) \int_0^{2\pi} \int_0^\infty \rho g S_{br} d\sigma d\theta + D_{rol} \right] - \frac{c_{ds}}{\rho} \int_0^{2\pi} \int_0^\infty \rho g \sigma S_{ds} d\sigma d\theta \quad (3.63)$$

where c_{br} and c_{ds} control the amount of energy injected into the water column from wave breaking and whitecapping respectively. c_{br} can range between 0.01 and 0.25 according to *Feddersen and Trowbridge (2005)* while *Bakhoday Paskyabi et al. (2012)* suggested $c_{ds} \sim 1$. Here, the values of 0.15 for c_{br} and 1 for c_{ds} are retained.

At the bottom, a Dirichlet boundary condition is used :

$$k = \frac{u_*^{bot}}{c_\mu^{0.2}} \quad (3.64)$$

where u_*^{bot} is the bottom friction velocity :

$$u_*^{bot} = \sqrt{\tau_{wc} + \sqrt{\tau_{dissbot,x}^2 + \tau_{dissbot,y}^2}} \quad (3.65)$$

u_*^{bot} is typically taken equal to $\sqrt{\tau_{wc}}$ where τ_{wc} is the wave-current bottom stress. We additional account for the turbulent kinetic energy produced by wave frictional dissipation, which can be substantial on rough areas such as rock platforms. ($\tau_{dissbot,x}, \tau_{dissbot,y}$) then correspond to the dissipation stress due to bottom friction.

3.2.2 2DH configuration - Radiation stress formalism

In order to analyse the effects of the depth-varying wave-induced circulation on the wave setup, comparisons between 3D VF and 2DH radiation stress (RS) configurations are conducted. The RS formalism of *Longuet-Higgins and Stewart (1964)* has been implemented in SCHISM by *Roland et al. (2012)*. In a 2DH horizontal barotropic configuration,

the Saint-Venant Equations with additional source terms associated with storm surges (wind, atmospheric pressure, waves) are solved :

$$\frac{\partial \bar{\eta}}{\partial t} + \frac{\partial(hU)}{\partial x} + \frac{\partial(hV)}{\partial y} = 0 \quad (3.66)$$

$$\frac{\partial U}{\partial t} + U \frac{\partial U}{\partial x} + V \frac{\partial U}{\partial y} = -g \frac{\partial \bar{\eta}}{\partial x} + \frac{\tau_{s,x} - \tau_{b,x}}{\rho h} + F_x \quad (3.67)$$

$$\frac{\partial V}{\partial t} + U \frac{\partial V}{\partial x} + V \frac{\partial V}{\partial y} = -g \frac{\partial \bar{\eta}}{\partial y} + \frac{\tau_{s,y} - \tau_{b,y}}{\rho h} + F_y \quad (3.68)$$

in which (F_x, F_y) are given by :

$$F_x = fV - \frac{1}{\rho} \frac{\partial P_A}{\partial x} + \alpha_T g \frac{\partial \psi}{\partial x} + \frac{\partial}{\partial x} \left(\mu \frac{\partial U}{\partial x} \right) + \frac{\partial}{\partial y} \left(\mu \frac{\partial U}{\partial y} \right) + R_{sx} \quad (3.69)$$

$$F_y = -fU - \frac{1}{\rho} \frac{\partial P_A}{\partial y} + \alpha_T g \frac{\partial \psi}{\partial y} + \frac{\partial}{\partial x} \left(\mu \frac{\partial V}{\partial x} \right) + \frac{\partial}{\partial y} \left(\mu \frac{\partial V}{\partial y} \right) + R_{sy} \quad (3.70)$$

where (U, V) are the horizontal components of the depth-integrated velocity. As in 3D configuration, either the tidal potential nor the horizontal viscosity terms are considered in the 2DH simulations. (R_{sx}, R_{sy}) corresponds to the divergence of the radiation stress tensor (*Longuet-Higgins and Stewart, 1962, 1964*), which additionally accounts for the surface roller contributions :

$$R_{sx} = -\frac{1}{\rho h} \left(\frac{\partial S_{xx} + S_{xx,r}}{\partial x} + \frac{\partial S_{xy} + S_{xy,r}}{\partial y} \right) \quad (3.71)$$

$$R_{sy} = -\frac{1}{\rho h} \left(\frac{\partial S_{yy} + S_{yy,r}}{\partial y} + \frac{\partial S_{xy} + S_{xy,r}}{\partial x} \right) \quad (3.72)$$

where S_{xx} , S_{yy} and S_{xy} are the components of the radiation stress tensor computed following the approach of *Battjes (1974)* for an irregular wave spectrum :

$$S_{xx} = \rho g \int_0^{2\pi} \int_0^\infty N \sigma \left[\frac{c_g}{c} (\cos^2 \theta + 1) - \frac{1}{2} \right] d\theta d\sigma \quad (3.73)$$

$$S_{yy} = \rho g \int_0^{2\pi} \int_0^\infty N \sigma \left[\frac{c_g}{c} (\sin^2 \theta + 1) - \frac{1}{2} \right] d\theta d\sigma \quad (3.74)$$

$$S_{xy} = \rho g \int_0^{2\pi} \int_0^\infty N \sigma \frac{c_g}{c} \sin \theta \cos \theta d\theta d\sigma \quad (3.75)$$

where c is the phase velocity.

$S_{xx,r}$, $S_{yy,r}$ and $S_{xy,r}$ are the surface roller contributions to the radiation stress, given by :

$$S_{xx,r} = 2E_{rol} \cos^2 \theta_m \quad (3.76)$$

$$S_{yy,r} = 2E_{rol} \sin^2 \theta_m \quad (3.77)$$

$$S_{xy,r} = 2E_{rol} \cos \theta_m \sin \theta_m \quad (3.78)$$

Since the velocity at the bottom is not available in a 2DH configuration, the bottom drag coefficient is calculated according to the Manning's law :

$$C_d^{bot} = \frac{g.n^2}{h^{1/3}} \quad (3.79)$$

with n the Manning coefficient, which is commonly fixed to 0.02 in the open ocean while it can be spatially varying on continental shelves, coastal zones and estuaries with values adapted to the nature of the substrate (e.g., *Bunya et al.*, 2010).

3.2.3 Numerical approaches

In its 3D configuration, SCHISM solves the phase-averaged free surface elevation and the 3D velocity according to the following steps (*Zhang and Baptista*, 2008; *Zhang et al.*, 2015, 2016) :

1. The depth-integrated continuity equation (Eq. 3.36) and the momentum equations (Eqs 3.37 and 3.38) along with the vertical boundary conditions (Eqs 3.49 and 3.50) are discretized semi-implicitly in time.
2. The velocity at time t^n , called "back-tracked velocity", is calculated using an Eulerian-Lagrangian method. In more details, this method allows to find the location of a particle at time t^n from its position at time $t^n + \Delta t$, and calculate its velocity by interpolation.
3. A semi-implicit Galerkin finite-element method is then applied to the discretized continuity equation and with the aid of the vertically-integrated form of the discretized momentum equations, an equation for $\bar{\eta}$ alone can be obtained and solved at nodes (Fig. 3.2-b).
4. A semi-implicit Galerkin finite-element method is then also applied to the discretized momentum equations, from which the horizontal velocities are solved at each vertical level and side center (Fig. 3.2-b).
5. The vertical velocity is finally solved at each vertical level at the center of each element with a finite-volume method (Fig. 3.2-b).

On the vertical dimension, the use of a hybrid S (terrain-following s -coordinates) and shaved Z coordinates allows a more flexible representation of the vertical structure of the water column (Fig. 3.2-a).

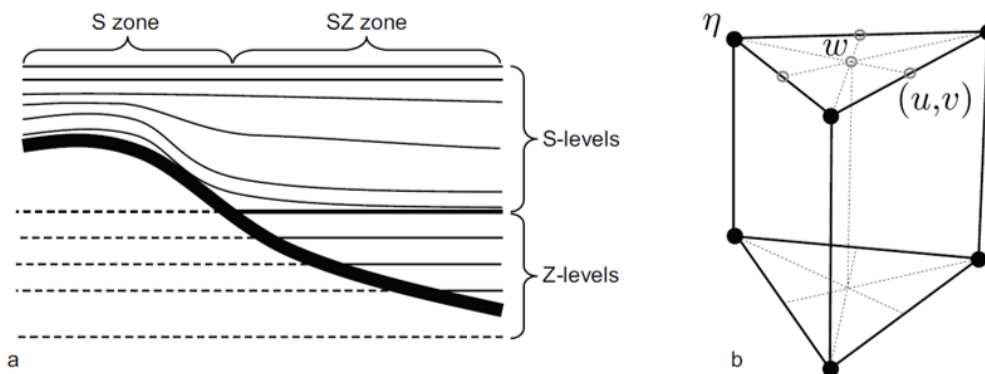


FIGURE 3.2 – (a) Hybrid SZ vertical coordinate system and (b) 3D computational unit in SCHISM where variables are solved. Figure adapted from *Zhang and Baptista (2008)*.

Chapitre 4

Data acquisition and processing

This research work combines numerical modelling and field observations collected during field campaigns conducted on the shore platform near La Cotinière on Oléron Island and on the salt marsh of Brouage. The deployment relative to each campaign will be presented in the corresponding chapters (chapter 6 and chapter 7 respectively). Nevertheless, in the present section, all the instruments that have been used to measure water levels, currents and wave parameters during these field campaigns, are described. After that, data processing methods are presented. Number of these methods have been applied during the shore platform experiment, such that number of examples are given relative to this campaign.

4.1 Data acquisition techniques

4.1.1 In-situ observations of random waves

During the field campaigns, wave measurements have been collected from surface-following buoys, and subsurface pressure sensors (PT) deployed during the experiment period. These are the most common instruments used on the field to measure waves but other systems exist such that ADCP or PUV sensors which are deployed in the water column, video techniques such as stereo-photography (e.g., *Benetazzo*, 2006), and radar remote sensing such as satellite altimeters (e.g., *Queffelec*, 2004) or airborne scanning radars (e.g., *Hwang et al.*, 2000). In addition, certain technologies are able to provide a direct measurement of the free surface elevation such as the AST (Acoustic Surface Tracking; e.g., *Mouragues et al.*, 2019), the lidar scanner (LIght Detection And Ranging; e.g., *Martins et al.*, 2018) or capacitance/resistive types of wave gauges, the latter being rather used for laboratory experiments (*Flick et al.*, 1979). We describe in more details the instruments used during the field campaigns below.

4.1.1.1 Wave buoys

Wave buoys are the most commonly used systems to measure waves in intermediate or deep water depth (*Tucker and Pitt*, 2001). They vary in diameter and weight depending on the environment in which they are deployed and associated sea-state conditions (deep, coastal or nearshore-ports waters) (Fig. 4.1). Floating wave buoys dedicated to provide observations over a long time duration are usually anchored to the bottom with a strong and reliable mooring system. For a long time, wave buoys have been equipped with acce-

lerometers recording the vertical acceleration which provides, after double integration in time, a sea surface elevation signal. More recently, the wave direction can be determined through the measurement of the horizontal accelerations or pitch and roll. Processing of the collected data consists in spectral and wave-by-wave analyses over temporal window of 30 to 60 min which allow to compute frequency-directional wave spectra and statistical wave parameters such as the significant wave height, the mean wave period, the peak wave period and direction. Processed data are automatically transmitted in real time via radio or satellite links, and are made immediately available to users through the internet. Wave buoys data are important for many practical purposes. Navigation, fishing or recreation and sporting events benefit from accurate forecast and real-time data delivered by wave buoys. Climatological and real-time data are needed in the design and deployment phases of marine structures such as piers or breakwaters. They are required at the development stage of wave models (for model validation) and in storm surge forecasting. Wave buoys can also be used to compute long-term statistics of the sea state parameters (e.g., *Butel et al.*, 2002), with applications to the reconstruction or the projection of the wave climate at regional and global scale (e.g., *Komar et al.*, 2010; *Ruggiero et al.*, 2010). More locally, these data can be used as boundaries conditions to wave models.



FIGURE 4.1 – *Non-directional Biscay buoy (station 62001) located at 45.230 N 5.000 W in the Bay of Biscay (at 4500 m depth) operated by UK Met Office and Meteo France (credits : www.ndbc.noaa.gov).*

In environments with strong currents ($\sim 1 \text{ m.s}^{-1}$ or higher), drifting buoys are usually used instead of moored buoys which can be hardly deployed in these conditions because of the tension on the mooring line. Drifting buoys or "drifters" allow to measure waves following currents on a short time period, providing informations on the sea state conditions in the flow field (e.g., *Thomson*, 2012).

4.1.1.2 Pressure sensors

Bottom-mounted pressure sensors have been widely used to measure water waves for more than 50 years now (e.g., *Seiwell*, 1947; *Grace*, 1978; *Bishop and Donelan*, 1987; *Bertin et al.*, 2020). They are robust, easy to deploy and relatively low-cost. Usually deployed

near the bottom (Fig. 4.2-b and Fig. 4.3-c), the pressure sensors measure the pressure exerted by the water column from which both very long waves (e.g. tides) and short waves can be estimated. However, a reconstruction method is necessary to recover the free surface elevation from bottom pressure measurements (see section 4.2.3).

4.1.1.3 Direct measurements of the free surface elevation

Acoustic sensors are capable of directly measuring the free surface. One of these is the Acoustic Surface Tracking (AST), which is a newly-developed ADCP feature (see section 4.1.3 for ADCP description). A short acoustic pulse is transmitted vertically toward the free surface. This pulse is reflected on the free surface and the time lag between the transmitted and reflected ping is used to calculate the free surface elevation. The AST has been mainly tested and validated in water depth $> 10\text{ m}$ (e.g., *Pedersen and Nylund, 2004*). More recently, this technology has been successfully used to measure an undular tidal bore in the Garonne river (*Martins et al., 2017b*) and waves outside the surf zone (*Mouragues et al., 2019*). However, the AST is sensitive to the presence of air bubbles in the water column such as under breaking waves in surf zones. The acoustic signal is reflected before reaching the free surface, resulting in a severe underestimation of the measured water depth which prevents from reliably analysing waves in surf zones with the AST (*Birch et al., 2004*). Direct measurements of surf zone waves can be alternatively obtained by lidar scanners, which are very powerful tools to investigate cross-evolution of surf zone waves (e.g., *Brodie et al., 2015; Martins et al., 2018*). By providing reliable direct measurements of the free surface elevation, AST and lidar scanners can be used to assess the performances of the reconstruction methods from subsurface pressure measurements (see section 4.2.3).

4.1.2 In-situ observations of water levels

Water levels fluctuations are continuously monitored by tide gauges along the coasts. The first systems, based on float gauge recorders, are now widely substituted by fully automated radar devices (*Plater and Kirby, 2011*). Some tide gauges, mostly in the northwest of Europe, have recorded sea level time-series since the mid-nineteenth century, which is of particular interest for analysis of long-term trends (*Woodworth et al., 2009*). Tide gauges are commonly located in coastal areas sheltered from waves like harbours, lagoons or estuaries, where they measure the total water level due to tides and storm surges. Recorded water levels can include a wave setup signal if wave breaking occurs near the inlet/entrance (e.g., *Malhadas et al., 2009; Aucan et al., 2012; Olabarrieta et al., 2011; Fortunato et al., 2017; Woodworth, 2020*), although this is still unclear in the scientific community (*Melet et al., 2018; Lambert et al., 2020; Almar et al., 2021*). In chapter 5, the contribution of the wave setup to the water level in wave-sheltered environments during energetic conditions is identified and quantified. Water levels observations can also be obtained from pressure sensors deployed over short-term duration such as during field experiments of 5-10 days to longer period (several months to a year depending on the sampling frequency, memory capacity and battery life of the sensor). Section 4.2.1 details how storm surges can be computed from these water level time-series.

4.1.3 In-situ observations of currents

4.1.3.1 ADCP

An Acoustic Doppler Current Profiler (ADCP) measures the current profile across the entire water column. In more details, current velocities in the 3 directions of space are measured in a set of cells along 3-5 acoustic beams. The ADCP sends out high-frequency pulses which are reflected off particles that are suspended in the water column and advected by currents. The Doppler effect causes a change in the frequency of the reflected signal (Doppler shift), which is measured and processed by the ADCP to estimate current velocities. In coastal zones, the instrument is commonly installed near the seafloor, anchored to the bottom or fixed on a heavy structure (Fig 4.2-a and Fig 4.3-a). While such devices have proved to be robust and reliable for various applications (e.g., *Togneri et al.*, 2017), a particular attention should be paid to data collected from ADCPs deployed in surf zones, where the presence of air bubbles in the wave column can affect or even block the acoustic signal and lead to incoherent patterns of currents.

ADCPs can also be used to measure the wave spectrum. During wave burst measurements, the device collects near-bottom pressure data with an internal pressure sensor and horizontal velocities in a specific cell above the sea bottom defined by the user. The wave frequency-directional spectrum can be estimated via the wave orbital flow field (*Herbers and Lentz*, 2010) or a PUV (pressure-velocity) method (*Gordon and Lohrmann*, 2002), while the wave frequency spectrum can be computed independently from velocity measurements or near-bottom pressure measurements.

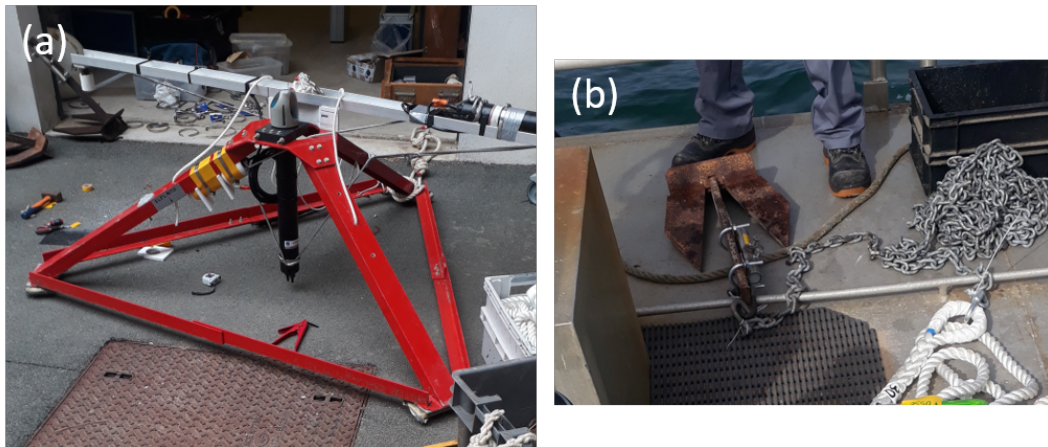


FIGURE 4.2 – Instruments deployed in the subtidal zone during the field campaign on the shore platform : (a) 600 kHz ADCP on a weighted tripod structure and (b) pressure sensor housed in a steel tube fixed to an anchor.

4.1.3.2 ADV

An ADV (Acoustic Doppler Velocimeter) records 3D current velocities based on the Doppler effect, however, in contrast with ADCPs, measurements are made at a single-point in the water column (Fig 4.3-b). The device allows for relatively high-frequency sample rate (e.g. 16, 32 or 64 Hz), which makes it suitable to resolve rapid small scale changes in 3D velocity, turbulence or boundary layer dynamics. As with ADCPs, ADVs can be used to measure the wave spectrum from velocity and/or pressure measurements (as the ADV is

also equipped with an internal PT).

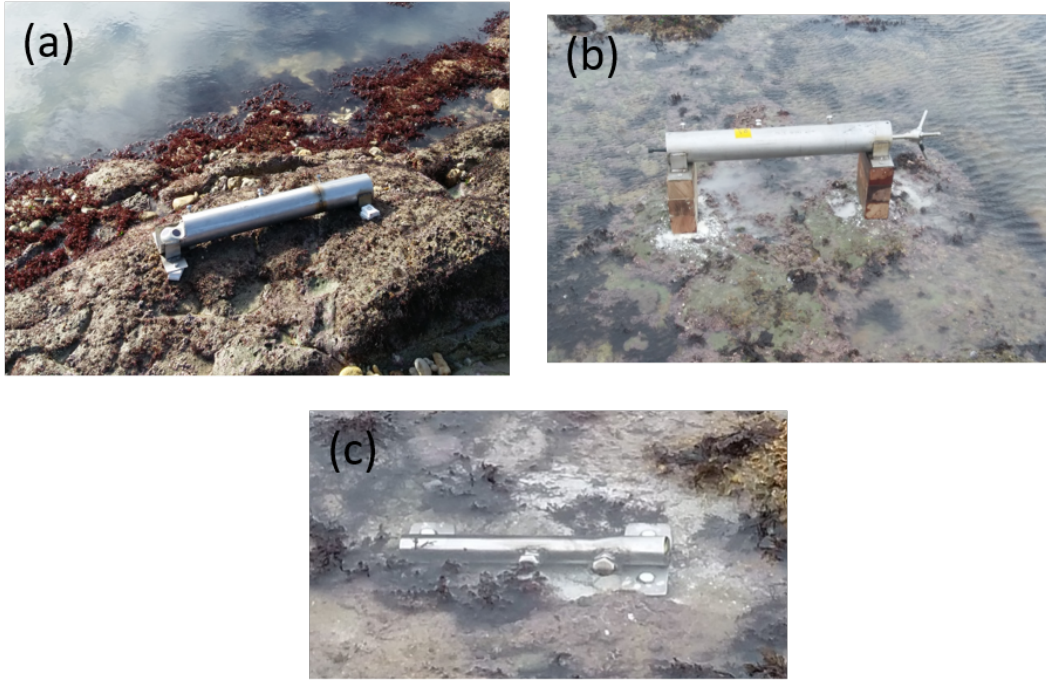


FIGURE 4.3 – Instruments deployed in the intertidal zone during the field campaign on the shore platform : (a) ADCP, (b) ADV and (c) pressure sensors. They are housed in stainless steel tubes screwed to the bedrock to protect them from stone motions (credits : Laura Lavaud).

4.2 Data processing

4.2.1 Estimation of storm surges

Storm surges are typically computed as the difference between the observed total water level and a tidal prediction at tide gauges (Fig. 4.4) (e.g., *Staneva et al.*, 2016; *Bertin et al.*, 2015a; *Brown et al.*, 2013a) or pressure sensors. To compute a tidal prediction, a harmonic analysis using the UTide Code of *Codiga* (2011) is first applied to the water level time series to determine the amplitude and phase of the tidal constituents. The free surface elevation η_T at any time t is typically expressed as the sum of the contributions of the individual tidal constituents (*Schureman*, 1958) :

$$\eta_T(t) = \sum_{i=1}^n b_i A_i \cos(w_i t + \{V_o + u\}_i - \varphi_i) \quad (4.1)$$

where n is the number of tidal constituents. A_i , φ_i and w_i are the amplitude, the phase and the angular frequency respectively, for the tidal constituent i . b_i is the node factor and $\{V_o + u\}_i$ is the equilibrium argument at $t = 0$ for the tidal constituent i . A_i and φ_i are extracted from a water depth time series by means of a least squares technique (*Foreman and Neufeld*, 1991). The duration of the time series should be long enough to meet the Rayleigh criterion (*Foreman and Henry*, 1989) : to resolve two constituents that have frequencies f_1 and f_2 , which are relatively close to one another, the difference between these frequencies must be greater than the inverse of the length of the time series

$T (|f_2 - f_1| > T^{-1})$. For instance, resolving M2 and S2 requires at least 15 days of record (Pairaud, 2005). For shorter records, the UTide code allows to compute the inference of multiple constituents based on a single reference one. This method requires the knowledge of inference parameters, which are amplitude ratios and phase differences between inferred and reference constituents (e.g., S2 and N2 inferred from M2), obtained from a harmonic analysis conducted on a long-term record at a nearby tide gauge or pressure sensor (for a detailed description of this method, the reader is referred to Foreman, 1977). The astronomical constituents previously extracted from the harmonic analysis are then used to reconstruct a tidal prediction. Note that the constituent Sa was not included in the tidal prediction since it results from a combination of thermo-steric and atmospheric effects as shown by Bertin et al. (2015b) and Payo-Payo and Bertin (2020) in the North-East Atlantic Ocean, and by Marcos and Tsimplis (2007) in the Mediterranean Sea and the Atlantic Iberian coast.

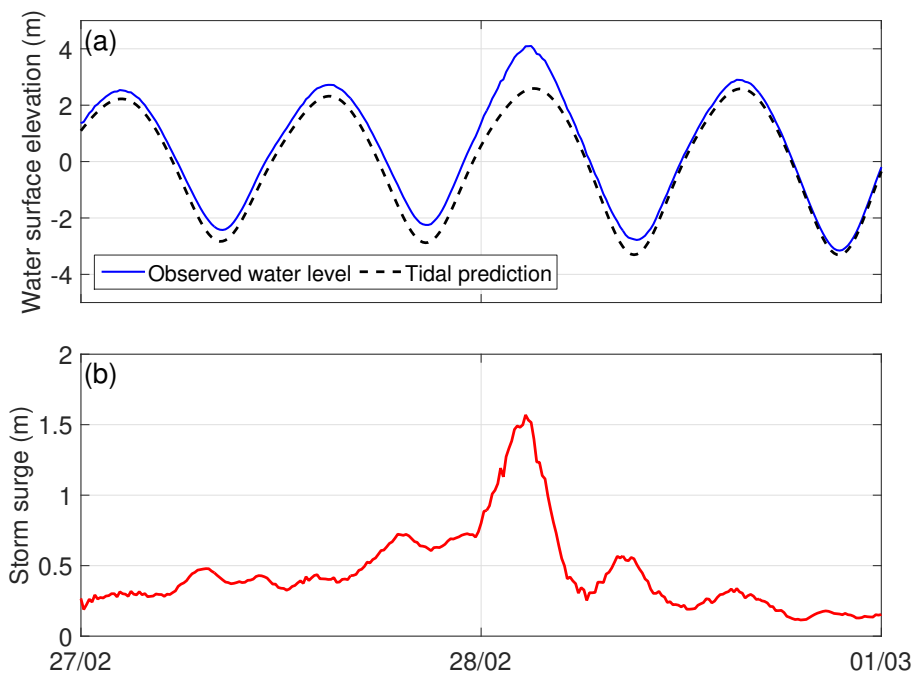


FIGURE 4.4 – (a) Water surface elevation and tidal prediction and (b) storm surge, during the storm Xynthia (2010) at La Pallice tide gauge (La Rochelle, France).

4.2.2 Relative estimation of wave setup

One of the main objective in this work is to better understand the development of the wave setup in contrasting nearshore zones. To investigate this process, wave setup estimations have been computed from water level signals obtained from pressure sensors deployed during the field campaigns. The pressure sensors were deployed over short periods of time (few days) only and those located in the intertidal zone were not continuously submerged, which limit the application of the least squares harmonic analysis. Also, the harmonic analysis would induce additional uncertainties in the estimation of the wave setup (± 0.05 - 0.10 m). Hence, a solution that we used consists in computing the wave setup as the change in mean free surface elevations between the deepest pressure sensor and the pressure sensors further onshore (Raubenheimer et al., 2001; Lowe et al., 2009; Rijnsdorp et al., 2021). Considering PT 1 at the deepest pressure sensor and PT 2 closer to shore

(Fig. 4.5), the wave setup is calculated as follows :

$$\bar{\eta}_s = \Delta h + d_1 - d_2 \quad (4.2)$$

where d_1, d_2 is the bathymetry relative to mean sea level and $\Delta h = h_2 - h_1$ is the difference between the mean (burst-averaged) water depths h_1, h_2 determined from pressure measurements assuming hydrostatic pressure (see section 4.2.3.2). $\bar{\eta}_s$ can be referred as a "relative wave setup", which nearly corresponds to the total wave setup since PT 1 is normally located outside the surf zone. Hence, $\bar{\eta}_1$ includes tidal and atmospheric surge elevations only. d_2 is supposedly leveled in the field while d_1 is not since the reference sensor (PT 1 here) is generally located in the subtidal zone where vertical levelling with a centimetric accuracy is very challenging. However, d_1 should be retrieved to compute the wave setup. For this, the calmest conditions of the experiment are identified (i.e. weak winds and both sensors located far outside the surf zone), so that the free surface elevation $\bar{\eta}$ can be considered horizontal between PT 1 and PT 2 at this instance (i.e. $\bar{\eta}_1 = \bar{\eta}_2$ with $\bar{\eta}_2$ known as d_2 is levelled), which allows to estimate the vertical position d_1 as $h_1 - \bar{\eta}_1$.

At the sensors located in the intertidal zone, samples where the minimum water depth was less than 0.50 m were discarded from the computation of the wave setup to avoid accounting for swash processes.

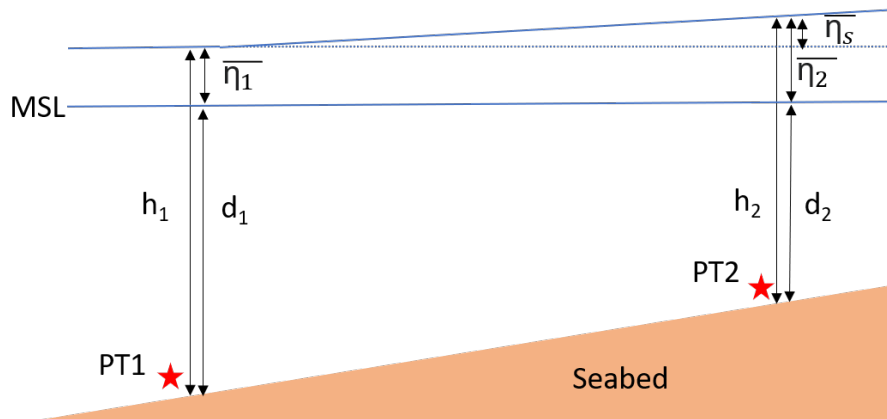


FIGURE 4.5 – Sketch detailing the variables used in the procedure for computing the wave setup between different pressure sensors. d_i is the bathymetry relative to mean sea level (MSL), h_i is the mean water depth and $\bar{\eta}_i$ is the mean free surface elevation with $i = 1, 2$. $\bar{\eta}_s$ corresponds to the wave setup at PT 2.

4.2.3 Reconstruction of the free surface from pressure measurements

4.2.3.1 Introduction

As shown above, pressure sensors have long been used to measure water waves in the nearshore but recovering the free surface from pressure measured near the bottom is not a trivial mathematical problem, particularly in the surf zone where waves are strongly non-linear. *Mouragues et al.* (2019) provides a recent review of the existing reconstruction methods from pressure measurements. Here, we present three methods which can be used to reconstruct the free surface : the hydrostatic reconstruction, the classic transfer function method based on the linear wave theory, and the non-linear weakly-dispersive reconstruction method proposed by *Bonneton et al.* (2018).

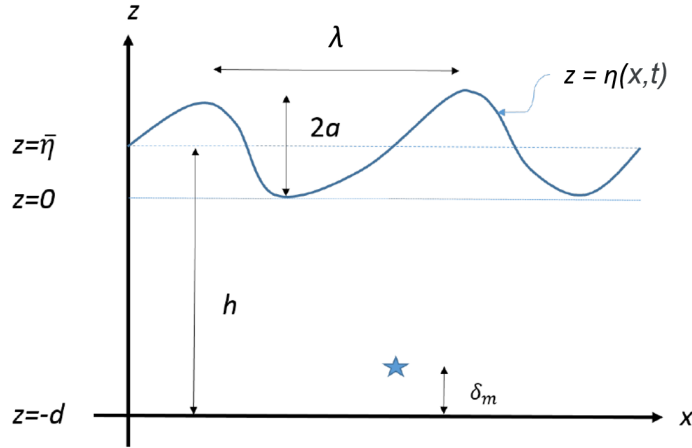


FIGURE 4.6 – Physical variables considered in the problem. d is the bathymetry relative to mean sea level at $z = 0$, $\bar{\eta}$ is the mean free surface elevation corresponding to the low-frequency contributions to the free surface variations (tides, storm surges including wave setup) and the blue star indicates the position of the pressure sensor in the water column.

The wave propagation can be characterized by two dimensionless parameters, namely a non linearity parameter ϵ and a dispersion (or shallowness) parameter μ , defined as follows :

$$\epsilon = \frac{a}{h} \quad (4.3)$$

$$\mu = \left(\frac{h}{L}\right)^2 = (kh)^2 \quad (4.4)$$

where a is the wave amplitude, L is the characteristic horizontal length scale ($L = \lambda/(2\pi) = 1/k$ with λ the wavelength and k the wave number) and h the mean water depth. Alternatively, ϵ and μ can be interrelated by the steepness parameter ς :

$$\varsigma = \epsilon\sqrt{\mu} \quad (4.5)$$

4.2.3.2 Hydrostatic reconstruction

The hydrostatic reconstruction consists in converting observed bottom pressure measurements into time series of free surface elevation assuming the hydrostatic approximation, that is neglecting the vertical acceleration of the fluid in the momentum equation. The hydrostatic free surface elevation η_H reads :

$$\eta_H = \frac{P_m - P_{atm} - P_0}{\rho g} + \delta_m - h \quad (4.6)$$

where η_H is the free surface elevation, δ_m is the height of the sensor above the seabed, P_m is the pressure measured at a distance δ_m from the seabed, P_{atm} is the atmospheric pressure, P_0 is the zero of the PT when not recently calibrated (see section 4.2.3.5), ρ is the water density and g is the acceleration due to gravity (Fig. 4.6). h is the mean total water depth computed as :

$$h = \frac{P_m - P_{atm} - P_0}{\rho g} + \delta_m \quad (4.7)$$

where the overbar denotes typically 20 or 30-min burst averaging.

The hydrostatic reconstruction provides good estimates of the free surface elevation for very long waves such as tsunamis, storm surges and tidal waves, characterized by a very small dispersion. The hydrostatic reconstruction has also been applied to estimate the free surface elevation of short waves in the inner surf zone, where the non-hydrostatic processes have been considered to be negligible (*Raubenheimer et al.*, 1996; *Sénéchal et al.*, 2001). However, this method has been shown to substantially underestimate the significant and individual wave height outside (e.g., *Martins et al.*, 2017a) and inside the entire surf zone (e.g., *Van Dorn*, 1978; *Martins et al.*, 2020). Indeed, while it is expected that non-hydrostatic effects are strong near the breaking point where waves are characterized by steep faces and strong vertical accelerations, *Martins et al.* (2020) shown that non-hydrostatic processes are also significant in the inner surf zone. Hence, non-hydrostatic reconstruction methods are required to estimate the wave field in coastal areas.

4.2.3.3 Transfer Function Method

The most commonly used non-hydrostatic method is the Transfer Function Method (TFM), which approximates the potential velocity to first order in wave steepness based on the linear wave theory (*Bishop and Donelan*, 1987). This linear reconstruction method can be written as follows :

$$\mathcal{F}\{\eta_L\}(x, w) = K_{p,L}(w)\mathcal{F}\{\eta_H\}(x, w) \quad (4.8)$$

where w is the wave absolute angular frequency, $\mathcal{F}\{\cdot\}$ is the Fourier transform and $K_{p,L}(w)$ is the (non-hydrostatic) correction factor (transfer function) applied to the hydrostatic reconstruction of the free surface elevation which reads :

$$K_{p,L}(w) = \frac{\cosh(kh)}{\cosh(k\delta_m)} \quad (4.9)$$

where k is computed from the dispersion relation given by the linear wave theory :

$$\omega^2 = gk \tanh(kh) \quad (4.10)$$

The presence of an ambient current induces a Doppler shift in the absolute wave frequency, such that the dispersion relation is modified as :

$$\omega^2 = \sqrt{gk \tanh(kh)} + kU \quad (4.11)$$

with U the velocity of a depth-uniform horizontal current. *Bonneton and Lannes* (2017) have shown that the effect of current can be neglected if $U < \epsilon\sqrt{gh}$, which is usually verified in coastal zones located far from inlets. Using the TFM without accounting for an ambient current with $U > \epsilon\sqrt{gh}$, can substantially deteriorate its performance, leading for instance to large errors in the significant wave height (e.g., *Smith*, 2002).

The TFM was early used to correct for the attenuation of the pressure signal with depth and compute wave characteristics in both deep and coastal waters (*Guza and Thornton*, 1980; *Jones and Monismith*, 2007). The TFM has demonstrated to well estimate bulk parameters associated with linear waves with errors less than 10 % (e.g., *Guza and Thornton*, 1980; *Tsai et al.*, 2005), however, the TFM is not recommended to estimate individual wave parameters such as wave height and shape of each wave (*Bishop and Donelan*, 1987; *Mouragues et al.*,

2019). When non-linearities become important in shallower depths, the correction factor is overestimated at relatively high frequencies (generally for frequency $f > 2f_p$ with f_p the peak frequency; e.g., *Smith, 2002; Martins et al., 2020*), which leads to a blow up of the TFM solution in this part of the spectrum. This overestimation has long been attributed to the presence of noise in pressure measurements (*Guza and Thornton, 1980; Smith, 2002*) (Fig. 4.7). Recently, *Bonneton and Lannes (2017)* and *Bonneton et al. (2018)* showed that the blow up of the high frequency part of the spectrum is also due to wave non-linearities and the presence of secondary harmonics. Since these harmonics are phase-locked to the fundamental components, the use of the linear dispersion relation (Eq. 4.10) in the TFM leads to a strong overestimation of their wavenumber k , which in turn overestimates $K_{p,L}$ (Eq. 4.9) (*Bonneton and Lannes, 2017*). This problem is commonly overcome by the use of a cut-off frequency f_{max} , which is usually defined empirically following two possible approaches (*Smith, 2002*). In the first one, f_{max} is defined as the frequency where the energy density is one order of magnitude higher than the noise floor. In the second approach, f_{max} is fixed such that $K_{p,L}$ is less than 10 to 1000. Nevertheless, the fact that the TFM requires a cut-off frequency prevents from accurately estimating the energy density in the high frequency part of the spectrum, which implies that the free surface of strongly non-linear waves cannot be correctly described (*Martins et al., 2017a; Bonneton et al., 2018; Mouragues et al., 2019; Martins et al., 2020*).

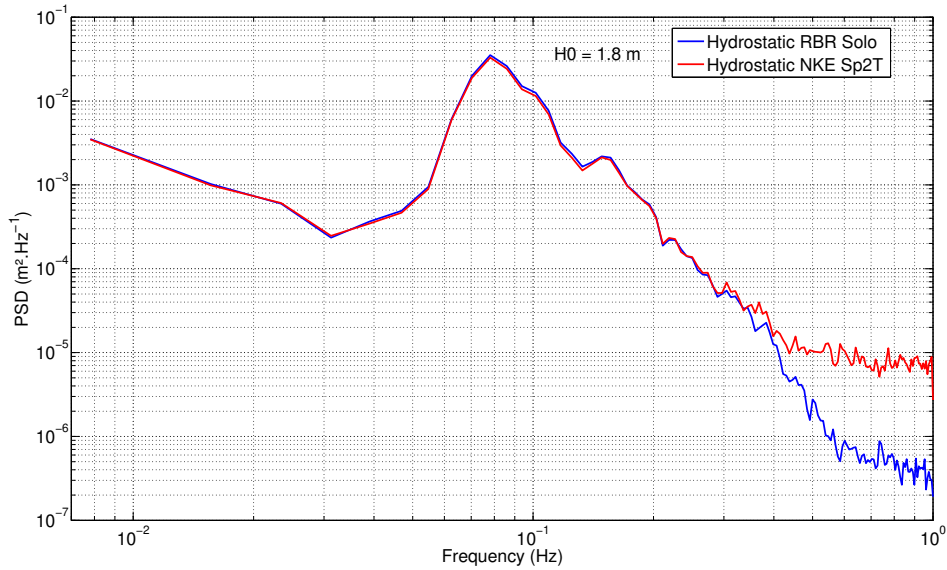


FIGURE 4.7 – Comparison of the noise floor between a RBR Solo and NKE Sp2T pressure sensors. For the NKE sensor, the noise floor appears from 0.5 Hz and reaches $\sim 10^{-5} \text{ m}^2 \cdot \text{Hz}^{-1}$, while for the RBR sensor, the noise floor appears from 0.6 Hz and is one order of magnitude lower.

4.2.3.4 Non-linear reconstruction methods

Recently, *Bonneton and Lannes (2017)* derived a non-linear reconstruction method for fully-dispersive waves. This method was found to provide an accurate description of energy levels at high harmonics, leading to a better reconstruction of the free surface and better estimations of third-order bulk parameters (*Bonneton and Lannes, 2017; Mouragues et al., 2019*). Based on this work, *Bonneton et al. (2018)* derived a non-linear formula for weakly-dispersive regime ($\mu \ll 1$) (hereafter referred as SNL), which reads :

$$\eta_{SL} = \eta_H - \frac{h}{2g} (1 - (\delta_m/h)^2) \frac{\partial^2 \eta_H}{\partial t^2} \quad (4.12)$$

$$\eta_{SNL} = \eta_{SL} - \frac{1}{g} \left(\frac{\partial}{\partial t} \left(\eta_{SL} \frac{\partial \eta_{SL}}{\partial t} \right) - (\delta_m/h)^2 \left(\frac{\partial \eta_{SL}}{\partial t} \right)^2 \right) \quad (4.13)$$

where η_{SL} is a linear shallow water reconstruction of the free surface which is used to formulate the non-linear reconstruction η_{SNL} . Unlike the TFM, the non-linear formula (Eq. 4.13) does not use the linear dispersion relation which allows to define a cut-off frequency much higher (Bonneton *et al.*, 2018; Mouragues *et al.*, 2019), while still excluding frequencies where the noise dominates. As compared to the TFM, the SNL provides better estimates of individual wave characteristics and bulk parameters, in particular high-order statistics such as skewness and asymmetry, in the shoaling (Bonneton *et al.*, 2018; Mouragues *et al.*, 2019) and surf zone (Martins *et al.*, 2020). For instance, Martins *et al.* (2020) compared these different reconstruction methods with direct measurements of the free surface by lidar scanner and reported that, compared to the TFM, the SNL improved by 80% and 50% the skewness and asymmetry respectively.

4.2.3.5 Wave parameters

In the field, bottom pressure sensors are generally configured in order to measure the pressure continuously with a sampling frequency of 1 or 2 Hz. Once collected, pressure time series P_m are first split into consecutive bursts of 20 or 30 min. P_m are then corrected from the atmospheric pressure P_{atm} recorded at the nearby meteorological station, and from the potential error of measurement of the sensor P_0 . P_0 is calculated as the value $P_m - P_{atm}$ recorded when the sensor is out of the water, such that $P_m - P_{atm} - P_0$ at that time is zero. In practice, the pressure sensors deployed during the shore platform experiment have been installed in shallow water pools to avoid drifting in the measurements owing to air pressure and temperature variations. In this case, P_0 is evaluated by comparing the water depth above the sensor (measured in the field) and the pressure measured by the sensor at a given time. The hydrostatic free surface elevation is then obtained by means of Eq. 4.6 and detrended to remove the tidal component. Non-hydrostatic effects can then be accounted for through the application of the TFM or the SNL (which is discussed later). For each burst, the energy density spectrum E is computed using Welch's method : it is obtained by averaging spectra computed by means of a Fast Fourier Transform (FFT) on overlapping sub-segments of the free surface signal. Before applying the FFT, each sub-segment is windowed (Hanning window) to reduce spectral leakage related to the finiteness of the measured signal. In the application presented below, 10 Hanning-windowed segments are used, overlapping by 50%, which allows a good compromise between statistical stability and frequency resolution. Bulk parameters such as the significant wave height H_{m0} , the mean wave period $T_{m0,2}$ and the continuous peak period T_{pc} are computed as :

$$H_{m0} = 4\sqrt{m_0} \quad (4.14)$$

$$T_{m0,2} = \sqrt{\frac{m_0}{m_2}} \quad (4.15)$$

$$T_{pc} = \frac{m_{-2}m_1}{m_0^2} \quad (4.16)$$

where p -order spectral moments are calculated with the following equation :

$$m_n = \int_{f_{min}}^{f_{max}} f^n E(f) df \quad (4.17)$$

In equation 4.17, f_{min} corresponds to the frequency cut-off between short and infragravity waves usually defined at a value of ~ 0.04 Hz. Alternatively, f_{min} can be adaptive (*Roelvink and Stive, 1989; Oh et al., 2020; Bertin et al., 2020*), defined as $1/1.8T_{p,inc}$ with $T_{p,inc}$ the continuous peak period recorded at an offshore pressure sensor or wave buoy. (The values of f_{max} and f_{min} for each coastal applications presented in this work are given in the chapter relative to each field campaign.)

4.2.3.6 Choice of the reconstruction method

Recovering the free surface elevation is a complex task. In this section, we compared which of the TFM or the SNL is the most adapted method to estimate the significant wave height and the mean wave period while assuming a relatively low frequency (e.g., 0.3 Hz), in order to make the most possible consistent comparison with the model. In the scope of this work, we did not calculate high-order parameters (i.e. asymmetry or skewness) nor investigate extreme waves.

The coastal application related to the shore platform used bottom pressure measurements collected from 10 m water depth to the swash zone under strong wind conditions, in a region surrounded by shoals promoting wave breaking and subsequent release of harmonics. The choice of the reconstruction method was not obvious in these challenging conditions. We thus compared the performance of the SNL and the TFM in such situation with direct measurements of the free surface, to retain the most adapted method to the need explained above. Since such measurements were not performed during the field experiment on the shore platform, we used data collected during a recent field campaign carried out along the south-western coast of Oléron Island. The instruments were deployed during a highly energetic event characterized by a swell reaching 10 m offshore in the Bay of Biscay. Locally, winds reached up to 15 m.s^{-1} . The TFM and SNL methods were applied to pressure measurements collected at 12 m water depth and the resulting free surface time-series were compared to a direct measurement of the free surface obtained by an AST co-located with the pressure sensor. First, the AST data has been filtered to remove spurious values using the despiking method of *Goring and Nikora (2002)*. Note that a large part of the AST data has been discarded due to incoherent signals during the most energetic events, probably explained by the presence of air bubbles in the water column induced by the breaking of storm waves. As a first remark, μ values are most of the time superior to 0.3 indicating a dispersive regime, which hence restrains the theoretical applicability of the SNL method to few data bursts only (Fig. 4.8 -e). In the following, two of these bursts ($\mu = 0.17$ and $\mu = 0.26$) are selected to compare the energy density spectra obtained from the TFM and SNL. The TFM and SNL yield comparable results until 0.2-0.3 Hz, where the TFM blows up (Fig. 4.9-a and -b). The SNL allows to estimate energy density in higher frequencies compared to the TFM, however, the energy density seems to be quite underestimated beyond ~ 0.3 Hz, which worsens for a larger μ , where the energy at this frequency is up to two orders of magnitude smaller than the value given by the AST (Fig. 4.9-b). This is

likely due to the presence of free components associated with a wind sea that developed under the local winds during the period of the experiment (see the peak in energy levels at 0.2 Hz in Fig. 4.9-b, which frequency does not correspond to a higher harmonic). As noted by *Martins et al.* (2021b), for broad or bimodal spectra, the application of the SNL should be limited to $\mu \lesssim 0.15$. At the time of this work, it was not possible to account for non-linear effects in the dispersive conditions described here. Recently, *Martins et al.* (2021b) proposed a non-linear moderately-dispersive reconstruction method, which is potentially more adapted to these conditions (which is presented at the end of this section). Since this method was out of the scope of this work, we retained the TFM here, which seems to be the best compromise for the objectives of this work, provided that the cut-off frequency is correctly defined. In the intercomparison performed in this section, the cut-off frequency was defined at 0.2 Hz, since the TFM blows up above this frequency (for instance, Fig. 4.9-b). The TFM provides fair estimations of the significant wave height and mean wave period computed from the AST over the same range of frequency (Fig. 4.8 -b and -c). For a sake of consistency, all the pressure sensors of a same field campaign, from the subtidal to the intertidal zone, were treated with an identical reconstruction method. The TFM has been used in the field experiments on the shore platform for the reasons detailed above, and on the salt marsh, for which the choice of the TFM is detailed in the relative chapter.

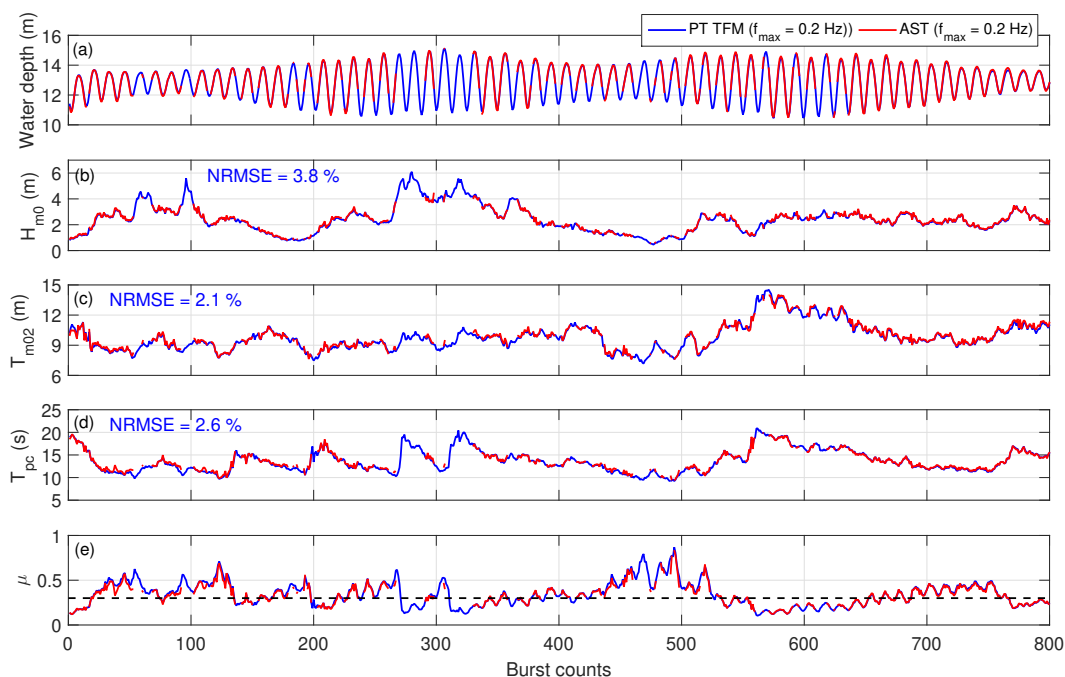


FIGURE 4.8 – Comparison of (a) the mean water depth, (b) significant wave height H_{m0} , (c) mean wave period T_{m02} and (d) continuous peak period T_{pc} computed from the free surface recorded by the AST ($f_{max} = 0.2 \text{ Hz}$) and from the free surface reconstructed with the TFM ($f_{max} = 0.2 \text{ Hz}$), from bottom-mounted pressure sensor measurements. (e) Dispersion parameter μ computed at the peak frequency where the black dotted line corresponds to $\mu = 0.3$.

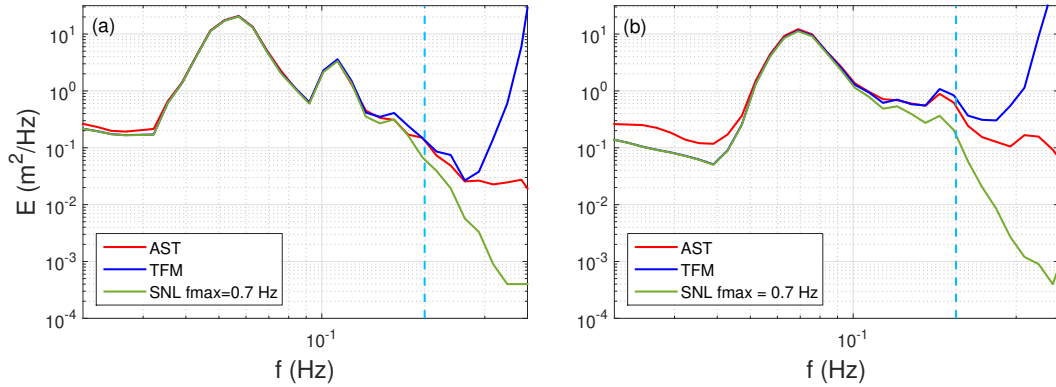


FIGURE 4.9 – (a) and (b), comparison of the energy density spectra calculated with the TFM and the SNL, with the spectra obtained from the AST data, for the bursts 585 ($H_{m0}=2.90\text{ m}/T_{pc}=19\text{ s}/\mu=0.17$) and 790 ($H_{m0}=2.45\text{ m}/T_{pc}=15\text{ s}/\mu=0.26$). The vertical light-blue dashed lines correspond to the cut-off frequency applied to the TFM ($f_{max} = 0.2\text{ Hz}$).

In the presence of strong wind seas or wave conditions characterized by broad or bimodal spectra, free components can still dominate over forced ones at high frequencies. In this case, the SNL is no longer valid since the conditions become too dispersive at high frequencies. For such situations, *Martins et al.* (2021b) proposed a non-linear fully-dispersive reconstruction method to account for both free components at high frequencies and non-linear effects that occur in the shoaling region. The method of *Martins et al.* (2021b) is based on the non-linear fully-dispersive reconstruction of *Bonneton and Lannes* (2017) and on the determination of the dominant wavenumber spectra, which allow to accurately assess the relative contribution of both free and forced components. They proposed two approaches to estimate the dominant wavenumber spectra. In a first application conducted in laboratory conditions, dominant wavenumber spectra have been accurately determined through cross-spectral analysis between adjacent wave gauges. The non-linear fully-dispersive reconstruction method of *Martins et al.* (2021b) was found to perform very well in contrasting non-linear and dispersive conditions, and for broad and narrow-banded incident wave conditions. In a second application conducted in the field, where measurements of the dominant wavenumbers were not available (as in most field situations), the dominant wavenumber spectra were approximated from the pressure and directly-measured surface elevation data obtained from single sensors, using the Boussinesq theory of *Herbers et al.* (2002). This approximation of the dominant wavenumbers is weakly dispersive, such that the reconstruction method proposed by *Martins et al.* (2021b) for field applications is currently applicable to moderately-dispersive wave conditions. While further research is required to define a fully-dispersive approximation of the dominant wavenumber spectra in field conditions, the non-linear moderately-dispersive reconstruction proposed by *Martins et al.* (2021b) appears to be a powerful method to reconstruct the free surface under storm wave conditions in the nearshore region (in intermediate water depths up to the surf zone). *Martins et al.* (2021b) provides a comprehensive schematic of the range of validity of the different reconstruction methods presented in this chapter.

4.2.3.7 Velocities

Both ADV and ADCP were deployed on the field to measure currents. During the field campaign on the shore platform, current data collected from a 2 MHz ADCP deployed in the surf zone showed incoherent patterns likely due to the presence of air bubbles which

altered the acoustic signal. Little confidence was given to this dataset and it was thus discarded from the analysis. Hence, a focus is made here on the processing of the ADV data. First, spike noise in the ADV recorded data was eliminated following the approach of *Mori et al. (2007)*, based on the 3D phase-space method of *Goring and Nikora (2002)* modified by *Wahl (2003)*. Then, since beam velocities are given in Earth normal coordinates (ENU - East, North and Up), they were corrected by the local magnetic declination and rotated into cross-shore and alongshore directions.

In order to compute the mean current, velocities were averaged over 20 min to avoid aliasing due to the presence of infragravity waves of period of about 50 s (Fig. 4.10).

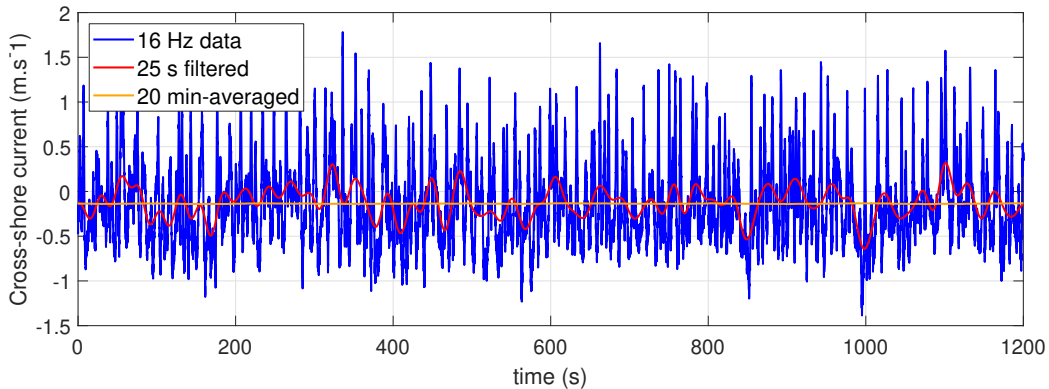


FIGURE 4.10 – Fraction of the time-series of the cross-shore current at the ADV. The blue line corresponds to the despiking data at 16 Hz, the red line is the low-pass filtered (despiking) data with a 0.04 Hz cut-off frequency and the orange line is the 20 min-averaged (despiking) data.

4.2.3.8 Bathymetric and topographic data

Accurate bathymetric data is primordial for accurately simulating wave propagation and storm surges in coastal zones. Several data sources were used in the modelling system. First, the deep water bathymetry used in the application of the WaveWatch III model (that provides directional wave spectra along the open boundaries of WWM-II) originates from the GEBCO global ocean bathymetric dataset. In SCHISM/WWM-II, bathymetric data collected in the scope of the HOMONIM project (*Shom, 2015*) conducted by the SHOM (French Naval Hydrographic and Oceanographic Service) are used for continental shelf and coastal areas. Closer to shore, topographic data in the intertidal zones of interest in the Pertuis Charentais area, such as the studied shore platform along Oléron Island and the salt marsh of Brouage, originate from a LiDAR survey carried out in 2010 in the scope of the National Project LITTO3D (conducted by the National Geographic Institute and the SHOM).

In addition, during the field campaign on the shore platform, a bathymetric survey was conducted with the laboratory ship (*ESTRAN*) on which can be installed a NORBIT iWBMS multi-beam echosounder equipped with an APPLANIX POS MV SurfMaster inertial unit. The sounder operates over a wide frequency range from 200 to 700 kHz, which allows the system to be very adaptable. The inertial unit provides in real-time the GPS positioning with centimeter accuracy and attitude data with a precision of the order of 0.03° on roll and pitch. The acquisition and processing of the bathymetric data are based on the TELEDYNE PDS software, which offers all the appropriate functions. In particular, its processing module allows for quality control of all recorded data (positioning, attitude

and bathymetric data) and offers state-of-the-art solutions for the complex task of data cleaning (e.g. via the CUBE algorithm, *Debes et al.*, 2012). The multi-beam bathymetric survey allowed to dispose of high resolution (0.2 m x 0.2 m regular grid) bathymetric data on approximately 1.73 km² on the shore platform.

Finally, GNSS receivers were used to survey several cross-shore profiles of the intertidal shore platform at low tide and carefully measure the position of each sensor, which was of particular importance to accurately calculate the wave setup (Section 4.2.2 and Fig. 4.11). A similar operation was conducted during the field campaign on the salt marsh of Brouage.



FIGURE 4.11 – *Levelling procedure during the field campaign on the shore platform (credits : Laura Lavaud).*

Chapitre 5

Spatial extension of the wave setup in estuaries and lagoons

5.1 Introduction

Several studies reported that the breaking of short waves occurring close to and over the ebb deltas of shallow inlets (*Malhadas et al.*, 2009; *Olabarrieta et al.*, 2011; *Dodet et al.*, 2013; *Wargula et al.*, 2018) or large estuaries (*Bertin et al.*, 2015a; *Fortunato et al.*, 2017) can induce a wave setup that extends at the scale of the whole lagoon or estuary. However, the contribution of the wave setup to the water level in these wave-sheltered environments is not fully clear in the scientific community, and often considered as negligible by a number of global-scale studies conducting coastal risk assessments (e.g., *Melet et al.*, 2018; *Lambert et al.*, 2020; *Almar et al.*, 2021). In this context, we investigated the contribution of short-wave breaking to storm surges in wave-sheltered environments during storm conditions and examined the underlying processes. We performed a high-resolution hindcast of the sea state and storm surge induced by the violent extra-tropical storm Klaus, which made landfall in the Bay of Biscay on the 24th of January 2009. As Klaus produced the most energetic waves ever recorded in the southern part of the bay, this storm represents a unique opportunity to investigate the contribution of short-wave breaking to storm surges. This process is examined in two sheltered areas of the French Aquitanian Coast where Klaus drove the largest storm surges observed over the last 20 years : the Arcachon Lagoon and the Adour Estuary. The 3D fully-coupled wave-current modelling system using the vortex force formalism is applied at the scale of the Bay of Biscay and the English Channel. The relevance of the 3D model in terms of storm surge and wave setup is compared against a conventional 2DH approach. Additional numerical experiments are conducted in order to analyse the impact of the wave forces on the momentum balance at the inlet of the Arcachon Lagoon and their tidal modulation at both studied locations. Lastly, a sensitivity analysis is carried out to analyse the impact of the grid resolution on storm surge and wave setup predictions. The results presented in this chapter were published in October 2020 (*Lavaud et al.*, 2020a).

5.2 The studied area and storm

5.2.1 Study area

The Bay of Biscay is located in the North-East Atlantic Ocean, bordered by France to the east and Spain to the south. The study area is the Aquitaine coast in the south-eastern part of the Bay of Biscay, which comprises two major geomorphologic settings : a first unit from the northern Spanish coast to the Adour Estuary, characterised by rocky cliffs and small creeks, and bordered by a continental shelf only 20 km-wide, and a second one from the Adour Estuary to the Gironde Estuary, with a sandy coast bordered by a continental shelf which width increases up to 150 km in front of the Gironde Estuary. This study focuses on two specific locations, the Arcachon Lagoon and the Adour Estuary further south (Fig. 5.1), which allows to investigate the influence of short-wave breaking in areas sheltered from this process.

The Arcachon Lagoon (Fig. 5.1-B) is a semi-enclosed bay, which extends at high-tide over an area of 160 km². The head of the embayment is occupied by intertidal muddy and sandy flats that account for 75 % of the lagoon, and divided by a large and complex network of secondary channels. The lagoon is connected to the ocean by a 5 km-wide tidal inlet, bounded to the north by the 18 km-long Cap Ferret sand-spit. The inlet is characterised by a well-developed ebb-tidal delta covering 12 km², two deep channels, called North Pass and South Pass, and a poorly-developed flood-tidal delta of 2.3 km² (*Michel and Howa, 1997*). The tidal regime is semi-diurnal and mesotidal, with a tidal range from 0.94 m to 4.93 m and a mean value of 2.94 m (*Dodet et al., 2019a*). The channels are tide-dominated, with currents 20-30 % stronger in the North Pass than in the South Pass (*Salles et al., 2015*). Because of the well developed ebb delta and the sandbar (continuation of Cap-Ferret), the swells do not propagate inside the Arcachon Lagoon (*Nahon, 2018*) and the outer inlet can be often saturated with wave breaking (*Senechal et al., 2013*). According to the hydrodynamic classification proposed by *Hayes (1980)*, the Arcachon Lagoon corresponds to a "transitional inlet" under a "mixed-energy regime".

The Adour Estuary (Fig. 5.1-C), located approximately 40 km north of the Spanish border, is defined by a narrower channel with a width varying between 150 (inlet mouth) and 500 m over the last 6 km of the river. Two breakwaters protect the entrance of the harbour of Bayonne from longshore currents and swell waves and help stabilizing the navigation channel. The influence of the breakwaters on the storm surge in the Adour Estuary will be discussed later in this study. The tidal regime of the area is semi-diurnal and mesotidal, with a tidal range varying from 0.78 to 4.32 m and a mean value of 2.53 m (*Dodet et al., 2019*). Tidal currents are weak in the outer part of the estuary with values lower than 0.20 m.s⁻¹ while in the river mouth, velocities reach values between 1 and 2 m.s⁻¹ during spring tides (*Brière, 2005*). The river flow discharge ranges from 30 to 2000 m³.s⁻¹ with an annual mean of about 300 m³.s⁻¹ (*Bellafont et al., 2018*).

Dodet et al. (2019a) analysed wave regimes along the metropolitan coasts of France and provided yearly means of wave parameters along the 30 m isobath line. According to their study, yearly-averaged significant wave height in front of Arcachon and Bayonne is about 1.65 m. Yearly averages of mean wave period and mean wave direction at Arcachon (respectively Bayonne) are about 6.3 s (resp. 7.15 s) and about 290° (resp. 310°). The wave climate is however characterised by important seasonal variations : at Arcachon (resp. Bayonne), the significant wave height has a winter average of 2.08 m (resp. 2.06 m) and a summer average of 1.24 m (resp. 1.20 m) and the mean period decreases by 2.5 s (resp. 1.5 s) bet-

ween winter and summer. Seaward of the Arcachon Lagoon, storm waves can exceed 9 m in water depths of 26 m (*Butel et al.*, 2002).

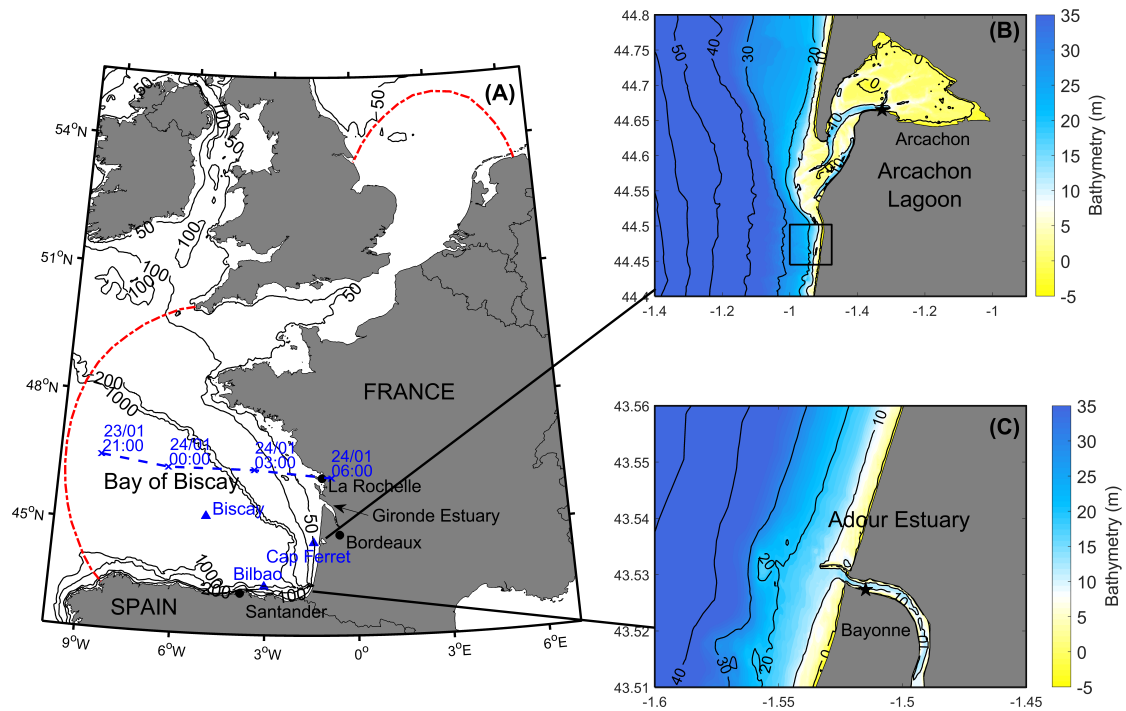


FIGURE 5.1 – (A) Bathymetric map and extension of the computational domain (red dash-dotted line), the storm track (blue dashed line and crosses) and the wave buoys (blue triangles) used in this study. (B) and (C) Detailed bathymetry of the studied areas with location of the tide gauges (black stars). The black box in (B) corresponds to the adjacent beach where the sensitivity of storm surge and wave setup predictions to the grid resolution is analysed.

5.2.2 The storm Klaus

The extra-tropical storm Klaus hit the French coasts in the night of the 23rd to the 24th of January 2009. It induced the largest storm surge observed over the last 20 years in this region of the Bay of Biscay, with 1.10 m at Bayonne Boucau station and 1.70 m at Arcachon Eyrac station (*Mugica et al.*, 2010; *Arnaud and Bertin*, 2014). Previous long-term records of wind speeds were exceeded in some French stations like Bordeaux and Bayonne with wind gusts of 44-50 m.s⁻¹ and 33-39 m.s⁻¹ respectively. It was considered as the most damaging wind storm to affect Northern Iberia and Southern France since the destructive storm Martin in late December 1999 (*Liberato et al.*, 2011). In 2009, Klaus was the most costly weather events worldwide with over US\$ 6.0 billion in losses reported, mainly in France and Spain (*Aon-Benfield*, 2010). *Liberato et al.* (2011) described the storm from its genesis to its impact on the French and Spanish coasts and the main features of its evolution are summarized here. Klaus was first detected on 21 January 2009 as a small atmospheric wave perturbation. Due to the southward displacement of the polar jet stream, the winter cyclone moved eastward at an unusually low latitude (between 35°N and 45°N), on the southern edge of the typical North-Atlantic storm track climatological envelope. It underwent an explosive development on 23 January around 21°W, with a deepening rate of 37 hPa in 24 hours, probably supported by an important tropical moisture export.

The storm rapidly reached the Bay of Biscay and followed a WNW to ESE track toward the

coasts (Fig. 5.1-A). The Spanish Oceanographic Institute (IEO) registered two individual wave heights over 24 m from a buoy 35 km north of Santander between 06:00 and 07:00 in the morning of January 24th. Bilbao and Cap-Ferret buoys recorded significant wave heights reaching 13 m with a peak period of 15 s during the storm. The centre of the low-pressure system passed at 5:00 am on January 24th over La Rochelle with a minimum of 965.8 hPa recorded at the nearby station of Chassiron (Fig. 5.1-A). The highest sustained wind speeds were measured further south, with a maximum of 36 m.s⁻¹ at Cap-Ferret station (Arcachon Lagoon) for a lowest pressure of 976 hPa. At Bayonne, sustained wind speed reached 21 m.s⁻¹ with a minimum pressure of 983.6 hPa.

5.3 Model implementation

In this study, the vortex formalism is used to represent the effects of waves on currents, in both 3D and 2DH configurations.

The wave model WWM-II accounts for wind input and energy dissipation by whitecapping following *Ardhuin et al.* (2010). Energy dissipation due to bottom friction is computed according to the JONSWAP formulation of *Hasselmann et al.* (1973), and depth-induced breaking is calculated with the model of *Battjes and Janssen* (1978) in which the breaking index γ and the breaking coefficient α have to be defined. Since wave measurements in the surf zone were not available during the storm, γ and α are set to the default values of 0.73 and 1 respectively. Yet, the adaptive approach proposed by *Pezerat et al.* (2021) to compute the breaking coefficient has been also considered, which is discussed in section 5.6.1.

The circulation model is forced at its open boundaries by the 16 main astronomical constituents linearly interpolated from the regional model of *Bertin et al.* (2012). The tidal potential is switched off since a sensitivity analysis revealed a negligible effect on tidal predictions. In 2DH, the model uses a Manning coefficient and the depth-integrated current velocity to evaluate the bottom stress, while in 3D, the model uses the bottom roughness and the velocity computed at the top of the bottom cell. The 3D model can account for the wave-enhanced bottom stress, but a sensitivity analysis did not result in significant improvements, which corroborates the findings of *Bertin et al.* (2015a) in the central part of the Bay of Biscay. Therefore, wave effects on the bottom stress are not considered in the study. After calibration of the tidal model, the bed roughness in the 3D model is set to 0.0001 m in the open ocean and 0.002 m in the Arcachon Lagoon and the Adour Estuary. In the 2DH model, a Manning coefficient of 0.02 is employed for the open ocean while a value of 0.029 is considered for the Adour Estuary and the Arcachon Lagoon. The Manning coefficient used for the Arcachon Lagoon is between the values used by *Cayocca* (1996) (~ 0.028) and *Nahon* (2018) (0.032). Two parametrizations of the surface stress have been considered : a bulk formula (Eq. 3.55) in which the drag coefficient is computed according to *Hwang et al.* (2019), and a wave-dependent approach using the friction velocity (Eq. 3.58 ; note that the air-side stress was not corrected from the wave-supported stress at the time of this study). The influence of the surface stress and its effect on the storm surge are discussed later in the chapter.

The unstructured computational grid used to perform the hindcast of the storm covers the whole Bay of Biscay from 10°W to the French coasts, the English Channel and a part of the North Sea (up to 55°N) (Fig. 5.1-A). The grid has ~ 281000 nodes in the horizontal, with a spatial resolution ranging from 5000 m along the open boundary to 35 m along the

shoreline of the studied areas (*i.e.* the Arcachon Lagoon and the Adour Estuary). In the vertical, the grid is discretized in 35 S levels for the 3D simulations. The simulations are started on the 22th of January 2009, two days before the peak of the storm and last 4 days. The time step is set to 60 s for both the hydrodynamic and the wave models, in the 2DH and 3D simulations.

Over the whole domain, the circulation model is forced by hourly 10 m wind speed and sea-level pressure fields from the Climate Forecast System Reanalysis CFSR (*Saha et al.*, 2010). The datasets are provided on a regular grid with a spatial resolution of 0.312° and 0.5° for the wind and the atmospheric pressure respectively. WWM-II is forced with the CFSR wind fields over the whole domain. WWM-II is also forced along the open boundaries by time series of directional wave spectra, previously computed from a regional application of the WaveWatch III (WW3) spectral wave model described in *Bertin et al.* (2015a). Wind fields from CFSR are also used to run the WW3 model over the North Atlantic Ocean.

5.4 Wave and water level observations

The accuracy of the wave predictions is evaluated with the measurements recorded by three buoys in the Bay of Biscay (see Fig. 5.1-A, for their location). The Biscay buoy is a non-directional buoy located by 4500 m depth, operated by Météo-France and UK Met Office. The Cap Ferret and Bilbao buoys are located in more intermediate water depths of the southern part of the Bay of Biscay (depths of 50 m and 600 m respectively) and are operated by CEREMA and Puerto del Estado respectively. The three buoys provide time series of significant wave height (H_s) while the mean wave period (T_{m02}) is available at Cap Ferret and Biscay buoys and the peak wave period (T_p) at Bilbao buoy. Wave bulk parameters are estimated every 60 minutes at Biscay and Bilbao buoys and every 30 minutes at Cap Ferret buoy. Since the atmospheric data used to force the model has a hourly time resolution, the wave predictions cannot represent the sub-hourly variability and the measurements at Cap Ferret buoy are therefore averaged over one hour to yield a consistent comparison with the model predictions.

Simulated water levels are validated through a comparison against observations recorded with a 10-min sampling interval during the storm period at the two tide gauges of Arcachon Eyrac and Bayonne Boucau (see Fig. 5.1-B and 5.1-C, for their respective location). A tidal prediction is obtained based on a 5 year-long time series (2008-2012) with a harmonic analysis using the UTide code (*Codiga*, 2011). Tides are reconstructed with the 67 main astronomical constituents previously computed. Storm surges are then computed as the difference between the observed water level and the astronomic tidal prediction.

5.5 Modelling results

Comparisons between observations and modelled results are conducted. The model performance for each quantity is assessed by computed the BIAS, the root mean square error (RMSE) and the RMSE normalized by the mean of the observations (NRMSE) :

$$BIAS = \frac{\sum_{t=1}^T \hat{X}_t - X_t}{T} \quad (5.1)$$

$$RMSE = \sqrt{\frac{\sum_{t=1}^T (\hat{X}_t - X_t)^2}{T}} \quad (5.2)$$

$$NRMSE = \frac{RMSE}{\overline{X_t}} \quad (5.3)$$

where \hat{X}_t and X_t are the modelled and measured quantity respectively and T is the length of the time series. The overbar denotes the average over the time series.

5.5.1 Atmospheric forcing

In order to validate the atmospheric forcing originating from CFSR, a comparison is performed against field observations available during the storm and collected at the meteorological stations of Cap Ferret and Bayonne (see Fig. 5.1-A, for their location). The comparison (Fig. 5.2) of modelled against observed 10 m wind speeds (hereafter U_{10}) and sea-level pressure (hereafter SLP) reveals that SLP is well reproduced with a RMSE lower than 1.5 hPa at both locations. At Cap Ferret, U_{10} is accurately predicted with a RMSE of 2.3 m.s^{-1} , although with a slight underestimation of approximately 4 m.s^{-1} two hours before the peak of the storm. Since the meteorological station at Bayonne is located at 75 m above sea level and 3 km inland, the model, providing 10 m wind speed with a 0.3° resolution, does not accurately reproduce the observations, which probably explains the positive bias of 1.6 m.s^{-1} . Overall, it should be noted that the intensity of the storm is correctly represented : peak values of U_{10} are reasonably predicted with stronger values at Cap Ferret (34 m.s^{-1}) than at Bayonne (22 m.s^{-1}).

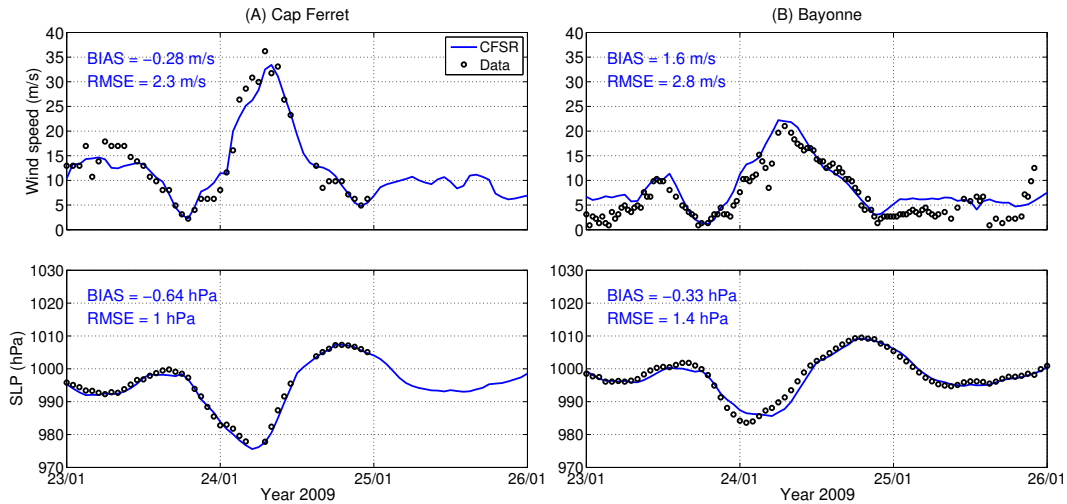


FIGURE 5.2 – Modelled (blue solid line) against observed wind speeds and sea level pressure (black dots) at Cap Ferret (A) and Bayonne (B) stations.

5.5.2 Wave predictions

Modelled wave bulk parameters are compared against the measurements available during Klaus at Cap Ferret, Bilbao and Biscay buoys (Fig. 5.3). The comparison reveals a good agreement between modelled and measured data : H_s is well reproduced with a RMSE ranging from 0.51 to 1 m which corresponds to a 10-17 % NRMSE. However, for the three stations, the model displays a positive bias of 0.35-0.50 m at Cap Ferret and Biscay buoys and 0.70 m at Bilbao buoy. It should be noted that the larger error at Bilbao buoy is partly due to a one-hour time lag, representing 35 % of the bias and the NRMSE, which we are unable to explain. The model correctly captures the peak storm wave height with less than

10 % error at the three buoys. T_{m02} , available at Cap Ferret and Biscay buoys, is well predicted with a NRMSE less than 6 % while at Bilbao buoy, T_p is adequately reproduced with a 10 % NRMSE.

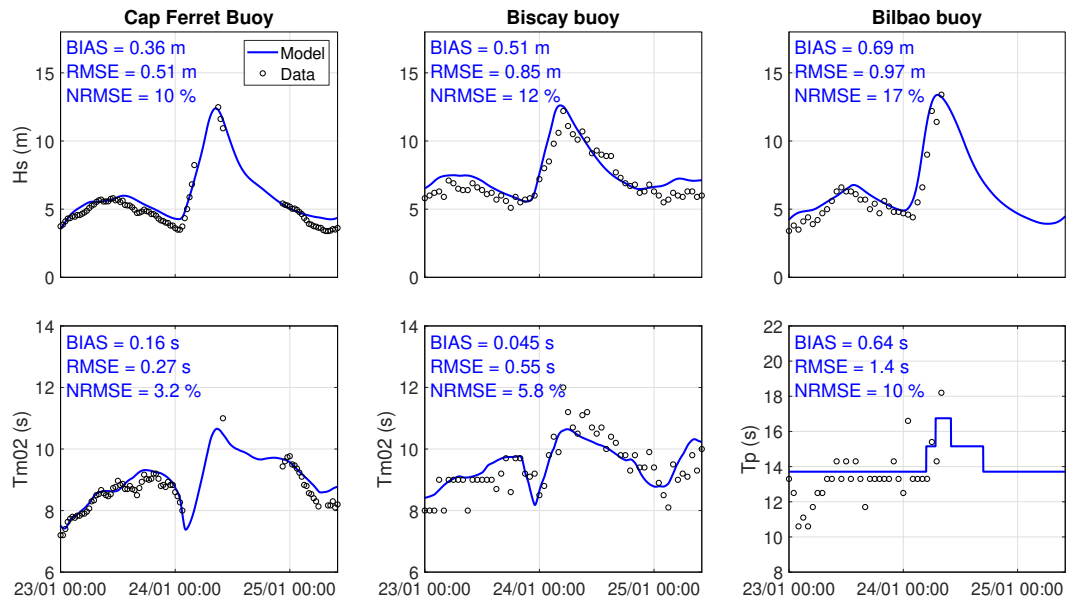


FIGURE 5.3 – Observed (black dots) against modelled wave parameters (blue solid line) at Cap Ferret, Biscay and Bilbao buoys during Klaus.

5.5.3 Storm surge and water level predictions

A tide-only 3D simulation is first performed and the modelled water levels are compared against the tidal predictions based on the observations at each station. The tidal forcing together with the distribution of the Manning coefficient yields good results with a RMSE on tides of 0.11 m at Bayonne and 0.08 m at Arcachon (not shown).

The effect of the parametrisation of the surface stress on the storm surge is investigated by comparing 3D simulations using the bulk formula of *Hwang et al.* (2019) and a wave-dependent approach (see section 5.3). This comparison reveals moderate differences between both parametrisations (lower than 0.05 m), with the predictions of the model using the bulk formula slightly better matching the observations. To explain the negligible effects of the wave-dependent approach on the storm surge predictions, the sea state is characterised by the wave age, defined as C_p/U_{10} where C_p is the peak wave phase speed. Considering a 20-hour window centred on the storm peak, the wave age varies from 0.7 to 2.3, with an average value of 1.32 (with a standard deviation of 0.5), which is characteristic of a mature sea state and explains the very slight impact of the wave-dependent approach on the results. This behaviour corroborates the study of *Bertin et al.* (2015a), who showed that the surface stress was little dependent on the sea state for the storm Joachim, characterised by comparable wave height and peak period as during Klaus. According to these results, the bulk formula of the surface stress is adopted in the rest of the study.

The contribution of short-wave breaking to the storm surge is analysed by comparing a 3D simulation without wave forces and a fully-coupled 3D simulation, *i.e.* including wave forces, hereafter referred to as the baseline model. The modelled storm surges are obtained by subtracting the tide-only simulation to each case of simulation.

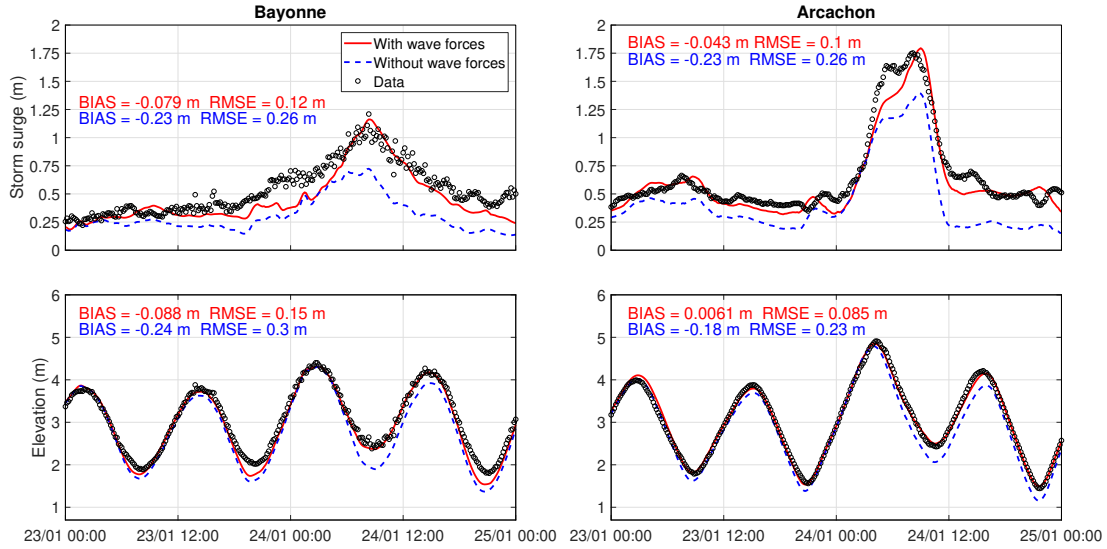


FIGURE 5.4 – Observed (black dots) against modelled storm surges with the (3D) baseline model (red solid line) and the (3D) model without wave forces (blue dashed line) at Bayonne (left) and Arcachon (right).

The results are presented in Figure 5.4, where each simulation is compared against storm surges and water levels observed at Bayonne and Arcachon during the storm. The baseline model accurately reproduces the water levels with a RMSE of 0.09 and 0.15 m at Arcachon and Bayonne respectively. The storm surges are well predicted by the model, with a RMSE of 0.12 m at Bayonne and 0.10 m at Arcachon, although a 0.25 m underestimation is noticed at this station approximately two hours before the storm peak. Without wave forces, storm surge and water level predictions considerably deteriorate compared to the baseline model with a RMSE two to three times larger at both locations. The modelled water levels display a negative bias ranging from 0.18 to 0.24 m. The surge peak is underestimated by 0.40-0.45 m at Arcachon and Bayonne, which results in a negative bias of 0.23 m over the duration of the storm.

The comparison of both simulations reveals that the wave setup driven by the wave forces in the baseline model accounts for 40 % and 23 % of the surge peak in the Adour Estuary and the Arcachon Lagoon respectively, which explains that the baseline model much better matches the observed peak values.

In order to get a spatial overview of this process, modelled storm surges with and without wave forces, as well as their difference, are computed at the scale of the Arcachon Lagoon and the Adour Estuary (Fig. 5.5). In the Adour Estuary, the storm surge in the fully-coupled simulation increases by more than 0.5 m at adjacent beaches while being almost constant inside the estuary (Fig. 5.5-a). The comparison between Figure 5.5-c (atmospheric surge only) and Figure 5.5-e (wave setup only) reveals that this behaviour is due to the development of a wave setup along adjacent shorelines, reaching up to 0.75 m and extending at the scale of the whole estuary where it raises the water level by 0.45 m. A different pattern can be observed in the Arcachon Lagoon, where the storm surge in the fully-coupled simulation increases from the inlet to the lagoon head (Fig. 5.5-b). The comparison between Figure 5.5-d and Figure 5.5-f suggests that this behaviour results from the increase in atmospheric surge towards the lagoon head combined with the development of a wave setup reaching 0.40 m at the scale of the lagoon. As in the Adour Estuary, the wave setup develops at the inlet and then exhibits a plateau inside the lagoon. Along the adjacent shorelines of

the lagoon, the maximum wave setup reaches 0.80 m (The maximum wave setup along the adjacent shorelines are not shown in Figures 5.5-e and 5.5-f as computational nodes dry in the tide-only simulation are not represented).

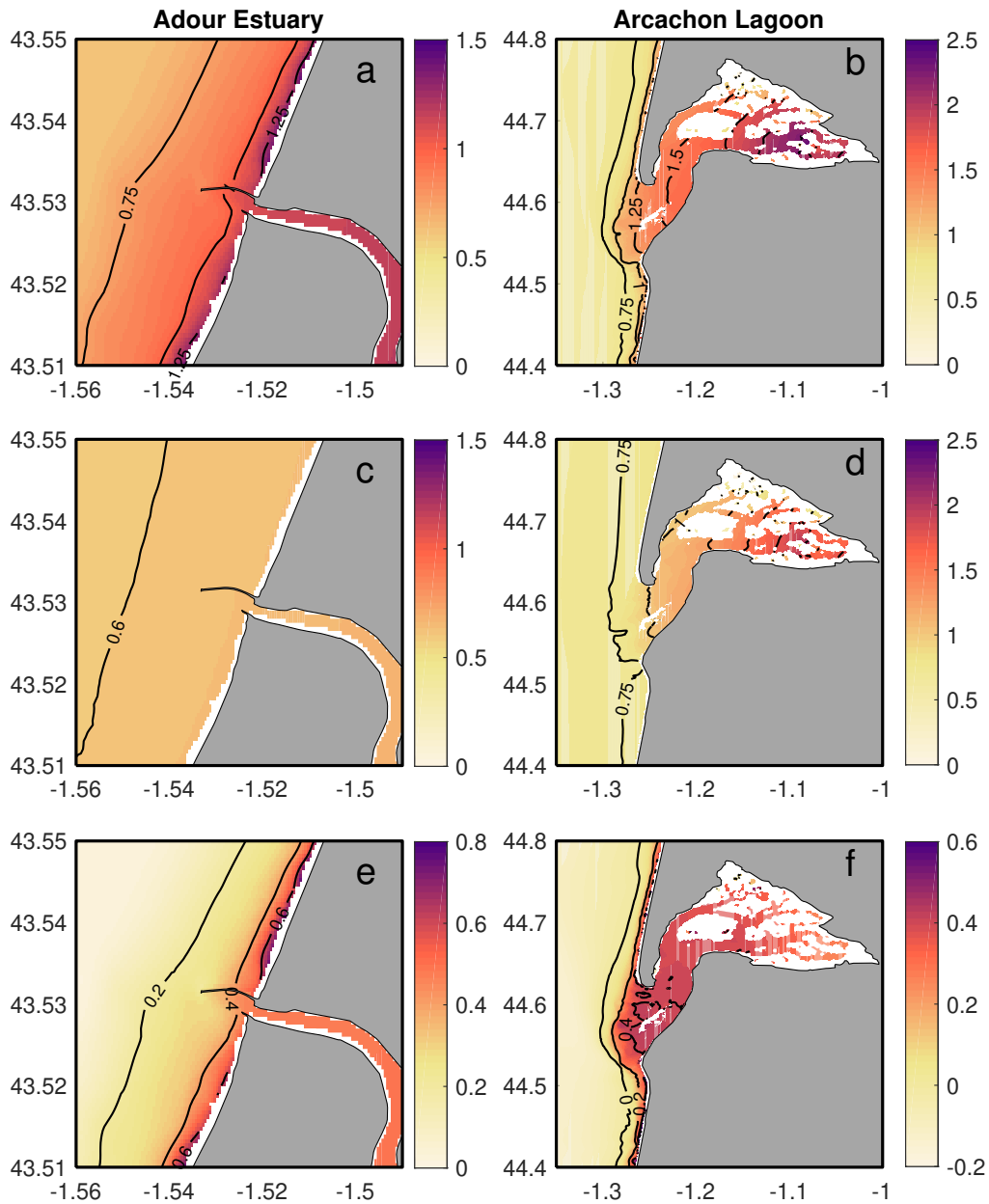


FIGURE 5.5 – Storm surge (in m) simulated with wave forces (a,b), without wave forces (c,d) and their difference (e,f), at the Adour Estuary (left) and the Arcachon Lagoon (right). The white color corresponds to dry nodes in the tide-only simulation.

5.6 Contribution of wave breaking to storm surges

5.6.1 Model predictive skills

Wave parameters are accurately reproduced by the model and correspond to the state-of-the-art considering previously published studies led under storm wave conditions (e.g., *Kerr et al.*, 2013; *Bertin et al.*, 2012; *Staneva et al.*, 2016). Storm surges are also well predicted, with errors similar or even lower compared to previously published studies (e.g., *Kerr et al.*, 2013; *Brown et al.*, 2013; *Bertin et al.*, 2015a). In details, the storm surge is underestimated by up to 0.25 m during the first part of the storm peak at Arcachon. This can be explained by an underestimation of the CFSR sustained wind speeds by up to $4 \text{ m}\cdot\text{s}^{-1}$ during this period (Fig. 5.2), which leads to a wind-induced surge lower than expected. This hypothesis was tested by correcting wind speeds empirically on the time steps corresponding to this period (see Appendix). The results reveal that this correction almost cancels out the local underestimation in the surge, thus supporting this hypothesis. In the Adour Estuary, model results at an earlier stage of this study showed a 0.05 to 0.1 m negative bias in the storm surge before the storm peak when the breakwaters bounding the estuary mouth were considered as impermeable wall. In fact, these breakwaters are made of large blocks (4 to 40 tons) that allow large amounts of water to flow through the structures when a gradient in water levels exists on both sides of the structure (Prof. Abadie, pers. com.). Such flows can take place when a wave setup develops at adjacent beaches, a process already reported at other engineered estuaries (*Hanslow and Nielsen*, 1992; *Hanslow et al.*, 1996). In order to account for these possible flows, we took advantage of hydraulic structure options implemented in the code. Although this parametrisation improves storm surge prediction by 0.04 m, verifying the adequate representation of these flows is outside the scope of the study and would deserve a specific analysis.

The comparison of the results between the baseline model and the model without wave forces (Fig. 5.4) reveals that including wave forces in the circulation model substantially improves its predictive skills. The analysis of the different terms included in wave forces (Eq. 3.41 and 3.42) shows that the wave dissipation term by depth-induced breaking is clearly dominant over the vortex force and the wave mean pressure terms. In accordance with previous studies (*Staneva et al.*, 2016), this analysis highlights the importance of accounting for short waves in storm surge modelling systems, provided that wave energy dissipation due to wave breaking is correctly represented. *Guérin et al.* (2018) investigated wave-induced circulation in a surf zone with varying bed slope. The authors computed the wave breaking process according to the model of *Thornton and Guza* (1983) in which they calculated the breaking index γ and the breaking coefficient B as a linear function of the beach slope. The authors showed that this adaptive approach improved the predictions of short-waves bulk parameters and wave setup by 30 %. Following this study, *Pezerat et al.* (2021) showed that a breaking coefficient B' taken at 40 times the local bed slope strongly improves wave predictions at gently sloping shorefaces ($\sim 1:1000$). At both study sites, bottom slopes are much steeper (1:50 to 1:100), so that this adaptive parametrisation results in values for B' close to the default value of 1. Indeed, a sensitivity analysis shows that the adaptive parametrisation of *Pezerat et al.* (2021) yields very similar short wave and setup predictions compared to the default values for the breaking index γ and the breaking coefficient α in the model of *Battjes and Janssen* (1978). New field experiments are required to investigate further wave dissipation mechanisms in coastal zones and validate the numerical model under very high energetic conditions, although such field deployments remain very challenging.

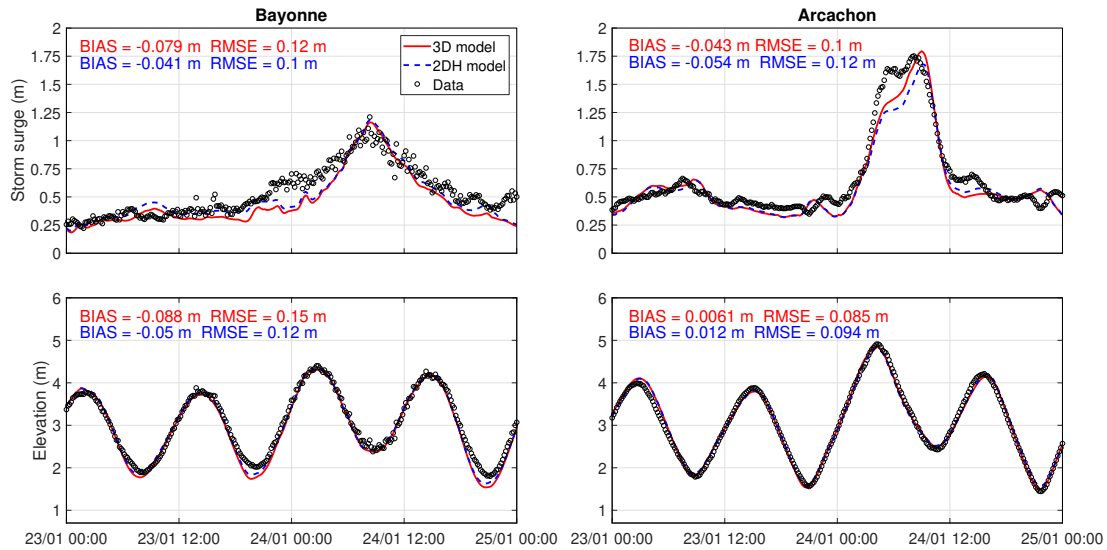


FIGURE 5.6 – Observed (black dots) against modelled storm surges with the 3D baseline model (red solid line) and the 2DH model (blue dashed line) at Bayonne (left) and Arcachon (right).

Finally, a 2DH simulation is performed and compared to our 3D baseline model. The comparison reveals only modest differences, with water level and surge predictions slightly improved in 3D in Arcachon and slightly deteriorated in Bayonne (Fig. 5.6). In the Arcachon Lagoon, improved storm surge predictions are obtained before and during the storm peak, when winds blow from SW to W and drive an Ekman transport towards the coast, a process better represented with a 3D model (Roland *et al.*, 2012). In the case of the Adour Estuary, maximum wave setup at adjacent beaches is slightly lower in 2DH compared to 3D but extends further offshore, thereby more impacting water levels in the estuary. Guérin *et al.* (2018) showed that the depth-varying circulation driven by short waves in surf zones can increase the wave setup along the coast but this process is only substantial at steep beaches (i.e. mean slope of 1:30 and over). Also, these authors reported that 3D runs yield larger wave setup compared to 2DH runs very close to the shoreline, so that reproducing these differences requires a spatial resolution of a few meters, that is one order a magnitude finer than in this study.

5.6.2 Momentum balance

Previous studies already reported the development of a wave setup in inlets, river entrances and shallow lagoons (Hanslow and Nielsen, 1992; Hanslow *et al.*, 1996; Dunn *et al.*, 2001; Oshiyama *et al.*, 2001; Tanaka *et al.*, 2001, 2003; Nguyen *et al.*, 2007; Bertin *et al.*, 2009; Malhadas *et al.*, 2009; Olabarrieta *et al.*, 2011; Dodet *et al.*, 2013; Wargula *et al.*, 2018), which can be further investigated by analysing the momentum balance at the inlet. Hench and Luettich Jr (2003) analysed the momentum balance without waves in the Beaufort Inlet in North Carolina and in an idealized inlet and reported that near maximum flood and ebb, the along-stream momentum balance in both cases is dominated by advection, barotropic pressure gradient and bottom friction. Olabarrieta *et al.* (2011) corroborated these results in a study conducted in Willapa Bay (USA) during a storm event. By activating the wave forces in their fully-coupled modelling system, they also revealed that they can substantially change the barotropic pressure gradient and the bottom friction while being one of the dominant terms in the momentum balance in the inlet area. These

findings were then corroborated by *Dodet et al.* (2013) and *Wargula et al.* (2014). In particular, *Dodet et al.* (2013) combined both modelling and observations to study wave-current interactions on the Albufeira Lagoon, a shallow wave-dominated tidal inlet in Portugal, during energetic oceanic swells conditions. The authors showed that the wave forces term oriented toward the lagoon was of the same order of magnitude as the other terms in the momentum balance in the inlet, which therefore had a significant impact on the hydrodynamics, including a setup that developed within the lagoon. Recently, *Fortunato et al.* (2017) conducted a high-resolution hindcast of the storm surge associated with the 1941 storm that made landfall in the North of Portugal and has driven the development of a large surge in the Tagus Estuary. Their model results suggested that the breaking of storm waves generated a wave setup up to 0.50 m in the Tagus Estuary, showing that a substantial wave setup can also impact water levels at the scale of a large estuary. This phenomenon is explained by the authors as the result of large onshore-directed wave forces owing to storm waves breaking over the ebb delta, generating a wave setup that extended beyond the surf zone and in the inlet. The previous analysis of Fig. 5.4 and Fig. 5.5 suggests that such a phenomenon occurred at the Arcachon Lagoon during Klaus : large wave breaking on the ebb delta generated a wave setup that affected the whole lagoon.

To understand the underlying mechanisms, the magnitude of the leading terms of the momentum equations (Eqs. 3.37 and 3.38), *i.e.* the barotropic pressure gradient term (first term of the right hand-side terms), the wave forces ($F_{w,x}$, $F_{w,y}$) and the bottom stress and surface stress terms are computed at the inlet of the Arcachon Lagoon (Fig. 5.7). In order to analyse the momentum balance at mid-flood and mid-ebb under similar forcing corresponding to the peak of the storm, two additional 3D simulations are performed where tides are shifted.

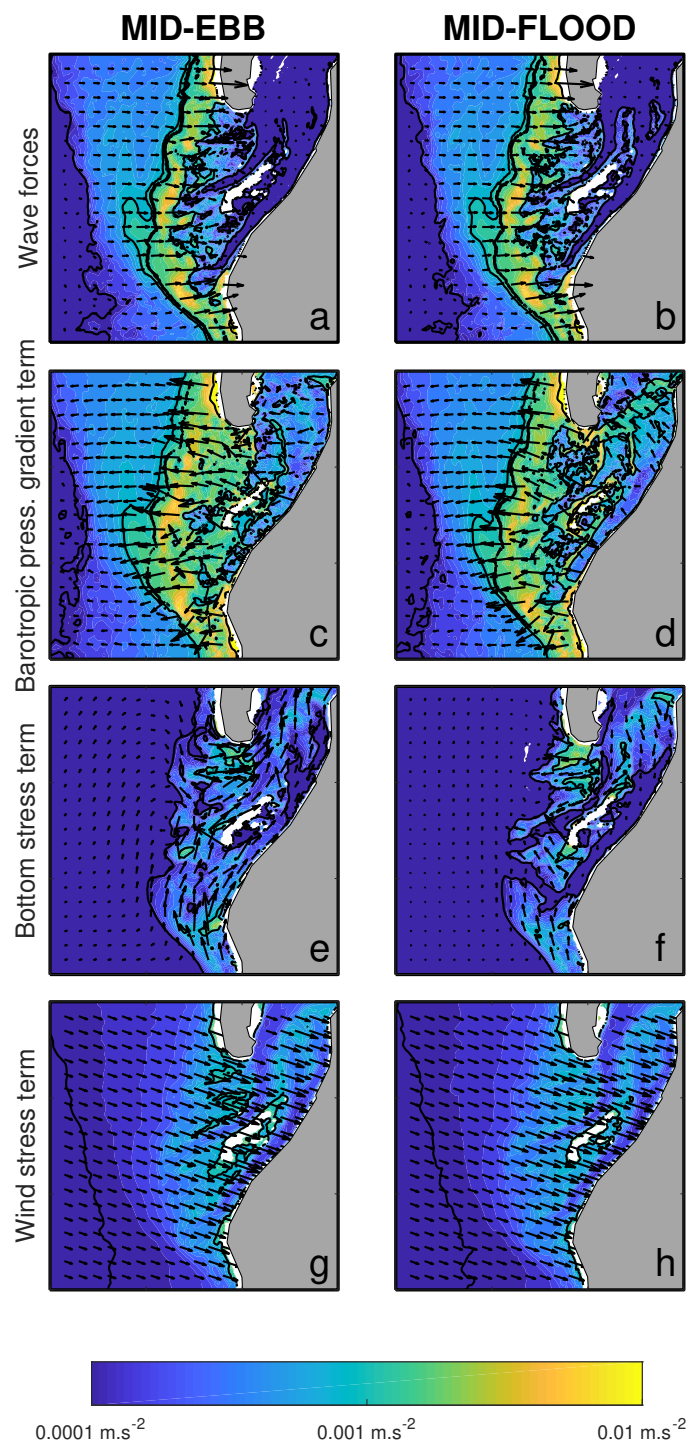


FIGURE 5.7 – Leading terms of the momentum balance at mid-ebb and mid-flood : wave forces (a-b), barotropic pressure gradient term (c-d), bottom stress term (e-f) and wind stress term (g-h), at mid-ebb (left) and mid-flood (right). The magnitude and direction of each term are represented by the map colors and the vectors respectively.

The analysis of Fig. 5.7 shows that the outer part of the inlet behaves like a sandy beach, with a balance between the wave forces (hereafter WF) and the barotropic pressure gradient (hereafter BPG) term (*Battjes and Stive, 1985; Lentz and Raubenheimer, 1999*). In this area, the WF reach values one order of magnitude larger than the bottom stress (hereafter

BS) and the surface stress (hereafter SS) terms. The dominant role of WF in the momentum balance at the inlet corroborates the findings of *Olabarrieta et al.* (2011) and *Dodet et al.* (2013). In the inlet channel, the WF become much weaker and the alongstream dynamics is controlled by a balance between the BPGR and the BS terms, which is typical of tidal channels (*Hench and Luettich Jr.*, 2003). Between the flood and the ebb, the signs of the BPGR and the BS terms are inverted, except in the outer part of the inlet where the BPGR term compensates the WF during all tidal phases.

The major contribution of the wave forces to the momentum balance in the inlet directly explains the strong effect of short-wave breaking on the hydrodynamics, the main impact being a wave setup that reaches several tens of centimetres within the lagoon (Fig. 5.4). In more details, the rapid decrease in WF inside the lagoon explains that wave setup displays a plateau inside the lagoon (Fig. 5.5-f). Over the ebb delta, the wind-driven surge reaches approximately 0.4 m (Fig. 5.5-d and assuming 0.35 m of inverse barometer effect), which is comparable to the wave setup while SS are one order of magnitude lower than WF. This behaviour is explained by the fact that strong WF only extend over the 3 km-wide ebb delta while the wind effect is integrated across the 60 km-wide shelf. Inside the lagoon, the atmospheric surge further grows as the water depth decreases (Fig. 5.5-d). In the Adour Estuary, the weaker atmospheric surge (Fig. 5.5-c) is explained not only by weaker winds (Fig. 5.2) but also by the narrower continental shelf. Indeed, many studies already demonstrated that, for a given wind speed, the wind-driven surge is also controlled by the shelf width, such as in the Bay of Biscay (*Bertin et al.*, 2012), in North Sea (*Wolf and Flather*, 2005) or in the Gulf of Mexico (*Kennedy et al.*, 2012).

5.6.3 Tidal modulation of the wave setup

Some of the studies that highlighted the development of a wave setup in tidal inlets also suggested that the wave setup can be tidally-modulated (*Olabarrieta et al.*, 2011; *Dodet et al.*, 2013; *Fortunato et al.*, 2017). *Fortunato et al.* (2017) showed that the wave setup that developed in the Tagus Estuary mouth during the 1941 storm was strongly tidally-modulated with values of 0.10-0.15 m at high tide while being three times larger at low tide with values of 0.30-0.35 m. The authors attributed this phenomenon to more intense wave breaking on the ebb delta at low tide. When waves do not break over the ebb delta, they propagate into the inlet or to the coast in the vicinity of the estuary mouth, and thus, their contribution to the setup inside the estuary is lower. In this section, the tidal modulation of the wave setup is investigated at the Arcachon Lagoon and the Adour Estuary with additional numerical experiments.

The Arcachon lagoon exhibits large intertidal flats, which makes the tidal propagation and asymmetry very sensitive to the mean water depth. Therefore, tidal propagation is different when the wave setup raises the mean water level of the lagoon. Computing the wave setup as the difference between a simulation including tides and waves and a simulation with tides only results in difference not only including the wave setup but also the differences in tidal levels due to the higher mean water level in the coupled simulation, a process also referred to as tide surge interactions. To overcome this problem, a series of stationary 3D runs is performed with constant water levels and wave forcing (Fig. 5.8-A). Two sub-grids of smaller extent covering each studied area are forced at the ocean boundary by constant water elevations ranging from -1.5 m to 1.5 m, and a JONSWAP spectrum to simulate short waves. The spectrum is characterized by a significant wave height of 14 m and a peak period of 15 s, which corresponds to the peak values reached during Klaus in the region.

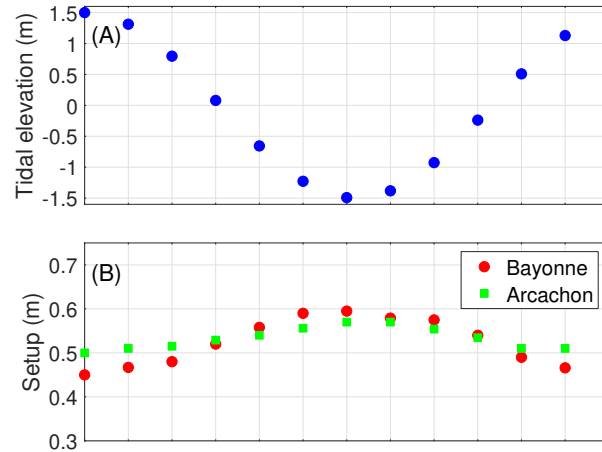


FIGURE 5.8 – (A) Constant water elevations prescribed at the open boundary (blue circles). (B) Tidal modulation of the wave setup at Arcachon (green squares) and Bayonne (red circles) during a tidal cycle.

In the case of the Arcachon Lagoon, the results reveal a small tidal modulation of the order of 0.07 m (Fig. 5.8-B), the wave setup being larger at low tide. At the Adour Estuary, the tidal modulation is stronger with a wave setup reaching 0.60 m when the mean sea level is lowered by 1.5 m and decreasing to 0.45 m when the mean sea level is increased by 1.5 m.

Contrary to the Tagus Estuary where the ebb delta is submerged, with depths of the order of 5 m relative to the mean sea level, the ebb delta of the Arcachon Lagoon extends 3 km offshore and includes an elongated supratidal bank, the Arguin Bank. This setting causes the wave breaking to be almost full in front of the inlet, even at high tide. At lower tidal elevations, wave energy mostly dissipates on the terminal lobe while at higher tidal stages, waves also break over the supratidal sand bank. The wave setup exhibits therefore a slight tidal modulation, unlike the Tagus Estuary (*Fortunato et al.*, 2017). At the Adour Estuary, the bathymetry is subtidal, which implies that the lower the water level, the larger is the wave energy dissipation and the wave setup.

These results indicate that tide-induced water level variations change the spatial gradients of short-wave energy dissipation rates, which in turn controls the wave setup. Depending on the morphology of the inlet, the wave setup along the shoreline and in the lagoons or estuaries can experience significant tidal modulations as well. Tidal currents, which are strong in estuaries or tidal inlets, can also affect the propagation of short waves (*Ardhuin et al.*, 2012; *Rusu et al.*, 2011; *Dodet et al.*, 2013; *Bertin et al.*, 2019) and subsequently the wave setup. During flood, waves following currents decrease while during ebb, waves propagating against currents increase, shifting the position of the breaking point seaward (*Dodet et al.*, 2013). The impact of tidal currents on short-waves propagation is verified by comparing water elevations from runs including tides and waves, and activating or not the feedback of currents on waves. Model results at the Arcachon Lagoon and at the Adour Estuary show that switching off the effects of tidal currents on short-wave propagation has a small impact on wave setup (lower than 0.01 m). This finding corroborates the study of *Fortunato et al.* (2017) which reported that the tide-induced water level variations at the mouth of the Tagus Estuary are the main driver for the tidal modulation of the wave setup compared to tidal currents effects.

The comparison of the effect of tides on wave setup between both studied locations emphasises that tidal modulation is site-specific. In areas such as the Adour Estuary, the higher

wave setup is produced close to low tide, and the tidal modulation amplitude increases with increasing tidal range. Such tidal modulation can therefore limit the contribution of short-wave breaking to coastal flooding, which mostly occurs during high tide in macro tidal regions.

5.6.4 Sensitivity of storm surge and wave setup calculation to spatial resolution

Recently, several storm surge numerical models using unstructured grids have been developed (e.g., *Kerr et al.*, 2013). Such models allow to correctly represent complex shorelines and coastal embayments, using a variable grid resolution, usually coarse in the deep ocean (several kilometers to tens of kilometers) and down to few hundreds of meters in the nearshore. However, such resolution in coastal areas may not be sufficient to adequately represent small coastal morphological features, such as lagoons, and thus, enable the model to provide accurate storm surge predictions (*Shen et al.*, 2006). Also, this study reveals that the wave setup generated by wave breaking during extreme events can greatly contribute to the storm surge, even in areas sheltered from wave breaking such as lagoons and estuaries. Accounting for short waves in storm surge operational modelling is thus of key importance to correctly predict water levels in coastal areas during storm events and thereby, improve emergency responses. However, a good evaluation of the wave setup requires a resolution fine-enough in the surf zones, which is not always possible in operational modelling systems (*Kohno et al.*, 2018). Therefore, an important question rises here : how well do surf zones need to be spatially resolved in order to correctly estimate the contribution of wave setup to the storm surge ?

The sensitivity of the storm surge/wave setup to the model resolution is analysed at the Arcachon Lagoon region by simulating the sea state and storm surge associated with Klaus with different grid resolutions in the 3D model. The grid resolution used for the baseline model (hereafter BM), which goes down to 35 m in the nearshore, is modified to get two additional computational grids with spatial resolution from the inner shoreface to the nearshore degraded to 200 and 1000 m. The surge is evaluated at two locations along the coastline : in the inner part of the lagoon at the Eyrac tide gauge and at the shoreline exposed to the ocean, computed as the average value of the storm surge in an area defined to the south of the inlet (see Fig. 5.1-B). This sensitivity analysis is not carried out at the Adour Estuary since the inlet mouth, with a maximum width of 150 m, cannot be represented with such resolutions.

The results show that the modelled water levels and storm surge on the open ocean beach are lower when the grid resolution coarsens (Fig. 5.9). Indeed, while tidal predictions show little sensitivity to the grid resolution, the peak of the surge simulated with the BL resolution reaches 1.65 m while being 30 % and 65 % higher than the surges obtained with the 200 m and 1000 m resolutions respectively. A detailed analysis reveals that these differences are mostly explained by wave setup, which is poorly represented with a coarse grid.

In the lagoon, the results reveal a different behaviour of the model (Fig. 5.9). Surprisingly, the predicted storm surge is less sensitive to the grid resolution compared to the open ocean beach. The three grid resolutions well reproduce the peak of the surge, with the 200 m and 1000 m grid resolutions resulting in a slightly lower surge than the BM resolution (0.05 m). However, the storm surge modelled over the total duration of the storm is deteriorated with the 1000 m resolution (RMSE of 0.17 m) compared to the BM and 200 m resolutions

(RMSE of ~ 0.1 m). Also, water elevation is poorly predicted with the 1000 m resolution, which yields a RMSE of 0.48 m, against 0.085 m and 0.14 m with the BM and 200 m grid resolutions respectively. As soon as the channels of the lagoon are not correctly represented, the tidal propagation in the lagoon is poorly reproduced, which impacted the predictions of water level and storm surge.

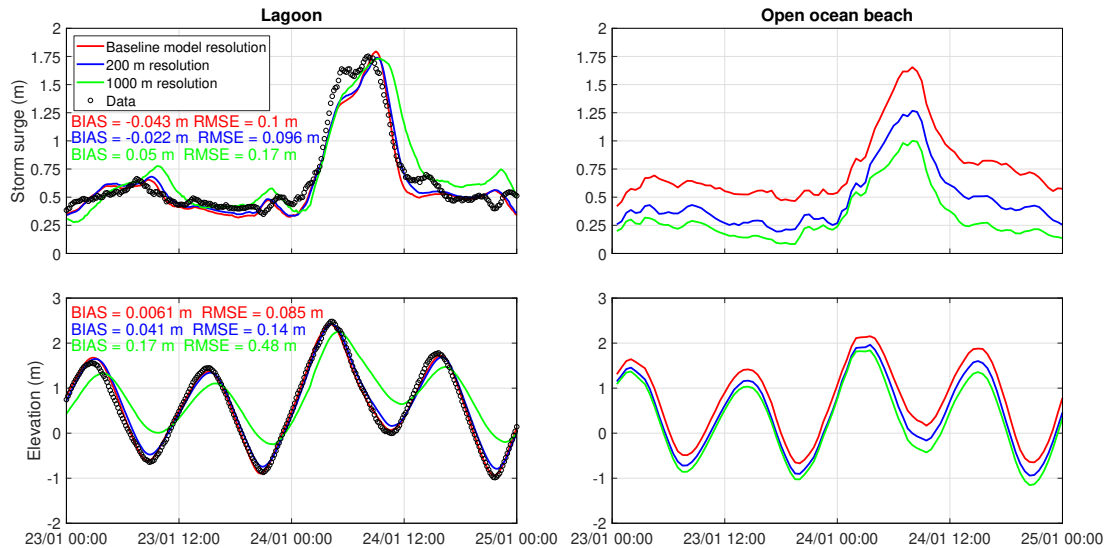


FIGURE 5.9 – Simulated storm surge in the inner part of the lagoon and at the adjacent beach to the south, with the baseline model resolution, 200 m resolution and 1000 m resolution.

This sensitivity analysis of model results to grid resolution reveals a contrasting situation between the inner lagoon, where wave setup is reasonably represented even with a coarse resolution and adjacent sandy beaches, where modelled wave setup is almost nil when using a coarse resolution. This behaviour is directly explained by the cross shore extension of the surf zone, which is of the order of 1000 m at adjacent beaches but range from 3000 to 5000 m in front of the lagoon. As a rough guideline, we estimate that accounting for wave setup in storm surge models requires at least 5 grid elements across the surf zone, which implies the use of a finer spatial resolution when the beach slope increases and the wave height decreases. This corroborates the findings of *Nayak et al.* (2012), who investigated the sensitivity of wave setup predictions to grid resolution considering idealized beaches of slope ranging from 1:80 to 1:10.

5.7 Conclusion

The 3D fully-coupled modelling system SCHISM using a vortex force formalism was used to hindcast the sea state and storm surge associated with the strongest storm that occurred in the southern part of the Bay of Biscay for the last 20 years. After the verification of the model with wave and water level observations available during the storm, the analyses of the simulations revealed that the predictions of the storm surges at the Arcachon Lagoon and the Adour Estuary were improved by 50 to 60 % when the wave forces were accounted for. The wave setup induced by the storm waves breaking in the vicinity of these two inlets extended outside the surf zones and significantly increased the water level at the scale of the whole lagoon and estuary. This finding demonstrates that the wave setup can contribute to the water level, even in environments sheltered from the direct action of waves, such as

lagoons and estuaries.

To understand the impact of storm wave breaking on the hydrodynamics of the tidal inlets, the local momentum balance was analysed at the inlet of the Arcachon Lagoon. By reaching values one order of magnitude larger than the bottom stress and the surface stress terms, the wave forces were one of the leading terms of the momentum balance and thereby greatly affected hydrodynamics in the inlet, the main impact being the development of a wave setup at the scale of the whole lagoon.

Further analysis showed that the wave setup in tidal inlets can be tidally-modulated while this phenomenon is site-specific and depends on the morphology of the inlet. At Arcachon, as the ebb delta is characterised by supra-tidal sand banks, wave breaking is total at all tidal phases, the wave setup exhibits therefore a slight tidal modulation. At Bayonne, waves are subjected to more intense breaking at low tide than at high tide, the tidal modulation of the wave setup is thus more pronounced.

Finally, a sensitivity analysis of the storm surge and wave setup to the spatial resolution of the computational grid was carried out. This work revealed that the calculated wave setup at the shoreline is highly sensitive to the grid resolution. In the lagoon, the modelled storm surge and wave setup were found to be comparable between different grid resolutions, while tidal propagation cannot be accurately represented with a resolution of 1000 m. This study highlighted the need to account for wave breaking in operational storm surge models, although resolving the wave setup requires a spatial resolution that depends on the width of the surf zone, itself controlled by the bottom slope and the wave height.

Appendix

The underestimation of the storm surge before the peak of the surge can be attributed to a negative bias in the 10 m wind speed of CFSR. In order to verify this hypothesis, the modelled wind speed from CFSR is increased by 12-15 % over three time steps before the storm peak (Fig. 5.10-A).

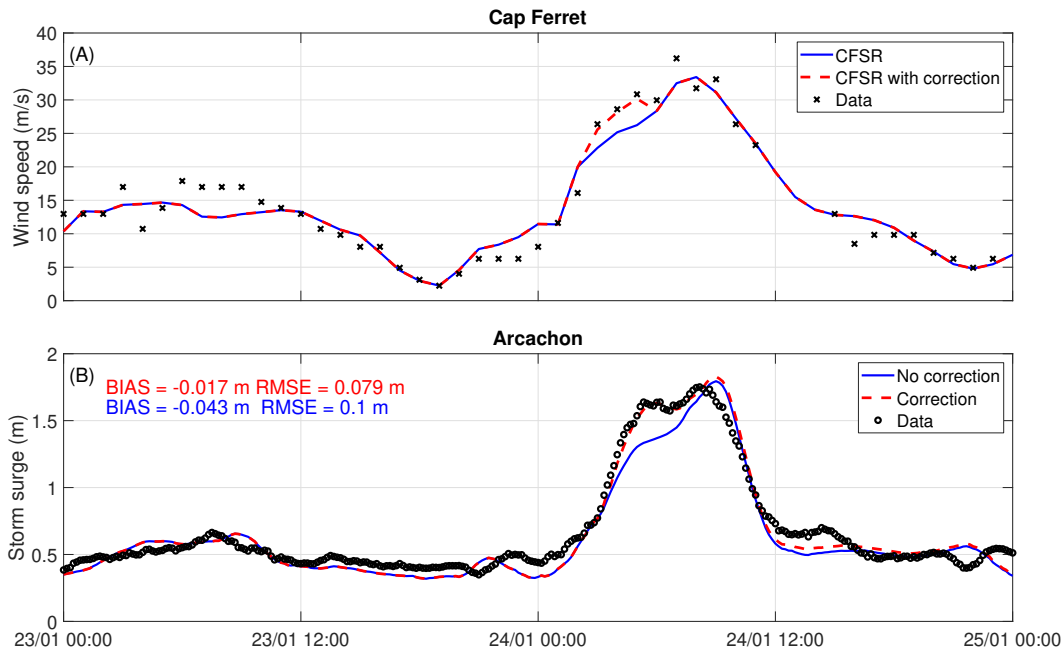


FIGURE 5.10 – (A) Measured (black crosses) against CFSR wind speed with correction (red dashed line) and original data (blue line). (B) Observed (black dots) against modelled storm surges with the corrected wind speed (red dashed line) and the original wind speed (blue line).

The comparison between the original modelled storm surge and the storm surge computed with the tuned wind speed (Fig. 5.10-B) shows a significant difference at the considered period. The RMSE is improved by 20 % and the localised error is cancelled out. These results confirm that the underestimation of the storm surge at this stage of the storm is due to a local negative bias in the modelled wind speed of the order of $4 \text{ m}\cdot\text{s}^{-1}$.

Chapitre 6

Wave dissipation and mean circulation on a shore platform

6.1 Introduction

Shore platforms are distinctive landforms of rocky coast environments. These erosional rock surfaces are found within or close to the intertidal zone and are usually backed by cliffs, but can also be topped by beaches, dunes or coastal structures. They are generally classified into two different types : gently-sloping platforms that extend in the subtidal zone without a break in slope (Type A), and sub-horizontal platforms with a sharp seaward edge (Type B) (*Sunamura, 1992*). Sloping platforms are predominantly found in meso to macrotidal ranges while sub-horizontal, or Type B, platforms are more common on microtidal coasts (*Trenhaile, 1987*). While there has been a long-standing debate on which of wave processes or subaerial weathering dominate shore platform development, it is now recognized that these mechanisms act together (*Naylor et al., 2010*). However, their relative contribution is still unclear, which is partly due to a limited number of field observations of wave processes on shore platforms (*Stephenson, 2000a; Naylor et al., 2010*). Only recently, the understanding of wave processes on shore platforms has advanced thanks to field-based studies examining the transformation of both short (frequencies $> 0.04 - 0.05$ Hz) and infragravity (frequencies $< 0.04 - 0.05$ Hz) waves over such environments (*Stephenson and Kirk, 2000b; Trenhaile and Kanyaya, 2007; Beetham and Kench, 2011; Ogawa et al., 2011; Marshall and Stephenson, 2011; Ogawa et al., 2015; Poate et al., 2018; Stephenson et al., 2018; Savige et al., 2021*). Several of these studies reported the depth-limited character of surf zone waves (*Farrell et al., 2009; Ogawa et al., 2011, 2015; Poate et al., 2018*) and the strong tidal modulation of wave energy dissipation across platforms (*Ogawa et al., 2011; Marshall and Stephenson, 2011*). In addition to the effect of tides, the morphological characteristics of the platform, such as the elevation, the gradient, the presence or absence of a seaward edge, and the width (*Ogawa et al., 2011; Ogawa, 2013; Marshall and Stephenson, 2011; Beetham and Kench, 2011*), have been observed to exert a key control on wave processes, likely explaining the contrasted rates of wave dissipation reported so far in the literature (*Stephenson and Kirk, 2000b; Stephenson and Thornton, 2005; Ogawa et al., 2012*). *Poate et al.* (2018) combined field data analyses and the application of a 1D model of wave energy flux conservation to investigate bottom roughness effects on wave transformation across several macrotidal platforms of contrasting roughnesses (measured bottom roughness ranging from 0.07 to 0.17 m). The authors suggested that bottom friction

is only important outside the surf zone, for very rough, low gradient ($< 1:50$) platforms and weak wave conditions. The latter study, together with the work of *McCall et al.* (2017) using the same dataset to calibrate their model, are ones of the very few numerical studies investigating wave dissipation processes on shore platforms, particularly frictional effects. Hence, additional field deployments combined with numerical simulations are necessary to further understand short-wave dissipation on shore platforms through both wave breaking and bottom friction. This is critical to assess the role of waves in platform erosion and cliff recession, which has been one of the main focus of studies conducted on shore platforms so far (*Stephenson and Kirk*, 2000b; *Trenhaile and Kanyaya*, 2007), but also to investigate wave-induced hydrodynamics on shore platforms, such as the wave setup.

On mildly-sloping sandy beaches, the wave setup has usually been computed assuming a balance between the cross-shore radiation stress and barotropic pressure gradients in the wave-averaged cross-shore momentum equation (*Battjes and Stive*, 1985; *Lentz and Raubenheimer*, 1999; *Guza and Thornton*, 1981; *Raubenheimer et al.*, 2001) (see section 2.1.2.2). However, *Guza and Thornton* (1981) and *Raubenheimer et al.* (2001) reported severe underestimations of the wave setup in very shallow depths with this simple approach. *Apotsos et al.* (2007) suggested that wave setup predictions can be improved by including the mean bottom stress associated with the mean offshore-directed flow (the undertow) in the cross-shore momentum balance. The undertow causes the mean bottom stress to be onshore-directed, which increases the wave setup. More recently, *Guérin et al.* (2018) used a 3D phase-averaged modelling system and showed that the wave-induced circulation (mostly horizontal advection and vertical mixing) could increase the wave setup when the bottom slope steepens. The relevance of this process has yet to be evaluated on rough bottoms, where wave setup dynamics can be different from that on sandy beaches, principally due to a higher bottom roughness (*Dean and Bender*, 2006; *Buckley et al.*, 2016). Indeed, platform roughness can range from smooth like a sandy beach, to extremely rough similar to coral reefs (*Poate et al.*, 2018). *Lowe et al.* (2005) reported that rough coral reefs could induce energy dissipation rates by friction of similar order (or event dominant) with that induced by depth-induced breaking processes over the fore reef, which could decrease the wave setup on the reef (*Lowe et al.*, 2009). *Buckley et al.* (2016) verified these findings by conducting high-resolution laboratory measurements of wave setback and setup across a fringing reef profile characterized by a 1:5 reef slope and a large bottom roughness. The authors showed that the presence of bottom roughness enhanced wave dissipation by friction which in turn modified radiation stress gradients and resulted in a predicted wave setup 18 % lower on average compared to smooth experiments, when the mean bottom stress was neglected in the momentum balance. However, once accounted for, the mean bottom stress, generated by interactions of the undertow with roughness, increased the predicted wave setup by 16 % on average. Because of these two opposing mechanisms, the wave setup measured on the reef for both rough and smooth bottoms was similar.

To date, only one study reported observations of wave setup on shore platforms (*Ogawa et al.*, 2015), but the influence of bottom roughness on its development was not examined. Understanding wave setup dynamics is important, as it can greatly contribute to extreme water levels (*Lerma et al.*, 2017; *Guérin et al.*, 2018) and potential subsequent flooding. At present, little is known about flooding risks when platforms are backed by low-lying coasts (*Naylor et al.*, 2014; *Didier et al.*, 2016), as most of the studies were conducted on shore platforms backed by coastal cliffs to study their vulnerability to the potential erosion of waves. In this study, wave transformation and wave setup dynamics are investigated on a gently-sloping shore platform that extends from the nearshore subtidal region to the intertidal zone and which is backed by a sandy dune. A first field campaign was carried

out in fair weather conditions on the intertidal zone of the shore platform while a second one, more extensive, was conducted under storm wave conditions with instruments deployed on the platform from 10 m water depth up to the shoreline. Field data analyses are complemented with numerical simulations performed with a fully-coupled (wave-current) 3D modelling system that uses the vortex force formalism implemented in the model. The field data collected in fair weather conditions are used to adequately represent wave bottom friction in the wave model, while observations in storm wave conditions allow to assess the ability of the modelling system to reproduce the transformation of short waves, as well as the resulting circulation and the wave setup on the platform. Based on the results, the relative importance of depth-induced breaking to wave bottom friction is examined. The impact of both wave dissipation and resulting circulation on the wave setup in such a rough environment is then analysed through additional numerical experiments considering idealised shore platforms and sandy beaches of varying uniform slopes. After presenting the study area in section 6.2, the model implementation for this application is described in section 6.3. The ability of the modelling system to simulate the transformation of short waves, water levels and mean current velocities over the considered shore platform is investigated in section 6.4. In section 6.5, the sensitivity of the model to parameterizations and the relative importance of short-wave dissipation by depth-induced breaking and bottom friction are discussed. The effects of bottom roughness affecting wave setup through wave dissipation and resulting circulation are then developed, followed by conclusions in section 6.6. This chapter is based on a first publication that detailed the field campaign conducted in fair weather conditions as well as the associated results (*Lavaud et al.*, 2020b), and on a second publication related to the results of the field campaign conducted in storm wave conditions (*Lavaud et al.*, 2022).

6.2 Study area and field experiments

6.2.1 Study area

The studied shore platform is located in the central part of the French Atlantic Coast along the western coast of Oléron Island (Fig. 6.1-a). The coast in the region is bordered by a 150 km-wide shelf, which exhibits gently-sloping shorefaces. According to *Dodet et al.* (2019a), the tidal regime is semi-diurnal and macrotidal, with a tidal range varying from 1.10 to 5.50 m. These authors also analysed wave regimes along the 30 m isobath line of the metropolitan coasts of France and reported in the region, yearly-averaged significant wave height (hereafter H_{m0}) of 1.60 m and yearly averages of mean wave period and wave direction of 5.9 s and 275° respectively. Winter storms can, however, drive waves of H_{m0} over 10 m in the Bay of Biscay (*Bertin et al.*, 2015a).

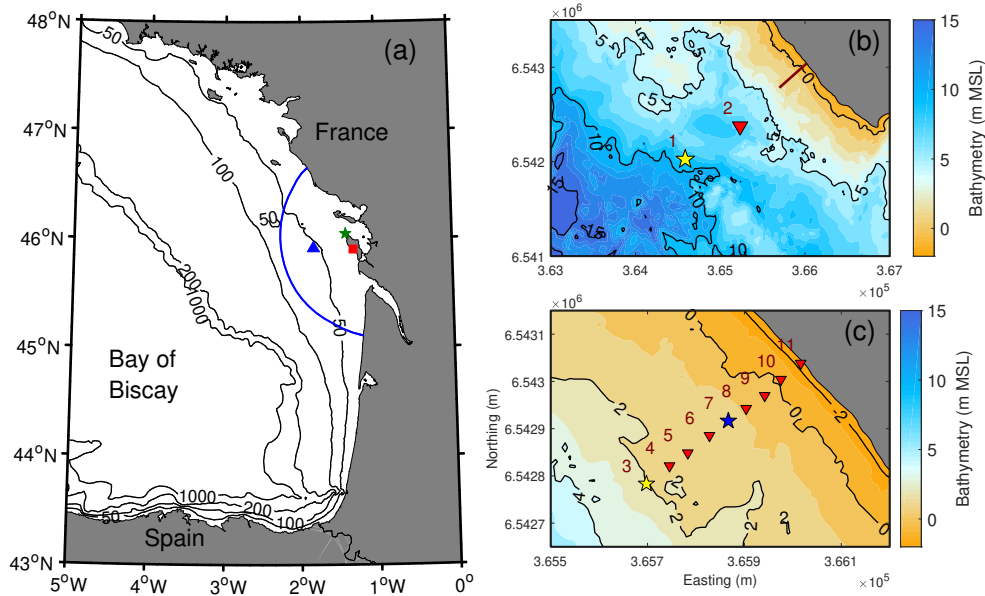


FIGURE 6.1 – Location of the study area (red square), Oléron wave buoy (blue triangle), meteorological station (green star) and extension of the computational domain (blue line) (a). Bathymetry of the study area relative to mean sea level (MSL) with location of stations 1 and 2 (b) and stations 3 to 11 (c), deployed during the field campaign in storm wave conditions.

The intertidal shore platform is 450 m-wide (full spring intertidal range), with a very gentle slope of 1:250 increasing up to 1:50 at the top of the platform (x between 300 m and 445 m, see Fig. 6.2). The platform is a marl-limestone formation characterised by shallow steps and pools, except at the beginning of the profile (before $x = 50$ m) where steep pools (~ 1 m deep) can develop. At its landward edge (from $x = 445$ m), the platform is backed by a sandy dune with a steep sandy beach (slope of 1:10) at the platform-dune junction. At its seaward edge (before $x = 0$ m), the subtidal portion of the platform plunges into the sea with a slope of 1:65 before being more gently-sloping, and extends until ~ 3000 m offshore.

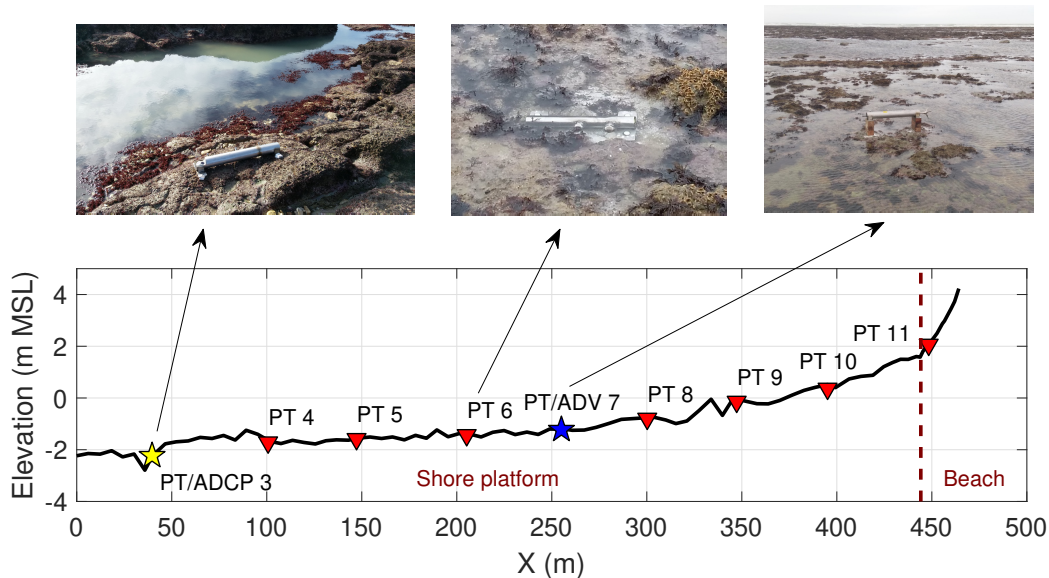


FIGURE 6.2 – Cross-shore profile of the intertidal zone with location of the stations 3 to 11 deployed during storm wave conditions.

6.2.2 Field experiments

Two field campaigns were conducted on the shore platform under contrasting wave-energy conditions. The first one was carried out on the intertidal part of the platform during one day (two tidal cycles) in March 2019, under spring tides with a 5.50 m tidal range and weak-energy wave conditions (hereafter referred to as fair weather conditions). Maximum significant wave height and peak period of 1.5 m and 15 s respectively, were recorded at the Datawell Oléron buoy (operated by CEREMA and located at a depth of 50 m; see Fig. 6.1-a for its location). A detailed description of this campaign and the associated results on short wave transformation using a simple energy flux model can be found in *Lavaud et al.* (2020b). Since this field experiment is characterized by small waves and low wind conditions, it is specifically used in the present study to investigate bottom friction effects on wave dissipation and in particular, to determine the roughness length k_n (see section 6.3) of the platform through a sensitivity analysis of the model to this parameter. The second field campaign was conducted from February 7 to 13 2020, under spring tides with a maximum tidal range of 5.20 m, and storm wave conditions (maximum significant wave height and peak period of ~ 6 m and 17 s respectively, recorded at Oléron buoy). This field campaign was more extensive than the first one, since it covered not only the intertidal zone but also the subtidal part of the platform. In the intertidal zone, a 400 m-long cross-shore transect was instrumented from February 9 with 7 pressure transducers (hereafter PT), a 2 MHz ADCP and a 6 MHz ADV, both equipped with an internal PT (Fig. 6.1-c and Fig. 6.2). The instruments were spaced at 45 m intervals, allowing to cover most of the full spring intertidal zone, and were all housed in stainless steel tubes screwed to the bedrock (Fig. 6.2), except the most landward PT (PT 11) which was fixed to a rock buried in 0.10 m of sand on the backing beach. However, this sensor was not considered in this analysis as it was located in the swash zone and hence, not continuously submerged. Also, pressure signals recorded at PT 3 and 7 showed drifting and were therefore discarded from the analysis of water levels and wave setup. In the subtidal zone, a 600 kHz ADCP equipped with an internal PT (PT 1) and an additional PT aiming at identifying possible sensor drifting (PT 0, not shown) were deployed about 1750 m offshore at a depth of approximately 9 m relative to mean sea level. Another single PT was deployed closer to shore, at 1000 m in a depth of approximately 8 m relative to mean sea level (Fig. 6.1-b). Both subtidal stations were located on the shore platform, although PT 2 was deployed in a small sandy zone surrounded by the rocky bottom. The PTs of the overall deployment measured at 2 Hz except the internal PT of the ADV, which measured at 16 Hz.

Data from both field experiments were analysed following the procedure detailed in section 4.2.3.5. Bottom pressure measurements were first corrected for sea level atmospheric pressure measured at the nearby meteorological station of Chassiron (Fig. 6.1-a). Each data record was then analysed using consecutive bursts of 30 min (20 min for the internal PTs of ADCPs). At each sensor located in the intertidal zone, bursts of mean water depth less than 0.50 m were discarded from this analysis as the sensors were intermittently dry due to the presence of fluctuations induced by infragravity waves. Hydrostatic surface elevation spectra were computed by averaging estimates from 10 Hanning-windowed segments overlapping by 50 % (20 degrees of freedom). Non-hydrostatic effects were accounted for using the TFM. As explained in section 4.2.3.6, the SNL was not used here as the development of wind seas under the strong local winds and the presence of rocky shoals promoting wave breaking and subsequent release of harmonics, can limit the applicability of this method. The cut-off frequency f_{max} in the TFM is set to 0.3 Hz. The frequency cut off between short and infragravity waves f_{min} is adaptive and defined as $1/1.8T_p$ with T_p the continuous peak

period recorded at Oléron buoy (Fig. 6.1-a).

In the subtidal zone, a high resolution (0.2 m x 0.2 m regular grid) multibeam bathymetric survey was performed on approximately 1.73 km² to dispose of accurate bathymetric data of the study area. This high-resolution dataset was also used to physically quantify the bottom roughness length k_n of the platform : it was estimated as four times the standard deviation of the bed elevation (Lowe *et al.*, 2005; Poate *et al.*, 2018) and was computed by averaging several estimates from 1 m² tiles across the platform, leading to an averaged value of 0.15 m.

At the intertidal PTs (except stations 3, 7 and 11 discarded from this analysis), the wave setup was computed as the difference in mean free surface elevations between each PT and the deepest one (PT 1), which requires an estimate of its vertical position (not known in the field a priori). The Figure 6.3-a shows the mean free surface elevation $\bar{\eta}$ at the intertidal sensors at high tide on March 12 afternoon, which corresponds to the calmest conditions during the field campaign (high tide, wind velocity inferior to 5 m.s⁻¹ and weak wave contribution). The vertical position of PT 1 (in the subtidal zone) was determined at this instance, by assuming an horizontal plane between PT 1 and PT 4 (that is no contributions from surface stress or wave setup to the mean free surface elevation between PT 1 and PT 4). On the Figure 6.3-b, the mean free surface elevation was corrected from the modelled wave setup developed between the offshore PT (PT 1) and each sensor. At PT 4, the modelled wave setup is 0.01 m, which can support our assumption made in the determination of the vertical position of PT 1. Also, the resulting mean free surface elevation at all the intertidal sensors (from PT 4 to PT 10) are on a same horizontal plan (+/- 0.01 m), which can attest of the accuracy of the levelling procedure. The wave setup was then calculated at each sensor except at PT 2, as this instrument progressively sank into the sand during the field campaign. A detailed description of the procedure used to retrieve the wave setup between two pressure sensors is given in section 4.2.2.

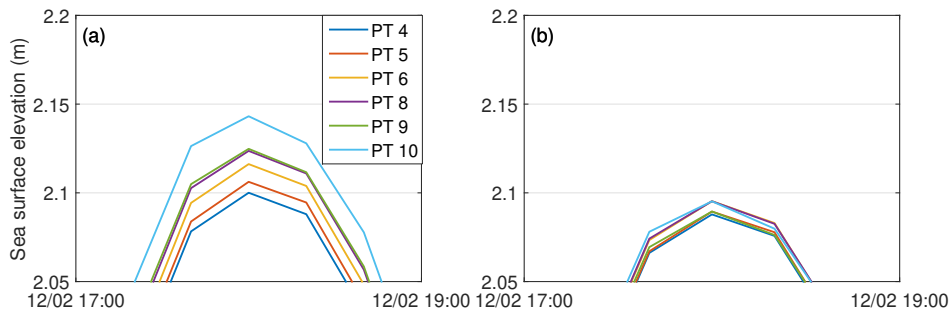


FIGURE 6.3 – Sea surface elevation on March 12 afternoon at high tide at the intertidal sensors without correction (a) and corrected from the wave setup obtained from the model (b).

6.3 Model implementation

In this application, the 3D circulation module of SCHISM is coupled to WWM-II and the vortex formalism is used to represent the effects of waves on currents.

The wave model accounts for energy dissipation due to whitecapping and wind input according to the WAM-Cycle 4 formulation (Bidlot *et al.*, 2007). Wave energy dissipation by depth-induced breaking is computed following the approach of *van der Westhuysen* (2010). While the breaking coefficient B is originally set to 1 in *van der Westhuysen*

(2010), we use here the adaptive approach of *Pezerat et al.* (2021). Both parametrizations are compared in section 6.4.1.2. In the bottom friction formulation, the drag coefficient C_f is computed according to the eddy-viscosity model of *Madsen et al.* (1989) (Eq. 3.21). The default value for the Nikuradse roughness length k_n in WWM-II is 0.05 m, which relates to a sandy bottom with bedforms. The spatial distribution of bottom types, and in particular the extension of the studied rock platform, is here based on the sediment database of the SHOM (French Naval Oceanographic Service). Considering the direct estimates of k_n from the high-resolution multibeam bathymetric survey (see section 6.2.2), the value of k_n on the platform was then adjusted by minimizing the discrepancies between model predictions and observations during fair weather conditions (see section 6.4.1.1). Outside of the rocky area, k_n is set to its default value 0.05 m. In order to evaluate the influence of the bottom friction formulation on the performance of the model, simulations were also carried out with the Madsen’s formulation using a uniform k_n set to 0.05 m, and with the widely-used JONSWAP formulation of *Hasselmann et al.* (1973), based on a friction coefficient C_f spatially uniform and fixed to the empirical value of $0.038 \text{ m}^2 \cdot \text{s}^{-3}$.

The circulation model is forced at its open boundary with the 16 main astronomical constituents linearly interpolated from the regional model of *Bertin et al.* (2012). The bottom roughness length z_0^{bot} in the circulation model is spatially variable to account for the different bottom types in the modelled domain. After a sensitivity analysis (see section 6.4.2), z_0^{bot} was set to 0.0001 m in sandy areas and to 0.02 m on the studied shore platform and other rocky bottoms. The model of *Soulsby* (1997) is used to compute the bottom stress under the combined action of waves and currents. The surface stress is wave-dependent according to the formulation of *Donelan et al.* (1993). The wave streaming acceleration (Eq. 3.46) is assumed to decrease upward across the wave boundary layer according to the vertical function given by Eq. 3.47. In the expression of the decay length k_{wd} , $a_{wd} = 1$ allows to retrieve the theoretical thickness of the wave bottom boundary layer under monochromatic waves. In this study, a_{wd} is fixed to 5, which is discussed in section 6.5.1. We assume a full conversion of energy from breaking waves to surface rollers with $\alpha_r = 1$.

The unstructured computational grid used in the hindcast of the field experiments extends over the Pertuis Charentais area (Fig. 6.1-a), from the land boundary to ~ 73 km offshore corresponding to a depth of 90 m. Such a large extent is necessary to realistically reproduce the generation and propagation of storm surges over the continental shelf (*Blain et al.*, 1994; *Oliveira et al.*, 2020). The grid has ~ 76000 nodes in the horizontal, with a spatial resolution ranging from 1800 m along the open boundary to 10 m along the shoreline in the study area. In the vertical, the grid is discretized in 24 terrain-following S-layers that are denser close to the bottom and surface. The hydrodynamic time step is set to 15 s while the wave model is run every 60 s and uses implicit schemes for propagation and source term integration (*Roland et al.*, 2012).

Over the whole domain, the circulation model is forced with hourly 10 m wind speed U_{10} and sea-level pressure fields from the Climate Forecast System Reanalysis CFSR (*Saha et al.*, 2010). The datasets are provided on a regular grid with a spatial resolution of 0.2° and 0.5° for the wind and the atmospheric pressure respectively. WWM-II is forced with CFSR wind fields over the whole domain and time series of directional wave spectra along its open boundary, which were previously computed from a regional application of the WaveWatch III spectral wave model also forced with wind fields from CFSR.

6.4 Results

In this section, we assess the ability of the modelling system to reproduce the observed water levels, the transformation of short waves and the associated circulation over the shore platform. Modelled wave parameters are first compared against field observations collected during fair weather conditions in order to determine the Nikuradse roughness length k_n that characterized the platform. Indeed, at high tides during this period, waves are predominantly dissipated by bottom friction on a large portion of the intertidal shore platform as the surf zone is located very close to the shoreline, making this period particularly suitable for analysing wave bottom friction dissipation and the sensitivity of the model to k_n . The value of k_n yielding the best-fit results is then used in the simulation of storm wave conditions, from which short waves, currents and wave setup predictions are examined. Model errors are quantified by computing for each variable, the BIAS, the RMSE and the NRMSE (Eqs. 5.1, 5.2 and 5.3) .

6.4.1 Wave predictions

6.4.1.1 Fair weather conditions

During the one-day field campaign conducted in fair weather conditions, offshore significant wave height H_{m0} varied between 1.1 and 1.5 m at Oléron buoy (see Fig. 6.1-a for its location), which is well predicted by the model with a RMSE of 0.09 m, yielding a NRMSE of 7 % (not shown). Figure 6.4 compares at the second high tide the cross-shore evolution of H_{m0} measured, and modelled with different bottom friction formulations. At this tidal stage (water depth of 4.50 m at the offshore sensor), the surf zone is relatively narrow and starts approximately at $x \sim 225$ m, implying that wave dissipation at the three most offshore sensors principally occurs through bottom friction. The data at these cross-shore locations are hence suitable to calibrate the Nikuradse roughness length k_n in the Madsen's formulation.

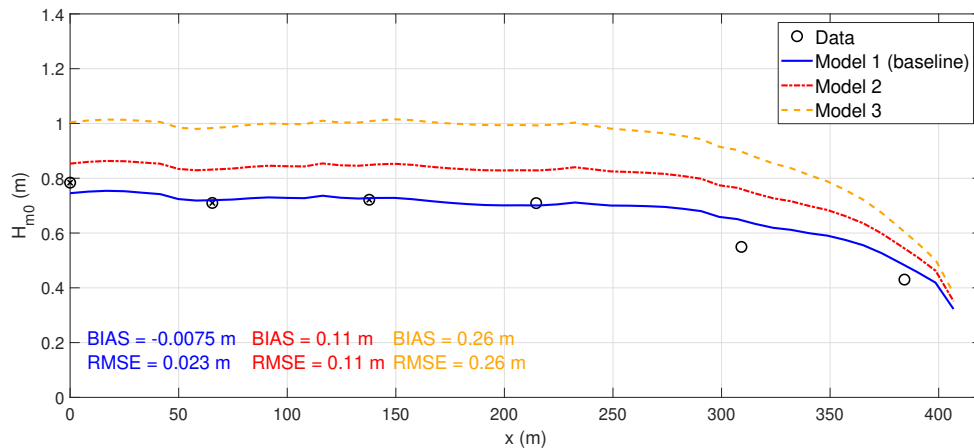


FIGURE 6.4 – Observed (black dots) against significant wave height H_{m0} modelled with the baseline model using Madsen's formulation with $k_n = 0.13$ m for rocky areas and 0.05 m outside (model 1), the model using the Madsen's formulation with k_n set uniform to the default value 0.05 m (model 2) and the model using the JONSWAP formulation with $C_f = 0.038 \text{ m}^2 \cdot \text{s}^{-3}$ (model 3), at the second high tide along the intertidal transect instrumented during fair weather conditions. The black crosses correspond to where statistical errors are computed (RMSE, BIAS).

A sensitivity analysis to this parameter revealed that the value of $k_n = 0.13$ m taken on the platform (and 0.05 m outside) best reproduces the observed wave height at the three offshore sensors with a RMSE of 0.023 m. Keeping the default value $k_n = 0.05$ m uniform over the whole computational domain (model 2 in Fig. 6.4) or using the JONSWAP bottom friction formulation with $C_f = 0.038$ m².s⁻³ (model 3 in Fig. 6.4) leads to an underestimation of wave frictional dissipation with RMSE of 0.11 and 0.26 m respectively. Based on these results, the Madsen's formulation with k_n set to 0.13 m on the platform was used in the hindcast of the second field campaign conducted in storm wave conditions.

6.4.1.2 Storm wave conditions

As in fair weather conditions, simulated offshore wave parameters are compared against measurements recorded at Oléron buoy (Fig. 6.1-a). The comparison reveals a very good agreement between observed and modelled significant wave height H_{m0} with a RMSE of 0.26 m which corresponds to a 6 % NRMSE. The mean wave period T_{m02} was of the order of 8-10 s and the peak period T_p varied between 13 and 17 s during the field campaign, which is well reproduced by the model with RMSE of ~ 0.40 and 0.50 s respectively, corresponding to NRMSE less than 5 %. The peak direction P_{dir} is also well predicted by the model with a RMSE of 6°. It is worth noting that H_{m0} reached almost 6 m during the field campaign, a value reached 5 times since January 2020, therefore corresponding to energetic but not exceptional winter conditions (Fig. 6.5).

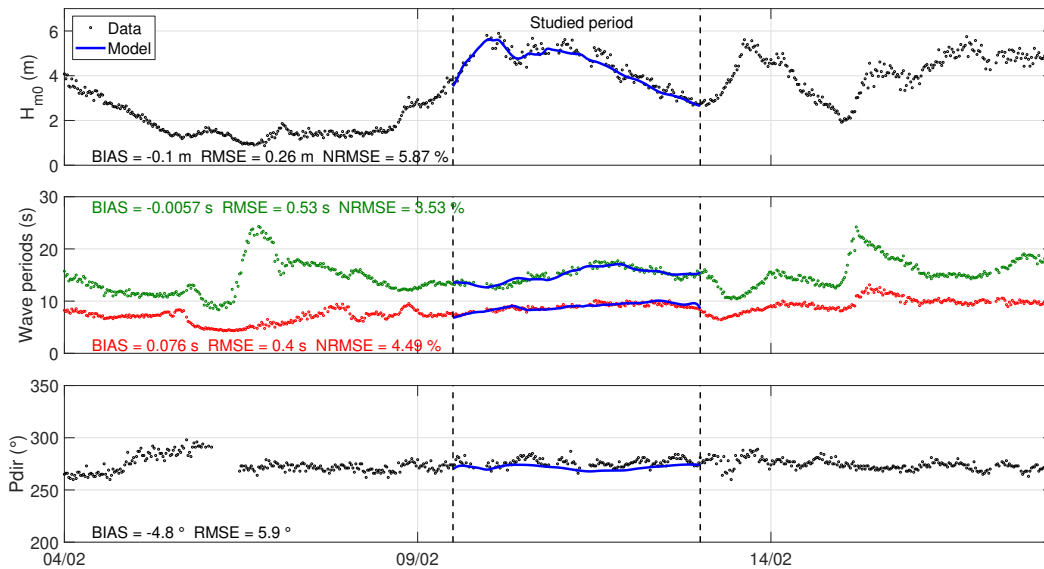


FIGURE 6.5 – Assessment of the model at the offshore Oléron buoy with comparisons of the modelled (blue line) against observed significant wave height H_{m0} , peak direction P_{dir} (black dots), mean wave period $T_{m0,2}$ (red dots) and peak period T_p (green dots).

In the nearshore region, the water levels at PT 1 and PT 2 are well reproduced by the model with RMSE of 0.08-0.09 m (Fig. 6.6). At both sensors, H_{m0} is tidally-modulated with H_{m0} decreasing as the water depth decreases, suggesting that wave breaking is already significant at these depths. Maximum H_{m0} values were measured at PT 1 in the morning of 10/02 at high tide, with a value of 3.60 m for a corresponding mean wave period T_{m02} of ~ 7.5 s. At PT 1, H_{m0} is predicted relatively accurately with RMSE of 0.30 m, yielding a 13 % NRMSE although H_{m0} is slightly over-estimated during the whole period with a

positive bias of 0.26 m. At PT 2, H_{m0} is well predicted by the model with a NRMSE of 9.6 %. Mean wave periods T_{m02} are slightly over-estimated at PT 1 with a positive bias of ~ 0.40 s, while at PT 2, it is accurately reproduced by the model with a NRMSE of 3.6 %. Similar to the significant wave height, T_{m02} also exhibits a tidal modulation at both sensors, which is slightly more pronounced at PT 2, with T_{m02} being smaller at low tides by up to 2 s. When the triad interactions source term is turned off in the simulation, the wave period exhibits an inverse and weaker tidal modulation, revealing that the observed tidal modulation is due to triad interactions in shallow waters. At a given sensor, more energy is transferred from the primary peak to super harmonics as the water depth decreases, explaining the lower wave period.

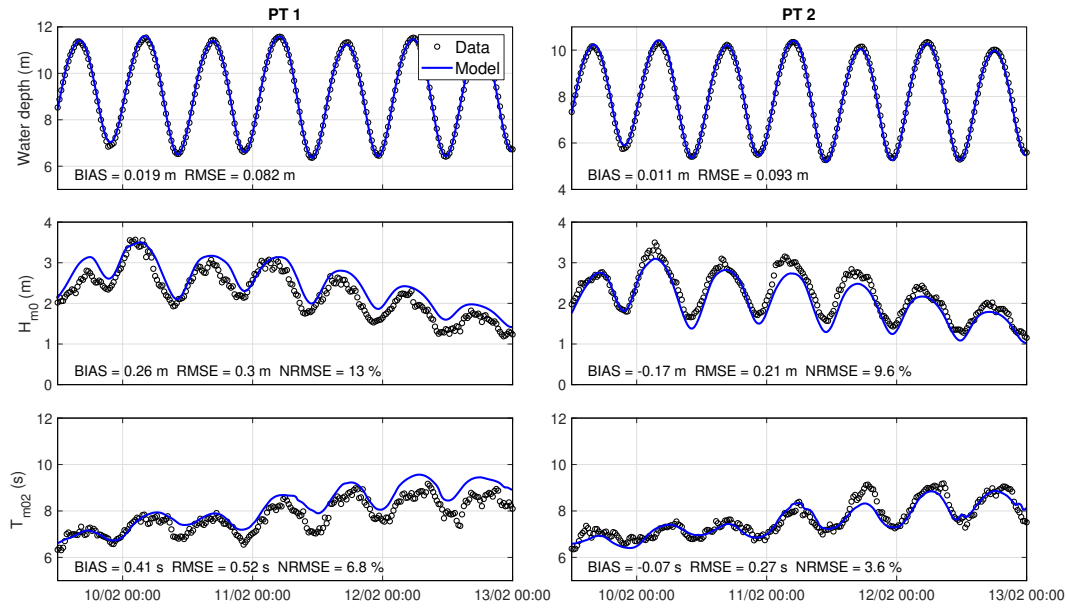


FIGURE 6.6 – Assessment of the model at the subtidal sensors (PT 1 and PT 2) with comparisons of the modelled (blue line) against observed water depth, H_{m0} and $T_{m0,2}$ (black dots).

As a general trend, wave heights in the intertidal zone (Fig. 6.7-b to Fig. 6.7-g) are highest at the most seaward sensor (PT 4) and decrease across the platform towards the shoreline. At the first sensor in the intertidal zone (PT 4, Fig. 6.7-b), the wave height is depth-limited over the first 6 tidal cycles. Over the last one, the same behaviour can be observed from low to mid tidal stages while from mid to high tidal stages, the wave height does not increase when the water depth increases (water depth at PT 1, Fig. 6.7-a), suggesting that this sensor was located outside the surf zone. At the landward sensors (from PT 5 to PT 10; Fig. 6.7-c to Fig. 6.7-g), short waves are depth-limited during the whole period, so that they were always located in the surf zone. The comparison with the model shows that wave heights at all stations are well predicted by the model with NRMSE ranging from 8 to 14 %. In more details, H_{m0} is slightly underestimated by 0.15 to 0.20 m at PT 9 and 10 at high tides over the last two days of the experiment, which is possibly due to wave reflection on the 1:10 sloping beach, a process not represented in the model. Note that using a default parameterization for depth-induced breaking ($B = 1$), wave predictions considerably deteriorate at PT 2 (negative bias of 0.60 m and NRMSE of 30 %) and in the intertidal zone with a negative bias of 0.40 m resulting in a NRMSE of 43 % in average. On the contrary, using a default parameterization for bottom friction (JONSWAP formulation with $C_f = 0.038 \text{ m}^2 \cdot \text{s}^{-3}$) results in positive bias of 0.70 m and 0.17 m and NRMSE of 30 %

and 20 % in average, at the sensors of the subtidal and intertidal zones respectively. The importance of accurately representing short-wave dissipation on wave setup is discussed in sections 6.4.3 and 6.5.1.

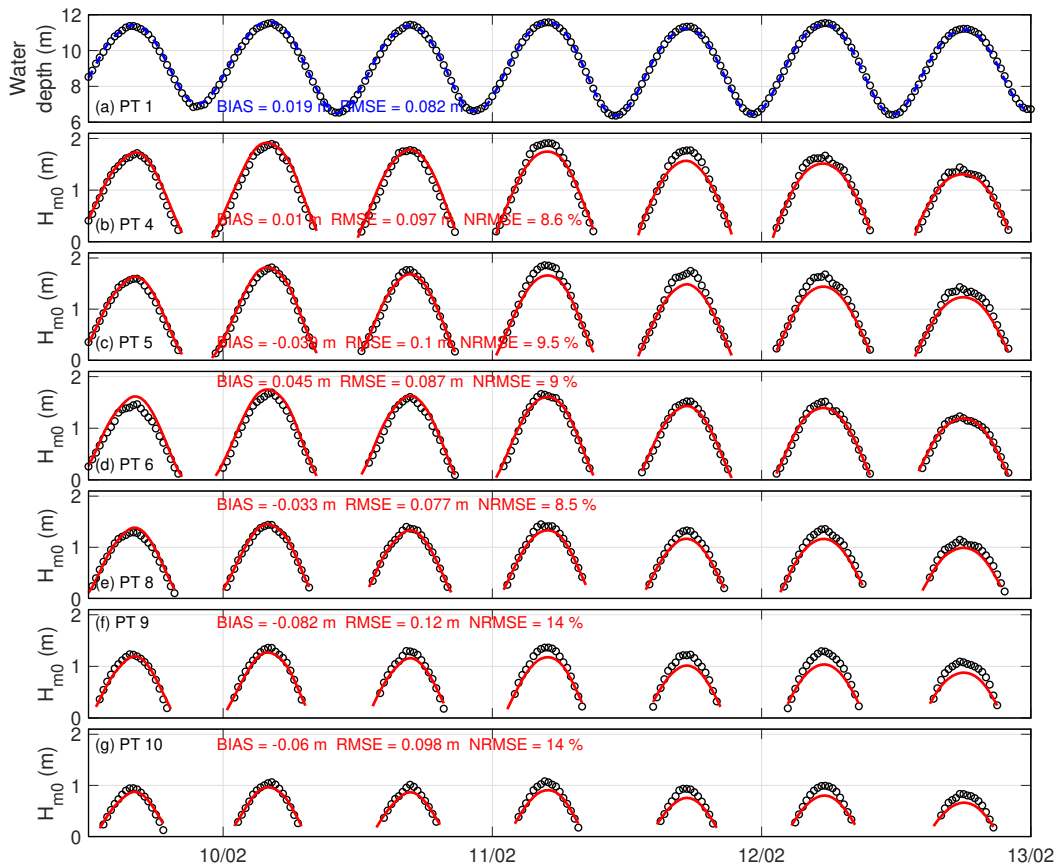


FIGURE 6.7 – Modelled (blue line) against observed water depth at the subtidal sensor PT 1 (panel a) and assessment of the model at the intertidal sensors (from PT 4 to PT 10) with comparisons of the modelled (red line) against observed H_{m0} (black dots) (panels b to g).

6.4.2 Cross-shore and long-shore current predictions

The ability of the model to reproduce mean currents is assessed through a comparison with currents measured at the ADV (corresponding to PT 7 location), located at a height of 0.25 m above the seabed. The use of the ADCP in the surf zone provided incoherent patterns, possibly owing to the presence of air bubbles in the wave column affecting or even blocking the acoustic signal, which did not allow to analyse mean currents at this location. At the ADV, measured velocities and modelled quasi-Eulerian velocities at 0.25 m above the bed (vertical position of the ADV) were time-averaged over bursts of 20 min. The measured cross-shore velocity is always seaward-oriented, which suggests the presence of an undertow, reaching up to $-0.20 \text{ m}\cdot\text{s}^{-1}$ (Fig. 6.8-b). Also, a slight asymmetry can be observed between flood and ebb in the measured cross-shore velocity, which suggests the influence of tidal currents (Fig. 6.8-a and b). The negative values of the longshore velocity, up to $-0.12 \text{ m}\cdot\text{s}^{-1}$ indicate the presence of a weak longshore drift to the South-East of Oléron Island (Fig. 6.8-c). As in previous studies (Longuet-Higgins, 1970a,b; Thornton and Guza, 1986), the reproduction of longshore currents is very sensitive to z_0^{bot} . Best agreements in longshore currents between the model and the measurements were obtained with z_0^{bot}

$= 0.02 \text{ m}$ (RMSE of 0.030 m.s^{-1}), while halving this value yields an error twice as large. Predictions of the cross-shore velocity depart more from the measurements, mostly owing to a negative bias of 0.06 m.s^{-1} with local underestimations up to 0.10 m.s^{-1} (Fig. 6.8-b), yielding a RMSE of 0.064 m.s^{-1} .

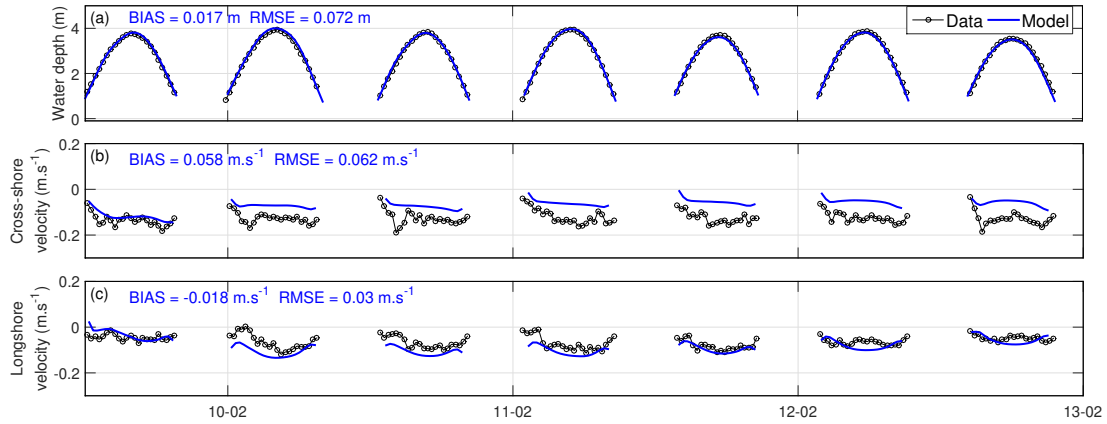


FIGURE 6.8 – Water depth at PT 6 (a). Measured cross-shore (b) and longshore (c) currents (black dots) against modelled quasi-Eulerian velocities (blue line) at the vertical position of the ADV (0.25 m above the bed, PT 7 location).

6.4.3 Storm surge and wave setup predictions

Figure 6.9 presents modelled against observed surges at the different intertidal stations. Similar to the surge computed from the measurements, the modelled surge was calculated as the difference between mean free surface elevations at each PT in the intertidal zone and the most seaward sensor (PT 1). The modelled and observed surges comprise the wave setup and a part of the wind-induced surge that developed from PT 1 to the shoreline. According to the model results, the atmospheric surge ranged from 0.00 to 0.03 m most of the time during the field campaign but could reach up to 0.06 m at low tide during episodic strong wind events of up to 15 m.s^{-1} recorded at the meteorological station of Chassiron (see Fig. 6.1-a for its location). Besides this effect, the surge was mainly due to the wave setup, representing at least 80% of the surge. The measured surge reached up to 0.30 m at low tide during energetic wave conditions in the evening of the 9th of February. The comparison between the surge measured and simulated with the baseline model shows a relatively good agreement with RMSE of the order of 0.02 - 0.03 m for all the PTs. In more details, the model displays local underestimations of up to 0.08 m at certain low tides. In comparison, the model using a default parameterization for depth-induced breaking ($B = 1$) results in an underestimation of the wave setup at the water line, with negative bias up to 0.04 m at PT 10 and RMSE increased by 50 to 90% compared to our baseline model. In opposite, using the default JONSWAP bottom friction formulation ($C_f = 0.038 \text{ m}^2.\text{s}^{-3}$) leads to a wave setup overestimated at all sensors in the intertidal zone with a positive bias of 0.065 - 0.085 m and RMSE 2 to 4 times larger compared to our baseline model (Fig. 6.9).

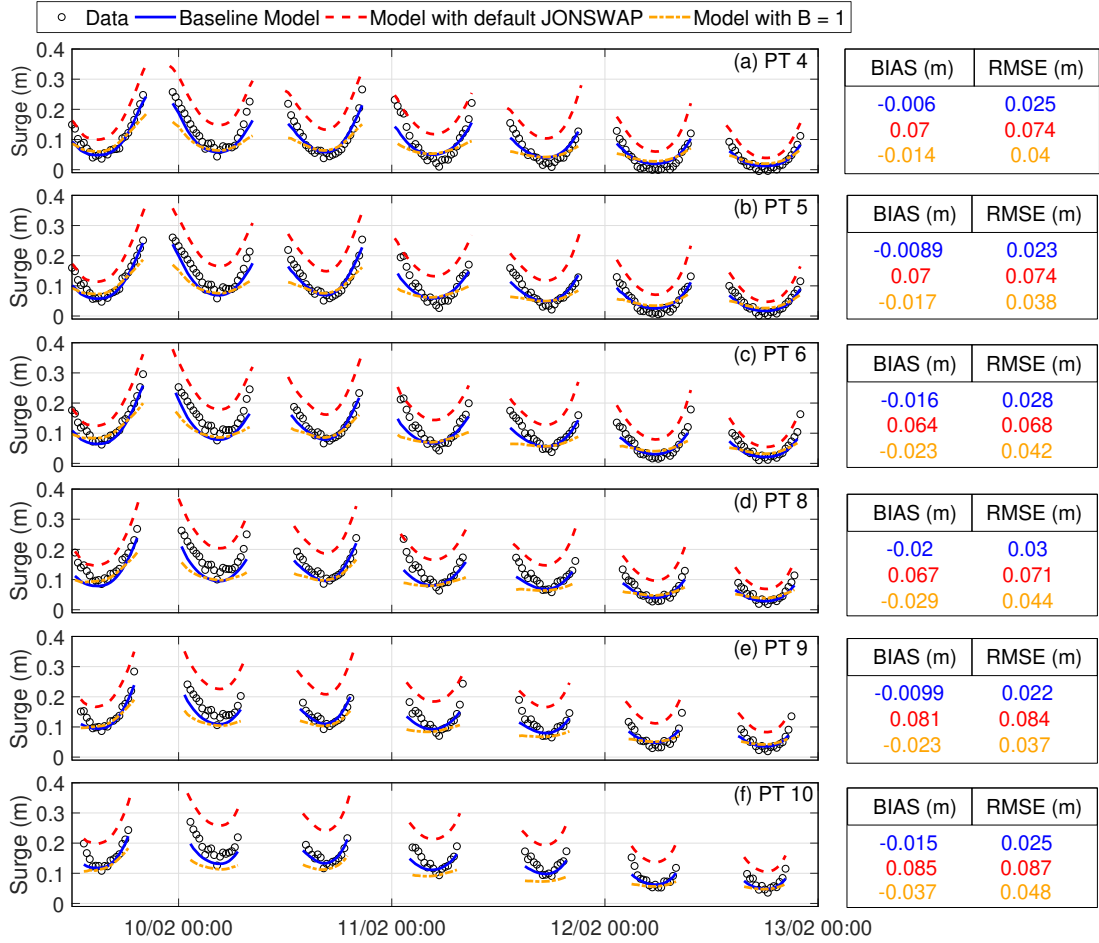


FIGURE 6.9 – Observed (black dots) against modelled storm surges with the baseline model (blue line), with the default JONSWAP formulation (red dashed line) and with $B = 1$ in the depth-induced breaking formulation (orange dashed dotted line), at the intertidal PTs.

6.5 Discussion

6.5.1 Model sensitivity to parameterizations

The accurate modelling of short-wave energy dissipation and the associated wave setup over the studied shore platform largely relies on the correct representation of the depth-induced breaking and bottom friction processes. Recently, *Pezerat et al.* (2021) reported that common parameterizations for depth-induced breaking in spectral wave models yield significant over-dissipation of storm waves propagating over gently-sloping shorefaces, potentially leading to an underestimation of the wave setup at the shoreline. In line with their findings, our results showed that the approach proposed by these authors (Eq. 3.19) strongly improves wave height and wave setup predictions (Fig. 6.9). Regarding frictional wave dissipation, the evolution of the wave height on the shore platform is only correctly represented with a parameterization that accounts for its roughness, which here corresponds to the Madsen’s formulation with $k_n = 0.13$ m. This value is close to the platform roughness length of 0.15 m obtained from our centimetre-scale bathymetric survey (see section 6.2.2), which is in the range of the values measured by *Poate et al.* (2018) on contrasting shore platforms (0.07 to 0.17 m). This value is also comparable to the values of 0.10 m used

by *Delpey et al.* (2014) and 0.12 m used by *Roland and Ardhuin* (2014) to represent rocky bottoms in their modelling systems. In these studies, together with the one of *Guillou* (2014), representing shallow rough areas in spectral wave models was also found to improve nearshore waves predictions. In addition, the present results showed that an inadequate modelling of the dissipation by bottom friction impacts wave setup predictions (Fig. 6.9). Once well represented, the strong frictional effects occurring on the platform seaward off the surf zone dissipate more wave energy before wave breaking, which modifies wave accelerations and results in a decreased wave setup, a process that was already reported by *Buckley et al.* (2016) on a fringing reef. In spite of the limitations suggested above, the JONSWAP bottom friction formulation with the constant value $C_f = 0.038 \text{ m}^2 \cdot \text{s}^{-3}$ is still commonly used in spectral wave models implemented at regional scales, possibly because sediment distribution in many coastal zones is not available (*Siadatmousavi et al.*, 2011).

Wave dissipation by friction at the bottom also affects the nearshore circulation through the generation of a near-bottom streaming along the wave propagation direction (*Longuet-Higgins*, 1953). *Wang et al.* (2020) suggested that a high bottom roughness, which enhances the dissipation by wave bottom friction, can result in a stronger bottom streaming that can weaken the undertow close to the surf zone. A similar behaviour was observed in our study, in which both the undertow and the wave setup were found to be sensitive to the vertical distribution of the bottom streaming (Eq. 3.47), and particularly to the decay length k_{wd} . While k_{wd} with a_{wd} taken to 1 corresponds to the theoretical thickness of the turbulent wave bottom boundary layer, the laboratory experiments of *Klopman* (1994) suggest that a_{wd} can significantly increase under random waves. A value of 5 for a_{wd} was here retained, which is close to the value of 3 used by *Reniers et al.* (2004). Taking such a small value of a_{wd} may excessively reduce the undertow in the surf zone, which could partly explain the underestimated cross-shore current velocities at the ADV (Fig. 6.8). This hypothesis was verified by running the model with a uniform vertical distribution of the bottom streaming acceleration, which indeed increased the undertow and almost cancelled out the remaining bias in the wave setup. The present approach to represent the effects of the bottom streaming on the nearshore circulation follows *Uchiyama et al.* (2010) and is based on theoretical analyses for progressive waves propagating in deep to intermediate water depths. However, several studies reported that the bottom streaming is reduced under asymmetric oscillatory flows (*e.g.* non-linear waves) and can even become offshore-directed (*Trowbridge and Madsen*, 1984; *Kranenburg et al.*, 2012; *Xie et al.*, 2021). Hence, the present modelling approach of the bottom streaming might not be adapted in the surf zone, which is characterized by strongly asymmetric flows. Further research is needed to better understand the contribution of the bottom streaming to the surf zone mean circulation, and in particular, the vertical distribution of the associated acceleration should be verified. Other potential processes might also contribute to the discrepancy between modelled and measured cross-shore current at the ADV. The latter exhibits an asymmetric form between flood and ebb, suggesting the presence of tidal currents in addition to the undertow. A detailed inspection of the intertidal zone indicates that the rock topography is very complex, likely driving specific patterns of tidal-induced currents and locally forcing rip currents of small amplitude. In addition, the ADV location is surrounded by topography features of the same order of magnitude than the setting height of the ADV (0.25 m from the bed; see the photo of the ADV site, Fig. 2), locally affecting the circulation. However, this topography is not well represented with the 10 m grid resolution, possibly explaining a limited prediction of these processes.

6.5.2 Relative importance of wave breaking to frictional dissipation on the platform

The importance of wave breaking and wave bottom friction processes is analysed by calculating rates of wave energy dissipation D_{br}/ρ and D_{fr}/ρ along a cross-shore profile at high tide during both fair weather and storm wave conditions (Fig. 6.10). D_{br}/ρ and D_{fr}/ρ are then integrated along the cross-shore profile to analyse their relative contribution to the total wave dissipation. In both contrasting wave energy conditions (calm/storm), the analysis reveals that wave energy dissipation is dominated by bottom friction outside the surf zone. In more details, during fair weather conditions, bottom friction occurring on the subtidal part of the platform and on a major part of the intertidal region accounts for 40 % of the total wave energy dissipation, before wave breaking becomes the leading process of dissipation in the surf zone located very close the shoreline (from $x = 1500$ m, Fig. 6.10-e). In storm wave conditions, wave breaking occurs locally in the subtidal zone but with dissipation rates weaker than bottom friction, the latter in this region representing ~ 25 % of the total wave energy dissipation (from $x = 0$ to $x = 1100$ m, Fig. 6.10-f and 6.10-h). Closer to shore and in the intertidal zone, wave breaking mostly dominates the dissipation, particularly when the bottom slope increases from $x = 1100$ to 1400 m with a maximum dissipation rate 8 times larger compared to bottom friction (Fig. 6.10-f). This zone is very effective in dissipating wave energy through wave breaking, acting similarly to the sharp seaward edge that characterized near-horizontal platform in micro-tidal settings (*Ogawa et al.*, 2011). Overall, it should be noted that bottom friction across the entire platform represents approximately 50 and 42 % of the total wave energy dissipation in fair weather and storm wave conditions respectively (Fig. 6.10-g and 6.10-h). The latter represents significant dissipation effects as the total wave energy dissipated under storm wave conditions is large. In their analysis, *Poate et al.* (2018) found that bottom friction is negligible in the surf zone of these environments, being only important outside the surf zone for very rough, low-gradient platforms, during small wave conditions. Hence, they suggested that for the majority of Type A platforms, bottom friction could be discarded when investigating short wave transformation on shore platforms. While the dominance of wave breaking dissipation in the surf zone is also observed in the present study, high frictional dissipation occurs in the subtidal part of the platform during storm wave conditions which significantly decreases wave height before wave breaking. This notable effect of platform roughness on wave dissipation was not reported by *Poate et al.* (2018), as they instrumented intertidal shore platforms only. In addition to bottom friction, the complex nearshore bathymetry can enhance shallow-water processes such as refraction and diffraction (*Stephenson and Kirk*, 2000b; *Marshall and Stephenson*, 2011; *Kowalczyk*, 2016), which also control wave energy that reaches the intertidal zone of the platform.

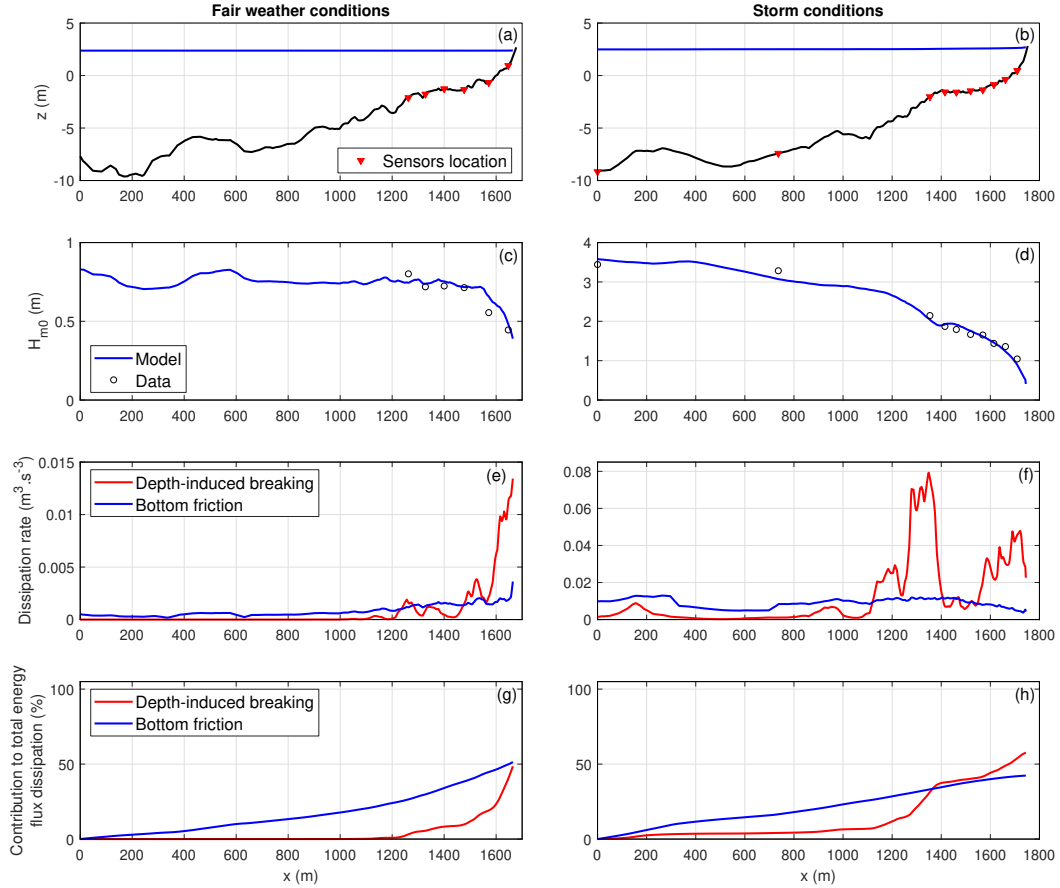


FIGURE 6.10 – Water levels (a,b), H_{m0} (c,d), rates of wave energy dissipation by depth-induced breaking and bottom friction normalized by the water density (e,f) and their contribution to total wave energy flux dissipation (g,h) along the transect from the subtidal to the intertidal zone, in fair weather and storm wave conditions. The instrumented profiles during the two field campaigns were not exactly the same (200 m spacing), explaining the differences observed in the bathymetry (black lines in (a) and (b)).

6.5.3 Effect of the wave-induced circulation on wave setup

Several studies showed that the wave setup near the shoreline does not only result from wave dissipation but can also be increased by the wave-driven, depth-varying circulation in the surf zone of sandy beaches (Apotsos *et al.*, 2007; Guérin *et al.*, 2018) or alongshore-uniform fringing reefs (Buckley *et al.*, 2016). On sandy beaches, Guérin *et al.* (2018) suggested that the wave-driven circulation could have a larger contribution to the wave setup when the bottom slope increases. A similar trend is expected to occur on shore platforms, although the presence of a rougher bottom could result in substantial differences compared to the mechanisms identified by Guérin *et al.* (2018). To investigate this process, the wave setup obtained with our 3D baseline model is first compared to the one obtained with a 2DH simulation using the radiation-stress formalism of Longuet-Higgins and Stewart (1964), which does not represent the depth-varying circulation induced by waves (Fig. 6.11). To perform a consistent comparison between 3D and 2DH simulations, the bottom drag coefficient is computed similarly using the formulation of Bretschneider *et al.* (1986) as in Zheng *et al.* (2013). The comparison reveals that the wave setup predictions are improved with the 3D simulation with a RMSE reduced by 26 % and up to 30 % for values of wave

setup superior to the 90th percentile (Fig. 6.11). These results suggest a non-negligible contribution of the wave-induced circulation to the wave setup.

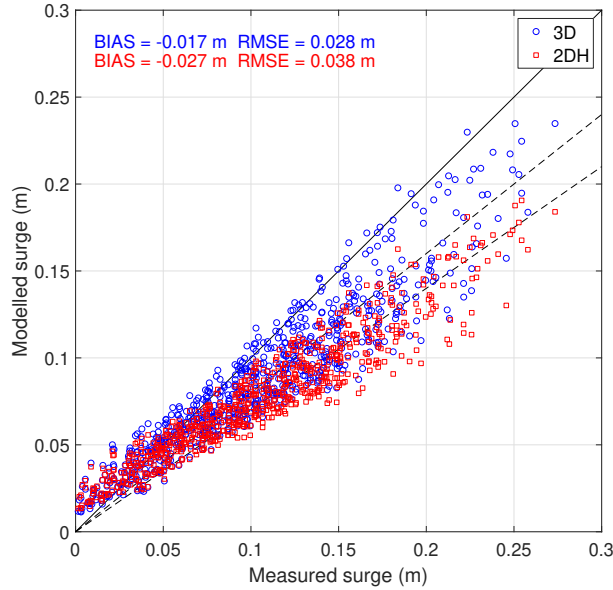


FIGURE 6.11 – Observed against modelled surges with a 3D (blue circles) and a 2DH simulation (red squares). The dashed lines correspond to the 0.8:1 and 0.7:1 lines.

To understand the underlying mechanisms of this contribution, an analysis of the 3D cross-shore momentum balance is conducted. The complex topography (i.e. subtidal rocky shoals and alongshore non-uniformity of the bathymetry, see cross-shore transects of Fig. 6.10) of our study site induces locally strong longshore advection that can contribute to the wave setup and which are represented in both the 2DH and 3D simulations. To discard these effects unrelated to 2DH/3D differences and also the non-stationnarity of the wave, tide and wind forcings, we apply the 3D model to idealised cases with an alongshore uniform bathymetry. Six simulations are performed with three different constant slopes of 1:200, 1:50 and 1:20 and two different bottom types, a sandy beach and a rock platform (hereafter SB and RP respectively), such that the influence of both the gradient and nature of the bottom can be analysed. The SB is characterized by a z_0^{bot} of 0.0001 m in the hydrodynamic model and a k_n of 0.05 m in the Madsen's formulation in the wave model while the RP is represented with the parameters of our real case ($z_0^{bot} = 0.02$ m and $k_n = 0.13$ m). Wave dissipation by depth-induced breaking is also calculated with *van der Westhuysen* (2010). The grid resolution ranges from 15 m at the open boundary to 2 m at the shoreline. A JONSWAP spectrum is prescribed at the ocean boundary, characterized by shore-normal incident waves of significant wave height of 3 m and peak period of 13 s. Tidal and atmospheric forcings are turned off. Under steady state, the wave setup is balanced by the following depth-integrated terms in the cross-shore momentum equation :

$$g \frac{\partial \bar{\eta}}{\partial x} = \frac{1}{h} \int_{-d}^{\bar{\eta}} \left(-\hat{u} \frac{\partial \hat{u}}{\partial x} - \hat{v} \frac{\partial \hat{u}}{\partial y} - \hat{w} \frac{\partial \hat{u}}{\partial z} + \frac{\partial}{\partial z} \left(\nu \frac{\partial \hat{u}}{\partial z} \right) + F_{w,x} \right) dz \quad (6.1)$$

where $\bar{\eta}$ is the mean free surface elevation and $F_{w,x}$ is the cross-shore component of the wave forces (see Eq. 3.41). Following the methodology of *Guérin et al.* (2018), the analysis is carried out by computing the contribution of each right-hand side (hereafter RHS) term

of Eq. 6.1 to the wave setup along a cross-shore profile from a water depth of 35 m to the shoreline (Fig. 6.12). On this figure, $\bar{\eta}_{\hat{u}}$, $\bar{\eta}_{\hat{w}}$, $\bar{\eta}_{\nu}$ correspond to the contribution of the terms associated with the wave-induced circulation, which are the horizontal (cross-shore) advection, the vertical advection and the vertical viscosity terms respectively. $\bar{\eta}_{wf}$ is the contribution of the wave forces term. One should note that the contribution of the alongshore advection term ($\bar{\eta}_{\hat{v}}$) is nil as waves are shore-normal. In Figure 6.12, the sum of the contribution of the RHS terms of Eq. 6.1, $\bar{\eta}_{\hat{u}+\hat{w}+\nu+wf}$, compares well with the wave setup obtained from the model, $\bar{\eta}_{model}$, which shows that our momentum balance is accurately closed.

For all the simulations, wave forces are the main contributors to the wave setup, with $\bar{\eta}_{wf}$ representing between 74 % and 92 % of the total wave setup $\bar{\eta}_{\hat{u}+\hat{w}+\nu+wf}$ (Fig. 6.12). On both bottom types, the absolute value of the wave setup due to wave forces increases with the slope while their relative contribution decreases in favour to the terms associated with the wave-induced circulation. Among these terms, the vertical advection term becomes dominant for steeper SB, accounting for 15% of the wave setup for a 1:20 slope ($\bar{\eta}_{\hat{w}}$, Fig. 6.12-a, -c and -e). Note that *Guérin et al.* (2018) found a larger contribution of horizontal advection to wave setup, but these authors employed a simpler parameterization for vertical mixing, which results in more sheared currents and hence, a larger horizontal advection compared to the present study. For RP, the vertical viscosity term contributes the most to the wave setup (after wave forces), with larger importance as the slope steepens, reaching up to 16 % on the 1:20 slope ($\bar{\eta}_{\nu}$, Fig. 6.12-b, -d and -f). Regarding the differences between SB and RP, one can note that for a given slope, the contribution of the vertical advection term $\bar{\eta}_{\hat{w}}$ is more important for SB than RP, which is explained by a higher (negative) vertical velocity in the surf zone of SB. In addition, the maximum of the undertow on RP is reached higher in the water column than on SB. As vertical gradients of the cross-shore velocity are negative from the bottom up to this point, the contribution of the depth-integrated vertical advection term to the wave setup is reduced for RP. Conversely, the vertical viscosity term appears to be more relevant on RP than on SB for a given slope. The increased bottom roughness z_0^{bot} modifies the vertical profile of the eddy viscosity and the vertical gradient of the cross-shore velocity in the lower part of the water column, which yields a greater contribution of the vertical viscosity term ($\bar{\eta}_{\nu}$).

Overall, the wave-induced circulation increasingly contributes to the wave setup with the slope, accounting for 20 % for 1:20 sloping SB, which is in line with the results of *Guérin et al.* (2018), and up to 26 % for 1:20 sloping RP. Therefore, this analysis reveals that a higher roughness enhances the contribution of the wave-induced circulation to the wave setup (mainly through the vertical viscosity term). Contrarily, wave dissipation by friction reduces the wave height before depth-induced breaking, resulting in a weaker wave setup due to wave forces for RP than SB of 1:200 slope, with $\bar{\eta}_{wf} = 15.2$ and 13.6 cm respectively (Fig. 6.12-a and -b). As the slope increases, less wave energy is dissipated by friction prior to wave breaking, yielding a comparable contribution of wave forces to wave setup for SB and RP.

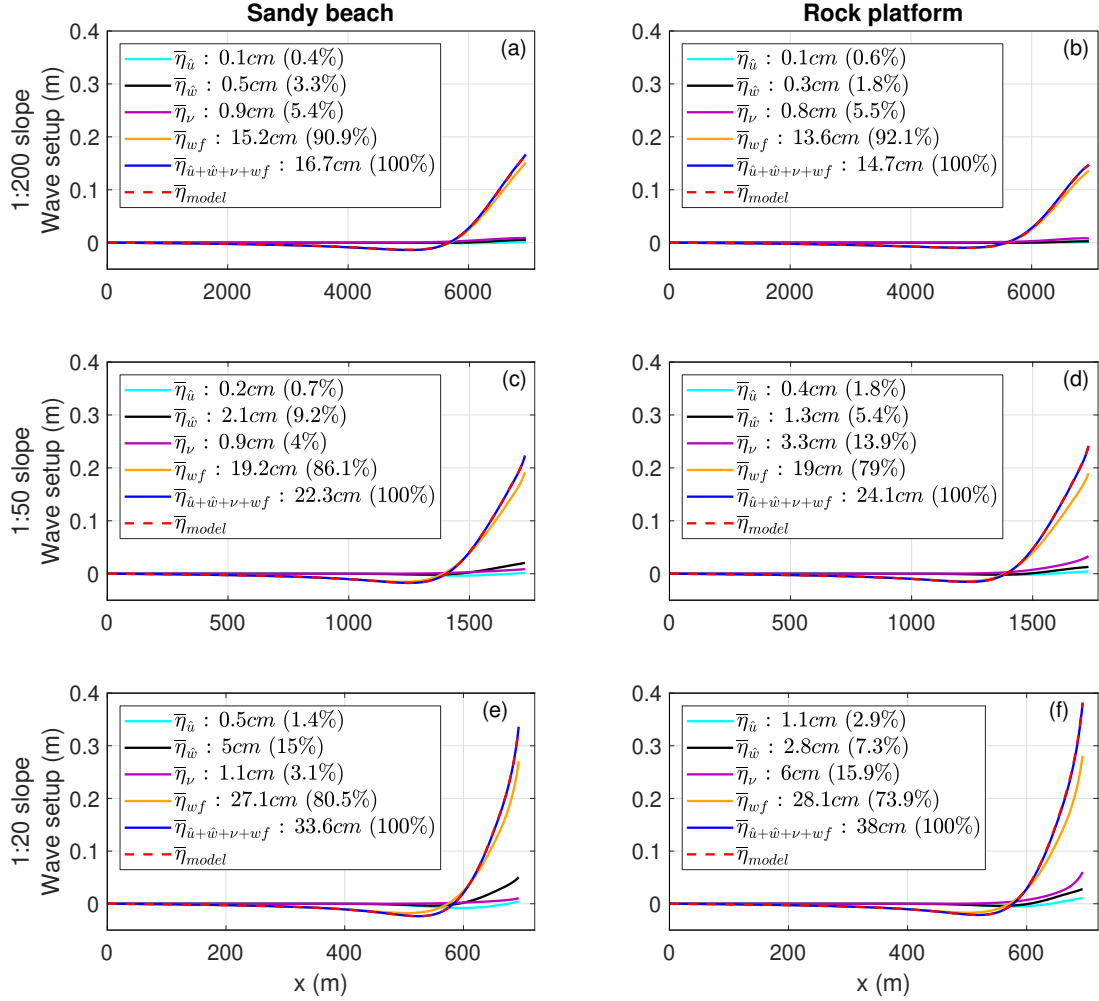


FIGURE 6.12 – Contribution of each right-hand side terms of Eq. 6.1 to the wave setup ($\bar{\eta}_{\hat{u}}$, $\bar{\eta}_{\hat{w}}$, $\bar{\eta}_{\nu}$ and $\bar{\eta}_{wf}$), total contribution of these terms ($\bar{\eta}_{\hat{u}+\hat{w}+\nu+wf}$), compared to the wave setup obtained from the model ($\bar{\eta}_{model}$), on a sandy beach and on a rock platform for 1:200, 1:50 and 1:20 slopes.

In conclusion to this analysis, the roughness of the shore platform influences wave setup dynamics through two opposing mechanisms : (1) wave frictional effects prior to breaking reduce the wave setup and (2) the wave-induced circulation increases the wave setup, this process being enhanced by interactions with a rough bottom. These two counteracting effects of platform roughness on the wave setup corroborate the results of *Buckley et al.* (2016) on fringing reefs. Process (1) appears to be dominant on gently-sloping rock platforms, as shown by the smaller wave setup for RP than SB of 1:200 slope (Comparison of $\bar{\eta}_{\hat{u}+\hat{w}+\nu+wf}$ between Fig. 6.12-a and -b). As the slope steepens, the effect of process (1) is reduced and that of process (2) increases, the latter becomes hence predominant over process (1), which leads to a larger wave setup for RP than SB (Comparison of $\bar{\eta}_{\hat{u}+\hat{w}+\nu+wf}$ between Fig. 6.12-e and -f). However, depending on the environment, its geometry, roughness magnitude and distribution, the contribution and relative importance of these processes can be different, as discussed by *Buckley et al.* (2016) and *Rijnsdorp et al.* (2021) for reef environments.

6.6 Conclusion

This study investigated the role of bed roughness on wave dissipation, mean circulation, and wave setup dynamics on a gently-sloping shore platform. Two field experiments were conducted under fair weather and storm wave conditions. Data analysis was complemented with numerical simulations conducted with the fully-coupled modelling system SCHISM with the vortex force formalism to represent the effects of short waves on the mean circulation. The results showed first that a bottom friction formulation that accounts for the bottom roughness of the platform is required to adequately model associated frictional effects. The correct representation of wave bottom friction, together with the adaptive depth-induced breaking formulation of *Pezerat et al. (2021)*, led to quite accurate wave and wave setup predictions at the coast. Further analysis conducted on the relative contribution of depth-induced breaking to wave bottom friction revealed that wave breaking is dominant in the surf zone, but frictional effects that occur from the subtidal zone account for 50 % and 42 % of the total wave energy dissipation in fair weather and storm wave conditions respectively. As an important effect, wave bottom friction decreases wave height before breaking, which in turn reduces the wave setup (mechanism 1). Conversely, an analysis of the cross-shore momentum balance on idealised rock platforms and sandy beaches revealed that the contribution of the wave-induced depth-varying circulation to the wave setup is enhanced over rough bottoms (mechanism 2), explaining up to 26 % of the wave setup at the shoreline of 1:20 sloping shore platforms (mechanism 2). While mechanism 1 appears dominant over mechanism 2 on gently-sloping shore platforms, a steeper slope would induce less wave frictional dissipation before breaking and a larger contribution of the depth-varying circulation to the wave setup, resulting in an increased wave setup compared to a sandy beach.

This study provides new insights into waves, currents and wave setup dynamics on shore platforms. Although wave transformation processes and the associated circulation were well predicted overall, further research is needed to better understand the contribution of the bottom streaming to the surf zone mean circulation and to verify the vertical distribution of the associated acceleration. This will imply new field experiments on shore platforms with high-resolution velocity measurements at several positions in the water column. In addition, the processes affecting wave setup dynamics on shore platforms highlighted in this study, in particular the contribution of the wave-induced circulation to the wave setup, will have to be verified on steeper shore platforms.

Chapitre 7

Wave dissipation and mean circulation on a salt marsh

7.1 Introduction

The combined effects of climate change and increasing anthropic pressure on the coasts stress the urgent need for adapting current coastal protection strategies. While the cost and environmental impact of hard engineering solutions is expected to become locally unsustainable (*Bulleri and Chapman, 2010; Hinkel et al., 2014*), nature-based solutions are progressively identified as alternative or complementary solutions to address disaster risk reduction (*Morris et al., 2018*). In particular, vegetation developing in coastal zones have received a growing attention owing to their natural ability in mitigating coastal hazards (*Duarte et al., 2013; Leonardi et al., 2018*). Aquatic vegetation in the coastal zone such as salt marshes, seagrass, kelp or mangroves, can efficiently dissipate wave energy (e.g., *Knutson et al., 1982; Fonseca and Cahalan, 1992; Quartel et al., 2007; Dubi and Tørum, 1995; Möller et al., 1999*), and reduce wind-induced storm surges (e.g., *Loder et al., 2009; Wamsley et al., 2010; Sheng et al., 2012; Temmerman et al., 2012*) and mean flow velocities (e.g., *Shi et al., 1995; Nepf, 1999*). The latter process promotes sedimentation and retention of suspended sediments, thereby limiting coastal erosion (*Gacia and Duarte, 2001; Madsen et al., 2001; Le Hir et al., 2007; Van der Wal et al., 2008*) and providing adaptation to sea level rise (*French, 1993; Duarte et al., 2013*). In addition to their mitigation capacities, these ecosystems provide cobenefits, including water quality improvements, fishery habitat and carbon sequestration and storage (*Barbier et al., 2011*).

The attenuation of waves by aquatic vegetation has been investigated through several field and laboratory experiments, with a particularly active research on salt marshes. In these ecosystems, significant attention has been paid to the *Spartina* plant community, which is widely developed in the upper part of the intertidal zones along the Atlantic coast of the USA and Western Europe (*Jackson et al., 1985*). Hydrodynamic conditions such as water depth, wave height and period along with wave-current interactions have been demonstrated to have a determinant role on the capacity of the intertidal vegetation in dissipating wave energy. In addition, energy dissipation rate has been observed to vary with plant characteristics such as density, stiffness, height and spatial configuration, which are in turn often controlled by seasonal cycles (*Möller and Spencer, 2002; Lambert, 2009; Paul and Amos, 2011*) and local hydrodynamics (*Mork, 1996; Koehl, 2015*). While a few of the experiments conducted on wave-vegetation interactions have been conducted in the field (e.g.,

Möller *et al.*, 1999; Yang *et al.*, 2012; Jadhav *et al.*, 2013; Garzon *et al.*, 2019), the majority are based on laboratory measurements with vegetation mimics (e.g., Dubi and Tørum, 1995; Løvås and Tørum, 2001; Augustin *et al.*, 2009; Anderson and Smith, 2014; Wu and Cox, 2015). Yet, one can question up to which extent the conclusions based on these lab experiments are valid in realistic physical conditions. A first limitation resides in the use of vegetation mimics, which cannot realistically reproduce the plant morphology and its mechanical behaviour (Lara *et al.*, 2016; Maza *et al.*, 2015). In addition, many studies have been performed in either current conditions (e.g., Bouma *et al.*, 2013) or waves (e.g., Möller *et al.*, 2014), while aquatic vegetation such as salt marshes are exposed to their concomitant actions. In an attempt to address these shortcomings, some laboratory studies used real vegetation such as Möller *et al.* (2014) or Maza *et al.* (2015). The latter authors grew *Spartina anglica* and *Puccinellia maritima* and examined wave-current-vegetation interactions in an large scale experimental basin. Among their findings, the authors reported that higher vegetation stiffness, density and biomass increase dissipation rates. While such hybrid approaches (i.e. true vegetation in the lab) substantially contributed to advance the understanding of vegetation-hydrodynamic interactions, they were conducted under small waves and do not reproduce the spatial variability in plant characteristics of a real salt marsh (Garzon *et al.*, 2019). Nevertheless, field and particularly laboratory measurements have been used to support the development of numerical models necessary to further represent the dynamics between waves and vegetation.

While several studies successfully represented wave energy damping by vegetation in terms of an equivalent bottom roughness (e.g., Bradley and Houser, 2009; Paul and Amos, 2011), early pioneering studies have developed analytical models with a more physically-based approach to predict wave dissipation across a submerged vegetation field (Dalrymple *et al.*, 1984; Dubi and Tørum, 1997; Kobayashi *et al.*, 1993; Mendez *et al.*, 1999). The widely-used formulation of Dalrymple *et al.* (1984) is based on the determination of the wave energy losses owing to the work done by the drag force on a field of rigid cylinders, assuming linear wave theory and monochromatic waves propagating over a flat bottom. Mendez and Losada (2004) extended the approach of Dalrymple *et al.* (1984) to account for irregular breaking and non-breaking waves and bottom slope variations. Based on the calibration and validation of their model on the flume experiments of Dubi and Tørum (1997) for non-breaking waves and by Løvås and Tørum (2001) for breaking waves, they found that the bulk drag coefficient \tilde{C}_{dv} is inversely related to the local Keulegan–Carpenter number for a specific type of plant (Eq. 3.29). The parameterisation of Mendez and Losada (2004) has been implemented in phase-averaged models such as Xbeach surf-beat (van Rooijen *et al.*, 2016), TOMAWAC (Bacchi *et al.*, 2014), CMS-Wave (Wu, 2014) and SWAN (Suzuki *et al.*, 2012), the latter including a vertical layer schematization of the vegetation. However, only a few studies have analysed the effect of the vegetation on a combined wave-current fields through fully-coupled wave-current modelling systems (Wu, 2014; Beudin *et al.*, 2017). Alternatively, several phase-resolving models have been developed or extended to account for the effects of the vegetation, such as the model of Li and Yan (2007) based on the RANS equations, COULWAVE (Augustin *et al.*, 2009), NHWAVE (Ma *et al.*, 2013), XBeach non-hydrostatic (van Rooijen *et al.*, 2016) or SWASH (Suzuki *et al.*, 2019). Phase-resolving models allow to study in details the wave field and the velocity structure at the intra-wave scale, but are more computationally expensive than phase-averaged models. Most of the existing models, either phase-resolving or phase-averaged models, are based on the assumption of a rigid vegetation. Yet, the plant flexibility implies a more complex wave attenuation process, which led to the development of methods and models that accounts for it (Abdelrhman, 2007; Mullarney and Henderson, 2010; Yin *et al.*, 2021). Some studies

have shown that a flexible vegetation can reduce its potential to dampen waves compared to a more rigid canopy (*Riffe et al.*, 2011; *Paul et al.*, 2016; *van Veelen et al.*, 2020). For instance, *van Veelen et al.* (2020) found that wave dissipation by flexible vegetation is up to 70% less than by rigid vegetation.

While the direct effect of the vegetation on waves is now well recognized, additional complex wave-vegetation interactions changing the dynamics of the wave setup have been more recently identified. *Dean and Bender* (2006) showed theoretically that the wave setup can be reduced in case of emergent vegetation and/or non-linear waves propagating in a vegetation field. This process and other mechanisms through which the vegetation can affect the wave setup, are described in details by *van Rooijen et al.* (2016) :

1. In the coastal zone, the vegetation dissipates wave energy from relative deep water, which tends to decrease wave heights before breaking compared to a case without vegetation. Hence, similarly to wave bottom friction studied in the previous chapter, this decreases the contribution of wave forces to the wave setup, which is in turn reduced.
2. The presence of an undertow induces a net mean drag force acting on the plants, which causes an onshore-directed reaction acting on the water column. Similarly to the bottom stress generating by the interactions of the undertow with a rough bottom studied in the previous chapter, the mean drag force is expected to increase the wave setup.
3. The drag force exerted by waves on the plants causes a resulting vegetation force acting on the water column which reads (neglecting plant swaying and inertial forces) (*Morison et al.*, 1950; *Dalrymple et al.*, 1984) :

$$F_D = \frac{1}{2}\rho C_{dv} b_v N_v |u|u \quad (7.1)$$

where C_{dv} is the drag coefficient, b_v is the plant diameter, N_v is the vegetation density and u is the horizontal velocity in the vegetation region due to wave motion. Considering linear wave theory and fully submerged vegetation, Eq. 7.1 integrated over a wave period leads to a zero net force on the water column. However, in case of emergent vegetation, this net force is not nil since the height of the plant interacting with the water column varies over a wave cycle (*Dean and Bender*, 2006; *van Rooijen et al.*, 2016). This force is directed in the opposite direction of wave propagation and hence, tends to decrease the wave setup. The propagation of non linear, skewed waves in a vegetation field (even entirely submerged) leads to a similar effect on the wave setup. Indeed, in case of skewed waves, the orbital velocity under the wave crest is larger than under the wave trough, which results in an asymmetric profile of the vegetation drag force over a wave cycle (Eq. 7.1). Hence, the integration of the drag force over a wave period results in a non-zero net force that acts opposite to the wave direction and decreases the wave setup (*Dean and Bender*, 2006; *van Rooijen et al.*, 2016).

It should be noted that the relative contribution of these processes and their effects on the wave setup depend on the local environment, i.e. the topographic features such as the bottom slope and elevation, vegetation characteristics such as height and location, and incident conditions (water depth, wave height, bandwidth and period).

In their study, *van Rooijen et al.* (2016) compared numerical simulations conducted with XBeach surf-beat (that solves the wave action on the scale of wave groups) and XBeach non-hydrostatic (phase-resolving) with observations originating from experiments conducted in

wave flumes. While the effects on non-linear wave shape and emergent vegetation are directly accounted for in the phase-resolving model, they are accounted for with a wave shape model in surf beat mode. The authors found that the wave setup is overpredicted in surf beat mode when the wave shape model is not included, while the prediction is improved once accounted for. In line with *Dean and Bender (2006)*, this result showed that non-linear waves propagating in a vegetation field and/or emergent vegetation can decrease the mean water level through a reduction of the wave setup and can even cause a set-down. These important findings have yet to be confirmed in naturally-vegetated bottoms, where measurements of the effect of the vegetation on the wave setup are currently lacking.

Overall, laboratory studies provide quantifiable insights to the underlying mechanisms of wave energy dissipation by vegetation and more recently to wave setup dynamics, but the applicability of their outcomes in field conditions should be verified. In parallel, considerable efforts have been devoted to develop numerical models in order to reproduce and understand the effect of the vegetation on waves and currents. However, these models are rarely applied to field conditions, in particular phase-averaged models, while the latter are used for storm surge modelling in coastal areas and operational purposes. This study investigates wave dissipation by vegetation and wave setup dynamics on a cross-shore transect in the salt marsh of Moëze-Brouage (France) in moderate-energy wave conditions. This salt marsh comprises several plant species including *Halimione portulacoides*, which effect on waves has been rarely studied. Field data measurements collected in 2016 before this PhD thesis are analysed and used to test the ability of the modelling system SCHISM to reproduce wave transformation and wave setup dynamics in the vegetation field. The study area and the field campaign are first detailed in sections 7.2 and 7.3 respectively, followed by the description of the model implementation in section 7.4. The results are then presented in section 7.5, and discussed in section 7.6. This last section also exposes future perspectives considered in this research work.

7.2 Study area

The study area is the salt marsh of Brouage, located in the central part of the French Atlantic Coast in the Bay of Marennes-Oléron (Fig. 7.1). According to *Dodet et al. (2019)*, the tidal regime is semi-diurnal and macrotidal in the region, with a tidal range varying from 1.10 to 6.60 m. The salt marsh develops in the supratidal zone of the mudflat of Brouage, which is 4 km-wide for a total surface area of 42 km², with a mean slope of $\sim 1:800$ and tidal currents that reach ~ 0.3 and 0.5 m.s^{-1} during neap and spring tides respectively (*Le Hir et al., 2000*). Although the mudflat is protected from the action of Atlantic swell by the Oléron Island (Fig. 7.1) (*Bassoullet et al., 2000*), northwest winds can develop a fetch of several tens of kilometres which generates wind sea of significant wave height H_{m0} reaching up to 1 m (*Le Hir et al., 2000*). The salt marsh is composed of several plant species organized in successive floors, which are from the lower to the upper part of the salt marsh : *Spartina maritima*, *Puccinellia maritima*, *Halimione portulacoides* and *Suaeda maritima* (Fig. 7.2).

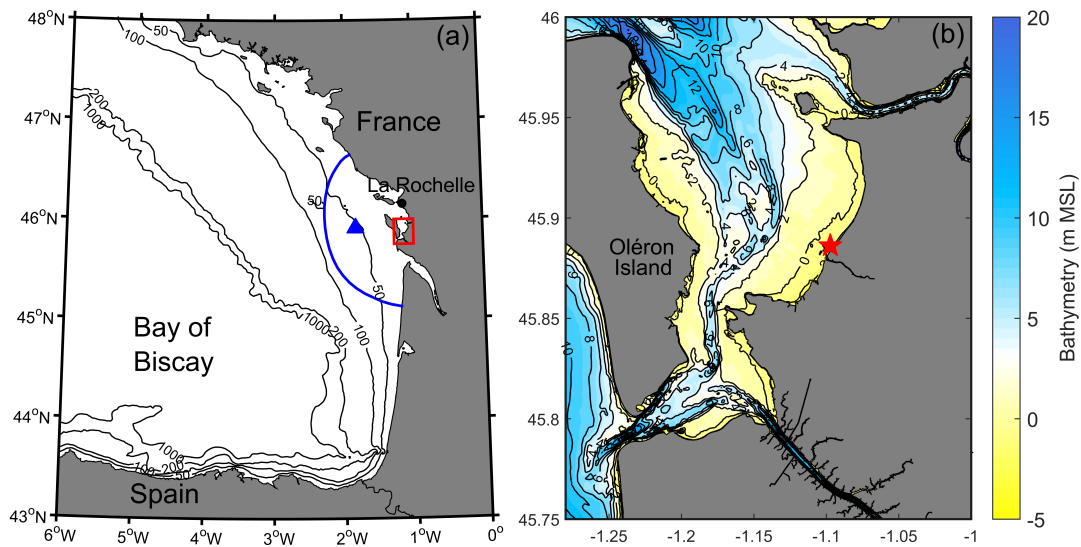


FIGURE 7.1 – (a) Location of the study area in the Bay of Biscay (red square), open boundary of the computational grid (blue line) and Oléron buoy (blue triangle). (b) Study area with location of the studied transect on the salt marsh of Brouage (red star).

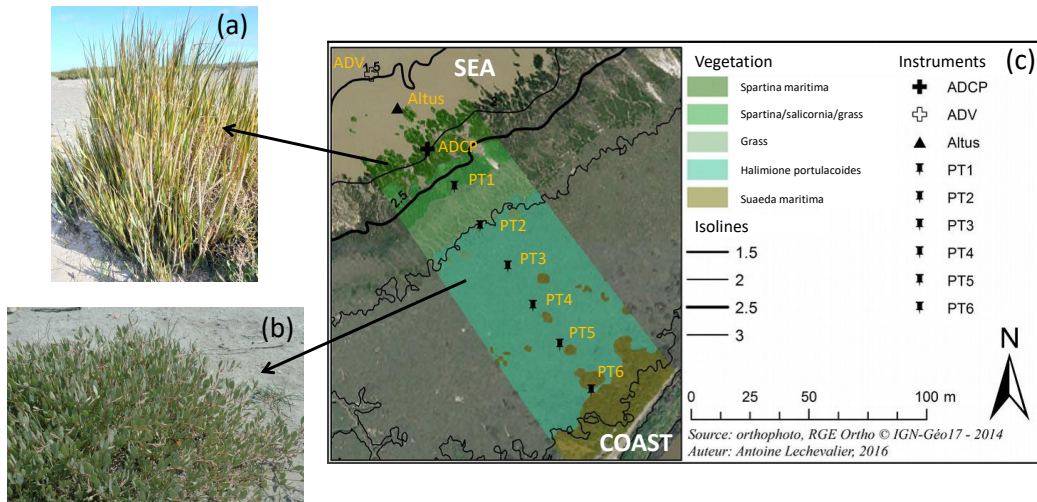


FIGURE 7.2 – Photos of (a) *Spartina maritima* and (b) *Halimione portulacoides*. (c) Location of the sensors and plant species along the cross-shore transect.

7.3 Field campaign

The field campaign was conducted from March 8 to 11 2016 during spring tides. On the 9th during the high tide of the afternoon, northwest winds with a sustained wind speed up to 17 m.s^{-1} (and wind gusts up to 24 m.s^{-1}) induced the development of a wind sea with a maximum H_{m0} of 0.65 m on the study area (Fig. 7.3).

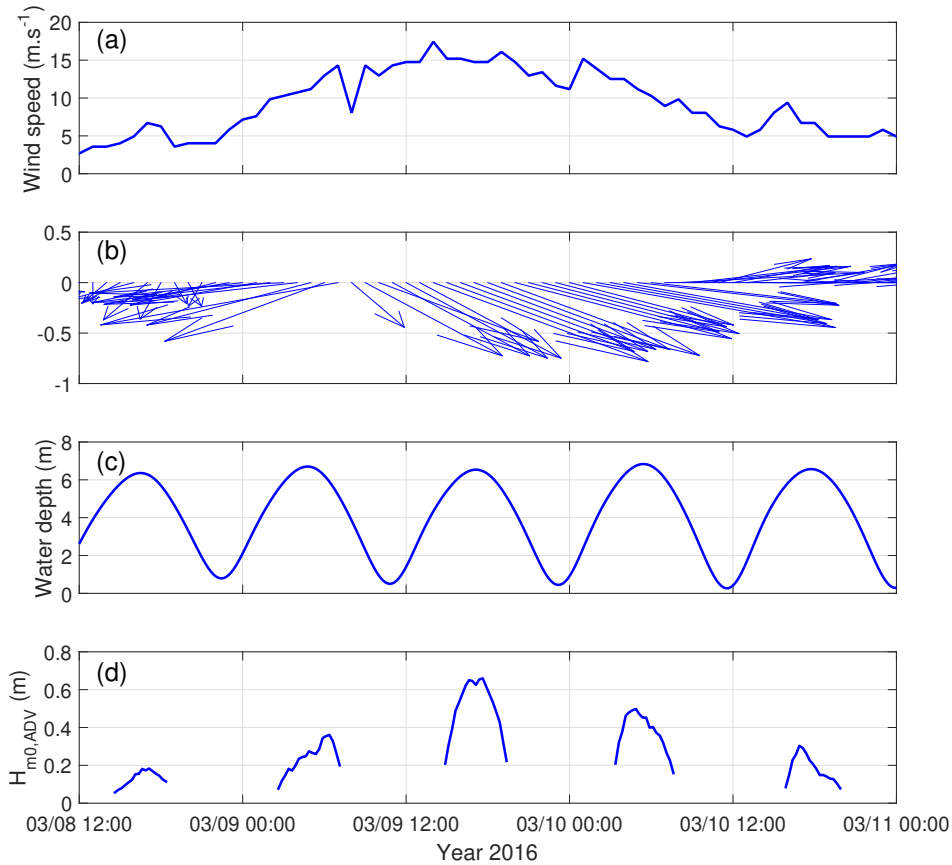


FIGURE 7.3 – (a) Wind speed, (b) wind direction, (c) tides at the nearby tide gauge of Aix Island and (d) significant wave height at the ADV.

A 160 m-long cross-shore transect with a mean slope of 1:125 was instrumented with an altimeter (ALTUS), 6 pressure transducers (PT) measuring at 4 Hz, a 6 MHz ADV and a 2 MHz ADCP, both equipped with internal PTs measuring at 16 and 2 Hz respectively. The instruments were placed at 20 m intervals (Fig. 7.2-c). The PTs were positioned in stainless steel tubes, which were vertically buried 0.80 m deep (Fig. 7.4-b), while the ADV and ADCP were disposed on stainless steel structures screwed into the soil (Fig. 7.4-a). Unfortunately, the first pressure sensor PT 1 stopped recording at 05:00 pm on March 09. A GNSS receiver was used to survey the cross-shore transect and measure the position of each sensor. Note that this field campaign was carried out in 2016, in the scope of the Master2 internship of Antoine Lechevalier supervised by Xavier Bertin. A new field campaign should have been conducted on the salt marsh during this thesis, which is discussed at the end of this chapter (section 7.6).

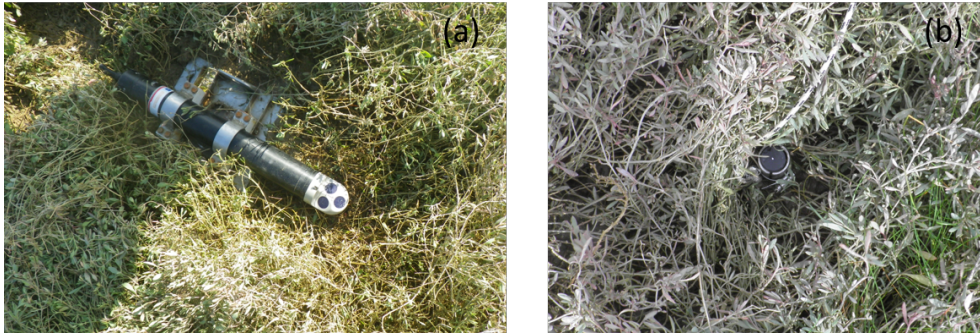


FIGURE 7.4 – Deployment of (a) the ADCP and (b) a pressure sensor on the cross-shore transect (credits : Antoine Lechevalier).

Bottom pressure measurements are analysed following the procedure described in section 4.2.3.5. The reconstruction method of the free surface the most adapted for this application is the TFM. Indeed, preliminary data analysis indicates dispersive conditions, which does not allow to apply the non-linear weakly-dispersive method of *Bonneton et al.* (2018). Accounting for non-linear effects, which can effectively occur under strong wind seas (*Mitsuyasu et al.*, 1979), could be considered through the non-linear fully-dispersive method of *Martins et al.* (2021b). However, the application of this method requires the knowledge of the dominant wavenumber spectra of the wave field, which is not the case here. At this time, the approach used by the authors to approximate the dominant wavenumber spectra when the latter are not available is based on Boussinesq theory (*Herbers et al.*, 2002), whose assumptions are not respected here (see the end of section 4.2.3.6). This explains why we retained the TFM in this application. A visual inspection of the spectra calculated with the TFM showed that it blows up above 0.5 Hz, this frequency is thus defined as the cut-off. The cut-off frequency between infragravity and short waves is set to 0.04 Hz.

An issue that we particularly faced here is the instrument noise. As it will be shown later, energy levels on the second half part of the transect were very low. In high frequencies, they can be hardly distinguished with the noise floor, which was important with the NKE sensors used for this field experiment (Fig. 4.7). The uncertainties on the high-frequency part of the spectrum related to the use of the TFM and instrument noise are discussed in the perspectives of this study.

The PTs and the ADV were split into consecutive bursts of 15 min while bursts of 8 min 30 are considered for the ADCP. Hydrostatic surface elevation spectra were computed by averaging estimates from 13 Hanning-windowed segments overlapping by 50%. The TFM is then applied to account for non-hydrostatic effects. Note that the currents reached a maximum of $0.17 \text{ m}\cdot\text{s}^{-1}$ at the ADCP and were mostly longshore during the field campaign. Accounting for them in the linear dispersion relation resulted in minor difference in the wavenumber k (<6%) compared to the case where they are neglected. We thus do not consider currents in the dispersion relation since they were not measured at all sensors locations. The reconstructed sea surface elevation energy density spectra are used to compute the significant wave height H_{m0} and mean wave period T_{m02} . From PT 3 to PT 6, waves were less than 0.01 m during the whole field campaign. Since the resolution of the pressure sensors used during the field campaign did not allow to measure such small waves, the data from PT 3 to PT 6 are considered with low confidence but are still retained to show that waves were almost fully dissipated at these PTs.

7.4 Model implementation

In this study, wave dissipation along the transect has been simulated with the wave model WWM-II coupled to the hydrodynamic module of SCHISM. This study constitutes one of the first applications of SCHISM/WWM-II that simulates the effect of the vegetation on waves. In this context, the circulation model is used in a 2DH configuration and the wave forces are represented with the radiation stress formalism.

In WWM-II, the depth-induced breaking is computed according to the formulation of *Battjes and Janssen (1978)*. In this parameterization, the breaking index γ is adjusted to 0.55, after a sensitivity analysis conducted at the ADV, which is located outside the vegetation. The breaking coefficient B' is computed as a function of the local bottom slope (Eq. 3.19) following *Pezerat et al. (2021)*. Note that wave surface rollers are not accounted for in this application. The bottom friction is computed here with the JONSWAP formulation of *Hasselmann et al. (1973)* with a dissipation coefficient C_f of $0.038 \text{ m}^2 \cdot \text{s}^{-3}$. Preliminary sensitivity tests with the formulation of *Madsen et al. (1989)* indicate that a spatially-variable Nikuradse roughness length k_n is needed to account for the different bottom substrates in the model domain, and particularly the bottom nature of the mudflat. At this time, we use the JONSWAP formulation, while keeping in mind future simulations with Madsen's formulation.

Wave energy dissipation by vegetation is computed according to the formulation of *Mendez and Losada (2004)* (Eq. 3.25), which requires the definition of the plant height h_v , density N_v and diameter b_v . We consider in the model the two main species present over the salt marsh, that is *Spartina maritima* and *Halimione portulacoides*. *Spartina maritima* is located from $x = 30 \text{ m}$ to 75 m on the transect while *Halimione portulacoides* covers the region from $x = 75 \text{ m}$ to 160 m (Fig. 7.6-b). The characteristics of these plants have been measured in the field and are presented in Table 7.1. The drag coefficient \tilde{C}_{dv} has been computed as a function of the Keulegan Carpenter number following *Mendez and Losada (2004)* (Eq. 3.27). We applied here constant drag coefficients by considering the mean values obtained from this formulation, equal to 0.09 and 0.54 for *Spartina maritima* and *Halimione portulacoides* respectively.

	<i>Spartina maritima</i>	<i>Halimione portulacoides</i>
Height h_v (m)	0.27 ± 0.05	0.80 ± 0.20
Density N_v (plants.m ⁻²)	990 ± 10	680 ± 10
Diameter b_v (m)	0.032 ± 0.002	0.03 ± 0.01

TABLE 7.1 – Characteristics of the main plants along the cross-shore transect.

The hydrodynamic time step is fixed to 60 s while WWM-II is run every 600 s and uses implicit schemes for propagation and source term integration. The unstructured grid extends over the Pertuis Charentais area, with a spatial resolution ranges from 1300 m along the open boundary to 5 m in the study area (Fig. 7.1-a). The circulation model is forced at the open boundary by the 16 main tidal constituents linearly interpolated from the global tidal model FES 2014 (*Lyard et al., 2017*). Over the whole domain, the circulation model is forced with hourly 10 m wind speed and sea-level pressure fields from CFSR (*Saha et al., 2010*). The datasets are provided on a regular grid with a spatial resolution of 0.2° and 0.5° for the wind and the atmospheric pressure respectively. WWM-II is forced with CFSR wind fields over the whole domain and time series of directional wave spectra along its open boundary, which were computed from a regional application of the WaveWatch III

spectral wave model also forced with wind fields from CFSR.

7.5 Results

7.5.1 Incident wave conditions

Data analysis shows that the incident significant wave height H_{m0} at the ADV reached up to 0.65 m during the high tide on March 09 afternoon, with a mean wave period T_{m02} of 3-4 s. The model well reproduces the water depth, H_{m0} and T_{m02} with NRMSE of 10, 16 and 20% respectively (Fig. 7.5). These results also suggest that the model correctly captures the bi-modal sea state characterized by a North-West swell with a peak period of 11 s and H_{m0} of 5 m recorded at the Oléron wave buoy (see Fig. 7.1-a for its location), and a wind sea locally generated by North-West winds up to 17 m.s^{-1} . Note that these results show the good predictions of the incident wave conditions on the salt marsh but do not assess the ability of the model to reproduce wave dissipation by vegetation since the ADV is not yet located in the vegetation field (Fig. 7.2-c).

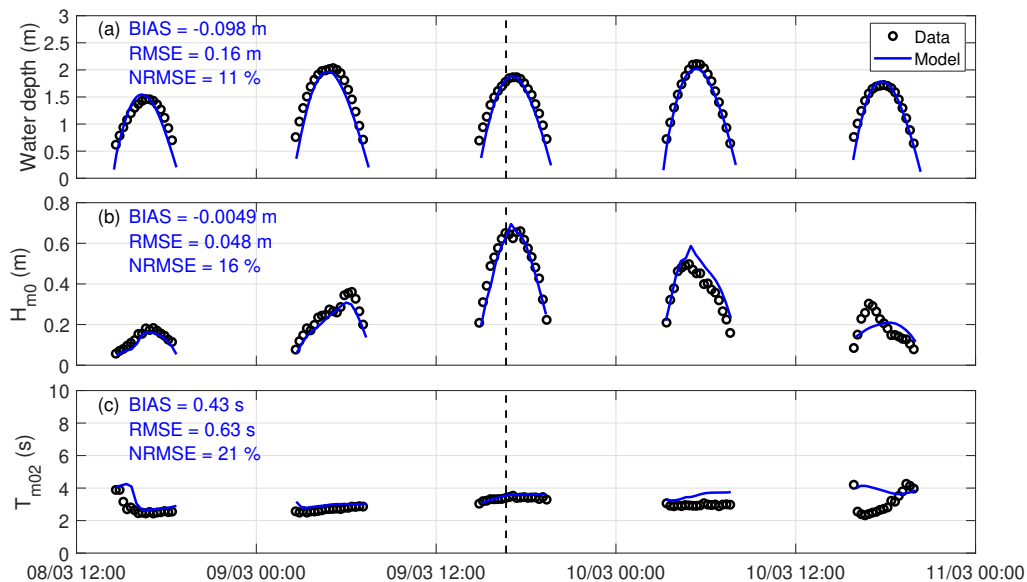


FIGURE 7.5 – Comparison between modelled and observed (a) water depth, (b) significant wave height H_{m0} and (c) mean wave period T_{m02} at the first sensor (ADV) on the studied transect. The black dashed line corresponds to the time of the time-series presented in Figure 7.6.

7.5.2 Wave transformation along the cross-shore transect

In order to analyse the effect of the vegetation on wave transformation along the transect, the model is run with (VEG), and without (NOVEG) wave dissipation by vegetation. Figure 7.6 shows the comparison between the observed wave height along the transect and the results from the simulations VEG and NOVEG at high tide on March 09 afternoon (the selected time step is slightly before high tide, which corresponds to the last burst recorded at PT 1). As it can be clearly seen, wave heights along the transect are well predicted when wave dissipation by vegetation is accounted for in the model with a RMSE of 0.045 m and a bias lower than 0.015 m. In contrast, when the vegetation source term is turned off, the predictions strongly deteriorate with a RMSE about 4 times higher and a bias of 0.14 m.

The contribution of wave dissipation by vegetation is examined by integrating the associated rate of wave energy dissipation along the cross-shore profile for this water depth conditions. This analysis reveals that vegetation effects represent 65% of the total wave energy dissipation from the ADV to the upper salt marsh edge. Note that the depth-induced breaking explains the remaining 35% of the dissipation, bottom friction and whitecapping contributions being almost nil.

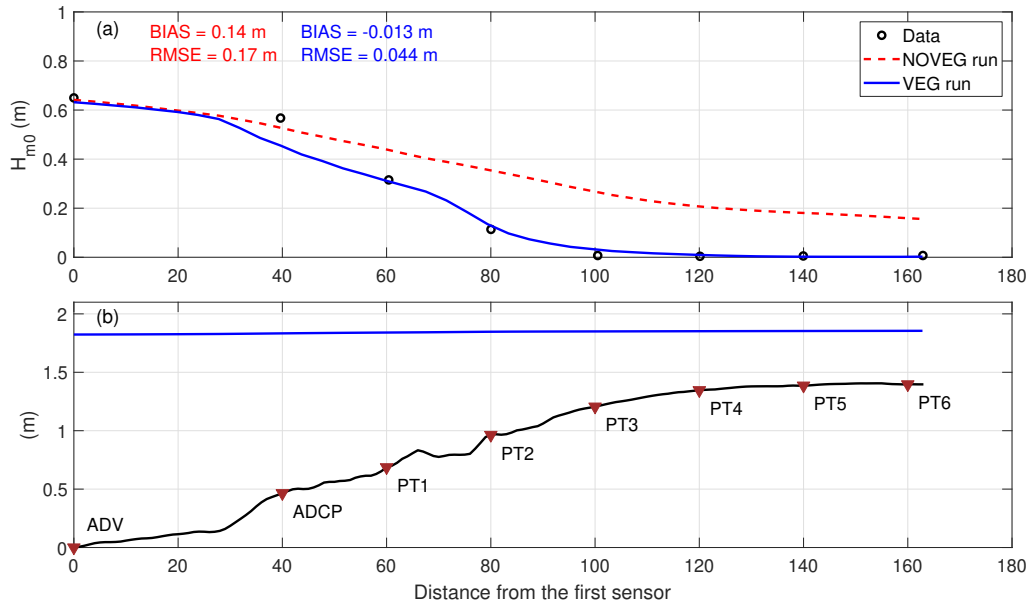


FIGURE 7.6 – (a) Comparison between observed and modelled significant wave height H_{m0} obtained from VEG (blue line) and NOVEG (red dashed line) simulations, along the studied transect during the high tide of March 09 afternoon. (b) Bathymetry (black line) and surface elevation (blue line) along the transect (both given relative to the topographic elevation of the first sensor). The water depth is computed as the difference between the blue and black lines along the transect.

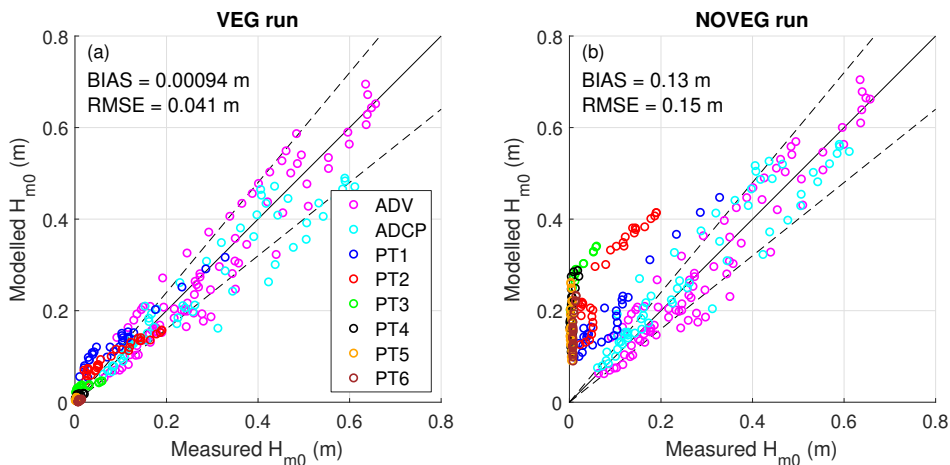


FIGURE 7.7 – (a) Measured against modelled wave height obtained from (a) VEG and (b) NOVEG simulations at all sensors during the entire experiment period. The dashed lines correspond to the 0.8:1 and 1.2:1 lines. The statistical errors at calculated at the ADCP and the PTs.

The comparison of measured and modelled wave height obtained from VEG and NOVEG simulations during the whole experiment are presented in Figure 7.7. Although the results

at all sensors are plotted, the statistical errors are only computed at the ADCP and the PTs, since the ADV is located outside the vegetation field. The NOVEG simulation yields a positive bias of 0.13 m and a RMSE of 0.15 m, while with the VEG simulation, the bias is almost cancelled out and the RMSE divided by 3. However, we can note a slight underestimation of the significant wave height at the ADCP with the NOVEG simulation, which worsens with the VEG simulation (Fig. 7.6 and Fig. 7.7).

7.5.3 Energy density spectra evolution along the cross-shore transect

We have considered so far mean quantities to evaluate the effect of the vegetation on the wave field. Further analyses are conducted by inspecting the evolution across the salt marsh of the observed wave spectra including in a period of 2 hours centered on the high tide of March 09 afternoon (Fig. 7.8). At the ADV and the ADCP, the peak frequency is located at 0.25 Hz. The evolution of the energy density spectra along the transect shows that losses of wave energy predominantly occur at the peak frequency at the ADCP, PT 1 and PT 2. For higher frequencies and at PTs located shoreward (PT 3 to 6), the PSD is too close to the level of noise of the sensors, which prevents from any reliable analysis. By the end of the transect, wave energy in the gravity band is almost fully dissipated while wave energy persists in the infragravity band ($f < 0.04$ Hz). The most important gravity energy loss occurs between PT 2 and PT 3 where energy levels decrease by 3 orders of magnitude.

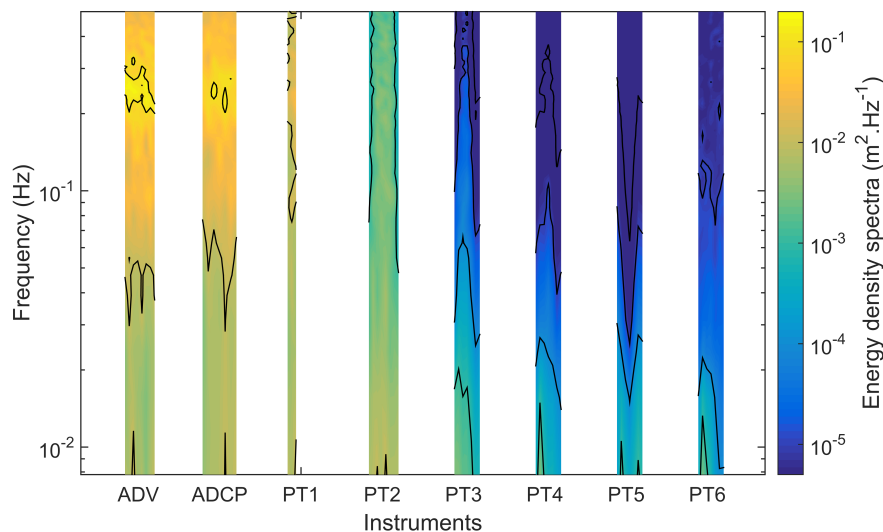


FIGURE 7.8 – Evolution of the measured energy density including in a period of 2 h hours centered on the high tide of March 09 afternoon. At PT 1, the spectra are truncated since the sensor stopped measuring at that time. The black lines correspond to a change in order of magnitude.

The model performance is now evaluated through a spectral comparison between measured and modelled energy density spectra from VEG and NOVEG simulations at a burst during this high tide (same time as Fig. 7.6). First, it is worth noting that the underestimation of the low-frequency part in the gravity wave spectra is related to the fact that the spectral model does not account for the energy in the infragravity frequency band. Both simulations VEG and NOVEG very well reproduce the incident bi-modal spectrum, characterized by a swell and wind-sea components with peak period of 11 s and 4 s respectively (Fig. 7.9-a). At the ADCP, both simulations underestimate the measured spectrum from 0.1 to 0.5 Hz

while the NOVEG gives slightly better results, in line with the bulk analysis (Fig. 7.9-b). Closer to shore however, the observed energy spectra are poorly predicted with the NOVEG simulation, with an increasing positive bias as waves propagate into the vegetation field (Fig. 7.9-c to d). While the VEG simulation globally better represents the evolution of the measured spectra, discrepancies can be noted among frequencies. At the ADCP, the VEG simulation underestimates the energy, particularly in the high frequency part of the spectrum between 0.4 and 0.5 Hz, which is also observed at PT 1 and PT 2. In contrast, the model overestimates the energy levels at the peak frequency (between ~ 0.2 and 0.3 Hz), by a factor of 5 at PT 2 and then over 2 orders of magnitude at the following sensors. In the model, wave dissipation by vegetation is computed according to the formulation of *Mendez and Losada* (2004), in which the action density is multiplied by a constant factor across all frequencies, this factor depending on the mean wavenumber and mean frequency. This could explain the limited skills of the model in representing the different dissipation rates among frequencies.

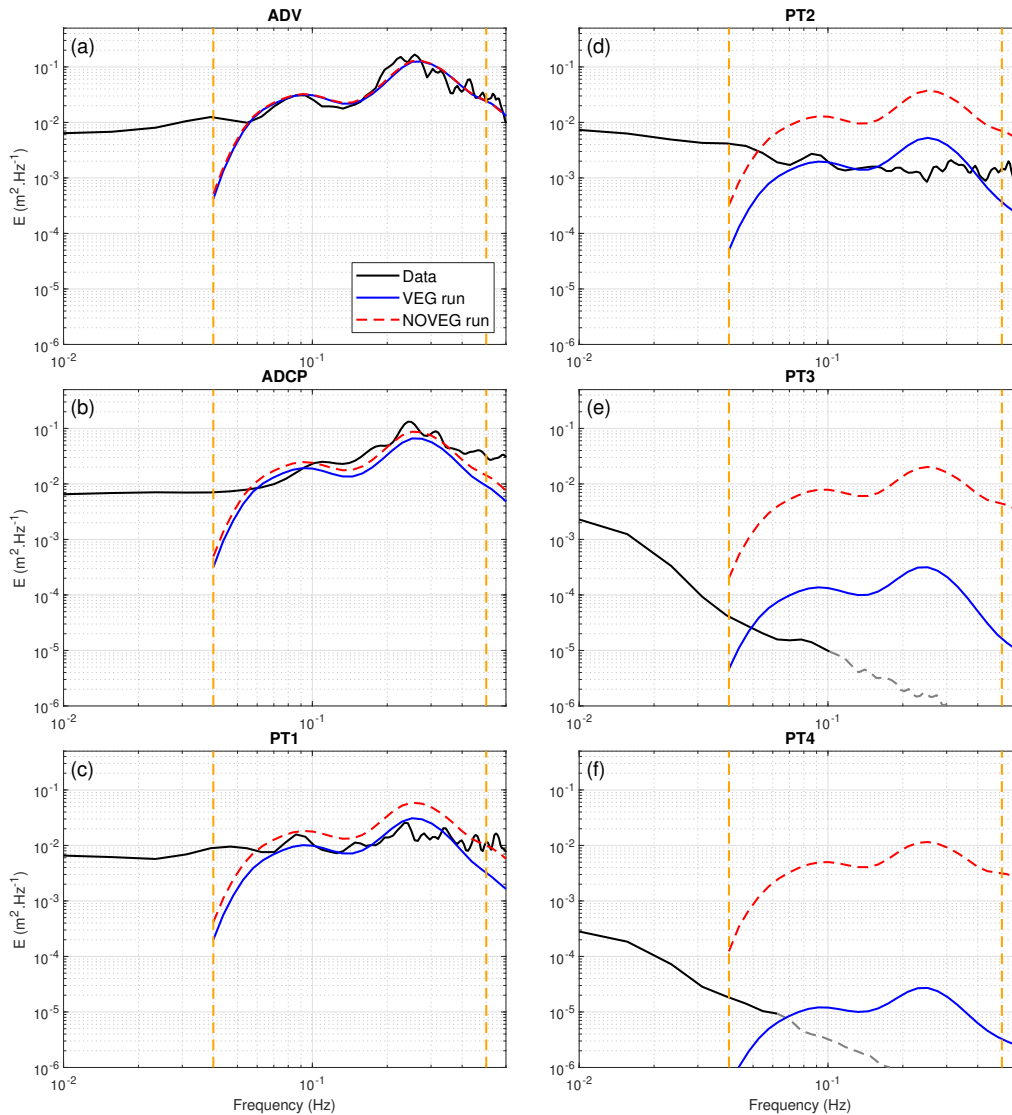


FIGURE 7.9 – Comparison between measured and modelled energy density spectra with VEG and NOVEG simulations (from the ADV to PT 4) at high tide on March 09 afternoon. The vertical orange dashed lines correspond to the cut-off frequencies. The grey curves in panels (e) and (f) indicate energy associated with instrument noise.

7.5.4 Water level predictions along the cross-shore transect

In this section, we examine the effect of the vegetation on the wave setup development in the nearshore. Similarly to the previous analysis, results from the VEG and NOVEG simulations are compared. However, they cannot be validated against wave setup observations. Indeed, variations in mean water levels on the transect were very small during the experiment (<0.05 m), such that they were close to the experimental uncertainty range (pressure sensors measurements and vertical referencing of the PTs). It was thus preferred to discard these observations. Alternatively, we use these numerical simulations (VEG and NOVEG) to examine the different effects that can have the vegetation on the wave setup. At this time, we focussed on the effect of wave dissipation on the wave setup, since wave assymetry and emergent vegetation effects being not yet accounted for in the model.

In the VEG simulation, the wave setup increases more rapidly than in the NOVEG simulation at $x = 30$ m, that is the beginning of the vegetation. However, at $x = 80$ m, the opposite occurs, and the wave setup becomes more important in the NOVEG simulation than in the VEG run at $x = 120$ m, resulting in a 30% higher wave setup in the NOVEG simulation. These differences are explained by the fact that waves start to be dissipated in deeper water in the VEG simulation, which causes the radiation stress gradients to be higher in deeper water and reduced in shallow water. As in the momentum equations, the radiation stress gradient term is inversely proportional to the water depth, the maximum wave setup along the shoreline is reduced. A similar effect has been observed on the rock platform, where the bottom friction reduces the wave height before breaking, which tends to reduce the wave setup.

The difference observed in the wave setup between the VEG and NOVEG simulations shows a relatively marginal effect of the vegetation on the wave setup. However, wave energy conditions were moderate during this field experiment. As the wave setup directly scaled with the incident wave energy, it is expected that the effect of vegetation could be more important in storm wave conditions.

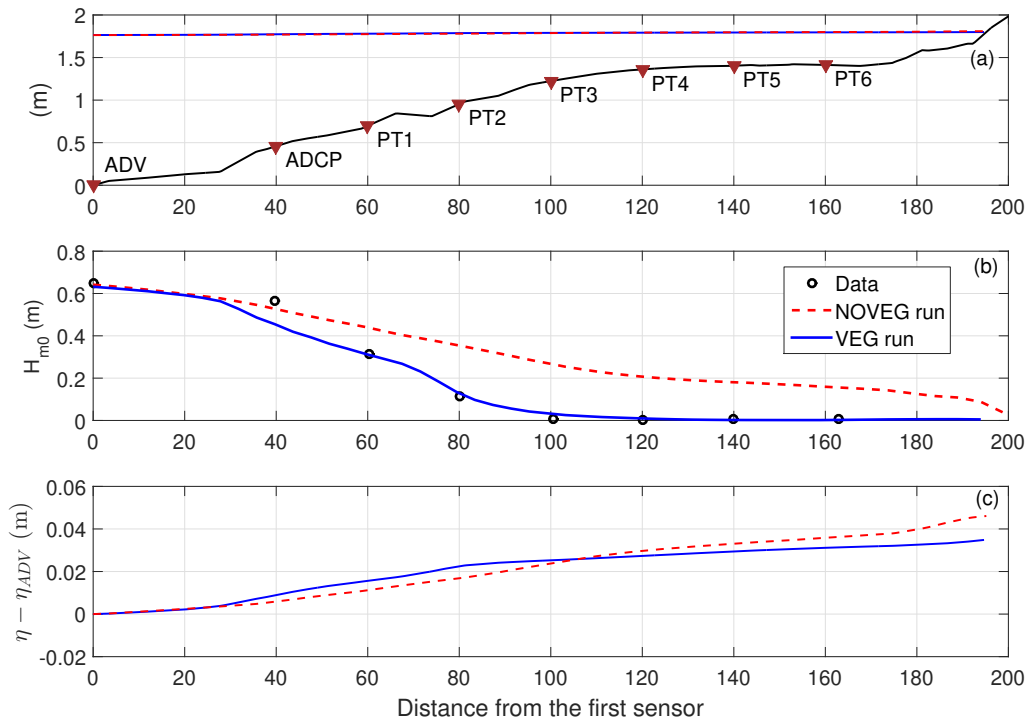


FIGURE 7.10 – (a) Topography (black line) and surface elevation (blue and red lines) along the transect (both given relative to the topographic elevation of the first sensor). The water depth is computed as the difference between the blue/red and black lines along the transect. (b) Observed and modelled significant wave height with VEG and NOVEG simulations. (c) Modelled wave setup that develops from the ADV, computed as the change in mean free surface elevations between the ADV and shoreward computational grid nodes.

7.6 Discussion and perspectives

7.6.1 Discussion

The comparison of the simulations with and without wave dissipation by vegetation clearly demonstrates that the wave dissipation cannot be solely attributed to depth-induced breaking. Indeed, vegetation damping effects represent 65% of the total wave energy dissipation along the transect at the studied high tide.

From the bulk parameters analysis, the model accounting for the vegetation shows quite good skills in predicting wave transformation along the transect. It can be noted however that the wave height at the ADCP is always underpredicted with underestimations up to 40% (Fig. 7.6 and Fig. 7.7-a). In the present model, the vegetation on the salt marsh has been represented by the two main plant species, with a spatially constant density for each along the transect. Yet, the density of *Spartina maritima* seems to be lower at the transition between the mud flat and the salt marsh (Fig. 7.2-c), that is few meters before the ADCP, which might explain the model negative bias at this sensor. Another simplification has been made by considering only the two main species that inhabit the salt marsh while there are several other plants. In a next stage of this research, it would be relevant to better account for the different plant species and their respective spatial variation.

If vegetation characteristics are available, the (bulk) drag coefficient \tilde{C}_{dv} is the only remaining parameter that needs to be calibrated in the wave dissipation by vegetation model of *Mendez and Losada* (2004). While \tilde{C}_{dv} is set to a constant value in the original formulation of *Dalrymple et al.* (1984), several authors developed different formulations to estimate realistic \tilde{C}_{dv} values. In that sense, processes that are neglected in the original formulation of *Dalrymple et al.* (1984) can be accounted for based on a physical approach. For instance, \tilde{C}_{dv} has been related to the local Keulegan-Carpenter number (K) (e.g., *Mendez and Losada*, 2004) or Reynolds number (e.g., *Augustin et al.*, 2009; *Lara et al.*, 2016) which allows to consider the variations of \tilde{C}_{dv} with hydrodynamic conditions. In our study, \tilde{C}_{dv} was estimated using the K number following *Mendez and Losada* (2004). For now, the mean value obtained from this relation was defined in the model. Nevertheless, the use of a variable drag coefficient based on the local K number computed in the model at each time step should be further tested. Also, approaches that account for the flexibility and the buoyancy of the vegetation (not represented in the rigid cylinders concept used by *Dalrymple et al.* (1984)) could be considered (e.g., *Luhar and Nepf*, 2016).

Previous studies have reported contrasting dissipation rates of wave energy among the spectral components (e.g., *Bradley and Houser*, 2009; *Jadhav et al.*, 2013; *Lowe et al.*, 2007; *Anderson and Smith*, 2014), with a more efficient dissipation for the high frequency part of the spectrum. For instance, *Bradley and Houser* (2009) reported that wave energy was preferentially dissipated in the range of 0.75-1 Hz. Through cospectral analysis between oscillatory and seagrass blade velocities, they suggested that these quantities were in phase at the lower secondary frequency, while moving out of phase at the higher peak frequency which promotes wave attenuation. In contrast, *Nowacki et al.* (2017) observed a greater attenuation in lower frequencies. They suggested that this can be in part due to other wave processes including nonlinear wave-wave interactions, frequency-dependent frictional dissipation and wave generation by wind, which can overcome possible frequency-dependent rates of dissipation by vegetation. In our study, the evolution of the measured energy density spectra also suggests a frequency-dependent dissipation with a maximum dissipation at the spectral peak. By the end of the transect, wave energy in the gravity band

is almost fully dissipated while wave energy in the infragravity band penetrates the vegetation field more easily and becomes dominant. Similarly, *Phan et al.* (2014) showed through numerical experiments that infragravity waves become dominant over short waves after a certain distance of propagation into mangrove trees. In that sense, the vegetation can act as a low-pass filter. In regards to our modelled results, they show that the model does not correctly reproduce the different dissipation rates among frequencies, which can be likely explained by the use of mean wavenumber and frequency in the parameterization of wave dissipation by vegetation in the model. The frequency-dependent dissipation suggested by the observations cannot be reproduced in the absence of frequency-dependent quantities in the parameterization. *Nowacki et al.* (2017) reported a similar limitation in their spectral analysis. Further research is hence required on the way dissipation by vegetation is represented in the spectral model, particularly on the need for a frequency-dependent formulation.

In this study, we focus on the effect of the vegetation on waves and wave setup dynamics but did not consider its concomitant action on mean and turbulent flows. In SCHISM, *Zhang et al.* (2020) developed a flow-vegetation module to represent the 3D effects of the vegetation on surrounding flows, the vegetation term being treated implicitly to enable numerical efficiency and stability, even if strong shear develops around the vegetation. Conducting 3D simulations representing wave-current-vegetation interactions could be used to model and investigate the nonlinear interdependency between mean flow and waves in a vegetation field (*Beudin et al.*, 2017).

7.6.2 Future field campaign

The field campaign presented in this work was the first field campaign conducted by our team on the salt marsh of Brouage. While rather convincing results on the role of the vegetation on the nearshore hydrodynamics have been obtained, we identified several limitations to the experimental protocol used during this campaign and propose potential improvements to further assess the effect of the vegetation. First, it appears that *Halimione portulacoides* has a stronger capacity in dissipating wave energy than *Spartina maritima*, due in part, to a higher relative vegetation height to water depth ratio. However, waves entering *Halimione portulacoides* area were already strongly attenuated (<0.20 m). Hence, the capacity of *Halimione portulacoides* to dissipate larger waves cannot be evaluated in the scope of this campaign, while the incident wave height has been shown to influence wave damping rates (e.g., *Maza et al.*, 2015; *Garzon et al.*, 2019). Storm conditions are thus required with higher water levels on the salt marsh to observe larger waves on *Halimione portulacoides* area. In addition, more pressure sensors should be deployed at the transition between *Spartina maritima* and *Halimione portulacoides* to efficiently identify the effect of *Halimione portulacoides*. A pressure sensor has to be installed further offshore on the mudflat, since the first sensor in this field campaign (the ADV) was already located in the surf zone during the most energetic conditions. Storm wave conditions, together with the new disposition of the pressure sensors, would be the opportunity to measure quantifiable waves setup/set-down on the salt marsh, and properly investigate the different underlying mechanisms.

Waves were very short and dispersive on the salt marsh, and an accurate description of this wave field requires to correctly resolve the high-frequency part of the spectrum. Resolving this part of the spectrum is limiting with the TFM, since it requires the use of a cut-off frequency relatively low due to the limitations of the dispersion relation in predicting

wavenumbers in the presence of non-linearities. As mentioned in the section relative to the field campaign, accounting for these non-linearities is not feasible yet without the knowledge of the wavenumbers in this dispersive wave regime. Hence, it appears difficult to both account for the high-frequency energy levels associated with the wind sea and non-linear effects in this nearshore application. In addition, the pressure sensors used during this field campaign were of relatively low resolution and with a high level of noise (Fig. 4.7), which limits the possibility to measure small waves in the vegetation zone. In this context, it appears that bottom pressure sensors are not the most appropriate technique to measure waves and spectral transformation across the vegetation field. The solution proposed is the use of techniques capable of directly measuring the free surface such as acoustic sensors located above the surface (e.g., *Turner et al.*, 2008). Also, capacitive or resistant type wave gauges could be considered (e.g., *Flick et al.*, 1979). The lidar scanner could be another option. Lidar scanners require the presence of air bubbles (as this is usually the case in surf zones) (*Blenkinsopp et al.*, 2010) or turbid water (*Blenkinsopp et al.*, 2012; *Martins et al.*, 2017b) to return a continuous signal. Here, while the presence of air bubbles seems to be limited on the vegetation area, the turbidity of the water is important (see Fig. 7.11), which could allow the collection of reliable data with a lidar scanner.



FIGURE 7.11 – *Photo of waves propagating on the salt marsh of Brouage during the field campaign conducted in 2016. We can note a net decrease in the wave height when waves entering the vegetation field (credits : Antoine Lechevalier).*

Based on these considerations, a secondary field campaign should have been conducted during this thesis. However, we faced difficulties that prevent us to carry out this campaign. First, the study of wave transformation on this salt marsh requires to meet very specific hydrodynamic and atmospheric conditions. The experiment has to be conducted during spring tides and/or storm conditions inducing a storm surge, such that the salt marsh, located in the supratidal part of the mudflat, should be sufficiently inundated. At the same time, a wind sea should be generated in the Pertuis Charentais area by northwest winds since the salt marsh is protected from Atlantic swells by the Oléron Island. Vegetated coastal habitats usually develop in fetch-limited low-lying coastal environments characterized by low wave energy conditions as in our case, but can however experience strong wave energy during extreme events (*Bernatchez et al.*, 2011; *Didier et al.*, 2015). Overall, these particular conditions required to develop a wind sea in the study area only occur 2 to 3 times during winter, which makes challenging the execution of this field campaign. And, last but not least, the sanitary crisis that we faced further limited our possibilities to deploy the instruments. Hence, this field campaign is scheduled for the winter 2021/2022.

Chapitre 8

Conclusions and perspectives

Synthesis of this research

The main goal of this work was to gain a better understanding of the contributions of short waves to storm surges, with a particular attention paid to the wave setup in contrasting coastal environments. Previous studies reported that the breaking of short waves occurring close to and over the ebb deltas of shallow inlets or large estuaries can induce a wave setup that extends at the scale of the whole lagoon or estuary. Despite these findings, the possible contribution of the wave setup to the water level in wave-sheltered environments is not clearly recognized in the scientific community. The first goal of this work was to identify and quantify the contribution of the wave setup to storm surges in two wave-sheltered environments during storm conditions, and provide an explanation to this process by analysing the underlying mechanisms.

At a more local scale, the phenomenon of wave setup has been well documented and described in sandy environments but received much less attention in other common coastal environments such as shore platforms and salt marshes with comparatively very few field-based studies. However, wave setup dynamics can be substantially different from that on sandy beaches, namely due to a higher bed roughness on shore platforms or the interactions between waves and vegetation on salt marshes. Better understand these specific dynamics by combining field measurements and numerical modelling was the second main goal of this PhD thesis.

Through these different objectives, this comprehensive work covered a wide range of spatial and temporal scales. The main results of this PhD thesis are recalled below.

- Spatial extension of the wave setup in estuaries and lagoons

The fully-coupled wave-current modelling system SCHISM using a vortex force formalism has been first used to hindcast the sea state and storm surge associated with the storm Klaus that made landfall in the southern part of the Bay of Biscay in January 2009. This storm produced the most energetic waves ever recorded in this region and the largest storm surges observed over the last 20 years in the Arcachon Lagoon and the Adour Estuary (France). In that sense, Klaus represented a unique opportunity to investigate the contribution of the wave setup to storm surges in wave-sheltered environments. After the verification of the model with wave and water level observations available during the storm, the analyses of the modelled results revealed that the wave setup contributed by up to 40% and 23% to the storm surge peak in the Adour Estuary and the Arcachon

Lagoon respectively. Hence, accounting for wave forces in the circulation model improved storm surge predictions by 50 to 60%. In regards to the Arcachon Lagoon, wave forces reached values one order of magnitude larger than the bottom and surface stress terms at the inlet, which explains their major impact on the hydrodynamics there, and particularly, the extension of the wave setup outside the surf zone which significantly raised the water level at the scale of the whole lagoon. The wave setup is found to be tidally-modulated in the Arcachon Lagoon and the Adour Estuary, although the magnitude of this phenomenon is contrasted between the two study areas and other large estuaries. The tidal modulation of the wave setup is thus site-specific and depends on the morphology of the inlet and the subsequent degree of wave dissipation. Finally, a sensitivity analysis of the wave setup calculation to the grid resolution was conducted. Along the adjacent open-ocean coasts of the Lagoon, the wave setup prediction is strongly deteriorated when using a 1000 m grid resolution, such that the storm surge predicted with this coarse resolution is 65% lower than the one obtained with a 35 m grid resolution. In the lagoon, the wave setup and storm surge are found to be reasonably predicted with the 1000 m grid resolution, while the tidal propagation cannot be accurately represented with such resolution. This contrasting behaviour between the open-ocean and inner lagoon is directly explained by the cross-shore extension of the surf zone. As a rough guideline, accounting for wave setup in storm surge models should require at least 5 grid elements across the surf zone, whose width is controlled by the bottom slope and the wave height. This study demonstrates that the wave setup can significantly contribute to the water level in wave-sheltered environments under energetic wave conditions. More generally, these findings show that accounting for wave breaking in storm surge modelling and forecasting is essential to accurately predict storm surges, provided that the grid resolution is adapted to the surf zone width to correctly resolve the wave setup. We note that, depending on the resolutions needed and the extension of the computational domain, the resolution of the wave setup can still be computationally challenging for operational storm surge forecasting.

- Wave dissipation and mean circulation on a shore platform

In this application, the dynamics of the wave setup have been studied at a finer scale on a shore platform, where the bottom roughness effects on hydrodynamics can be much more important than on sandy beaches. Yet, the role of bed roughness on wave dissipation and wave setup dynamics in these environments has been little addressed. In this context, we conducted two field experiments under fair weather and storm wave conditions on a gently-sloping shore platform located on the western coast of Oléron Island. Data analysis was complemented with 3D numerical simulations conducted with the fully-coupled modelling system SCHISM with the vortex force formalism to represent the effects of short waves on the mean circulation. The accurate representation of wave dissipation by both bottom friction, that should account for the roughness of the platform, and depth-induced breaking, is found essential to reproduce the transformation of short waves across the platform and the resulting wave setup. Wave energy dissipation by bottom friction is dominant in the subtidal part of the platform and contributes to about 40% of the total wave energy dissipation. The enhanced wave bottom friction on the platform decreases the wave height for a given water depth, which, compared to a smooth bottom, decreases the contribution of wave forces to the wave setup, which is in turn reduced. Comparison of 2DH and 3D simulations showed a limited contribution of the wave-induced, depth-varying circulation to the wave setup on the studied shore platform. An idealised analysis of the cross-shore momentum balance revealed that this contribution increases as the slope steepens. In more details, the contribution of the wave-induced circulation to the wave setup occurs mostly through the vertical advection term on a smooth bottom while the contribution of the

vertical mixing term becomes dominant for a rougher bottom. Overall, a high roughness enhances the contribution of the wave-induced circulation to the wave setup. The latter process counteracts wave frictional effects on the wave setup and becomes dominant as the bottom slope increases, accounting for up to 26% of the wave setup for a 1:20 sloping shore platform. The identification of these processes provides new insights into the understanding of waves, currents and wave setup dynamics on shore platforms, while raising new perspectives of research.

- **Wave dissipation and mean circulation on a salt marsh**

Vegetated coastal ecosystems such as salt marshes are known to dissipate wave energy and limit storm surges, which explains the growing interest they receive as a nature-based solution for coastal protection. While several experiments have been conducted on wave-vegetation interactions, a majority corresponds to laboratory conditions with vegetation mimics, whose findings can be questioned in real physical conditions. In addition, several processes through which the vegetation can affect wave setup dynamics have been recently identified, which have not yet been verified in the field. In this context, analysis of field data collected on the salt marsh of Brouage in 2016 under moderate-energy wave conditions were combined with numerical simulations. The results showed that the vegetation explains 65% of wave dissipation on the salt marsh. The model accounting for the vegetation quite well predicted bulk parameters such as the evolution of the significant wave height along the transect. However, the model was not adapted to represent the frequency-dependent dissipation observed in the measured energy density spectra. This is likely explained by the use of the mean frequency and mean wavenumber in the parameterization of wave dissipation by vegetation. Unfortunately, the wave setup observations collected during this field campaign were too close to the experimental uncertainty range, such that they could not be used. However, the numerical results allowed to identify one of the effect of the vegetation on the wave setup. Wave dissipation by vegetation is found to reduce wave height before breaking, which reduces the contribution of the wave forces to the wave setup compared to a case without a vegetation, and in turn decreases it. Other processes such as nonlinear intrawave drag forces can further reduce the wave setup while additional research is needed to quantify these effects.

Perspectives

3D wave-current modelling approach

For a long time, 2DH approaches have been used to model storm surges, including modelling systems where waves and currents are fully coupled to account for the wave setup. The 2DH approach has been shown to well describe the main characteristics of the storm surge and are cheaper in terms of computational time compared to 3D models. However, 3D models allow a more realistic representation of the hydrodynamics, namely the vertical structure of currents. Therefore an important question rises here : in which conditions a 2DH approach would lead to a limited representation of the processes driving the wave setup and hence the storm surge, such that a 3D approach should be rather used ?

In this work, comparisons between 2DH and 3D simulations have been conducted to quantify the potential differences between both approaches, analyse them and try to give some responses to this complex question. In the regional study conducted in the Arcachon Lagoon and in the Bayonne Estuary, improved storm surge predictions are obtained in 3D before and during the storm peak, which is due to a better representation of the Ekman

transport. In the study conducted on the shore platform, the representation of the wave-induced depth-varying circulation results in a modest but significant improvement of wave setup predictions. These modest differences were explained by the gently-sloping bottom of the shore platform. Thus, further 3D idealised simulations with varying bottom slopes and roughnesses have been conducted to better understand through which mechanisms the wave-induced depth-varying circulation contributes to the wave setup. This analysis allowed us to identify certain configurations in which the 3D model should be preferred to compute the wave setup, although this choice also depends on the desired level of accuracy. Our results indicate that the contribution of the wave-induced depth-varying circulation increases as the slope steepens. As an indication, for a 1:20 slope, the wave-induced depth-varying circulation explains already 20% of the wave setup on a sandy beach and 26% on a shore platform, a contribution which cannot be represented with a 2DH approach. Hence, in environments such as steep rocky shores (e.g., *Dodet et al.*, 2018), where these 3D effects on the wave setup are potentially more important, a 3D modelling approach would be more adapted.

One point should be however noted. The previous findings were based on idealised cases. Hence, there is an essential need to verify these conclusions in the field, in particular on steeper shore platforms, so that the wave-induced circulation would have a larger effect on the wave setup. The field campaign presented in this work was based on measurements of currents at a single point in the water column. To go one step further into the understanding of the hydrodynamics on shore platforms, measurements of vertical currents profiles should be conducted in the future field campaigns. This would allow to thoroughly analyse the effect of the wave-enhanced vertical mixing on the vertical shear of cross-shore currents, but also better understand the contribution of the bottom streaming to the surf zone mean circulation, in particular, the vertical distribution of the associated acceleration.

Vegetation effects on waves and wave setup : future measurements

This is well recognized that aquatic vegetation can dissipate wave energy and reduce wind-induced storm surges by slowing their advance, but there is a need to better quantify these effects in naturally vegetated coastal environments in various geomorphological configurations and hydrodynamic conditions of waves, currents and water depths. The field campaign presented in this work was the first one that our team conducted on a salt marsh. While field data analysis complemented with numerical simulations allowed to investigate the effect of the vegetation on waves and showed promising results, several limitations related to the experimental protocol have been raised. First, stronger energetic conditions are needed to study the capacity of *Halimione portulacoides* in dissipating wave energy, which is very little documented. More energetic wave conditions can induce larger variations of the mean water level through wave setup/set-down, providing more reliable measurements. While pressure sensors seem appropriate to measure mean sea level variations, they appeared to be limited to measure the high-frequency part of the wave spectrum in these environments. Indeed, the dispersive regime of the wave field restrained the choice of the reconstruction method to the TFM. With this method, non-linear effects are not accounted for and uncertainties remain on the high-frequency part of the wave spectrum. To address these shortcomings, we propose the use of techniques capable of directly measuring the free surface elevation such as acoustic sensors deployed above the sea surface, or lidar scanners. Such a campaign should have been conducted during this PhD thesis, however, its execution requires specific atmospheric and hydrodynamic conditions, which were reached only a limited number of times and our possibilities were further limited by the sanitary crisis

that we face.

Overall, these investigations can help to assess the potential of halophytic vegetation as a viable alternative or complementary solutions for coastal protection. For instance, the effect of the vegetation on the wave setup is not yet accounted for in flood risk assessments. Also, research can contribute to the design of hybrid engineering projects combining hard infrastructures with natural ecosystems (*Spalding et al.*, 2014; *Sutton-Grier et al.*, 2015). Vegetated foreshores can attenuate storm wave impacts on hardened flood defence infrastructures, which can in turn reduce their construction and maintenance cost (*Vuik et al.*, 2016; *Keimer et al.*, 2021).

Bibliography

- Abdalla, S., and J. Bidlot (2002), Wind gustiness and air density effects and other key changes to wave model in CY25R1, *Tech. Rep. Memorandum R60. 9/SA/0273, Research Department, ECMWF, Reading, U. K.*
- Abdelrhman, M. A. (2007), Modeling coupling between eelgrass *Zostera marina* and water flow, *Marine Ecology Progress Series*, *338*, 81–96.
- Abgrall, R. (2006), Residual distribution schemes: Current status and future trends, *Computers & Fluids*, *35*(7), 641–669, doi:10.1016/j.compfluid.2005.01.007, special Issue Dedicated to Professor Stanley G. Rubin on the Occasion of his 65th Birthday.
- Agrawal, Y. C. (1992), Enhanced dissipation of kinetic energy beneath surface waves, *Nature*, *359*, 219–220.
- Almar, R., et al. (2021), A global analysis of extreme coastal water levels with implications for potential coastal overtopping, *Nature Communications*, *12*, doi:10.1038/s41467-021-24008-9.
- Anderson, M., and J. Smith (2014), Wave attenuation by flexible, idealized salt marsh vegetation, *Coastal Engineering*, *83*, 82–92, doi:10.1016/j.coastaleng.2013.10.004.
- Anderson, T., C. Fletcher, M. Barbee, L. Frazer, and B. Romine (2015), Doubling of coastal erosion under rising sea level by mid-century in Hawaii, *Natural Hazards: Journal of the International Society for the Prevention and Mitigation of Natural Hazards*, *78*(1), 75–103, doi:10.1007/s11069-015-1698-6.
- Andrews, D. G., and M. E. McIntyre (1978), An exact theory of nonlinear waves on a Lagrangian-mean flow, *Journal of Fluid Mechanics*, *89*(4), 609–646, doi:10.1017/S0022112078002773.
- Aon-Benfield (2010), Annual global climate and catastrophe report: Impact forecasting - 2009.
- Apotsos, A., B. Raubenheimer, S. Elgar, R. T. Guza, and J. A. Smith (2007), Effects of wave rollers and bottom stress on wave setup, *Journal of Geophysical Research: Oceans*, *112*(C2), doi:10.1029/2006JC003549.
- Ardhuin, F., and A. D. Jenkins (2006), On the Interaction of Surface Waves and Upper Ocean Turbulence, *Journal of Physical Oceanography*, *36*(3), 551 – 557, doi:10.1175/JPO2862.1.
- Ardhuin, F., W. O’reilly, T. Herbers, and P. Jessen (2003), Swell transformation across the continental shelf. Part I: Attenuation and directional broadening, *Journal of Physical*

- Oceanography*, 33(9), 1921–1939, doi:10.1175/1520-0485(2003)033<1921:STATCS>2.0.CO;2.
- Ardhuin, F., A. D. Jenkins, and K. A. Belibassakis (2008a), Comments on “The Three-Dimensional Current and Surface Wave Equations”, *Journal of Physical Oceanography*, 38(6), 1340 – 1350, doi:10.1175/2007JPO3670.1.
- Ardhuin, F., N. Rascle, and K. Belibassakis (2008b), Explicit wave-averaged primitive equations using a generalized Lagrangian mean, *Ocean Modelling*, 20(1), 35–60, doi:10.1016/j.ocemod.2007.07.001.
- Ardhuin, F., B. Chapron, and F. Collard (2009), Observation of swell dissipation across oceans, *Geophysical Research Letters*, 36(6), doi:10.1029/2008GL037030.
- Ardhuin, F., et al. (2010), Semiempirical dissipation source functions for ocean waves. Part I: Definition, calibration, and validation, *Journal of Physical Oceanography*, 40(9), 1917–1941, doi:10.1175/2010JPO4324.1.
- Ardhuin, F., et al. (2012), Numerical wave modeling in conditions with strong currents: Dissipation, refraction, and relative wind, *Journal of Physical Oceanography*, 42(12), 2101–2120, doi:10.1175/JPO-D-11-0220.1.
- Arnaud, G., and X. Bertin (2014), Contribution du setup induit par les vagues dans la surcote associée à la tempête Klaus, *XIII emes Journées Nationales Génie Côtier Génie Civil, Paralia Ed., Dunkerque, France*, pp. 2–4.
- Aucan, J., R. Hoeke, and M. Merrifield (2012), Wave-driven sea level anomalies at the Midway tide gauge as an index of North Pacific storminess over the past 60 years, *Geophysical Research Letters*, 39(17), doi:10.1029/2012GL052993.
- Augustin, L. N., J. L. Irish, and P. Lynett (2009), Laboratory and numerical studies of wave damping by emergent and near-emergent wetland vegetation, *Coastal Engineering*, 56(3), 332–340, doi:10.1016/j.coastaleng.2008.09.004.
- Bacchi, V., E. Gagnaire, N. Durand, and M. Benoit (2014), Wave energy dissipation by vegetation in TOMAWAC.
- Bakhoday Paskyabi, M., I. Fer, and A. D. Jenkins (2012), Surface gravity wave effects on the upper ocean boundary layer: Modification of a one-dimensional vertical mixing model, *Continental Shelf Research*, 38, 63–78, doi:10.1016/j.csr.2012.03.002.
- Barbier, E. B., S. D. Hacker, C. Kennedy, E. W. Koch, A. C. Stier, and B. R. Silliman (2011), The value of estuarine and coastal ecosystem services, *Ecological Monographs*, 81(2), 169–193, doi:10.1890/10-1510.1.
- Bassoullet, P., P. Le Hir, D. Gouleau, and S. Robert (2000), Sediment transport over an intertidal mudflat: field investigations and estimation of fluxes within the “Baie de Marenngres-Oleron” (France), *Continental Shelf Research*, 20(12), 1635–1653, doi:10.1016/S0278-4343(00)00041-8.
- Battjes, J. (1972), Set-Up Due to Irregular Waves, in *Coastal Engineering 1972*, pp. 1993–2004, doi:10.1061/9780872620490.116.

- Battjes, J. A. (1974), Computation of set-up, longshore currents, runup and overtopping due to wind generated waves, *Department of Civil Engineering, Delft University of Technology, Delft, the Netherlands, Report, 74*(2).
- Battjes, J. A., and J. Janssen (1978), Energy loss and set-up due to breaking of random waves, in *Coastal Engineering 1978*, pp. 569–587, doi:10.1061/9780872621909.034.
- Battjes, J. A., and M. J. F. Stive (1985), Calibration and verification of a dissipation model for random breaking waves, *Journal of Geophysical Research: Oceans*, *90*(C5), 9159–9167, doi:10.1029/JC090iC05p09159.
- Beetham, E. P., and P. S. Kench (2011), Field observations of infragravity waves and their behaviour on rock shore platforms, *Earth Surface Processes and Landforms*, *36*(14), 1872–1888, doi:10.1002/esp.2208.
- Bellafont, F., D. Morichon, V. Roeber, G. André, and S. Abadie (2018), Oscillations portuaires forcées par les ondes infra-gravitaires dans un chenal de navigation, in *XVèmes Journées Nationales Génie Côtier – Génie Civil*, pp. 1–8, Paralia CFL, La Rochelle, France, France, doi:10.5150/jngcgc.2018.001.
- Benetazzo, A. (2006), Measurements of short water waves using stereo matched image sequences, *Coastal Engineering*, *53*(12), 1013–1032, doi:10.1016/j.coastaleng.2006.06.012.
- Bennis, A.-C., F. Ardhuin, and F. Dumas (2011), On the coupling of wave and three-dimensional circulation models: Choice of theoretical framework, practical implementation and adiabatic tests, *Ocean Modelling*, *40*(3), 260–272, doi:10.1016/j.ocemod.2011.09.003.
- Bennis, A.-C., F. Dumas, F. Ardhuin, and B. Blanke (2014), Mixing parameterization: Impacts on rip currents and wave set-up, *Ocean Engineering*, *84*, 213, doi:10.1016/j.oceaneng.2014.04.021.
- Benoit, M., F. Marcos, and F. Becq (1997), Development of a third generation shallow-water wave model with unstructured spatial meshing, in *Coastal Engineering 1996*, pp. 465–478, doi:10.1061/9780784402429.037.
- Bernatchez, P., C. Fraser, D. Lefaivre, and S. Dugas (2011), Integrating anthropogenic factors, geomorphological indicators and local knowledge in the analysis of coastal flooding and erosion hazards, *Ocean & Coastal Management*, *54*(8), 621–632, doi:10.1016/j.ocecoaman.2011.06.001.
- Bertin, X., A. B. Fortunato, and A. Oliveira (2009), A modeling-based analysis of processes driving wave-dominated inlets, *Continental Shelf Research*, *29*(5-6), 819–834, doi:"10.1016/j.csr.2008.12.019".
- Bertin, X., N. Bruneau, J.-F. Breilh, A. B. Fortunato, and M. Karpytchev (2012), Importance of wave age and resonance in storm surges: The case Xynthia, Bay of Biscay, *Ocean Modelling*, *42*, 16–30, doi:10.1016/j.ocemod.2011.11.001.
- Bertin, X., K. Li, A. Roland, Y. J. Zhang, J. F. Breilh, and E. Chaumillon (2014), A modeling-based analysis of the flooding associated with Xynthia, central Bay of Biscay, *Coastal Engineering*, *94*, 80–89, doi:10.1016/j.coastaleng.2014.08.013.

- Bertin, X., K. Li, A. Roland, and J.-R. Bidlot (2015a), The contribution of short-waves in storm surges: Two case studies in the Bay of Biscay, *Continental Shelf Research*, *96*, 1–15, doi:10.1016/j.csr.2015.01.005.
- Bertin, X., A. B. Fortunato, and G. Dodet (2015b), Processes controlling the seasonal cycle of wave-dominated inlets, *Revista de Gestão Costeira Integrada-Journal of Integrated Coastal Zone Management*, *15*(1), 9–19.
- Bertin, X., D. Mendes, K. Martins, A. B. Fortunato, and L. Lavaud (2019), The closure of a shallow tidal inlet promoted by infragravity waves, *Geophysical Research Letters*, *46*(12), 6804–6810, doi:10.1029/2019GL083527.
- Bertin, X., K. Martins, A. de Bakker, T. Chataigner, T. Guérin, T. Coulombier, and O. de Viron (2020), Energy Transfers and Reflection of Infragravity Waves at a Dissipative Beach Under Storm Waves, *Journal of Geophysical Research: Oceans*, *125*(5), e2019JC015714, doi:10.1029/2019JC015714.
- Beudin, A., T. S. Kalra, N. K. Ganju, and J. C. Warner (2017), Development of a coupled wave-flow-vegetation interaction model, *Computers & Geosciences*, *100*, 76–86, doi:10.1016/j.cageo.2016.12.010.
- Bidlot, J., P. Janssen, and S. Abdalla (2007), *A revised formulation of ocean wave dissipation and its model impact*, vol. no. 509 in ECMWF technical memorandum.
- Birch, R., D. Fissel, K. Borg, V. Lee, and D. English (2004), The capabilities of Doppler current profilers for directional wave measurements in coastal and nearshore waters, in *Oceans '04 MTS/IEEE Techno-Ocean '04 (IEEE Cat. No.04CH37600)*, vol. 3, pp. 1418–1427 Vol.3, doi:10.1109/OCEANS.2004.1406330.
- Bishop, C. T., and M. A. Donelan (1987), Measuring waves with pressure transducers, *Coastal Engineering*, *11*(4), 309–328, doi:10.1016/0378-3839(87)90031-7.
- Blain, C. A., J. J. Westerink, and R. A. Luettich Jr. (1994), The influence of domain size on the response characteristics of a hurricane storm surge model, *Journal of Geophysical Research: Oceans*, *99*(C9), 18,467–18,479, doi:10.1029/94JC01348.
- Blenkinsopp, C., M. Mole, I. Turner, and W. Peirson (2010), Measurements of the time-varying free-surface profile across the swash zone obtained using an industrial LIDAR, *Coastal Engineering*, *57*(11), 1059–1065, doi:10.1016/j.coastaleng.2010.07.001.
- Blenkinsopp, C. E., I. L. Turner, M. J. Allis, W. L. Peirson, and L. E. Garden (2012), Application of lidar technology for measurement of time-varying free-surface profiles in a laboratory wave flume, *Coastal Engineering*, *68*, 1–5, doi:10.1016/j.coastaleng.2012.04.006.
- Blumberg, A. F., and G. L. Mellor (1987), A Description of a Three-Dimensional Coastal Ocean Circulation Model, in *Three-Dimensional Coastal Ocean Models*, pp. 1–16, American Geophysical Union (AGU), doi:10.1029/CO004p0001.
- Bode, L., and T. Hardy (1997), Progress and Recent Developments in Storm Surge Modeling, *Journal of Hydraulic Engineering-asce - J HYDRAUL ENG-ASCE*, *123*, doi:10.1061/(ASCE)0733-9429(1997)123:4(315).
- Boers, M. (1997), Simulation of a surf zone with a barred beach; part 1: wave heights and wave breaking, *Oceanographic Literature Review*, *44*(4), 292.

- Bolaños, R., J. M. Brown, and A. J. Souza (2014), Wave–current interactions in a tide dominated estuary, *Continental Shelf Research*, *87*, 109–123, doi:10.1016/j.csr.2014.05.009, oceanography at coastal scales.
- Bonneton, P., and D. Lannes (2017), Recovering water wave elevation from pressure measurements, *Journal of Fluid Mechanics*, *833*, 399–429, doi:10.1017/jfm.2017.666.
- Bonneton, P., D. Lannes, K. Martins, and H. Michallet (2018), A nonlinear weakly dispersive method for recovering the elevation of irrotational surface waves from pressure measurements, *Coastal Engineering*, *138*, 1–8, doi:10.1016/j.coastaleng.2018.04.005.
- Bouma, T., et al. (2013), Organism traits determine the strength of scale-dependent biogeomorphic feedbacks: A flume study on three intertidal plant species, *Geomorphology*, *180-181*, 57–65, doi:10.1016/j.geomorph.2012.09.005.
- Bouws, E., and G. J. Komen (1983), On the Balance Between Growth and Dissipation in an Extreme Depth-Limited Wind-Sea in the Southern North Sea, *Journal of Physical Oceanography*, *13*(9), 1653 – 1658, doi:10.1175/1520-0485(1983)013<1653:OTBBGA>2.0.CO;2.
- Bowen, A. J., D. L. Inman, and V. P. Simmons (1968), Wave ‘set-down’ and set-up, *Journal of Geophysical Research (1896-1977)*, *73*(8), 2569–2577, doi:10.1029/JB073i008p02569.
- Bradley, K., and C. Houser (2009), Relative velocity of seagrass blades: Implications for wave attenuation in low-energy environments, *Journal of Geophysical Research: Earth Surface*, *114*(F1), doi:10.1029/2007JF000951.
- Bretherton, F. P., C. J. R. Garrett, and M. J. Lighthill (1968), Wavetrains in inhomogeneous moving media, *Proceedings of the Royal Society of London. Series A. Mathematical and Physical Sciences*, *302*(1471), 529–554, doi:10.1098/rspa.1968.0034.
- Bretschneider, C., H. Krock, E. Nakazaki, and F. Casciano (1986), Roughness of typical Hawaiian terrain for tsunami run-up calculations: A users manual, *JKK Look Laboratory Report, University of Hawaii*, *42*.
- Brière, C. (2005), Etude de l’hydrodynamique d’une zone côtière anthropisée: l’embouchure de l’Adour et les plages adjacentes d’Anglet, Ph.D. thesis, Pau.
- Brodie, K. L., B. Raubenheimer, S. Elgar, R. K. Slocum, and J. E. McNinch (2015), Lidar and Pressure Measurements of Inner-Surfzone Waves and Setup, *Journal of Atmospheric and Oceanic Technology*, *32*(10), 1945 – 1959, doi:10.1175/JTECH-D-14-00222.1.
- Brown, J. M. (2010), A case study of combined wave and water levels under storm conditions using WAM and SWAN in a shallow water application, *Ocean Modelling*, *35*(3), 215–229, doi:10.1016/j.ocemod.2010.07.009.
- Brown, J. M., R. Bolaños, and J. Wolf (2011), Impact assessment of advanced coupling features in a tide–surge–wave model, POLCOMS-WAM, in a shallow water application, *Journal of Marine Systems*, *87*(1), 13–24, doi:10.1016/j.jmarsys.2011.02.006.
- Brown, J. M., R. Bolaños, and J. Wolf (2013a), The depth-varying response of coastal circulation and water levels to 2D radiation stress when applied in a coupled wave–tide–surge modelling system during an extreme storm, *Coastal Engineering*, *82*, 102–113, doi:10.1016/j.coastaleng.2013.08.009.

- Brown, S., R. J. Nicholls, C. D. Woodroffe, S. Hanson, J. Hinkel, A. S. Kebede, B. Neumann, and A. T. Vafeidis (2013), Sea-Level Rise Impacts and Responses: A Global Perspective, in *Coastal Hazards*, edited by C. W. Finkl, pp. 117–149, Springer Netherlands, Dordrecht, doi:10.1007/978-94-007-5234-4_5.
- Buckley, M. L., R. J. Lowe, J. E. Hansen, and A. R. Van Dongeren (2016), Wave setup over a fringing reef with large bottom roughness, *Journal of Physical Oceanography*, *46*(8), 2317–2333, doi:10.1175/JPO-D-15-0148.1.
- Bulleri, F., and M. G. Chapman (2010), The introduction of coastal infrastructure as a driver of change in marine environments, *Journal of Applied Ecology*, *47*(1), 26–35.
- Bunya, S., et al. (2010), A High-Resolution Coupled Riverine Flow, Tide, Wind, Wind Wave, and Storm Surge Model for Southern Louisiana and Mississippi. Part I: Model Development and Validation, *Monthly Weather Review*, *138*(2), 345 – 377, doi:10.1175/2009MWR2906.1.
- Burchard, H., K. Bolding, and M. R. Villarreal (1999), *GOTM, a general ocean turbulence model: theory, implementation and test cases*, Space Applications Institute.
- Butel, R., H. Dupuis, and P. Bonneton (2002), Spatial variability of wave conditions on the French Atlantic coast using in-situ data, *Journal of Coastal Research*, *36*(sp1), 96–109, doi:10.2112/1551-5036-36.sp1.96.
- Cartwright, D. E., G. E. R. Deacon, and n. surName (1968), A unified analysis of tides and surges round North and East Britain, *Philosophical Transactions of the Royal Society of London. Series A, Mathematical and Physical Sciences*, *263*(1134), 1–55, doi:10.1098/rsta.1968.0005.
- Cayocca, F. (1996), Modélisation morphodynamique d’une embouchure tidale: application aux passes d’entrée du Bassin d’Arcachon, Ph.D. thesis, Bordeaux 1.
- Charnock, H. (1955), Wind stress on a water surface, *Quarterly Journal of the Royal Meteorological Society*, *81*(350), 639–640, doi:10.1002/qj.49708135027.
- Chen, C., H. Liu, and R. C. Beardsley (2003), An Unstructured Grid, Finite-Volume, Three-Dimensional, Primitive Equations Ocean Model: Application to Coastal Ocean and Estuaries, *Journal of Atmospheric and Oceanic Technology*, *20*(1), 159 – 186, doi:10.1175/1520-0426(2003)020<0159:AUGFVT>2.0.CO;2.
- Chen, C., et al. (2012), *An unstructured-grid, finite-volume community ocean model: FVCOM user manual*, Sea Grant College Program, Massachusetts Institute of Technology Cambridge
- Codiga, D. L. (2011), *Unified tidal analysis and prediction using the UTide Matlab functions*, Graduate School of Oceanography, University of Rhode Island Narragansett, RI.
- Collins, J. I. (1972), Prediction of shallow-water spectra, *Journal of Geophysical Research (1896-1977)*, *77*(15), 2693–2707, doi:10.1029/JC077i015p02693.
- Connell, J. H. (1961), The Influence of Interspecific Competition and Other Factors on the Distribution of the Barnacle *Chthamalus Stellatus*, *Ecology*, *42*(4), 710–723.

- Cooper, C., and B. Pearce (1982), Numerical Simulations of Hurricane-Generated Currents, *Journal of Physical Oceanography*, *12*(10), 1071 – 1091, doi:10.1175/1520-0485(1982)012<1071:NSOHGC>2.0.CO;2.
- Craig, P. D., and M. L. Banner (1994), Modeling Wave-Enhanced Turbulence in the Ocean Surface Layer, *Journal of Physical Oceanography*, *24*(12), 2546–2559, doi:10.1175/1520-0485(1994)024<2546:MWETIT>2.0.CO;2.
- Craik, A., and S. Leibovich (1976), A rational model for Langmuir circulations, *Journal of Fluid Mechanics*, *73*(3), 401–426, doi:10.1017/S0022112076001420.
- Dalrymple, R. A., J. T. Kirby, and P. A. Hwang (1984), Wave Diffraction Due to Areas of Energy Dissipation, *Journal of Waterway, Port, Coastal, and Ocean Engineering*, *110*(1), 67–79, doi:10.1061/(ASCE)0733-950X(1984)110:1(67).
- Das, P. K. (1972), Prediction Model for Storm Surges in the Bay of Bengal, *Nature*, *239*(5369), 211–213, doi:10.1038/239211a0.
- Davies, A. (1981), Three-dimensional modelling of surges.
- Dayton, P. K. (1971), Competition, Disturbance, and Community Organization: The Provision and Subsequent Utilization of Space in a Rocky Intertidal Community, *Ecological Monographs*, *41*(4), 351–389, doi:10.2307/1948498.
- De Goede, E. D. (2020), Historical overview of 2D and 3D hydrodynamic modelling of shallow water flows in the Netherlands, *Ocean Dynamics*, *70*(4), 521–539, doi:10.1007/s10236-019-01336-5.
- Dean, R. G., and C. J. Bender (2006), Static wave setup with emphasis on damping effects by vegetation and bottom friction, *Coastal Engineering*, *53*(2), 149–156, doi:10.1016/j.coastaleng.2005.10.005.
- Debese, N., R. Moitié, and N. Seube (2012), Multibeam echosounder data cleaning through a hierarchic adaptive and robust local surfacing, *Computers & Geosciences*, *46*, 330–339, doi:10.1016/j.cageo.2012.01.012.
- Deigaard, R. (1993), A note on the three-dimensional shear stress distribution in a surf zone, *Coastal Engineering*, *20*(1), 157–171, doi:10.1016/0378-3839(93)90059-H.
- Deigaard, R., and J. Fredsøe (1989), Shear stress distribution in dissipative water waves, *Coastal Engineering*, *13*(4), 357–378, doi:10.1016/0378-3839(89)90042-2.
- Deigaard, R., P. Justesen, and J. Fredsøe (1991), Modelling of undertow by a one-equation turbulence model, *Coastal Engineering*, *15*(5), 431–458, doi:10.1016/0378-3839(91)90022-9.
- Delpey, M. (2012), Etude de la dispersion horizontale en zone littorale sous l’effet de la circulation tridimensionnelle forcée par les vagues-Application à la baie de Saint Jean de Luz-Ciboure et au littoral de Guéthary-Bidart, Ph.D. thesis, Université de Bretagne occidentale-Brest.
- Delpey, M. T., F. Ardhuin, P. Otheguy, and A. Jouon (2014), Effects of waves on coastal water dispersion in a small estuarine bay, *Journal of Geophysical Research: Oceans*, *119*(1), 70–86, doi:10.1002/2013JC009466.

- Didier, D., P. Bernatchez, G. Boucher-Brossard, A. Lambert, C. Fraser, R. L. Barnett, and S. Van-Wierst (2015), Coastal Flood Assessment Based on Field Debris Measurements and Wave Runup Empirical Model, *Journal of Marine Science and Engineering*, 3(3), 560–590, doi:10.3390/jmse3030560.
- Didier, D., P. Bernatchez, G. Marie, and G. Boucher-Brossard (2016), Wave runup estimations on platform-beaches for coastal flood hazard assessment, *Natural Hazards*, 83(3), 1443–1467, doi:10.1007/s11069-016-2399-5.
- Dietrich, J., et al. (2010), A high-resolution coupled riverine flow, tide, wind, wind wave, and storm surge model for southern Louisiana and Mississippi. Part II: Synoptic description and analysis of Hurricanes Katrina and Rita, *Monthly Weather Review*, 138(2), 378–404, doi:10.1175/2009MWR2907.1.
- Dietrich, J., et al. (2011), Modeling hurricane waves and storm surge using integrally-coupled, scalable computations, *Coastal Engineering*, 58(1), 45–65, doi:10.1016/j.coastaleng.2010.08.001.
- Dodet, G., X. Bertin, N. Bruneau, A. B. Fortunato, A. Nahon, and A. Roland (2013), Wave-current interactions in a wave-dominated tidal inlet, *Journal of Geophysical Research: Oceans*, 118(3), 1587–1605, doi:10.1002/jgrc.20146.
- Dodet, G., F. Leckler, D. Sous, F. Ardhuin, J. F. Filipot, and S. Suanez (2018), Wave Runup Over Steep Rocky Cliffs, *Journal of Geophysical Research: Oceans*, 123, 7185–7205, doi:10.1029/2018JC013967.
- Dodet, G., X. Bertin, F. Bouchette, M. Gravelle, L. Testut, and G. Wöppelmann (2019a), Characterization of sea-level variations along the metropolitan coasts of France: waves, tides, storm surges and long-term changes, *Journal of Coastal Research*, 88(sp1), 10–24, doi:10.2112/SI88-003.1.
- Dodet, G., A. Melet, F. Ardhuin, X. Bertin, D. Idier, and R. Almar (2019b), The Contribution of Wind-Generated Waves to Coastal Sea-Level Changes, *Surveys in Geophysics*, 40, doi:10.1007/s10712-019-09557-5.
- Doering, J., and A. Bowen (1995), Parametrization of orbital velocity asymmetries of shoaling and breaking waves using bispectral analysis, *Coastal Engineering*, 26(1), 15–33, doi:10.1016/0378-3839(95)00007-X.
- Donelan, M. A. (1982), The dependence of the aerodynamic drag coefficient on wave parameters, *Proc. First Int. Conf. on Meteorol. and Air-Sea Interaction of the Coastal Zone*, pp. 381–387.
- Donelan, M. A., F. W. Dobson, S. D. Smith, and R. J. Anderson (1993), On the dependence of sea surface roughness on wave development, *Journal of physical Oceanography*, 23(9), 2143–2149, doi:10.1175/1520-0485(1993)023<2143:OTDOSS>2.0.CO;2.
- Doodson, A. T. (1924), Meteorological perturbations of sea-level and tides, *Geophysical Supplements to the Monthly Notices of the Royal Astronomical Society*, 1(4), 124–147, doi:10.1111/j.1365-246X.1924.tb05363.x.
- Drennan, W. M., H. C. Graber, D. Hauser, and C. Quentin (2003), On the wave age dependence of wind stress over pure wind seas, *Journal of Geophysical Research: Oceans*, 108(C3), doi:10.1029/2000JC000715.

- Duarte, C. M., I. J. Losada, I. E. Hendriks, I. Mazarrasa, and N. Marbà (2013), The role of coastal plant communities for climate change mitigation and adaptation, *Nature Climate Change*, 3(11), 961–968, doi:10.1038/nclimate1970.
- Dube, S. K., T. S. Murty, J. C. Feyen, R. Cabrera, B. A. Harper, J. D. Bales, and S. Amer (2010), Storm Surge Modeling and Applications in Coastal Areas, in *Global Perspectives on Tropical Cyclones*, pp. 363–406, doi:10.1142/9789814293488_0012.
- Dubi, A., and A. Tørum (1995), Wave Damping by Kelp Vegetation, in *Coastal Engineering 1994*, pp. 142–156, doi:10.1061/9780784400890.012.
- Dubi, A., and A. Tørum (1997), Wave Energy Dissipation in Kelp Vegetation, in *Coastal Engineering 1996*, pp. 2625–2639, doi:10.1061/9780784402429.203.
- Dunn, S. L., P. Nielsen, P. A. Madsen, and P. Evans (2001), Wave setup in river entrances, in *Coastal Engineering 2000*, pp. 3432–3445, doi:10.1061/40549(276)267.
- Ekman, V. W. (1905), On the influence of earth’s rotation on ocean currents, *Arch. Mach. Astron. Phys.*, 2, 1–53.
- Eldeberky, Y. (1996), Nonlinear transformation of wave spectra in the nearshore zone (Ph. D. thesis), *Netherlands: Delft University of Technology, Department of Civil Engineering*.
- Eldeberky, Y., and J. A. Battjes (1996), Spectral modeling of wave breaking: Application to Boussinesq equations, *Journal of Geophysical Research: Oceans*, 101(C1), 1253–1264, doi:10.1029/95JC03219.
- Elgar, S., and R. T. Guza (1985), Observations of bispectra of shoaling surface gravity waves, *Journal of Fluid Mechanics*, 161, 425–448, doi:10.1017/S0022112085003007.
- Fairchild, J. (1958), Model study of wave set-up induced by hurricane waves at Narragansett pier, Rhode Island, *Bull. Beach Erosion Board*, 12, 9–20.
- Farrell, E., H. Granja, L. Cappietti, J. Ellis, B. Li, and D. Sherman (2009), Wave Transformation across a Rock Platform, Belinho, Portugal, *Journal of Coastal Research*, pp. 44–48.
- Fedderson, F., and J. H. Trowbridge (2005), The Effect of Wave Breaking on Surf-Zone Turbulence and Alongshore Currents: A Modeling Study, *Journal of Physical Oceanography*, 35(11), 2187–2203, doi:10.1175/JPO2800.1.
- Ferrarin, C., A. Roland, M. Bajo, G. Umgiesser, A. Cucco, S. Davolio, A. Buzzi, P. Malguzzi, and O. Drofa (2013), Tide-surge-wave modelling and forecasting in the Mediterranean Sea with focus on the Italian coast, *Ocean Modelling*, 61, 38–48, doi:10.1016/j.ocemod.2012.10.003.
- Flather, R. (1976), A tidal model of the north-west european continental shelf, *Mem. Soc. R. Sci. Liege.*, 10, 141–164.
- Flather, R. (1979), Recent Results from a Storm Surge Prediction Scheme for the North Sea, in *Marine Forecasting, Elsevier Oceanography Series*, vol. 25, edited by J. C. Nihoul, pp. 385–409, Elsevier, doi:10.1016/S0422-9894(08)71140-1.
- Flather, R. (1981), Practical surge prediction using numerical models, in *Floods due to high winds and tides*, pp. 21–43, Academic Press London.

- Flather, R. A. (1984), A numerical model investigation of the storm surge of 31 January and 1 February 1953 in the North Sea, *Quarterly Journal of the Royal Meteorological Society*, *110*(465), 591–612, doi:10.1002/qj.49711046503.
- Flather, R. A. (2000), Existing operational oceanography, *Coastal Engineering*, *41*(1), 13–40, doi:10.1016/S0378-3839(00)00025-9.
- Flather, R. A. (2001), Storm surges, in *Encyclopedia of Ocean Sciences*, edited by S. T. J. Steele and K. Turekian, pp. 2882–2892, Academic, San Diego, Calif., doi:10.1006/rwos.2001.0124.
- Flather, R. A., and R. Proctor (1983), Prediction of North Sea Storm Surges Using Numerical Models: Recent Developments in U. K., in *North Sea Dynamics*, edited by J. Sündermann and W. Lenz, pp. 299–317, Springer, Berlin, Heidelberg.
- Flick, R., R. Lowe, M. Freilich, and J. Boylls (1979), Coastal and Laboratory Wavestaff System, in *OCEANS '79*, pp. 623–625, doi:10.1109/OCEANS.1979.1151229.
- Fonseca, M. S., and J. A. Cahalan (1992), A preliminary evaluation of wave attenuation by four species of seagrass, *Estuarine, Coastal and Shelf Science*, *35*(6), 565–576, doi:10.1016/S0272-7714(05)80039-3.
- Foreman, M. (1977), Manual for tidal heights analysis and prediction. Pacific Marine Science Report 77-10, *Institute for Ocean Sciences, Sydney, Canada*.
- Foreman, M., and R. Henry (1989), The harmonic analysis of tidal model time series, *Advances in Water Resources*, *12*(3), 109–120, doi:10.1016/0309-1708(89)90017-1.
- Foreman, M. G., and E. Neufeld (1991), Harmonic tidal analysis of long time series, *The International Hydrographic Review*.
- Forristall, G. Z. (1974), Three-dimensional structure of storm-generated currents, *Journal of Geophysical Research (1896-1977)*, *79*(18), 2721–2729, doi:10.1029/JC079i018p02721.
- Fortunato, A. B., P. Freire, X. Bertin, M. Rodrigues, J. Ferreira, and M. L. Liberato (2017), A numerical study of the February 15, 1941 storm in the Tagus estuary, *Continental Shelf Research*, *144*, 50–64, doi:10.1016/j.csr.2017.06.023.
- Fredsøe, J., and R. Deigaard (1992), *Mechanics of Coastal Sediment Transport*, WORLD SCIENTIFIC, doi:10.1142/1546.
- French, J. R. (1993), Numerical simulation of vertical marsh growth and adjustment to accelerated sea-level rise, North Norfolk, U.K., *Earth Surface Processes and Landforms*, *18*(1), 63–81, doi:10.1002/esp.3290180105.
- Fritz, H. M., C. Blount, R. Sokoloski, J. Singleton, A. Fuggle, B. G. McAdoo, A. Moore, C. Grass, and B. Tate (2007), Hurricane Katrina storm surge distribution and field observations on the Mississippi Barrier Islands, *Estuarine, Coastal and Shelf Science*, *74*(1), 12–20, doi:10.1016/j.ecss.2007.03.015.
- Fritz, H. M., C. D. Blount, S. Thwin, M. K. Thu, and N. Chan (2009), Cyclone Nargis storm surge in Myanmar, *Nature Geoscience*, *2*, 448–449, doi:10.1038/ngeo558.
- Gacia, E., and C. Duarte (2001), Sediment Retention by a Mediterranean Posidonia oceanica Meadow: The Balance between Deposition and Resuspension, *Estuarine, Coastal and Shelf Science*, *52*(4), 505–514, doi:10.1006/ecss.2000.0753.

- Garrett, C., et al. (1976), Generation of Langmuir circulations by surface waves—A feedback mechanism, *J. Mar. Res.*, *34*(1), 117–130.
- Garzon, J. L., M. Maza, C. M. Ferreira, J. L. Lara, and I. J. Losada (2019), Wave Attenuation by Spartina Saltmarshes in the Chesapeake Bay Under Storm Surge Conditions, *Journal of Geophysical Research: Oceans*, *124*(7), 5220–5243, doi:10.1029/2018JC014865.
- Geernaert, G. L., S. E. Larsen, and F. Hansen (1987), Measurements of the wind stress, heat flux, and turbulence intensity during storm conditions over the North Sea, *Journal of Geophysical Research: Oceans*, *92*(C12), 13,127–13,139, doi:10.1029/JC092iC12p13127.
- Gill, A. E. (1982), *Atmosphere-ocean dynamics*, vol. 30, Academic press.
- Gillibrand, P. A., E. M. Lane, R. A. Walters, and R. M. Gorman (2011), Forecasting extreme sea level events and coastal inundation from tides, surge and wave setup, *Australian Journal of Civil Engineering*, *9*(1), 99–112, doi:10.1080/14488353.2011.11463961.
- Goda, Y. (1975), Irregular Wave Deformation in the Surf Zone, *Coastal Engineering in Japan*, *18*(1), 13–26, doi:10.1080/05785634.1975.11924196.
- Gordon, L., and A. Lohrmann (2002), Near-Shore Doppler Current Meter Wave Spectra, in *Ocean Wave Measurement and Analysis (2001)*, pp. 33–43, doi:10.1061/40604(273)4.
- Goring, D. G., and V. I. Nikora (2002), Despiking Acoustic Doppler Velocimeter Data, *Journal of Hydraulic Engineering*, *128*(1), 117–126, doi:10.1061/(ASCE)0733-9429(2002)128:1(117).
- Grace, R. A. (1978), Surface wave heights from pressure records, *Coastal Engineering*, *2*, 55–67, doi:10.1016/0378-3839(78)90005-4.
- Grant, W. D., and O. S. Madsen (1979), Combined wave and current interaction with a rough bottom, *Journal of Geophysical Research: Oceans*, *84*(C4), 1797–1808, doi:10.1029/JC084iC04p01797.
- Griggs, G., L. Davar, and B. G. Reguero (2019), Documenting a Century of Coastline Change along Central California and Associated Challenges: From the Qualitative to the Quantitative, *Water*, *11*(12), doi:10.3390/w11122648.
- Guérin, T., X. Bertin, T. Coulombier, and A. de Bakker (2018), Impacts of wave-induced circulation in the surf zone on wave setup, *Ocean Modelling*, *123*, 86–97, doi:10.1016/j.oceomod.2018.01.006.
- Guillou, N. (2014), Wave-energy dissipation by bottom friction in the English Channel, *Ocean Engineering*, *82*, 42–51, doi:10.1016/j.oceaneng.2014.02.029.
- Günther, H., S. Hasselmann, and P. A. Janssen (1992), The WAM model Cycle 4 (revised version).
- Guza, R. T., and E. B. Thornton (1980), Local and shoaled comparisons of sea surface elevations, pressures, and velocities, *Journal of Geophysical Research: Oceans*, *85*(C3), 1524–1530, doi:10.1029/JC085iC03p01524.
- Guza, R. T., and E. B. Thornton (1981), Wave set-up on a natural beach, *Journal of Geophysical Research: Oceans*, *86*(C5), 4133–4137, doi:10.1029/JC086iC05p04133.

- Hanslow, D. J., and P. Nielsen (1992), Wave setup on beaches and in river entrances, in *Coastal Engineering 1992*, pp. 240–252, doi:10.1061/9780872629332.018.
- Hanslow, D. J., P. Nielsen, and K. Hibbert (1996), Wave Setup at River Entrances, in *Coastal Engineering 1996*, pp. 2244–2257, doi:10.1061/9780784402429.174.
- Hargreaves, J. C., and J. D. Annan (2001), Comments on “Improvement of the Short-Fetch Behavior in the Wave Ocean Model (WAM)”, *Journal of Atmospheric and Oceanic Technology*, 18(4), 711 – 715, doi:10.1175/1520-0426(2001)018<0711:COIOTS>2.0.CO;2.
- Harris, D. L. (1963), *Characteristics of the hurricane storm surge*, 48, Department of Commerce, Weather Bureau.
- Hasselmann, K. (1962), On the non-linear energy transfer in a gravity-wave spectrum Part 1. General theory, *Journal of Fluid Mechanics*, 12(4), 481–500, doi:10.1017/S0022112062000373.
- Hasselmann, K. (1982), The Marsen experiment: principal results and conclusions, in *First int. Conf. Meteorology and Air-Sea interaction of the Coastal Zone*, The Hague, p. 391. American Meteorology Society, Massachusetts, (unpublished).
- Hasselmann, K., et al. (1973), Measurements of wind-wave growth and swell decay during the Joint North Sea Wave Project (JONSWAP), *Ergänzungsheft 8-12*.
- Hasselmann, K. F., and J. Collins (1968), Spectral dissipation of finite-depth gravity waves due to turbulent bottom friction, *Journal of Marine Research*, 26, 1–12.
- Hasselmann, K. F., W. Munk, and G. J. MacDonald (1963), Bispectra of ocean waves, in *Symposium on Time Series Analysis*, pp. 125–139, New York.
- Hasselmann, S., and K. Hasselmann (1985), Computations and Parameterizations of the Nonlinear Energy Transfer in a Gravity-Wave Spectrum. Part I: A New Method for Efficient Computations of the Exact Nonlinear Transfer Integral, *Journal of Physical Oceanography*, 15(11), 1369 – 1377, doi:10.1175/1520-0485(1985)015<1369:CAPOTN>2.0.CO;2.
- Hasselmann, S., K. Hasselmann, J. Allender, and T. Barnett (1985), Computations and parameterizations of the nonlinear energy transfer in a gravity-wave spectrum. Part II: Parameterizations of the nonlinear energy transfer for application in wave models, *Journal of Physical Oceanography*, 15(11), 1378–1391, doi:10.1175/1520-0485(1985)015<1378:CAPOTN>2.0.CO;2.
- Hayes, M. O. (1980), General morphology and sediment patterns in tidal inlets, *Sedimentary geology*, 26(1-3), 139–156.
- Heaps, N. S. (1977), Development of storm-surge models at Bidston.
- Heaps, N. S. (1983), Storm surges, 1967–1982, *Geophysical Journal International*, 74(1), 331–376, doi:10.1111/j.1365-246X.1983.tb01883.x.
- Heaps, N. S., and J. Proudman (1969), A two-dimensional numerical sea model, *Philosophical Transactions of the Royal Society of London. Series A, Mathematical and Physical Sciences*, 265(1160), 93–137, doi:10.1098/rsta.1969.0041.

- Hench, J. L., and R. A. Luettich Jr (2003), Transient tidal circulation and momentum balances at a shallow inlet, *Journal of Physical Oceanography*, *33*(4), 913–932, doi:10.1175/1520-0485(2003)33<913:TTCAMB>2.0.CO;2.
- Herbers, T. H. C., and S. J. Lentz (2010), Observing Directional Properties of Ocean Swell with an Acoustic Doppler Current Profiler (ADCP), *Journal of Atmospheric and Oceanic Technology*, *27*(1), 210 – 225, doi:10.1175/2009JTECHO681.1.
- Herbers, T. H. C., N. R. Russnogle, and S. Elgar (2000), Spectral Energy Balance of Breaking Waves within the Surf Zone, *Journal of Physical Oceanography*, *30*(11), 2723 – 2737, doi:10.1175/1520-0485(2000)030<2723:SEBOBW>2.0.CO;2.
- Herbers, T. H. C., S. Elgar, N. A. Sarap, and R. T. Guza (2002), Nonlinear Dispersion of Surface Gravity Waves in Shallow Water, *Journal of Physical Oceanography*, *32*(4), 1181 – 1193, doi:10.1175/1520-0485(2002)032<1181:NDOSGW>2.0.CO;2.
- Hervouet, J.-M. (2007), *Hydrodynamics of free surface flows: modelling with the finite element method*, John Wiley & Sons.
- Hinkel, J., et al. (2014), Coastal flood damage and adaptation costs under 21st century sea-level rise, *Proceedings of the National Academy of Sciences*, *111*(9), 3292–3297, doi:10.1073/pnas.1222469111.
- Holmedal, L. E., and H. Wang (2015), Combined tidal and wind driven flows and residual currents, *Ocean Modelling*, *89*, 61–70, doi:10.1016/j.ocemod.2015.03.002.
- Horsburgh, K., and C. Wilson (2007), Tide-surge interaction and its role in the distribution of surge residuals in the North Sea, *Journal of Geophysical Research*, *112*.
- Hwang, P. A., D. W. Wang, E. J. Walsh, W. B. Krabill, and R. N. Swift (2000), Airborne Measurements of the Wavenumber Spectra of Ocean Surface Waves. Part I: Spectral Slope and Dimensionless Spectral Coefficient, *Journal of Physical Oceanography*, *30*(11), 2753 – 2767, doi:10.1175/1520-0485(2001)031<2753:AMOTWS>2.0.CO;2.
- Hwang, P. A., N. Reul, T. Meissner, and S. H. Yueh (2019), Whitecap and Wind Stress Observations by Microwave Radiometers: Global Coverage and Extreme Conditions, *Journal of Physical Oceanography*, *49*(9), 2291–2307, doi:10.1175/JPO-D-19-0061.1.
- Idier, D., F. Dumas, and H. Muller (2012), Tide-surge interaction in the English Channel, *Natural Hazards and Earth System Sciences*, *12*(12), 3709–3718, doi:10.5194/nhess-12-3709-2012.
- Isozaki, I. (1968), An investigation on the variations of sea level due to meteorological disturbances on the coast of Japan Islands (II), *J. Oceanogr. Soc. Japan*, *24*, 178–190.
- Jackson, D., C. F. Mason, and S. P. Long (1985), Macro-invertebrate populations and production on a salt-marsh in east England dominated by *Spartina anglica*, *Oecologia*, *65*(3), 406–411, doi:10.1007/BF00378916.
- Jadhav, R. S., Q. Chen, and J. M. Smith (2013), Spectral distribution of wave energy dissipation by salt marsh vegetation, *Coastal Engineering*, *77*, 99–107, doi:10.1016/j.coastaleng.2013.02.013.

- Janssen, P. A. (1991), Quasi-linear theory of wind-wave generation applied to wave forecasting, *Journal of physical oceanography*, *21*(11), 1631–1642, doi:10.1175/1520-0485(1991)021<1631:QLTOWW>2.0.CO;2.
- Janssen, P. A. (2008), Progress in ocean wave forecasting, *Journal of Computational Physics*, *227*(7), 3572–3594, doi:10.1016/j.jcp.2007.04.029, predicting weather, climate and extreme events.
- Janssen, P. A. E. M. (1982), Quasilinear approximation for the spectrum of wind-generated water waves, *Journal of Fluid Mechanics*, *117*, 493–506, doi:10.1017/S0022112082001736.
- Jarvinen, B. R., and M. B. Lawrence (1985), An evaluation of the SLOSH storm-surge model, *Bulletin of the American Meteorological Society*, *66*(11), 1408–1411.
- Jelesnianski, C. P. (1965), A numerical calculation of storm tides induced by a tropical storm impinging on a continental shelf, *Monthly Weather Review*, *93*(6), 343 – 358, doi:10.1175/1520-0493(1993)093<0343:ANCOS>2.3.CO;2.
- Jelesnianski, C. P. (1967), Numerical computations of storm surges with bottom stress, *Monthly Weather Review*, *95*(11), 740 – 756, doi:10.1175/1520-0493(1967)095<0740:NCOSSW>2.3.CO;2.
- Jelesnianski, C. P. (1992), *SLOSH: Sea, lake, and overland surges from hurricanes*, vol. 48, US Department of Commerce, National Oceanic and Atmospheric Administration.
- Johns, B., S. K. Dube, U. C. Mohanty, and P. C. Sinha (1981), Numerical simulation of the surge generated by the 1977 Andhra cyclone, *Quarterly Journal of the Royal Meteorological Society*, *107*(454), 919–934, doi:10.1002/qj.49710745411.
- Jones, N. L., and S. G. Monismith (2007), Measuring short-period wind waves in a tidally forced environment with a subsurface pressure gauge, *Limnology and Oceanography: Methods*, *5*(10), 317–327, doi:10.4319/lom.2007.5.317.
- Jonsson, I. G. (1967), Wave Boundary Layers and Friction Factors, in *Coastal Engineering 1966*, pp. 127–148, doi:10.1061/9780872620087.010.
- Keimer, K., D. Schürenkamp, F. Miescke, V. Kosmalla, O. Lojek, and N. Goseberg (2021), Ecohydraulics of Surrogate Salt Marshes for Coastal Protection: Wave–Vegetation Interaction and Related Hydrodynamics on Vegetated Foreshores at Sea Dikes, *Journal of Waterway, Port, Coastal, and Ocean Engineering*, *147*(6), 04021,035, doi:10.1061/(ASCE)WW.1943-5460.0000667.
- Keller, J. B. (1958), Surface waves on water of non-uniform depth, *Journal of Fluid Mechanics*, *4*(6), 607–614, doi:10.1017/S0022112058000690.
- Kennedy, A. B., U. Gravois, B. Zachry, R. Luettich, T. Whipple, R. Weaver, J. Reynolds-Fleming, Q. J. Chen, and R. Avissar (2010), Rapidly installed temporary gauging for hurricane waves and surge, and application to Hurricane Gustav, *Continental Shelf Research*, *30*(16), 1743–1752, doi:10.1016/j.csr.2010.07.013.
- Kennedy, A. B., et al. (2011), Origin of the Hurricane Ike forerunner surge, *Geophysical Research Letters*, *38*(8), doi:10.1029/2011GL047090.
- Kennedy, A. B., et al. (2012), Tropical cyclone inundation potential on the Hawaiian Islands of Oahu and Kauai, *Ocean Modelling*, *52*, 54–68, doi:10.1016/j.ocemod.2012.04.009.

- Kernkamp, H. W. J., A. Dam, G. S. Stelling, and E. D. Goede (2011), Efficient scheme for the shallow water equations on unstructured grids with application to the Continental Shelf, *Ocean Dynamics*, *61*(8), 1175–1188, doi:10.1007/s10236-011-0423-6, this article is part of the Topical Collection on Joint Numerical Sea Modelling Group Workshop 2010.
- Kerr, P. C., et al. (2013), US IOOS coastal and ocean modeling testbed: Inter-model evaluation of tides, waves, and hurricane surge in the Gulf of Mexico, *Journal of Geophysical Research: Oceans*, *118*(10), 5129–5172, doi:10.1002/jgrc.20376.
- Ketabchi, H., D. Mahmoodzadeh, B. Ataie-Ashtiani, and C. T. Simmons (2016), Sea-level rise impacts on seawater intrusion in coastal aquifers: Review and integration, *Journal of Hydrology*, *535*, 235–255, doi:10.1016/j.jhydrol.2016.01.083.
- Kim, S. (2019), Storm Surges, in *Encyclopedia of Ocean Sciences (Third Edition)*, edited by J. K. Cochran, H. J. Bokuniewicz, and P. L. Yager, third edition ed., pp. 663–671, Academic Press, Oxford, doi:10.1016/B978-0-12-409548-9.10849-8.
- Kim, S., T. Yasuda, and H. Mase (2010), Wave set-up in the storm surge along open coasts during Typhoon Anita, *Coastal Engineering*, *57*(7), 631–642, doi:10.1016/j.coastaleng.2010.02.004.
- Kim, S., Y. Matsumi, T. Yasuda, and H. Mase (2014), Storm surges along the Tottori coasts following a typhoon, *Ocean Engineering*, *91*, 133–145, doi:10.1016/j.oceaneng.2014.09.005.
- Kim, S., N. Mori, H. Mase, and T. Yasuda (2015), The role of sea surface drag in a coupled surge and wave model for Typhoon Haiyan 2013, *Ocean Modelling*, *96*, 65–84, doi:10.1016/j.ocemod.2015.06.004, waves and coastal, regional and global processes.
- Kirby, J. T., and T.-M. Chen (1989), Surface waves on vertically sheared flows: Approximate dispersion relations, *Journal of Geophysical Research: Oceans*, *94*(C1), 1013–1027, doi:10.1029/JC094iC01p01013.
- Kirby, J. T., G. Wei, Q. Chen, A. B. Kennedy, and R. A. Dalrymple (1998), FUNWAVE 1.0: fully nonlinear Boussinesq wave model-Documentation and user's manual, *research report NO. CACR-98-06*.
- Klopman, G. (1994), Stokes transport, *WL-Delft Hydraulics Report H840.30, Part II*.
- Knutson, P. L., R. A. Brochu, W. N. Seelig, and M. Inskeep (1982), Wave damping in *Spartina alterniflora* marshes, *Wetlands*, *2*(1), 87–104.
- Kobayashi, N., A. Raichle, and T. Asano (1993), Wave attenuation by vegetation, *Journal of Waterway, Port, Coastal and Ocean Engineering*, *119*(1), 30–48, doi:10.1061/(ASCE)0733-950X(1993)119:1(30).
- Koehl, M. A. R. (2015), How Do Benthic Organisms Withstand Moving Water?, *American Zoologist*, *24*(1), 57–70, doi:10.1093/icb/24.1.57.
- Kohno, N., S. K. Dube, M. Entel, S. Fakhruddin, D. Greenslade, M.-D. Leroux, J. Rhome, and N. B. Thuy (2018), Recent Progress in Storm Surge Forecasting, *Tropical Cyclone Research and Review*, *7*(2), 128 – 139, doi:10.6057/2018TCRR02.04.
- Komar, P. D. (1998), *Beach processes and sedimentation*.

- Komar, P. D., J. C. Allan, and P. Ruggiero (2010), Ocean Wave Climates: Trends and Variations Due to Earth's Changing Climate, in *Handbook of Coastal and Ocean Engineering*, pp. 971–995, doi:10.1142/9789812819307_0035.
- Komen, G. J., L. Cavaleri, M. Donelan, K. Hasselmann, S. Hasselmann, and P. A. E. M. Janssen (1994), *Dynamics and Modelling of Ocean Waves*, Cambridge University Press, Cambridge, U.K., doi:10.1017/CBO9780511628955.
- Kowalczyk, H. (2016), Wave transformation at a rock platform in Victoria, Australia - A study combining field measurements with numerical modelling, student Paper.
- Kranenburg, W. M., J. S. Ribberink, R. E. Uittenbogaard, and S. J. M. H. Hulscher (2012), Net currents in the wave bottom boundary layer: On wavelshape streaming and progressive wave streaming, *Journal of Geophysical Research: Earth Surface*, 117(F3), doi:10.1029/2011JF002070.
- Krien, Y., et al. (2017), Towards improved storm surge models in the northern Bay of Bengal, *Continental Shelf Research*, 135, 58–73, doi:10.1016/j.csr.2017.01.014.
- Kumar, N., G. Voulgaris, J. C. Warner, and M. Olabarrieta (2012), Implementation of the vortex force formalism in the coupled ocean-atmosphere-wave-sediment transport (COAWST) modeling system for inner shelf and surf zone applications, *Ocean Modelling*, 47, 65–95, doi:10.1016/j.ocemod.2012.01.003.
- Kummu, M., H. de Moel, G. Salvucci, D. Viviroli, P. J. Ward, and O. Varis (2016), Over the hills and further away from coast: global geospatial patterns of human and environment over the 20th–21st centuries, *Environmental Research Letters*, 11(3), 034,010, doi:10.1088/1748-9326/11/3/034010.
- Lambert, E., J. Rohmer, G. L. Cozannet, and R. S. W. van de Wal (2020), Adaptation time to magnified flood hazards underestimated when derived from tide gauge records, *Environmental Research Letters*, 15(7), 074,015, doi:10.1088/1748-9326/ab8336.
- Lambert, N. (2009), Modélisation de la dissipation de l'énergie des vagues par la végétation de marais littoral, Ph.D. thesis, Université du Québec à Rimouski.
- Lane, E. M., J. M. Restrepo, and J. C. McWilliams (2007), Wave–Current Interaction: A Comparison of Radiation-Stress and Vortex-Force Representations, *Journal of Physical Oceanography*, 37(5), 1122 – 1141, doi:10.1175/JPO3043.1.
- Lange, B., H. K. Johnson, S. Larsen, J. Højstrup, H. Kofoed-Hansen, and M. J. Yelland (2004), On Detection of a Wave Age Dependency for the Sea Surface Roughness, *Journal of Physical Oceanography*, 34(6), 1441 – 1458, doi:10.1175/1520-0485(2004)034<1441:ODOAWA>2.0.CO;2.
- Lara, J., M. Maza, B. Ondiviela, J. Trinogga, I. Losada, T. Bouma, and N. Gordejuela (2016), Large-scale 3-D experiments of wave and current interaction with real vegetation. Part 1: Guidelines for physical modeling, *Coastal Engineering*, 107, 70–83, doi:10.1016/j.coastaleng.2015.09.012.
- Lavaud, L., X. Bertin, K. Martins, G. Arnaud, and M.-N. Bouin (2020a), The contribution of short-wave breaking to storm surges: The case Klaus in the Southern Bay of Biscay, *Ocean Modelling*, 156, 101,710, doi:10.1016/j.ocemod.2020.101710.

- Lavaud, L., M. Pezerat, T. Coulombier, X. Bertin, and K. Martins (2020b), Hydrodynamics on a Rocky Shore under Moderate-energy Wave Conditions, *Journal of Coastal Research*, 95(SI), 1473–1479, doi:10.2112/SI95-284.1.
- Lavaud, L., X. Bertin, K. Martins, M. Pezerat, T. Coulombier, and D. Dausse (2022), Wave dissipation and mean circulation on a shore platform under storm wave conditions, *Journal of Geophysical Research: Earth Surface*, 127(3), e2021JF006466, doi:10.1029/2021JF006466.
- Lazure, P., and F. Dumas (2008), An external–internal mode coupling for a 3D hydrodynamical model for applications at regional scale (MARS), *Advances in Water Resources*, 31(2), 233–250, doi:10.1016/j.advwatres.2007.06.010.
- Le Hir, P., W. Roberts, O. Cazaillet, M. Christie, P. Bassoullet, and C. Bacher (2000), Characterization of intertidal flat hydrodynamics, *Continental Shelf Research*, 20(12), 1433–1459, doi:10.1016/S0278-4343(00)00031-5.
- Le Hir, P., Y. Monbet, and F. Orvain (2007), Sediment erodability in sediment transport modelling: Can we account for biota effects?, *Continental Shelf Research*, 27(8), 1116–1142, doi:10.1016/j.csr.2005.11.016, natural Coastal Mechanisms - Flume and Field Experiments on Links between Biology, Sediments and Flow.
- Lentz, S., and B. Raubenheimer (1999), Field observations of wave setup, *Journal of Geophysical Research: Oceans*, 104(C11), 25,867–25,875, doi:10.1029/1999JC900239.
- Leonard, B. (1991), The ULTIMATE conservative difference scheme applied to unsteady one-dimensional advection, *Computer Methods in Applied Mechanics and Engineering*, 88(1), 17–74, doi:10.1016/0045-7825(91)90232-U.
- Leonardi, N., I. Carnacina, C. Donatelli, N. K. Ganju, A. J. Plater, M. Schuerch, and S. Temmerman (2018), Dynamic interactions between coastal storms and salt marshes: A review, *Geomorphology*, 301, 92–107, doi:10.1016/j.geomorph.2017.11.001.
- Lerma, A. N., R. Pedreros, A. Robinet, and N. Sénéchal (2017), Simulating wave setup and runup during storm conditions on a complex barred beach, *Coastal Engineering*, 123, 29–41, doi:10.1016/j.coastaleng.2017.01.011.
- Li, C. W., and K. Yan (2007), Numerical Investigation of Wave-Current-Vegetation Interaction, *Journal of Hydraulic Engineering*, 133(7), 794–803, doi:10.1061/(ASCE)0733-9429(2007)133:7(794).
- Liberato, M. L., J. G. Pinto, I. F. Trigo, and R. M. Trigo (2011), Klaus—an exceptional winter storm over northern Iberia and southern France, *Weather*, 66(12), 330–334, doi:10.1002/wea.755.
- Loder, N., J. Irish, M. Cialone, and T. Wamsley (2009), Sensitivity of hurricane surge to morphological parameters of coastal wetlands, *Estuarine, Coastal and Shelf Science*, 84(4), 625–636, doi:10.1016/j.ecss.2009.07.036.
- Longuet-Higgins, M. S. (1953), Mass transport in water waves, *Phil. Trans. Roy. Soc. London, A*, A245(903), 535–581, doi:10.1098/rsta.1953.0006.
- Longuet-Higgins, M. S. (1970a), Longshore currents generated by obliquely incident sea waves: 1, *Journal of Geophysical Research (1896-1977)*, 75(33), 6778–6789, doi:10.1029/JC075i033p06778.

- Longuet-Higgins, M. S. (1970b), Longshore currents generated by obliquely incident sea waves: 2, *Journal of Geophysical Research (1896-1977)*, *75*(33), 6790–6801, doi:10.1029/JC075i033p06790.
- Longuet-Higgins, M. S., and R. Stewart (1962), Radiation stress and mass transport in gravity waves, with application to ‘surf beats’, *Journal of Fluid Mechanics*, *13*(4), 481–504, doi:10.1017/S0022112062000877.
- Longuet-Higgins, M. S., and R. Stewart (1964), Radiation stresses in water waves; a physical discussion, with applications, in *Deep Sea Research and Oceanographic Abstracts*, vol. 11, pp. 529–562, Elsevier, doi:10.1016/0011-7471(64)90001-4.
- Lowe, R., S. Monismith, and M. Atkinson (2009), Wave-Driven Circulation of a Coastal Reef-Lagoon System, *Journal of Physical Oceanography*, *39*(4), 873–893, doi:10.1175/2008JPO3958.1.
- Lowe, R. J., J. L. Falter, M. D. Bandet, G. Pawlak, M. J. Atkinson, S. G. Monismith, and J. R. Koseff (2005), Spectral wave dissipation over a barrier reef, *Journal of Geophysical Research: Oceans*, *110*(C4), doi:10.1029/2004JC002711.
- Lowe, R. J., J. L. Falter, J. R. Koseff, S. G. Monismith, and M. J. Atkinson (2007), Spectral wave flow attenuation within submerged canopies: Implications for wave energy dissipation, *Journal of Geophysical Research: Oceans*, *112*(C5), doi:10.1029/2006JC003605.
- Luetlich, R. A., J. J. Westerink, N. W. Scheffner, et al. (1992), ADCIRC: an advanced three-dimensional circulation model for shelves, coasts, and estuaries. Report 1, Theory and methodology of ADCIRC-2DD1 and ADCIRC-3DL.
- Luhar, M., and H. Nepf (2016), Wave-induced dynamics of flexible blades, *Journal of Fluids and Structures*, *61*, 20–41, doi:10.1016/j.jfluidstructs.2015.11.007.
- Løvås, S. M., and A. Tørum (2001), Effect of the kelp laminaria hyperborea upon sand dune erosion and water particle velocities, *Coastal Engineering*, *44*(1), 37–63, doi:10.1016/S0378-3839(01)00021-7.
- Lyard, F., L. Carrere, M. Cancet, A. Guillot, and N. Picot (2017), FES2014, a new finite elements tidal model for global ocean, *Ocean Dynam.*, *in preparation*, *10*.
- Ma, G., F. Shi, and J. T. Kirby (2012), Shock-capturing non-hydrostatic model for fully dispersive surface wave processes, *Ocean Modelling*, *43-44*, 22–35, doi:10.1016/j.ocemod.2011.12.002.
- Ma, G., J. T. Kirby, S.-F. Su, J. Figlus, and F. Shi (2013), Numerical study of turbulence and wave damping induced by vegetation canopies, *Coastal Engineering*, *80*, 68–78, doi:10.1016/j.coastaleng.2013.05.007.
- Madsen, J. D., P. A. Chambers, W. F. James, E. W. Koch, and D. F. Westlake (2001), The interaction between water movement, sediment dynamics and submersed macrophytes, *Hydrobiologia*, *444*(1-3), 71–84, doi:10.1023/A:1017520800568.
- Madsen, O. S., Y.-K. Poon, and H. C. Graber (1989), Spectral Wave Attenuation by Bottom Friction: Theory, in *Coastal Engineering 1988*, pp. 492–504, doi:10.1061/9780872626874.035.

- Malhadas, M. S., P. C. Leitão, A. Silva, and R. Neves (2009), Effect of coastal waves on sea level in Óbidos Lagoon, Portugal, *Continental Shelf Research*, *29*(9), 1240–1250, doi:10.1016/j.csr.2009.02.007.
- Marcos, M., and M. N. Tsimplis (2007), Variations of the seasonal sea level cycle in southern Europe, *Journal of Geophysical Research: Oceans*, *112*(C12), doi:10.1029/2006JC004049.
- Marsaleix, P., F. Auclair, J. W. Floor, M. J. Herrmann, C. Estournel, I. Pairaud, and C. Ulses (2008), Energy conservation issues in sigma-coordinate free-surface ocean models, *Ocean Modelling*, *20*(1), 61–89, doi:10.1016/j.ocemod.2007.07.005.
- Marshall, R. J., and W. J. Stephenson (2011), The morphodynamics of shore platforms in a micro-tidal setting: Interactions between waves and morphology, *Marine Geology*, *288*(1), 18–31, doi:10.1016/j.margeo.2011.06.007.
- Martins, F. A. B. d. C. (1999), Modelacao matemática tridimensional de escoamentos costeiros e estuarinos usando uma abordagem de coordenada vertical genérica.
- Martins, K., C. E. Blenkinsopp, R. Almar, and J. Zang (2017a), The influence of swash-based reflection on surf zone hydrodynamics: a wave-by-wave approach, *Coastal Engineering*, *122*, 27–43, doi:10.1016/j.coastaleng.2017.01.006.
- Martins, K., P. Bonneton, F. Frappart, G. Detandt, N. Bonneton, and C. E. Blenkinsopp (2017b), High Frequency Field Measurements of an Undular Bore Using a 2D LiDAR Scanner, *Remote Sensing*, *9*(5), doi:10.3390/rs9050462.
- Martins, K., C. E. Blenkinsopp, R. Deigaard, and H. E. Power (2018), Energy Dissipation in the Inner Surf Zone: New Insights From LiDAR-Based Roller Geometry Measurements, *Journal of Geophysical Research: Oceans*, *123*(5), 3386–3407, doi:10.1029/2017JC013369.
- Martins, K., P. Bonneton, A. Mouragues, and B. Castelle (2020), Non-hydrostatic, Non-linear Processes in the Surf Zone, *Journal of Geophysical Research: Oceans*, *125*(2), e2019JC015521, doi:10.1029/2019JC015521.
- Martins, K., P. Bonneton, and H. Michallet (2021a), Dispersive characteristics of non-linear waves propagating and breaking over a mildly sloping laboratory beach, *Coastal Engineering*, *167*, 103,917, doi:10.1016/j.coastaleng.2021.103917.
- Martins, K., P. Bonneton, D. Lannes, and H. Michallet (2021b), Relation between Orbital Velocities, Pressure, and Surface Elevation in Nonlinear Nearshore Water Waves, *Journal of Physical Oceanography*, *51*(11), 3539 – 3556, doi:10.1175/JPO-D-21-0061.1.
- Mastenbroek, C., G. Burgers, and P. Janssen (1993), The dynamical coupling of a wave model and a storm surge model through the atmospheric boundary layer, *Journal of physical Oceanography*, *23*(8), 1856–1866, doi:10.1175/1520-0485(1993)023<1856:TDCOAW>2.0.CO;2.
- Maza, M., J. L. Lara, I. J. Losada, B. Ondiviela, J. Trinogga, and T. J. Bouma (2015), Large-scale 3-d experiments of wave and current interaction with real vegetation. part 2: Experimental analysis, *Coastal Engineering*, *106*, 73–86, doi:10.1016/j.coastaleng.2015.09.010.

- McCall, R. T., G. Masselink, M. Austin, T. Poate, and T. Jager (2017), Modelling incident-band and infra gravity wave dynamics on rocky shore platforms, in *Coastal Dynamics 2017*.
- McInnes, K. L., G. D. Hubbert, D. J. Abbs, and S. E. Oliver (2002), A numerical modelling study of coastal flooding, *Meteorology and Atmospheric Physics*, *80*(1-4), 217–233, doi:10.1007/s007030200027.
- McWilliams, J. C., J. M. Restrepo, and E. M. Lane (2004), An asymptotic theory for the interaction of waves and currents in coastal waters, *Journal of Fluid Mechanics*, *511*, 135–178.
- Melet, A., B. Meyssignac, R. Almar, and G. Le Cozannet (2018), Under-estimated wave contribution to coastal sea-level rise, *Nature Climate Change*, *8*(3), 234, doi:10.1038/s41558-018-0088-y.
- Mellor, G. (2002), Oscillatory bottom boundary layers, *Journal of Physical Oceanography*, *32*(11), 3075–3088, doi:10.1175/1520-0485(2002)032<3075:OBBL>2.0.CO;2.
- Mellor, G. (2003), The three-dimensional current and surface wave equations, *Journal of Physical Oceanography*, *33*(9), 1978–1989.
- Mellor, G. (2013), Waves, circulation and vertical dependence, *Ocean Dynamics*, *63*(4), 447–457, doi:10.1007/s10236-013-0601-9, this article is part of the Topical Collection on the 4th International Workshop on Modelling the Ocean in Yokohama, Japan 21–24 May 2012.
- Mellor, G. (2015), A combined derivation of the integrated and vertically resolved, coupled wave-current equations, *Journal of Physical Oceanography*, *45*(6), 1453–1463, doi:10.1175/JPO-D-14-0112.1, cited By 33.
- Mellor, G. L. (2008), The Depth-Dependent Current and Wave Interaction Equations: A Revision, *Journal of Physical Oceanography*, *38*(11), 2587 – 2596, doi:10.1175/2008JPO3971.1.
- Mendez, F., I. Losada, and M. Losada (1999), Hydrodynamics induced by wind waves in a vegetation field, *Journal of Geophysical Research: Oceans*, *104*(C8), 18,383–18,396.
- Mendez, F. J., and I. J. Losada (2004), An empirical model to estimate the propagation of random breaking and nonbreaking waves over vegetation fields, *Coastal Engineering*, *51*, 103–118, doi:10.1016/j.coastaleng.2003.11.003.
- Mentaschi, L., M. I. Vousdoukas, E. Voukouvalas, A. Dosio, and L. Feyen (2017), Global changes of extreme coastal wave energy fluxes triggered by intensified teleconnection patterns, *Geophysical Research Letters*, *44*(5), 2416–2426, doi:10.1002/2016GL072488.
- Michaud, H. (2011), Impacts des vagues sur les courants marins: Modélisation multi-échelle de la plage au plateau continental, Ph.D. thesis, Montpellier 2.
- Miche, M. (1944), Mouvements ondulatoires de la mer en profondeur constante ou décroissante, *Annales de Ponts et Chaussées*, *1944*, pp (1) 26-78,(2) 270-292,(3) 369-406.
- Michel, D., and H. Howa (1997), Morphodynamic behaviour of a tidal inlet system in a mixed-energy environment, *Physics and Chemistry of the Earth*, *22*(3-4), 339–343, doi:10.1016/S0079-1946(97)00155-9.

- Miles, J. W. (1957), On the generation of surface waves by shear flows, *Journal of Fluid Mechanics*, 3(2), 185–204, doi:10.1017/S0022112057000567.
- Mitsuyasu, H., Y.-Y. Kuo, and A. Masuda (1979), On the dispersion relation of random gravity waves. Part 2. An experiment, *Journal of Fluid Mechanics*, 92(4), 731–749, doi:10.1017/S0022112079000859.
- Möller, I., and T. Spencer (2002), Wave dissipation over macro-tidal saltmarshes: Effects of marsh edge typology and vegetation change, *Journal of Coastal Research*, (36 (10036)), 506–521, doi:10.2112/1551-5036-36.sp1.506.
- Möller, I., T. Spencer, J. French, D. Leggett, and M. Dixon (1999), Wave Transformation Over Salt Marshes: A Field and Numerical Modelling Study from North Norfolk, England, *Estuarine, Coastal and Shelf Science*, 49(3), 411–426, doi:10.1006/ecss.1999.0509.
- Möller, I., et al. (2014), Wave attenuation over coastal salt marshes under storm surge conditions, *Nature Geoscience*, 7, 727–731, doi:10.1038/NGEO2251.
- Moghim, S., J. Thomson, T. Özkan Haller, L. Umlauf, and S. Zippel (2016), On the modeling of wave-enhanced turbulence nearshore, *Ocean Modelling*, 103, 118–132, doi:10.1016/j.ocemod.2015.11.004, waves and coastal, regional and global processes.
- Monbaliu, J., R. Padilla-Hernández, J. C. Hargreaves, J. C. C. Albiach, W. Luo, M. Sclavo, and H. Günther (2000), The spectral wave model, WAM, adapted for applications with high spatial resolution, *Coastal Engineering*, 41(1), 41–62, doi:10.1016/S0378-3839(00)00026-0.
- Monserrat, S., I. Vilibić, and A. B. Rabinovich (2006), Meteotsunamis: atmospherically induced destructive ocean waves in the tsunami frequency band, *Natural Hazards and Earth System Sciences*, 6(6), 1035–1051, doi:10.5194/nhess-6-1035-2006.
- Moon, I.-J., J.-I. Kwon, J.-C. Lee, J.-S. Shim, S. K. Kang, I. S. Oh, and S. J. Kwon (2009), Effect of the surface wind stress parameterization on the storm surge modeling, *Ocean Modelling*, 29(2), 115–127, doi:10.1016/j.ocemod.2009.03.006.
- Mori, N., T. Suzuki, and S. Kakuno (2007), Noise of Acoustic Doppler Velocimeter Data in Bubbly Flows, *Journal of Engineering Mechanics*, 133(1), 122–125, doi:10.1061/(ASCE)0733-9399(2007)133:1(122).
- Morison, J., J. Johnson, and S. Schaaf (1950), The Force Exerted by Surface Waves on Piles, *Journal of Petroleum Technology*, 2(05), 149–154, doi:10.2118/950149-G.
- Mork, M. (1996), The effect of kelp in wave damping, *Sarsia*, 80(4), 323–327, doi:10.1080/00364827.1996.10413607.
- Morris, R. L., T. M. Konlechner, M. Ghisalberti, and S. E. Swearer (2018), From grey to green: Efficacy of eco-engineering solutions for nature-based coastal defence, *Global Change Biology*, 24(5), 1827–1842, doi:10.1111/gcb.14063.
- Mouragues, A., P. Bonneton, D. Lannes, B. Castelle, and V. Marieu (2019), Field data-based evaluation of methods for recovering surface wave elevation from pressure measurements, *Coastal Engineering*, 150, 147–159, doi:10.1016/j.coastaleng.2019.04.006.

- Mugica, J., E. Delvallée, and R. Pedreros (2010), Application de modèles numériques pour l'estimation de l'altitude du plan d'eau à Andernos-les-Bains, *Tech. rep.*, Rapport BRGM/RP-58723-FR.
- Mullarney, J. C., and S. M. Henderson (2010), Wave-forced motion of submerged single-stem vegetation, *Journal of Geophysical Research: Oceans*, *115*(C12), doi:10.1029/2010JC006448.
- Munk, W. (1949), Surf beats, *Eos, Transactions American Geophysical Union*, *30*(6), 849–854, doi:10.1029/TR030i006p00849.
- Murty, P. L. N., A. D. Rao, K. S. Srinivas, E. P. R. Rao, and P. K. Bhaskaran (2019), Effect of Wave Radiation Stress in Storm Surge-Induced Inundation: A Case Study for the East Coast of India, *Pure and Applied Geophysics*, *177*(6), 2993–3012, doi:10.1007/s00024-019-02379-x.
- Nahon, A. (2018), Évolution morphologique actuelle d'une flèche littorale holocène: le Cap Ferret, à l'embouchure du Bassin d'Arcachon, Ph.D. thesis, Bordeaux.
- Nayak, S., P. K. Bhaskaran, and R. Venkatesan (2012), Near-shore wave induced setup along Kalpakkam coast during an extreme cyclone event in the Bay of Bengal, *Ocean Engineering*, *55*, 52–61, doi:doi.org/10.1016/j.oceaneng.2012.07.036.
- Naylor, L., W. Stephenson, and A. Trenhaile (2010), Rock coast geomorphology: Recent advances and future research directions, *Geomorphology*, *114*(1), 3–11, doi:10.1016/j.geomorph.2009.02.004, rock Coast Geomorphology.
- Naylor, L. A., D. M. Kennedy, and W. J. Stephenson (2014), Chapter 17 Synthesis and conclusion to the rock coast geomorphology of the world, *Geological Society, London, Memoirs*, *40*(1), 283–286, doi:10.1144/M40.17.
- Needham, H. F., B. D. Keim, and D. Sathiaraj (2015), A review of tropical cyclone-generated storm surges: Global data sources, observations, and impacts, *Reviews of Geophysics*, *53*(2), 545–591, doi:10.1002/2014RG000477.
- Nepf, H. M. (1999), Drag, turbulence, and diffusion in flow through emergent vegetation, *Water Resources Research*, *35*(2), 479–489, doi:10.1029/1998WR900069.
- Neumann, B., A. T. Vafeidis, J. Zimmermann, and R. J. Nicholls (2015), Future coastal population growth and exposure to sea-level rise and coastal flooding—a global assessment, *PLoS one*, *10*(3), e0118571, doi:10.1371/journal.pone.0118571.
- Nguyen, X. T., H. Tanaka, and H. Nagabayashi (2007), Wave Setup at River and Inlet Entrances during the Low Pressure System in 2006, in *PROCEEDINGS OF COASTAL ENGINEERING, JSCE*, vol. 54, pp. 321–325, Japan Society of Civil Engineers.
- Nicholls, R. J. (2018), Adapting to sea-level rise, *Resilience: The Science of Adaptation to Climate Change*, pp. 13–29, doi:10.1016/B978-0-12-811891-7.00002-5.
- Nowacki, D. J., A. Beudin, and N. K. Ganju (2017), Spectral wave dissipation by submerged aquatic vegetation in a back-barrier estuary, *Limnology and Oceanography*, *62*(2), 736–753, doi:10.1002/lno.10456.

- Ogawa, H. (2013), Observation of wave transformation on a sloping type B shore platform under wind-wave and swell conditions, *Geo-Marine Letters*, *33*(1), 1–11, doi:10.1007/s00367-012-0303-1.
- Ogawa, H., M. Dickson, and P. Kench (2011), Wave transformation on a sub-horizontal shore platform, Tatapouri, North Island, New Zealand, *Continental Shelf Research*, *31*(14), 1409–1419, doi:10.1016/j.csr.2011.05.006.
- Ogawa, H., P. Kench, and M. Dickson (2012), Field Measurements of Wave Characteristics on a Near-Horizontal Shore Platform, Mahia Peninsula, North Island, New Zealand, *Geographical Research*, *50*(2), 179–192, doi:10.1111/j.1745-5871.2011.00715.x.
- Ogawa, H., M. E. Dickson, and P. S. Kench (2015), Hydrodynamic constraints and storm wave characteristics on a sub-horizontal shore platform, *Earth Surface Processes and Landforms*, *40*(1), 65–77, doi:10.1002/esp.3619.
- Oh, J.-E., W.-M. Jeong, Y. S. Chang, and S.-H. Oh (2020), On the Separation Period Discriminating Gravity and Infragravity Waves off Gyeongpo Beach, Korea, *Journal of Marine Science and Engineering*, *8*(3), doi:10.3390/jmse8030167.
- Olabarrieta, M., J. C. Warner, and N. Kumar (2011), Wave-current interaction in Willapa Bay, *Journal of Geophysical Research: Oceans*, *116*(C12), doi:10.1029/2011JC007387.
- Oliveira, A., et al. (2020), OPENCoastS: An open-access service for the automatic generation of coastal forecast systems, *Environmental Modelling & Software*, *124*, 104,585, doi:10.1016/j.envsoft.2019.104585.
- Oost, W., G. Komen, C. Jacobs, and C. Van Oort (2002), New evidence for a relation between wind stress and wave age from measurements during ASGAMAGE, *Boundary-Layer Meteorology*, *103*(3), 409–438, doi:10.1023/A:1014913624535.
- Oppenheimer, M., et al. (2019), Sea level rise and implications for low lying islands, coasts and communities, *The Intergovernmental Panel on Climate Change*.
- Oshiyama, S., H. Lee, and H. Tanaka (2001), Fluctuation characteristics of water level in medium-and-small scale River mouths, in *Proceedings of 25th International Conference on Coastal Engineering, JSCE*, vol. 48, pp. 411–415.
- Osuna, P., and J. Monbaliu (2004), Wave–current interaction in the Southern North Sea, *Journal of Marine Systems*, *52*(1), 65–87, doi:10.1016/j.jmarsys.2004.03.002.
- Ozer, J., R. Padilla-Hernández, J. Monbaliu, E. Alvarez Fanjul, J. C. Carretero Albiach, P. Osuna, J. C. Yu, and J. Wolf (2000), A coupling module for tides, surges and waves, *Coastal Engineering*, *41*(1), 95–124, doi:10.1016/S0378-3839(00)00028-4.
- Pachauri, R. K., et al. (2014), *Climate Change 2014: Synthesis Report. Contribution of Working Groups I, II and III to the Fifth Assessment Report of the Intergovernmental Panel on Climate Change*, 151 pp., IPCC, Geneva, Switzerland.
- Pairaud, I. (2005), Modélisation et analyse de la marée interne dans le golfe de Gascogne, Ph.D. thesis, Toulouse 3.
- Pattiaratchi, C. B., and E. M. S. Wijeratne (2015), Are meteotsunamis an underrated hazard?, *Philosophical Transactions of the Royal Society A: Mathematical, Physical and Engineering Sciences*, *373*(2053), 20140,377, doi:10.1098/rsta.2014.0377.

- Paul, M., and C. L. Amos (2011), Spatial and seasonal variation in wave attenuation over *Zostera noltii*, *Journal of Geophysical Research: Oceans*, *116*(C8), doi:10.1029/2010JC006797.
- Paul, M., et al. (2016), Plant stiffness and biomass as drivers for drag forces under extreme wave loading: A flume study on mimics, *Coastal Engineering*, *117*, 70–78, doi:10.1016/j.coastaleng.2016.07.004.
- Payo-Payo, M., and X. Bertin (2020), The Seasonal Cycle of Mean Sea Level in the North East Atlantic Ocean, *Journal of Coastal Research*, *95*(sp1), 1515–1519, doi:10.2112/SI95-292.1.
- Pedersen, T., and S. Nylund (2004), Wave height measurements using acoustic surface tracking, in *2004 USA-Baltic Internation Symposium*, pp. 1–8, doi:10.1109/BALTIC.2004.7296806.
- Pedrerros, R., D. Idier, H. Muller, S. Lecacheux, F. Paris, M. Yates-Michelin, F. Dumas, L. Pineau-Guillou, and N. Senechal (2018), Relative contribution of wave setup to the storm surge: observations and modeling based analysis in open and protected environments (Truc Vert beach and Tubuai island), *Journal of Coastal Research*, *85*(sp1), 1046–1050, doi:10.2112/SI85-210.1.
- Peng, M., L. Xie, and L. J. Pietrafesa (2004), A numerical study of storm surge and inundation in the Croatan–Albemarle–Pamlico Estuary System, *Estuarine, Coastal and Shelf Science*, *59*(1), 121–137, doi:10.1016/j.ecss.2003.07.010.
- Pezerat, M., X. Bertin, K. Martins, B. Mengual, and L. Hamm (2021), Simulating storm waves in the nearshore area using spectral model: Current issues and a pragmatic solution, *Ocean Modelling*, *158*, 101,737, doi:10.1016/j.ocemod.2020.101737.
- Phan, L. K., J. S. van Thiel de Vries, and M. J. Stive (2014), Coastal Mangrove Squeeze in the Mekong Delta, *Journal of Coastal Research*, *31*(2), 233–243, doi:10.2112/JCOASTRES-D-14-00049.1.
- Phillips, O. (1977), The dynamics of the upper ocean, *Cambridge University Press, London*, p. 336 p.
- Phillips, O. M. (1985), Spectral and statistical properties of the equilibrium range in wind-generated gravity waves, *Journal of Fluid Mechanics*, *156*, 505–531, doi:10.1017/S0022112085002221.
- Pineau-Guillou, L., M.-N. Bouin, F. Ardhuin, F. Lyard, J.-R. Bidlot, and B. Chapron (2020), Impact of wave-dependent stress on storm surge simulations in the North Sea: Ocean model evaluation against in situ and satellite observations, *Ocean Modelling*, *154*, 101,694, doi:10.1016/j.ocemod.2020.101694.
- Plater, A., and J. Kirby (2011), Sea-level change and coastal geomorphic response, *Treatise on Estuarine and Coastal Science*, *3*, 39–72.
- Plüß, A. (2003), Das Nordseemodell der BAW zur Simulation der Tide in der Deutschen Bucht, *Die Küste*, *67*, (67), 84–127.
- Poate, T., G. Masselink, M. J. Austin, M. Dickson, and R. McCall (2018), The Role of Bed Roughness in Wave Transformation Across Sloping Rock Shore Platforms, *Journal of Geophysical Research: Earth Surface*, *123*(1), 97–123, doi:10.1002/2017JF004277.

- Pond, S., and G. Pickard (1983), Introductory dynamical oceanography. Butterworth Heinemann.
- Powell, M., P. Vickery, and T. Reinhold (2003), Reduced drag coefficient for high wind speeds in tropical cyclones, *Nature*, *422*(6929), 279–283, doi:10.1038/nature01481.
- Prandle, D., and G. E. R. Deacon (1975), Storm surges in the southern North Sea and River Thames, *Proceedings of the Royal Society of London. A. Mathematical and Physical Sciences*, *344*(1639), 509–539, doi:10.1098/rspa.1975.0117.
- Prandle, D., and J. Wolf (1978), The interaction of surge and tide in the North Sea and River Thames, *Geophysical Journal International*, *55*(1), 203–216, doi:10.1111/j.1365-246X.1978.tb04758.x.
- Proctor, R. (1981), Tides and residual circulation in the Irish Sea: A numerical modelling approach., Ph.D. thesis, University of Liverpool.
- Proudman, J. (1929), The Effects on the Sea of Changes in Atmospheric Pressure, *Geophysical Supplements to the Monthly Notices of the Royal Astronomical Society*, *2*(4), 197–209, doi:10.1111/j.1365-246X.1929.tb05408.x.
- Proudman, J. (1957), Oscillations of tide and surge in an estuary of finite length, *Journal of Fluid Mechanics*, *2*(4), 371–382, doi:10.1017/S002211205700018X.
- Pugh, D. (2004), *Changing sea levels: effects of tides, weather and climate*, Cambridge University Press.
- Pugh, D. T. (1987), Tides, surges and mean sea level.
- Putnam, J., and J. Johnson (1949), The dissipation of wave energy by bottom friction, *Eos, Transactions American Geophysical Union*, *30*(1), 67–74, doi:10.1029/TR030i001p00067.
- Quartel, S., A. Kroon, P. Augustinus, P. Van Santen, and N. Tri (2007), Wave attenuation in coastal mangroves in the Red River Delta, Vietnam, *Journal of Asian Earth Sciences*, *29*(4), 576–584, doi:10.1016/j.jseaes.2006.05.008, morphodynamics of the Red River Delta, Vietnam.
- Queffelec, P. (2004), Long-Term Validation of Wave Height Measurements from Altimeters, *Marine Geodesy*, *27*(3-4), 495–510, doi:10.1080/01490410490883478.
- Raschle, N., F. Ardhuin, and E. A. Terray (2006), Drift and mixing under the ocean surface: A coherent one-dimensional description with application to unstratified conditions, *Journal of Geophysical Research: Oceans*, *111*(C3), doi:10.1029/2005JC003004.
- Raubenheimer, B., R. T. Guza, and S. Elgar (1996), Wave transformation across the inner surf zone, *Journal of Geophysical Research: Oceans*, *101*(C11), 25,589–25,597, doi:10.1029/96JC02433.
- Raubenheimer, B., R. Guza, and S. Elgar (2001), Field observations of wave-driven setdown and setup, *Journal of Geophysical Research: Oceans*, *106*(C3), 4629–4638, doi:10.1029/2000JC000572.
- Rego, J., and C. Li (2010), Nonlinear terms in storm surge predictions: Effect of tide and shelf geometry with case study from Hurricane Rita, *Journal of Geophysical Research: Oceans*, *115*(6), doi:10.1029/2009JC005285.

- Rego, J. L., and C. Li (2009), On the importance of the forward speed of hurricanes in storm surge forecasting: A numerical study, *Geophysical Research Letters*, *36*(7), doi:10.1029/2008GL036953.
- Reniers, A., E. Thornton, T. Stanton, and J. Roelvink (2004), Vertical flow structure during Sandy Duck: observations and modeling, *Coastal Engineering*, *51*(3), 237–260, doi:10.1016/j.coastaleng.2004.02.001.
- Resio, D. T., and J. J. Westerink (2008), Modeling the physics of storm surges, *Physics Today*, *61*(9), 33, doi:10.1063/1.2982120.
- Riffe, K. C., S. M. Henderson, and J. C. Mullarney (2011), Wave dissipation by flexible vegetation, *Geophysical Research Letters*, *38*(18), doi:10.1029/2011GL048773.
- Rijnsdorp, D. P., M. L. Buckley, R. F. da Silva, M. V. W. Cuttler, J. E. Hansen, R. J. Lowe, R. H. Green, and C. D. Storlazzi (2021), A Numerical Study of Wave-Driven Mean Flows and Setup Dynamics at a Coral Reef-Lagoon System, *Journal of Geophysical Research: Oceans*, *126*(4), e2020JC016811, doi:10.1029/2020JC016811.
- Roelvink, J. A., and M. J. F. Stive (1989), Bar-generating cross-shore flow mechanisms on a beach, *Journal of Geophysical Research: Oceans*, *94*(C4), 4785–4800, doi:10.1029/JC094iC04p04785.
- Roland, A. (2009a), *Entwicklung von WWM II (Wind Wellen Model II): zur Seegangmodellierung auf unregelmäßigen Gitternetzen*, Inst. für Wasserbau und Wasserwirtschaft.
- Roland, A., and F. Ardhuin (2014), On the developments of spectral wave models: numerics and parameterizations for the coastal ocean, *Ocean Dynamics*, *64*(6), 833–846, doi:10.1007/s10236-014-0711-z.
- Roland, A., A. Cucco, C. Ferrarin, T.-W. Hsu, J.-M. Liau, S.-H. Ou, G. Umgiesser, and U. Zanke (2009b), On the development and verification of a 2-D coupled wave-current model on unstructured meshes, *Journal of Marine Systems*, *78*, S244–S254, doi:10.1016/j.jmarsys.2009.01.026, coastal Processes: Challenges for Monitoring and Prediction.
- Roland, A., Y. J. Zhang, H. V. Wang, Y. Meng, Y.-C. Teng, V. Maderich, I. Brovchenko, M. Dutour-Sikiric, and U. Zanke (2012), A fully coupled 3D wave-current interaction model on unstructured grids, *Journal of Geophysical Research: Oceans*, *117*(C11), doi:10.1029/2012JC007952.
- Rosales, P., F. Ocampo-Torres, P. Osuna, J. Monbaliu, and R. Padilla-Hernández (2008), Wave-current interaction in coastal waters: Effects on the bottom-shear stress, *Journal of Marine Systems*, *71*(1), 131–148, doi:10.1016/j.jmarsys.2007.06.006.
- Rositer, J. R., and A. T. Doodson (1954), The north sea storm surge of 31 January and 1 February 1953, *Philosophical Transactions of the Royal Society of London. Series A, Mathematical and Physical Sciences*, *246*(915), 371–400, doi:10.1098/rsta.1954.0002.
- Ruggiero, P., P. D. Komar, and J. C. Allan (2010), Increasing wave heights and extreme value projections: The wave climate of the U.S. Pacific Northwest, *Coastal Engineering*, *57*(5), 539–552, doi:10.1016/j.coastaleng.2009.12.005.
- Rusu, L., M. Bernardino, and C. G. Soares (2011), Modelling the influence of currents on wave propagation at the entrance of the Tagus estuary, *Ocean Engineering*, *38*(10), 1174–1183, doi:10.1016/j.oceaneng.2011.05.016.

- Saha, S., et al. (2010), The NCEP climate forecast system reanalysis, *Bulletin of the American Meteorological Society*, *91* (8), 1015–1058, doi:10.1175/2010BAMS3001.1.
- Salles, P., A. Valle-Levinson, A. Sottolichio, and N. Senechal (2015), Wind-driven modifications to the residual circulation in an ebb-tidal delta: Arcachon Lagoon, Southwestern France, *Journal of Geophysical Research: Oceans*, *120*(2), 728–740, doi:10.1002/2014JC010311.
- Salmon, J., P. Smit, T. Janssen, and L. Holthuijsen (2016), A consistent collinear triad approximation for operational wave models, *Ocean Modelling*, *104*, 203–212, doi:10.1016/j.ocemod.2016.06.009.
- Savage, T. R., H. E. Kowalczyk, T. E. Fellowes, and D. M. Kennedy (2021), The role of seaward morphology on wave transformation onto and across a microtidal shore platform, *Continental Shelf Research*, *224*, 104,472, doi:10.1016/j.csr.2021.104472.
- Saville, T. (1961), Experimental determination of wave set-up, *Proc. 2nd Tech. Conf. Hurricanes*, pp. 242–252.
- Schureman, P. (1958), Manual of Harmonic Analysis and Prediction of Tides. [Revised 1940 edition reprinted 1958 with corrections, reprinted 2001]. Washington DC, United States Government Printing Office, 317 pp, (*US Coast and Geodetic Survey, Special Publication 98*), doi:10.25607/OBP-155.
- Seiwell, H. (1947), Investigation of underwater pressure records and simultaneous sea surface patterns, *Eos, Transactions American Geophysical Union*, *28* (5), 722–724, doi:10.1029/TR028i005p00722.
- Sembiring, L., M. van Ormondt, A. van Dongeren, and D. Roelvink (2015), A validation of an operational wave and surge prediction system for the Dutch coast, *Natural Hazards and Earth System Sciences*, *15* (6), 1231–1242, doi:10.5194/nhess-15-1231-2015.
- Senechal, N., A. Sottolichio, F. Bertrand, L. Goeldner-Gianella, and T. Garlan (2013), Observations of waves' impact on currents in a mixed-energy tidal inlet: Arcachon on the southern French Atlantic coast, *Journal of Coastal Research*, *65*(SIv2), 2053–2058, doi:10.2112/SI65-347.1.
- Shchepetkin, A. F., and J. C. McWilliams (2005), The regional oceanic modeling system (ROMS): a split-explicit, free-surface, topography-following-coordinate oceanic model, *Ocean Modelling*, *9*(4), 347–404, doi:10.1016/j.ocemod.2004.08.002.
- Shen, J., K. Zhang, C. Xiao, and W. Gong (2006), Improved Prediction of Storm Surge Inundation with a High-Resolution Unstructured Grid Model, *Journal of Coastal Research*, *2006* (226), 1309 – 1319, doi:10.2112/04-0288.1.
- Sheng, P. Y. (1986), *A three-dimensional mathematical model of coastal, estuarine and lake currents using boundary fitted grid*, ARAP Group.
- Sheng, Y. P., V. Alymov, and V. A. Paramygin (2010a), Simulation of storm surge, wave, currents, and inundation in the Outer Banks and Chesapeake Bay during Hurricane Isabel in 2003: The importance of waves, *Journal of Geophysical Research: Oceans*, *115*(C4), doi:10.1029/2009JC005402.

- Sheng, Y. P., Y. Zhang, and V. A. Paramygin (2010b), Simulation of storm surge, wave, and coastal inundation in the Northeastern Gulf of Mexico region during Hurricane Ivan in 2004, *Ocean Modelling*, *35*(4), 314–331, doi:10.1016/j.oceomod.2010.09.004.
- Sheng, Y. P., A. Lapetina, and G. Ma (2012), The reduction of storm surge by vegetation canopies: Three-dimensional simulations, *Geophysical Research Letters*, *39*(20), doi:10.1029/2012GL053577.
- Shi, L., M. Olabarrieta, D. S. Nolan, and J. C. Warner (2020), Tropical cyclone rainbands can trigger meteotsunamis, *Nature Communications*, *11*, 678, doi:10.1038/s41467-020-14423-9.
- Shi, Z., J. S. Pethick, and K. Pye (1995), Flow Structure in and above the Various Heights of a Saltmarsh Canopy: A Laboratory Flume Study, *Journal of Coastal Research*, *11*(4), 1204–1209.
- Shom (2015), Shom,2015. MNT Bathymétrie de façade Atlantique (Projet Homonim).
- Siadatmousavi, S. M., F. Jose, and G. Stone (2011), The effects of bed friction on wave simulation: implementation of an unstructured third-generation wave model, SWAN, *Journal of Coastal Research*, *27*(1), 140–152, doi:10.2112/JCOASTRES-D-10-00073.1.
- Smith, J. A. (2006), Wave–Current Interactions in Finite Depth, *Journal of Physical Oceanography*, *36*(7), 1403 – 1419, doi:10.1175/JPO2911.1.
- Smith, J. M. (2002), Wave Pressure Gauge Analysis with Current, *Journal of Waterway, Port, Coastal, and Ocean Engineering*, *128*(6), 271–275, doi:10.1061/(ASCE)0733-950X(2002)128:6(271).
- Smith, K. (2013), *Environmental hazards: assessing risk and reducing disaster*, Routledge.
- Smith, S. D., and E. G. Banke (1975), Variation of the sea surface drag coefficient with wind speed, *Quarterly Journal of the Royal Meteorological Society*, *101*(429), 665–673, doi:10.1002/qj.49710142920.
- Sénéchal, N., H. Dupuis, P. Bonneton, H. Howa, and R. Pedreros (2001), Observation of irregular wave transformation in the surf zone over a gently sloping sandy beach on the French Atlantic coastline, *Oceanologica Acta*, *24*(6), 545–556, doi:10.1016/S0399-1784(01)01171-9.
- Soulsby, R. (1997), *Dynamics of marine sands*, Thomas Telford Publishing, doi:10.1680/doms.25844.
- Spalding, M. D., S. Ruffo, C. Lacambra, I. Meliane, L. Z. Hale, C. C. Shepard, and M. W. Beck (2014), The role of ecosystems in coastal protection: Adapting to climate change and coastal hazards, *Ocean & Coastal Management*, *90*, 50–57, doi:10.1016/j.ocecoaman.2013.09.007.
- Staneva, J., K. Wahle, W. Koch, A. Behrens, L. Fenoglio-Marc, and E. V. Stanev (2016), Coastal flooding: impact of waves on storm surge during extremes – a case study for the German Bight, *Natural Hazards and Earth System Sciences*, *16*(11), 2373–2389, doi:10.5194/nhess-16-2373-2016.

- Stephenson, W. J. (2000a), Shore platforms: a neglected coastal feature?, *Progress in Physical Geography: Earth and Environment*, *24*(3), 311–327, doi:10.1177/030913330002400301.
- Stephenson, W. J., and R. M. Kirk (2000b), Development of shore platforms on Kaikoura Peninsula, South Island, New Zealand: Part One: The role of waves, *Geomorphology*, *32*(1), 21–41, doi:10.1016/S0169-555X(99)00061-6.
- Stephenson, W. J., and L. E. Thornton (2005), Australian Rock Coasts: review and prospects, *Australian Geographer*, *36*(1), 95–115, doi:10.1080/00049180500050946.
- Stephenson, W. J., L. A. Naylor, H. Smith, B. Chen, and R. P. Brayne (2018), Wave transformation across a macrotidal shore platform under low to moderate energy conditions, *Earth Surface Processes and Landforms*, *43*(1), 298–311, doi:10.1002/esp.4245.
- Stewart, R. (1974), The air-sea momentum exchange, *Boundary-Layer Meteorology*, *6*(1-2), 151–167.
- Stive, M., and H. Wind (1982), A study of radiation stress and set-up in the nearshore region, *Coastal Engineering*, *6*(1), 1–25, doi:10.1016/0378-3839(82)90012-6.
- Stokes, G. (1847), On the Theory of Oscillatory Waves. Transaction of the Cambridge Society 8. 441-455. Reprinted in Stokes, GG (1880). Mathematical and Physical Papers.
- Sunamura, T. (1992), *Geomorphology of rocky coasts*, vol. 302, Wiley Chichester.
- Sutton-Grier, A. E., K. Wowk, and H. Bamford (2015), Future of our coasts: The potential for natural and hybrid infrastructure to enhance the resilience of our coastal communities, economies and ecosystems, *Environmental Science & Policy*, *51*, 137–148, doi:10.1016/j.envsci.2015.04.006.
- Suzuki, T., M. Zijlema, B. Burger, M. C. Meijer, and S. Narayan (2012), Wave dissipation by vegetation with layer schematization in SWAN, *Coastal Engineering*, *59*(1), 64–71, doi:10.1016/j.coastaleng.2011.07.006.
- Suzuki, T., Z. Hu, K. Kumada, L. Phan, and M. Zijlema (2019), Non-hydrostatic modeling of drag, inertia and porous effects in wave propagation over dense vegetation fields, *Coastal Engineering*, *149*, 49–64, doi:10.1016/j.coastaleng.2019.03.011.
- Svendsen, I. (1984a), Wave heights and set-up in a surf zone, *Coastal Engineering*, *8*(4), 303–329, doi:10.1016/0378-3839(84)90028-0.
- Takagaki, N., S. Komori, N. Suzuki, K. Iwano, T. Kuramoto, S. Shimada, R. Kurose, and K. Takahashi (2012), Strong correlation between the drag coefficient and the shape of the wind sea spectrum over a broad range of wind speeds, *Geophysical Research Letters*, *39*(23), doi:10.1029/2012GL053988.
- Tanaka, H., H. Nagabayashi, and K. Yamauchi (2001), Observation of wave set-up height in a river mouth, in *Coastal Engineering 2000*, pp. 3458–3471.
- Tanaka, H., L. Hyun-seok, and K. Furumichi (2003), Influence of morphological change on water level rise at the Shiribetsu River mouth, *Journal of hydroscience and hydraulic engineering*, *21*(1), 71–78.

- Tasnim, K. M., T. Shibayama, M. Esteban, H. Takagi, K. Ohira, and R. Nakamura (2015), Field observation and numerical simulation of past and future storm surges in the Bay of Bengal: case study of cyclone Nargis, *Natural Hazards*, *75*(2), 1619–1647, doi:10.1007/s11069-014-1387-x.
- Teixeira, M. A. C., and S. E. Belcher (2002), On the distortion of turbulence by a progressive surface wave, *Journal of Fluid Mechanics*, *458*, 229–267, doi:10.1017/S0022112002007838.
- Teles, M. (2013), Wave-current modelling at local and regional scales, Ph.D. thesis, PhD thesis, University of Lisbon, Instituto Superior Tecnico, Lisbon.
- Temmerman, S., M. B. De Vries, and T. J. Bouma (2012), Coastal marsh die-off and reduced attenuation of coastal floods: A model analysis, *Global and Planetary Change*, *92-93*, 267–274, doi:10.1016/j.gloplacha.2012.06.001.
- Terray, E., M. Donelan, Y. Agrawal, W. Drennan, K. Kahma, A. Williams, P. Hwang, and S. Kitaigorodskii (1996), Estimates of Kinetic Energy Dissipation under Breaking Waves, *Journal of Physical Oceanography*, *26*(5), 792–807, doi:10.1175/1520-0485(1996)026<0792:EOKEDU>2.0.CO;2.
- Thompson, J., E. Renzi, A. Sibley, and D. R. Tappin (2020), UK meteotsunamis: a revision and update on events and their frequency, *Weather*, *75*(9), 281–287, doi:10.1002/wea.3741.
- Thompson, R. C., T. P. Crowe, and S. J. Hawkins (2002), Rocky intertidal communities: past environmental changes, present status and predictions for the next 25 years, *Environmental Conservation*, *29*(2), 168–191, doi:10.1017/S0376892902000115.
- Thomson, J. (2012), Wave Breaking Dissipation Observed with “SWIFT” Drifters, *Journal of Atmospheric and Oceanic Technology*, *29*(12), 1866 – 1882, doi:10.1175/JTECH-D-12-00018.1.
- Thornton, E. B., and R. T. Guza (1983), Transformation of wave height distribution, *Journal of Geophysical Research: Oceans*, *88*(C10), 5925–5938, doi:10.1029/JC088iC10p05925.
- Thornton, E. B., and R. T. Guza (1986), Surf Zone Longshore Currents and Random Waves: Field Data and Models, *Journal of Physical Oceanography*, *16*(7), 1165–1178, doi:10.1175/1520-0485(1986)016<1165:SZLCAR>2.0.CO;2.
- Togneri, M., M. Lewis, S. Neill, and I. Masters (2017), Comparison of ADCP observations and 3D model simulations of turbulence at a tidal energy site, *Renewable Energy*, *114*, 273–282, doi:10.1016/j.renene.2017.03.061, wave and Tidal Resource Characterization.
- Tolman, H. L. (1992), Effects of Numerics on the Physics in a Third-Generation Wind-Wave Model, *Journal of Physical Oceanography*, *22*(10), 1095 – 1111, doi:10.1175/1520-0485(1992)022<1095:EONOTP>2.0.CO;2.
- Tolman, H. L. (1994), Wind Waves and Moveable-Bed Bottom Friction, *Journal of Physical Oceanography*, *24*(5), 994 – 1009, doi:10.1175/1520-0485(1994)024<0994:WWAMBB>2.0.CO;2.

- Tracy, B. A., and D. T. Resio (1982), Theory and calculation of the nonlinear energy transfer between sea waves in deep water., in *Proceedings of the Army Numerical and Computers Analysis Conference*, p. 457, US Army Research Office.
- Trenhaile, A. S. (1987), *The geomorphology of rock coasts*, Clarendon Press.
- Trenhaile, A. S. (2002), Rock coasts, with particular emphasis on shore platforms, *Geomorphology*, *48*(1), 7–22, doi:10.1016/S0169-555X(02)00173-3, 29th Binghamton Geomorphology Symposium: Coastal Geomorphology.
- Trenhaile, A. S., and J. I. Kanyaya (2007), The role of wave erosion on sloping and horizontal shore platforms in macro-and mesotidal environments, *Journal of Coastal Research*, *23*(2), 298–309, doi:10.2112/04-0282.1.
- Trowbridge, J., and O. S. Madsen (1984), Turbulent wave boundary layers: 2. Second-order theory and mass transport, *Journal of Geophysical Research: Oceans*, *89*(C5), 7999–8007, doi:10.1029/JC089iC05p07999.
- Tsai, C.-H., M.-C. Huang, F.-J. Young, Y.-C. Lin, and H.-W. Li (2005), On the recovery of surface wave by pressure transfer function, *Ocean Engineering*, *32*(10), 1247–1259, doi:10.1016/j.oceaneng.2004.10.020.
- Tucker, M. J., and E. G. Pitt (2001), *Waves in ocean engineering*, Volume 5.
- Turner, I. L., P. E. Russell, and T. Butt (2008), Measurement of wave-by-wave bed-levels in the swash zone, *Coastal Engineering*, *55*(12), 1237–1242, doi:10.1016/j.coastaleng.2008.09.009.
- Uchiyama, Y., J. C. McWilliams, and A. F. Shchepetkin (2010), Wave–current interaction in an oceanic circulation model with a vortex-force formalism: Application to the surf zone, *Ocean Modelling*, *34*(1), 16–35, doi:10.1016/j.ocemod.2010.04.002.
- Umgiesser, G., et al. (2021), The prediction of floods in Venice: methods, models and uncertainty (review article), *Natural Hazards and Earth System Sciences*, *21*(8), 2679–2704, doi:10.5194/nhess-21-2679-2021.
- Umlauf, L., H. Burchard, and K. Bolding (2005), *GOTM-scientific documentation: version 3.2*, Institut für Ostseeforschung.
- Van der Wal, D., A. Wielemaker-Van den Dool, and P. M. Herman (2008), Spatial patterns, rates and mechanisms of saltmarsh cycles (Westerschelde, The Netherlands), *Estuarine, Coastal and Shelf Science*, *76*(2), 357–368, doi:10.1016/j.ecss.2007.07.017.
- van der Westhuysen, A. J. (2010), Modeling of depth-induced wave breaking under finite depth wave growth conditions, *Journal of Geophysical Research: Oceans*, *115*(C1), doi:10.1029/2009JC005433.
- van der Westhuysen, A. J. (2012), Spectral modeling of wave dissipation on negative current gradients, *Coastal Engineering*, *68*, 17–30, doi:10.1016/j.coastaleng.2012.05.001.
- Van Dorn, W. (1953), Wind stress on an artificial pond, *Journal of Marine Research*, *12*.
- Van Dorn, W. G. (1978), Breaking invariants in shoaling waves, *Journal of Geophysical Research: Oceans*, *83*(C6), 2981–2988, doi:10.1029/JC083iC06p02981.

- van Rooijen, A. A., R. T. McCall, J. S. van Thiel de Vries, A. R. van Dongeren, A. J. Reniers, and J. A. Roelvink (2016), Modeling the effect of wave-vegetation interaction on wave setup, *Journal of Geophysical Research: Oceans*, *121*, 4341–4359, doi:10.1002/2015JC011392.
- van Veelen, T. J., T. P. Fairchild, D. E. Reeve, and H. Karunaratna (2020), Experimental study on vegetation flexibility as control parameter for wave damping and velocity structure, *Coastal Engineering*, *157*, 103,648, doi:10.1016/j.coastaleng.2020.103648.
- van Vledder, G. P., and D. P. Hurdle (2002), Performance of Formulations for Whitecapping in Wave Prediction Models, pp. 155–163, doi:10.1115/OMAE2002-28146.
- Verlaan, M., A. Zijderveld, H. de Vries, and J. Kroos (2005), Operational storm surge forecasting in the Netherlands: developments in the last decade, *Philosophical Transactions of the Royal Society A: Mathematical, Physical and Engineering Sciences*, *363*(1831), 1441–1453, doi:10.1098/rsta.2005.1578.
- Verlaan, M., S. De Kleermaeker, and L. Buckman (2015), GLOSSIS: Global Storm Surge Forecasting and Information System, in *In: Australasian Coasts & Ports Conference 2015: 22nd Australasian Coastal and Ocean Engineering Conference and the 15th Australasian Port and Harbour Conference. Auckland, New Zealand: Engineers Australia and IPENZ, 2015: 229-234.*
- Vitousek, S., P. L. Barnard, C. H. Fletcher, N. Frazer, L. Erikson, and C. D. Storlazzi (2017), Doubling of coastal flooding frequency within decades due to sea-level rise, *Scientific Reports*, *7*, doi:10.1038/s41598-017-01362-7.
- Vuik, V., S. N. Jonkman, B. W. Borsje, and T. Suzuki (2016), Nature-based flood protection: The efficiency of vegetated foreshores for reducing wave loads on coastal dikes, *Coastal Engineering*, *116*, 42–56, doi:10.1016/j.coastaleng.2016.06.001.
- Wahl, T., S. Jain, J. Bender, S. D. Meyers, and M. E. Luther (2015), Increasing risk of compound flooding from storm surge and rainfall for major US cities, *Nature Climate Change*, *5*(12), 1093–1097, doi:10.1038/nclimate2736.
- Wahl, T. L. (2003), Discussion of "Despiking Acoustic Doppler Velocimeter Data" by Derek G. Goring and Vladimir I. Nikora, *Journal of Hydraulic Engineering*, *129*(6), 484–487, doi:10.1061/(ASCE)0733-9429(2003)129:6(484).
- WAMDI (1988), The WAM Model—A Third Generation Ocean Wave Prediction Model, *Journal of Physical Oceanography*, *18*(12), 1775 – 1810, doi:10.1175/1520-0485(1988)018<1775:TWMTGO>2.0.CO;2.
- Wamsley, T. V., M. A. Cialone, J. M. Smith, J. H. Atkinson, and J. D. Rosati (2010), The potential of wetlands in reducing storm surge, *Ocean Engineering*, *37*(1), 59–68, doi:10.1016/j.oceaneng.2009.07.018, a Forensic Analysis of Hurricane Katrina's Impact: Methods and Findings.
- Wang, P., J. C. McWilliams, Y. Uchiyama, M. D. Chekroun, and D. L. Yi (2020), Effects of Wave Streaming and Wave Variations on Nearshore Wave-Driven Circulation, *Journal of Physical Oceanography*, *50*(10), 3025–3041, doi:10.1175/JPO-D-19-0304.1.
- Wanstrath, J. J., R. E. Whitaker, R. O. Reid, and A. C. Vastano (1976), Storm Surge Simulation in Transformed Coordinates. Volume I. Theory and Application., *Tech. rep.*, TEXAS A AND M RESEARCH FOUNDATION COLLEGE STATION.

- Ward, P. J., A. Couasnon, D. Eilander, I. D. Haigh, A. Hendry, S. Muis, T. I. E. Veldkamp, H. C. Winsemius, and T. Wahl (2018), Dependence between high sea-level and high river discharge increases flood hazard in global deltas and estuaries, *Environmental Research Letters*, *13*(8), 084,012, doi:10.1088/1748-9326/aad400.
- Wargula, A., B. Raubenheimer, and S. Elgar (2014), Wave-driven along-channel subtidal flows in a well-mixed ocean inlet, *Journal of Geophysical Research: Oceans*, *119*(5), 2987–3001, doi:10.1002/2014JC009839.
- Wargula, A., B. Raubenheimer, S. Elgar, J.-L. Chen, F. Shi, and P. Traykovski (2018), Tidal Flow Asymmetry Owing to Inertia and Waves on an Unstratified, Shallow Ebb Shoal, *Journal of Geophysical Research: Oceans*, *123*(9), 6779–6799, doi:10.1029/2017JC013625.
- Webb, D. (1978), Non-linear transfers between sea waves, *Deep Sea Research*, *25*(3), 279–298, doi:10.1016/0146-6291(78)90593-3.
- Westerink, J. J., and W. G. Gray (1991), Progress in Surface Water Modeling, *Reviews of Geophysics*, *29*(S1), 210–217, doi:https://doi.org/10.1002/rog.1991.29.s1.210.
- Wolf, J. (1981), Surge-tide interaction in the North Sea and River Thames, *Floods due to high winds and tides*, pp. 75–94.
- Wolf, J. (2004), Coupling waves and currents in POLCOMS with measurements from the coastal observatory, in *Annales hydrographiques*.
- Wolf, J., and R. A. Flather (2005), Modelling waves and surges during the 1953 storm, *Philosophical Transactions of the Royal Society A: Mathematical, Physical and Engineering Sciences*, *363*(1831), 1359–1375, doi:10.1098/rsta.2005.1572.
- Woodworth, P. (2020), Wave setup at tristan da cunha, *African Journal of Marine Science*, *42*(2), 233–245, doi:10.2989/1814232X.2020.1776390.
- Woodworth, P. L., N. J. White, S. Jevrejeva, S. J. Holgate, J. A. Church, and W. R. Gehrels (2009), Evidence for the accelerations of sea level on multi-decade and century timescales, *International Journal of Climatology*, *29*(6), 777–789, doi:10.1002/joc.1771.
- Wu, W. (2014), A 3-D phase-averaged model for shallow-water flow with waves in vegetated water, *Ocean Dynamics*, *64*(7), 1061–1071, doi:10.1007/s10236-014-0739-0, this article is part of the Topical Collection on the 7th International Conference on Coastal Dynamics in Arcachon, France 24–28 June 2013.
- Wu, W.-C., and D. T. Cox (2015), Effects of wave steepness and relative water depth on wave attenuation by emergent vegetation, *Estuarine, Coastal and Shelf Science*, *164*, 443–450, doi:10.1016/j.ecss.2015.08.009.
- Xia, H., Z. Xia, and L. Zhu (2004), Vertical variation in radiation stress and wave-induced current, *Coastal Engineering*, *51*(4), 309–321, doi:10.1016/j.coastaleng.2004.03.003.
- Xia, M., M. Mao, and Q. Niu (2020), Implementation and comparison of the recent three-dimensional radiation stress theory and vortex-force formalism in an unstructured-grid coastal circulation model, *Estuarine, Coastal and Shelf Science*, *240*, doi:10.1016/j.ecss.2020.106771.

- Xie, D.-m., Q.-p. Zou, and J. W. Cannon (2016), Application of SWAN+ADCIRC to tide-surge and wave simulation in Gulf of Maine during Patriot’s Day storm, *Water Science and Engineering*, *9*(1), 33–41, doi:10.1016/j.wse.2016.02.003.
- Xie, L., H. Liu, and M. Peng (2008), The effect of wave–current interactions on the storm surge and inundation in Charleston Harbor during Hurricane Hugo 1989, *Ocean Modelling*, *20*(3), 252–269, doi:10.1016/j.ocemod.2007.10.001.
- Xie, M., C. Zhang, J. Li, S. Li, Z. Yang, H. Zhang, and K. Qu (2021), Flow structure and bottom friction of the nonlinear turbulent boundary layer under stormy waves, *Coastal Engineering*, *164*, 103,811, doi:10.1016/j.coastaleng.2020.103811.
- Xu, Z., and A. J. Bowen (1994), Wave- and Wind-Driven Flow in Water of Finite Depth, *Journal of Physical Oceanography*, *24*(9), 1850 – 1866, doi:10.1175/1520-0485(1994)024<1850:WAWDFI>2.0.CO;2.
- Yanenko, N. N. (1971), *The method of fractional steps*, vol. 160, Springer.
- Yang, S. L., B. W. Shi, T. J. Bouma, T. Ysebaert, and X. X. Luo (2012), Wave Attenuation at a Salt Marsh Margin: A Case Study of an Exposed Coast on the Yangtze Estuary, *Estuaries and Coasts*, *35*, 169–182, doi:10.1007/s12237-011-9424-4.
- Ye, F., et al. (2020), Simulating storm surge and compound flooding events with a creek-to-ocean model: Importance of baroclinic effects, *Ocean Modelling*, *145*, 101,526, doi:10.1016/j.ocemod.2019.101526.
- Yin, K., S. Xu, W. Huang, S. Liu, and M. Li (2021), Numerical investigation of wave attenuation by coupled flexible vegetation dynamic model and XBeach wave model, *Ocean Engineering*, *235*, 109,357, doi:10.1016/j.oceaneng.2021.109357.
- Yoon, J. J. (2014), Non-hydrostatic Modeling of Wave Transformation and Rip Current Circulation: A Case Study for Haeundae Beach, Korea, *Journal of Coastal Research*, (72 (10072)), 184–189, doi:10.2112/SI72-033.1.
- Zhang, M., and Y. Li (1996), The synchronous coupling of a third-generation wave model and a two-dimensional storm surge model, *Ocean Engineering*, *23*(6), 533–543, doi:10.1016/0029-8018(95)00067-4.
- Zhang, W.-Z., F. Shi, H.-S. Hong, S.-P. Shang, and J. T. Kirby (2010), Tide-surge Interaction Intensified by the Taiwan Strait, *Journal of Geophysical Research: Oceans*, *115*(C6), doi:10.1029/2009JC005762.
- Zhang, Y., and A. M. Baptista (2008), Selfe: A semi-implicit Eulerian–Lagrangian finite-element model for cross-scale ocean circulation, *Ocean Modelling*, *21*(3), 71 – 96, doi:10.1016/j.ocemod.2007.11.005.
- Zhang, Y. J., E. Ateljevich, H.-C. Yu, C. H. Wu, and J. C. Yu (2015), A new vertical coordinate system for a 3D unstructured-grid model, *Ocean Modelling*, *85*, 16 – 31, doi:10.1016/j.ocemod.2014.10.003.
- Zhang, Y. J., F. Ye, E. V. Stanev, and S. Grashorn (2016), Seamless cross-scale modeling with SCHISM, *Ocean Modelling*, *102*, 64 – 81, doi:10.1016/j.ocemod.2016.05.002.

- Zhang, Y. J., N. Gerdts, E. Ateljevich, and K. Nam (2020), Simulating vegetation effects on flows in 3D using an unstructured grid model: model development and validation, *Ocean Dynamics*, *70*(2), 213–230, doi:10.1007/s10236-019-01333-8.
- Zheng, F., S. Westra, M. Leonard, and S. A. Sisson (2014), Modeling dependence between extreme rainfall and storm surge to estimate coastal flooding risk, *Water Resources Research*, *50*(3), 2050–2071, doi:10.1002/2013WR014616.
- Zheng, L., R. H. Weisberg, Y. Huang, R. A. Luettich, J. J. Westerink, P. C. Kerr, A. S. Donahue, G. Crane, and L. Akli (2013), Implications from the comparisons between two- and three-dimensional model simulations of the Hurricane Ike storm surge, *Journal of Geophysical Research: Oceans*, *118*(7), 3350–3369, doi:10.1002/jgrc.20248.
- Zheng, X., R. Mayerle, Y. Wang, and H. Zhang (2018), Study of the wind drag coefficient during the storm Xaver in the German Bight using data assimilation, *Dynamics of Atmospheres and Oceans*, *83*, 64–74, doi:10.1016/j.dynatmoce.2018.06.001.
- Zijlema, M. (2010), Computation of wind-wave spectra in coastal waters with SWAN on unstructured grids, *Coastal Engineering*, *57*(3), 267–277, doi:10.1016/j.coastaleng.2009.10.011.
- Zijlema, M., G. Stelling, and P. Smit (2011), SWASH: An operational public domain code for simulating wave fields and rapidly varied flows in coastal waters, *Coastal Engineering*, *58*(10), 992–1012, doi:10.1016/j.coastaleng.2011.05.015.
- Zijlema, M., G. van Vledder, and L. Holthuijsen (2012), Bottom friction and wind drag for wave models, *Coastal Engineering*, *65*, 19–26, doi:10.1016/j.coastaleng.2012.03.002.